Electric Imaging in Weakly Electric Fish and Biomimetic Devices

---

Dissertation

zur

Erlangung des Doktorgrades (Dr. rer. nat.)

der

Mathematisch-Naturwissenschaftlichen Fakultät

der

Rheinischen Friedrich-Wilhelms-Universität Bonn

vorgelegt von

Martin Gottwald

aus Bonn-Bad Godesberg

Bonn 2021

Angefertigt mit Genehmigung der Mathematisch-Naturwissenschaftlichen Fakultät der Rheinischen Friedrich-Wilhelms-Universität Bonn.

1. Gutachter: Prof. Dr. Gerhard von der Emde

2. Gutachter: Priv.-Doz. Dr. Helmut Schmitz

Tag der Promotion: 06.07.2022

Erscheinungsjahr: 2022

Die im Rahmen dieser Dissertation durchgeführten Studien wurden wie folgt veröffentlicht:

1. **Gottwald, M., Matuschek, A. and von der Emde, G.** (2017). An active electrolocation catheter system for imaging and analysis of coronary plaques. *Bioinspiration & Biomimetics* **12**, 015002–1–17.

2. **Gottwald, M., Bott, R.A. and von der Emde, G.** (2017) Estimation of distance and electric impedance of capacitive objects in the weakly electric fish *Gnathonemus petersii*. *Journal of Experimental Biology* **220,** 3142–3153.

3. **Gottwald, M., Singh, N., Haubrich, A.N., Regett, S. and von der Emde, G.** (2018). Electric-Color Sensing in Weakly Electric Fish suggests Color Perception as a Sensory Concept beyond Vision. *Current Biology* **28,** 3648–3658. *

4. **Gottwald, M., Herzog, H. and von der Emde, G.** (2019) A bio-inspired electric camera for short-range object inspection in murky waters. *Bioinspiration & Biomimetics* **14,** 035002–1–10.

* Diese Veröffentlichung wird von der renommierten Post-publication peer review Plattform „Faculty opinions" als signifikanter Beitrag ihres Fachbereichs empfohlen:

Sawtell, N. (2019) Faculty Opinions Recomondation of [Gottwald M et al., Curr Biol 2018 28(22):3648-3653.e2]. In *Faculty Opinions*, *15 Apr 2019*; 10.3410/ f.734423232.793558631.

Table of Contents

Table of Contents

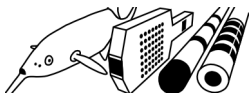

Zusammenfassung

Der nachtaktive und schwach elektrische Fisch *Gnathonemus petersii* besitzt einen aktiven elektrischen Sinn, der es ihm ermöglicht seine trüben Heimatgewässer mittels selbsterzeugter, elektrischer Signale zu erkunden; eine Anpassung die als aktive Elektroortung bezeichnet wird. Tiere, Pflanzen oder Steine, in der näheren Umgebung, verzerren die Signale des Fisches und erzeugen „elektrische Bilder", welche er über seine elektrorezeptive Hautoberfläche wahrnimmt. Die Bildparameter, die *G. petersii* zur Bestimmung von Beutetieren sowie anderer für ihn relevanter Lebewesen verwendet, sind bisher jedoch unbekannt. Ziel dieser Dissertation war es diese Parameter zu untersuchen, verifizieren und sie, neben anderen, für die Entwicklung neuartiger, technischer Geräte zu nutzen.

Elektrische-Bild-Messungen und Verhaltensversuche, in den ersten beiden Studien dieser Arbeit, zeigen, dass der Fisch Beutetiere wie Invertebraten primär durch „elektrische Farben" erkennt. Sie erlauben ihm ebenfalls schwach elektrische sowie andere Fische als auch Pflanzen zu identifizieren. Bestimmte Organismen werden, wie die Messergebnisse nahelegen, zusätzlich anhand ihrer „elektrischen Helligkeit" beurteilt, was mit früheren Verhaltensdaten übereinstimmt. Ausgehend von den hier gewonnenen Erkenntnissen lässt sich zum einen vermuten, dass neben *G. petersii* auch die vielen anderen nachtaktiven, invertivoren Arten elektrische Farben erkennen und somit ihre kritische Futter-Nische erschließen. Die Verarbeitung farbartiger Parameter im aktiven elektrischen Sinn zeigt zum anderen, dass es sich bei Farbwahrnehmung um ein sensorisches Konzept handelt das nicht auf passive und visuelle Sinnessysteme beschränkt ist.

In den letzten beiden Studien dieser Arbeit wurden Prototypen einer elektrischen Kamera für Objektinspektionen in trüben/dunklen Gewässern sowie eines Kathetersystems zur Diagnose arteriosklerotischer Plaques in Koronararterien entwickelt und getestet. Analog zum Fisch analysieren beide Systeme ihre Zielobjekte durch elektrische Bilder und deren Parameter. Die Kamera berechnet elektrische Farben und, über relative Steigungen, den Grad der Bildunschärfe; das Kathetersystem die Peaks der elektrischen Bilder sowie ihre rel. Steigungen. Die Testversuche zeigten, dass der Kamera-Prototyp in der Lage ist Organismen wie Fische und Pflanzen als auch Metall- oder Plastik-Objekte zu unterscheiden und Objektentfernungen zu übermitteln. Die grobe Form der Testobjekte konnte darüber hinaus durch deren „elektrische Umrisse" bestimmt werden – einen neuen

Bildparameter – der im Umkehrschluss auch von *G. petersii* genutzt werden könnte, um Form und Orientierung eines Objektes einzuschätzen. Das Kathetersystem absolvierte Testreihen in denen synthetische Versionen kleinerer bis hin zu Hochrisiko-Plaques erkannt und differenziert werden konnten. Die erfolgreichen Tests beider Elektroortungssysteme deuten an, dass sie, in ausgereifter Form, medizinische und industrielle Abläufe verbessern können. So ließe sich mit einem günstigen Elektroortungs-katheter die derzeit, durch hohe Kosten, eingeschränkte Diagnose von Hochrisiko-Plaques maßgeblich erhöhen, mitsamt der Chance tödliche Komplikationen dieser Plaques in vielen Patienten abzuwenden. In schnellwachsenden, ernährungsrelevanten Industrien wie beispielsweise Aquakulturen könnte die elektrische Kamera zu beliebigen Tages/Nachtzeiten, ohne künstliche Beleuchtung, defekte Netzkäfige erkennen und damit tierschonender Fisch/Produktionsverlusten vorbeugen.

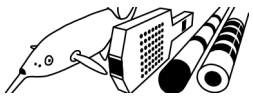

Summary

The nocturnal and weakly electric fish *Gnathonemus petersii* inspects its murky habitats by self-generated electric signals; an adaption called active electrolocation, enabled by the fish's active electric sense. Animals, plants or stones it encounters modulate the fish's emissions, evoking electric images across its electroreceptive skin. Yet, the cues *G. petersii* derives from these images to determine prey and other relevant organisms remain unknown. Revealing and verifying them experimentally as well as adapting them, along with others, for bio-inspired devices were the two goals of this thesis.

The electric image recordings and behavioral assays presented in the thesis' first two studies show that the fish primarily identifies its invertebrate prey via 'electric colors'. These cues also allow *G. petersii* to recognize weakly electric or other fishes and plants. According to the recording results, the fish may further judge some organisms by their 'electric brightness', which is also supported by previous behavioral data. Given the findings above, it can be assumed that besides *G. petersii* many other species of weakly electric fish do sense electric colors and thereby occupy their nocturnal invertebrate-feeder niche. On a broader scope, these color-like cues, determined in an active electrosensory system, suggest 'color' perception as a sensory concept beyond vision and passive sensing.

In the thesis' two final studies, prototypical versions of either an 'electric camera' for object inspections in murky waters or a low-cost catheter system to diagnose atherosclerotic plaques in coronary arteries were developed and tested. Like the fish, they analyze their targets via simple electric image parameters, i.e., electric colors and relative slopes – depicting image blurring – (in the electric camera) or image peaks and rel. slopes (in the catheter system). In doing so, the camera prototype was able to identify nearby fish, plants or metal and plastic objects and to infer object distances. It could also gauge the targets' basic shapes via 'electric outlines' – a novel image cue –, which, in turn, might also be used by *G. petersii* to estimate a target's geometry and orientation. The catheter system did detect and determine individual types of synthetic plaques, mimicking real low-to-high-risk ones. As suggested by these two successful proofs concepts, mature versions of the devices above should have the potential to improve medical and industrial routines. The use of inexpensive electrolocation catheters, in daily clinical practice, could significantly enhance, the otherwise costly and thus limited, identifications of high-risk plaques along with the chance of preventing their fatal complications in various patients. On the other

hand, in increasingly relevant food industries like aquacultures the electric camera could detect damaged net cages, anytime without any sort of lighting, which would save fish stocks without disturbing them.

I. General Introduction

1. Sensory ecology

The reception of and response to specific environmental cues is crucial for animals in many ways, e.g., finding food, avoiding predators, mating, communication and orientation. Only sensory systems that are adapted to an animal's environment can enable such actions, critical for survival and reproduction. Among organisms, different types of senses have evolved to cope with the individual characteristics of their habitats and to extract relevant information (e.g., from light, sound, chemicals, mechanical, magnetic or electrical stimuli) (Stevens, 2013).

Passive senses capture stimuli from biotic and abiotic environmental sources. Active senses, in contrast, process a self-generated signal of an animal (Nelson and MacIver, 2006), which is modulated by the surroundings. An example of a common, passive sensory system is the visual sense. It is beneficial in various habitats (aquatic and terrestrial) and is consequently found within the animal kingdom with a wide range of modifications (e.g., Cronin and Bok, 2016; Marshall and Cronin, 2011; Warrant and Locket, 1999). Active and 'exotic' senses like the active electric sense of weakly electric fish represent additional, highly-specific adaptions to environments and lifestyles (e.g., nocturnality) that are challenging for passive sensing (e.g., Lissmann, 1963; von der Emde, 2006).

As a scientific discipline, sensory ecology explores the way such 'ecologically-shaped' sensory systems work and how animals use them to obtain relevant sensory information. It therefore covers the physiological, neuronal and computational principles as well as the behavioral strategies used for information processing (Stevens, 2013). In this context, the active electric sense is a fascinating subject to investigate as it provides a highly specialized sensory system, whose computational and behavioral strategies, however, bear interesting similarities to those of other senses (especially vision).

2. The active electric sense in weakly electric fish

The active electric sense has evolved independently in two orders of teleost weakly electric fish (Crampton, 2019; Lavoué et al., 2012). The Mormyriformes, endemic to

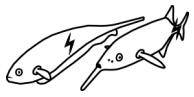

Africa, and the Gymnotiformes, native to South America, contain similar numbers of species (Mormyriformes ~229; Gymnotiformes ~244) (Crampton, 2019). Both groups employ their active electric sense, e.g., for foraging and navigation, which is termed active electrolocation (e.g., Lissmann and Machin, 1958; Nelson et al., 2002; Schumacher et al., 2017b; von der Emde and Bleckmann, 1998; Walton and Moller, 2010). In addition, it is used for species and sex recognition and social interactions during 'electrocommunication' (e.g., Benda et al., 2013; Gebhardt et al., 2012; Henninger et al., 2018; Hopkins, 1988).

As both Mormyriformes and Gymnotiformes rely on active electrolocation for probing their surroundings, the active electrosensory system can be considered partly as an adaption to similar habitat conditions. The natural habitats of weakly electric fish are tropical fresh water streams, rapids, flood plains or swamps, where usually vision is hindered by murky water (Crampton, 2011; Crampton, 2019; Moritz, 2010).

The low conductivity of the water (usually below 100 $\mu S\ cm^{-1}$), however, enables these fish to efficiently build up weak electric fields during active electrolocation (Crampton, 2019; Moller, 1980). The electric field around the fish is generated when the animal emits an electric signal by discharging its electric organ (EO) (Lissmann, 1958). Electric organs of Mormyriformes are short and located in the trunk of the tail, whereas Gymnotiformes can feature larger electric organs, which expand in length almost throughout the entire fish body (Bennett, 1971a). The 'electric organ discharges' (EODs) of weakly electric fish are either continuous, almost sinusoidal wave signals or short electric pulses, separated by pauses (Bass, 1986). In general, Mormyriformes are referred to as 'pulse-type' and Gymnotiformes as 'wave-type' electric fish. Exceptions, however, are found for some gymnotiform and one mormyriform species (Bass, 1986).

The self-generated electric field is sensed by high-frequency (tuberous) electroreceptor organs, distributed within the fish skin and tuned to the fish's electric signal (Zakon, 1986). Local field perturbations caused by nearby objects are 'projected' onto the electroreceptive epithelium and analyzed by the animals as so-called electric images (Caputi et al., 1998; Heiligenberg, 1975; Rasnow, 1996). Electrosensory cues derived from electric images enable the fish to estimate an object's position, distance, size, shape, and electrical properties (i.e., resistive, capacitive components and derived electrical impedance) (Assad et al., 1999; Rasnow, 1996; von der Emde and Schwarz, 2002). Most object properties acquired by active electrolocation are therefore analogous

to features, which are usually obtained through vision in sighted animals.

Electric and optical images, however, are fundamentally different. In the vertebrate eye, light is focused onto the retina through an adjustable lens, creating sharp visual images with contours and details of an object. As the active electric sense lacks such a focus mechanism, electric images on the fish body are always blurred (Rasnow, 1996; von der Emde, 2006) and have a fuzzy outline. They also do not resemble the optical representation of an object as electric images are heavily distorted in comparison. Here, the image profile is not only sculpted by the object properties, mentioned above, but also by the physical properties of the electric field, the shape and electrical impedance of the fish body and many other features (Caputi et al., 1998; Caputi et al., 2011; Caputi et al., 2002; Migliaro et al., 2005; Pusch et al., 2008).

As a result, electric images of the same object can change at different body regions of a fish (Caputi et al., 2011). Even when examined at only a single body location electric images are ambiguous because there are no simple one-to-one associations of image and object features (Assad et al., 1999; Rasnow, 1996; von der Emde, 2006).

To resolve electrosensory ambiguities, weakly electric fish may use various computational and behavioral strategies. For example, the unambiguous evaluation of a single object feature requires an integration of several parameters of an electric image (Assad et al., 1999; Rasnow, 1996; von der Emde and Schwarz, 2002). The fish also approach or swim by an object and perform stereotyped movements in front of it. In doing so, they proposedly analyze the induced changes in consecutive electric images for object inspection (Babineau et al., 2007; Fujita and Kashimori, 2019; Hofmann et al., 2017; Nelson and MacIver, 1999; Pedraja et al., 2018; Sim and Kim, 2011; Sim and Kim, 2012). Especially mormyrid fish conduct these so-called probing motor acts (Toerring and Belbenoit, 1979). Probing motions may also be used to optimize sensory acquisition within the short operational range that electric imaging provides (e.g., Hofmann et al., 2014; Pedraja et al., 2020). This is only a few centimeters as the animals' electric fields decay rapidly in the water, i.e., with a power function of distance (Chen et al., 2004; Knudsen, 1975; Pedraja et al., 2014; Westby, 1984).

Despite its rather short perceptual range, the active electric sense provides crucial advantages for weakly electric fish to compete/survive in their respective fresh water habitats:

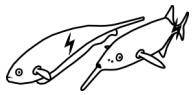

- Orientation (and communication) by self-generated electric fields enables a nocturnal lifestyle, which is beneficial for avoiding diurnal predators (e.g., other fish or birds) (e.g., Crampton, 2019; Lissmann, 1963).
- Unlike visual or acoustic signals, EODs are not distorted by turbid, noisy or fast streaming water (e.g., Crampton, 2019; Krahe, 2019).
- Instead, EODs are altered in their form/timing by electrical capacitive objects (von der Emde, 1990; von der Emde, 1998), which in the fishes' habitats are living organisms. This emphasizes such targets, e.g., prey insect larvae on and within the ground, during active electrolocation.
- As large portions of the fish bodies are electroreceptive, active electrolocation provides an 'omnidirectional electric view' (e.g., Snyder et al., 2007). This may improve foraging and close-up orientation.

Due to the features mentioned above, mormyriform and gymnotiform weakly electric fish occupy similar and convergent ecological niches. Both groups are principally nocturnal, benthic foragers of aquatic invertebrates (such as insect larvae and others) (Crampton, 2019; Winemiller and Adite, 1997).

One of the best-studied model organisms for exploring active electrolocation is the mormyrid 'elephant nose fish' *Gnathonemus petersii* (Günther 1862). Over the past 50 years, its electrosensory system has been investigated by applying various complementary methodologies. Anatomical and physiological work on the electric and receptor organs and brain structures has revealed stimulus features and their neuronal representation in *G. petersii* (e.g., Bell, 1989; Bell, 1990a; Hollmann et al., 2016; Maler et al., 1973; Meek et al., 1999; von der Emde and Bleckmann, 1997). Based on recording and modeling of the fish's electric field and object-evoked electric images, mechanisms for unequivocal object analysis (mainly distance perception) have been identified or hypothesized (e.g., Hofmann et al., 2017; von der Emde and Engelmann, 2011; von der Emde et al., 1998). The performance and roughly the motor behavior of electrolocating fish during distance, shape and electrical impedance discrimination has been addressed in behavioral experiments (e.g., Fechler, 2016; von der Emde, 1990; von der Emde and Fetz, 2007). Studies with a stronger focus on the fish's motor behavior were also conducted (e.g., Hofmann et al., 2014; Pedraja et al., 2020) recently. These findings combined provide a strong knowledge base for verifying sensory

concepts of electric imaging. In this thesis, active electrolocation in *G. petersii* is investigated by an interdisciplinary approach with regard to two consecutive goals. First, in the context of sensory ecology, electric imaging concepts are explored to uncover how the active electric sense enables the fish's efficient probing and recognition of its crucial environmental targets like prey. Second, identified principles of electric imaging are adapted for a usage in technical devices.

3. Biomimetics

In recent years, 'biomimetics' has become an emergent scientific branch, accompanying organismic research. Labeled by Schmitt in the 1960s (Harkness, 2002; Schmitt, 1969), it represents the study and technological imitation of biological mechanisms and processes (Bar-Cohen, 2005).

One purpose to make biomimetic devices is to invent new technologies for tasks that can't be performed by current methods. Furthermore, adding a bio-inspired design or function to existing devices might improve their performance. Unlike in conventional engineering approaches, processes/mechanisms within or applied by organisms have been fine-tuned over billions of years of evolution. Such 'biological designs', achieved through evolutionary processes, can be very different from man-made designs, which are usually built from scratch to serve a predefined task.

Probably the best-known bio-inspired technology that made its way into a commercial product is the Velcro® fastener, derived from the burr hooks attachment mechanism (Bar-Cohen, 2005; Hwang et al., 2015). The self-cleaning surface structure of the lotus leave is another example of a biological principle 'lotus effect' (Barthlott and Neinhuis, 1997) that was successfully commercialized. It was adapted for a dirt- and water-repellent house paint (Lotusan®).

Even though the number of bio-inspired commercial products or materials is rather limited, biomimetic-engineering approaches have become of increasing relevance in industry. Thus, more companies focus on biomimetics to develop concepts for innovative products and services (e.g., the German technology company Festo that recently invented a handling assistant inspired by the elephant trunk (Grzesiak et al., 2011)). In mid-2005, DaimlerChrysler introduced a concept car based on the shape and aerodynamics of the boxfish providing outstanding fuel efficiency (Hwang et al., 2015). Analysts estimate

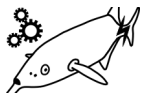

biomimetic products and services to reach a market size of $1 trillion by 2025 (Hwang et al., 2015).

To make bio-inspired devices two basic approaches can be applied. In the 'top-down approach' the task or technical problem is identified prior to screening organisms or processes in nature for a possible solution (Speck and Speck, 2008). In the 'bottom-up approach', which is used in this thesis, the initial focus lies on the examination of an organism or mechanism. Derived biological principles are then directly adapted or abstracted and implemented into technical designs that respond to a human problem (Speck and Speck, 2008). Usually these first steps of organismic research, technical abstraction and prototyping are performed by biologists or by an interdisciplinary group of researchers (e.g., biologists, physicists, chemists, engineers etc.). Prototypes of biomimetic devices are then used in basic experiments on a laboratory scale to show a proof of concept. This often takes several years of development and testing. When successful, academic research institutes might cooperate with industrial partners to optimize the achieved product design, production techniques and costs of commercialization (Speck and Speck, 2008).

Following an organismic-driven approach of biomimetics in my thesis, I initially analyzed imaging concepts of electrolocating *G. petersii*, which were then integrated into prototypical active electrolocation sensors. As active electrolocation enables efficient object explorations in rapid, murky and confined aquatic surroundings, sensors that work accordingly could do so in such or similarly challenging environments. Here, I focused on two main topics. First, a prototype of an active electrolocation camera was designed for object inspections in murky waters. Second, prototypical active electrolocation catheters were tested for an invasive inspection of blood vessels (i.e., the analysis of atherosclerotic plaques in arteries). The functionality of both biomimetic sensor systems was verified in basic experiments for a proof of principle.

II. Electric Imaging in *Gnathonemus petersii*

4. Introduction – Active electrolocation

4.1 *Gnathonemus petersii*

The elephant nose fish *G. petersii* (figure 4.1A) of West and Central Africa inhabits a wide range of freshwater habitats like savanna-dry or moist forest rivers (figure 4.1B) and floodplains (Moritz, 2010; Nwani et al., 2011; Ogbeibu and Ezeunara, 2002). Most of these environments feature rather fast flowing water of reddish color and with low electrical conductivity (below 100 µS cm^{-1}) (Moritz, 2010; Ogbeibu and Ezeunara, 2002; Ogbeibu and Ezeunara, 2005). These waters were also reported to have a relatively high turbidity (Ogbeibu and Ezeunara, 2002; Ogbeibu and Ezeunara, 2005), which might occur due to seasonal floods that increase the amount of dissolved or floating particles. Usually the water surface is shaded by nearby vegetation, which limits the surface light. *G. petersii* is typically found under roots and within holes or vegetation and stays in or close to the areas of faster water flow (Moritz, 2010). It is active at dusk and night and hides throughout the day. The fish's active and passive sensory systems are well adapted to the environmental conditions, mentioned above, and its crepuscular-nocturnal lifestyle.

The visual system of *G. petersii* has a poor spatial resolution (minimal visual angle of about 3°) but high temporal resolution, which renders it insensitive to distractions of the particle-rich water and makes it very effective in detecting distant, large and fast-moving objects (e.g., predators) (Kreysing et al., 2012; Pusch et al., 2012; Schuster and Amtsfeld, 2002). It is also optimized for dim light vision (Kreysing et al., 2012). In turn, the dominant sense for close-up object recognition (Schumacher et al., 2017a) and prey identification (von der Emde and Bleckmann, 1998) is the active electric sense.

For active electrolocation the fish discharges its electric organ located in the peduncle of the tail. It is organized into four columns (figure 4.1C). Each column is serially stacked with up to 170 electrocytes (Bruns, 1971; Westby, 1984). Derived from skeletal muscle, electrocytes do no more contribute to tail movements via contraction. Instead, they generate the EOD signal by synchronously changing their membrane potential when excited. The electric field, surrounding the fish with each EOD, stimulates the electroreceptive skin of the animal, which covers its head, back and stomach (figure 4.1C). In these areas electroreceptor organs, termed mormyromasts (Szabo and Wersäll, 1970), are spread with varying density (Hollmann et al., 2008; von der Emde and Schwarz, 2002).

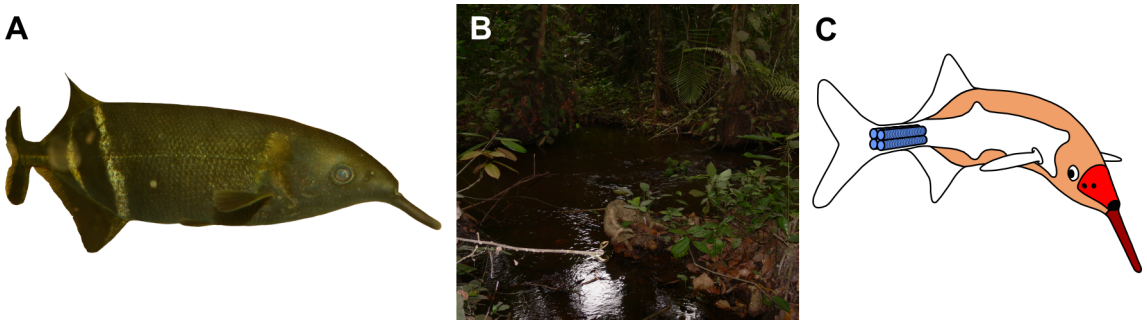

Figure 4.1: *Gnathonemus petersii* – Habitat and basic electrogenic and electrosensory adaptions.
(A) *G. petersii* (photo by Jacob Engelmann). **(B)** The fish inhabits red-colored and fast flowing forest creeks, shaded by vegetation, like the Iguidi river in Benin (photo by Vivica von Vietinghoff). **(C)** Scheme of the fish's basic electrogenic (blue) and electrosensory (red) adaptions for active electrolocation. Within the tail fin the electric organ (blue) is indicated, which generates the electric field. It consists of four cell columns. Electrosensory parts of the fish's skin surface are shown in shades of red. The fish's chin appendix (dark red) and the 'nasal region' (red) above the open mouth (black) constitute two electroreceptive foveae. The electroreceptive skin further covers the side of the fish's head, the back and stomach (light red). Figure 4.1C was prepared based on the information provided by (Hollmann et al., 2008; von der Emde and Schwarz, 2002; Westby, 1984).

It is highest (up to 65 organs per mm^2) at the tip of the fish's movable chin appendix (figures 4.1A and 4.1C). A moderate number of mormyromasts (~4.6 organs per mm^2) is still maintained in the area above the mouth, referred to as the 'nasal region' (figure 4.1C). A significantly lower density (~1.4 organs per mm^2) occurs at the rest of the head and the trunk's electroreceptive skin (Pusch et al., 2008; von der Emde and Schwarz, 2002). Besides mormyromasts the fish also has other epidermal electroreceptor organs (e.g., Hollmann et al., 2008). 'Ampullary' sense organs are used for low-frequency 'passive electrolocation'. They detect faint electric stimuli that emanate from aquatic organisms or are caused by abiotic sources (Derbin, 1974; Engelmann et al., 2010; Moller, 1995). 'Knollenorgans' enable electrocommunication with conspecifics (Bell, 1989; Derbin and Szabo, 1968).

While the fish uses its whole mormyromast epithelium for the electric imaging of objects, the chin appendix and the nasal region proposedly act as electric foveae (von der Emde and Schwarz, 2002). Often, a sensory fovea has a higher concentration of receptors compared to other contiguous sensory regions (e.g., Castelló et al., 2000; Cronin et al., 2014; Pettigrew and Frost, 1985). In addition, it is usually associated with morphological

specializations or structures that improve the stimulus and its perception (e.g., Bringmann, 2019; Castelló et al., 2000; Covey, 2005).

In *G. petersii*, as a result of its low inner resistance (Caputi et al., 1998) and its skin resistance and capacitance increasing from the back to the fish head (Migliaro et al., 2005; von der Emde and Schwarz, 2002), the slender fish body basically drags the electric field to the front of the animal. The low resistance of the steadily opened mouth even enhances this effect. It also leads to a very stable and homogenous distribution of the electric field along the nasal region (Pusch et al., 2008).

During foraging, the nasal region spots obstacles and items in front of the animal. The chin appendix is used for close-up inspections of the details of electrolocation targets. Its main function, however, is the electric imaging of small prey insect larvae (mainly chironomid larvae (Nwani et al., 2011), which are buried in the soil (von der Emde and Bleckmann, 1998; von der Emde et al., 2008). To do so, the fish scans the ground with the tip of the chin appendix, while moving the whole appendix from left to right and back in stereotyped fashion (von der Emde et al., 2008). The elongated shape of the chin appendix enhances the electric field at the chin's tip, where it remains stable even during chin movements (Pusch et al., 2008). Serving as an almost finger-like digging device (Amey-Özel, 2018) the chin appendix is also used to uncover identified prey items from the ground, which are then sucked into the fish's mouth.

4.2 Generation of electric images

The EOD signal (figure 4.2A), which is used by *G. petersii* to scan the environment, is a short (~400 µsec.) and basically biphasic current pulse with an initial positive and a second negative phase. Its amplitude, form ('waveform') and duration are determined by the morphology and physiology of the fish's electric organ (Harder et al., 1964; Westby, 1984). During active electrolocation the fish varies the repetition rate of the EODs generated. When *G. petersii,* for example, encounters an object of interest, it will increase the EOD repetition rate (up to ~80 Hz) to receive more electric images for object analysis (Hofmann et al., 2014; Hofmann et al., 2012; von der Emde and Schwarz, 2001). The electric field, which forms around the fish during EOD emission, is dipole-like and asymmetric (figure 4.2B) (von der Emde and Schwarz, 2001). It has a smaller pole at the fish's tail (figure 4.2B, bluish colors) and a larger pole that covers the whole fish body in

front of the electric organ (figure 4.2B reddish colors). The current induced by the electric organ flows through the fish and through the water back into the fish body (see vectors of electric field lines in figure 4.2B). The morymromasts are excited by the electrical current, which locally runs through them (Bennett, 1971b; Shuai et al., 1998). Because this is driven by the local transepidermal voltage (i.e., the voltage across the skin) (Migliaro et al., 2005), each mormyromast basically analyses the local EOD (lEOD) at its given skin position (Bennett, 1971b; Caputi et al., 1998; Shuai et al., 1998; von der Emde, 1990). All the mormyromasts, together, monitor a 'pattern' of lEODs along the fish skin.

When the animal is only surrounded by water, the electric field and lEOD pattern are stable. A nearby object, however, with different electrical impedance than water, perturbs the electric field (von der Emde and Schwarz, 2001). This will modulate the lEOD pattern

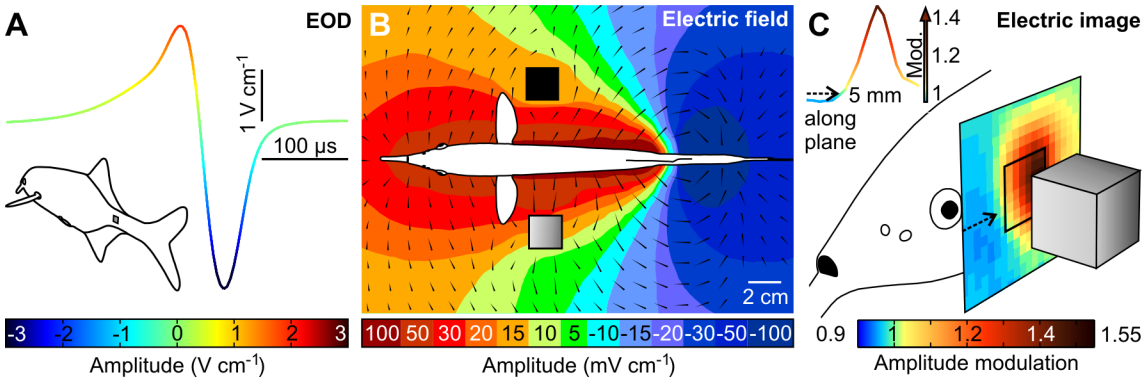

Figure 4.2: Electric image generation during active electrolocation in *G. petersii*.

(A) Electric signal (EOD) of a *G. petersii* (amplitude of the trace is shown color-coded). The local, biphasic EOD signal (lEOD) was recorded close to the fish's electric organ (indicated by the gray rectangle at the tail) (recording by M. Gottwald). **(B)** Electric field around the fish when an EOD is emitted (recorded during the peak amplitude of the first positive lEOD phase and within a horizontal plane at the fish's mid-body height). Electric field potential is shown color-coded and black arrowheads indicate the direction of electric field lines. A plastic (black) and a metal cube (gray) modulate the local field and thereby lEOD amplitudes at the electroreceptive fish body immediately adjacent to the objects. Figure 4.2B was redrawn after (von der Emde and Schwarz, 2001) **(C)** Electric image of a metal cube (268 mm^3, gray) at 5 mm object-to-fish distance. The cube-evoked modulations of the lEOD peak-to-peak (PP) amplitudes, which form the electric image on the fish skin, were recorded within a vertical plane close to the fish head (2-D electric image). The black rectangle shows the relative alignment of the cube to the measuring plane. The dashed arrow indicates a single row of modulations (1-D electric image), whose roughly 'bell-shaped' profile is shown at the top left as color-coded trace. For a detailed description of the electric image's center-surround ('Mexican hat') profile see main text. Figure 4.2C was prepared based on recording data provided by (Bott, 2014, supervised by M. Gottwald).

locally at the skin region opposite to the object. In other words, the object 'projects' an electric image onto the fish skin.

G. petersii likely computes the electric image modulations in the brain by relating the change produced by the object to the previous condition without the object present (Bell, 1989).

Experimentally, electric image formation has been investigated with artificial and electrical purely resistive objects, made of plastic or metal. A metal cube with a much higher conductivity than water attracts the electric field lines (figure 4.2B). On the fish body, a central region of concentrated electrical current surrounded by an area of reduced current density will form. A plastic cube, as an electric insulator, scatters the field lines (figure 4.2B) and thus causes the opposite effect. The mormyromasts will detect an increase of lEOD amplitudes, wherever current is condensed and a reduction in lEOD amplitudes, wherever current density is lowered on the fish skin.

Electric images that are formed by such lEOD amplitude patterns can be obtained by recording experiments, when moving an electrode at close distance along the fish skin (Fechler and von der Emde, 2012; Hofmann et al., 2012; Pusch et al., 2008; von der Emde et al., 1998). Amplitude modulations of the image are then calculated by dividing the object-evoked lEOD amplitudes by those recorded in the absence of the object. As an example, the electric image of a small metal cube is shown in figure 4.2C.

Within the image, modulations of 1 (green area, figure 4.2C) are a baseline ('basal condition'), which indicates that lEOD amplitudes obtained with and without the object do not differ. Consequently, the magnitude of such modulations, from a 'basal image region', is negligible small (equals zero). The basal region usually lies in between the image's center and rim (figure 4.2C). Modulations larger than 1 (yellow-red areas, figure 4.2C) in the image center depict the relative increase and modulations smaller than 1 (blue areas, figure 4.2C) at the reverse image rim depict the relative decrease of lEOD amplitudes evoked by the cube. Pronounced image modulations in both directions (larger or smaller 1) become stronger the more they deviate from 1 (basal condition).

Note that a plastic cube will generate an inverted but not exactly mirrored electric image compared to a metal cube (von der Emde, 1999b). The basic center-surround organization of the electric images is termed a Mexican hat profile (Caputi et al., 1998).

The individual appearance of an electric image varies according to the body region onto which it is 'projected' and the shape, size and distance of the projecting object. Electric

image profiles that form under such different conditions were depicted in recording and also modeling studies for resistive objects (Budelli et al., 2002; Caputi et al., 1998; Gómez-Sena et al., 2014; Pusch et al., 2008; von der Emde, 1999b; von der Emde et al., 1998). For simplification, only the electric image modulations within a single line along the fish skin were used to reference the image profile. Most of these 'one-dimensional' electric images do roughly resemble bell-shaped curves (figure 4.2C).

At the flat trunk of the animal objects with sharp edges (e.g., metal cubes) produce electric images with steep flanks, whereas at the curved forehead their image profile becomes less steep. In comparison, the image of a curved object (metal sphere) is less steep at the trunk region and gets steeper at the forehead (compare Budelli et al., 2002; Gómez-Sena et al., 2014; Pusch et al., 2008; von der Emde et al., 1998). Close to the fish skin an object will evoke a steeper and narrower electric image with stronger modulations than the same object located farther away. Thus, at farther distance its electric image will get 'blurrier' as it decreases in modulation magnitude and becomes less steep and more broad (e.g., Caputi et al., 1998; von der Emde, 1999b).

The size of an object will also affect an electric image in many ways. For example, compared to the electric image of a large metal cube or of a large conductive cylinder that of a small one will have weaker modulations, less steep flanks and it will also be narrower (Budelli et al., 2002; von der Emde et al., 1998).

Electric image profiles become even more complex when they are evoked by multiple and closely aligned objects. For two metal cubes, next to each other, their electric images will fuse and generate an 'inverted-w-shaped' profile (Fechler et al., 2012; Rother et al., 2003). When positioned behind one another the cubes will evoke a bell-shaped electric image (Rother et al., 2003). In addition, the presence of larger backgrounds, other than water, can alter the electric images of objects (Fechler and von der Emde, 2012).

4.3 Peripheral and central processing of electric images

In *G. petersii* the basic features of the electrosensory input (i.e., the lEOD pattern at the fish skin) are already processed by the mormyromasts (in the electroreceptive periphery). Each mormyromast transduces two different properties of the lEOD, the peak-to-peak (PP) amplitude and the lEOD waveform (figure 4.3A) (Bell, 1990b; von der Emde and Bleckmann, 1992; von der Emde and Bleckmann, 1997). Electrical purely resistive objects

of the fish's environment (e.g., stones, dead driftwood etc.) or experimentally used metal and plastic objects only affect the lEOD (PP) amplitudes. Crucially, living organisms with additional capacitive properties (e.g., other animals, water plants and prey insect larvae) cause both, lEOD (PP) amplitude changes and alterations or 'distortions' of the lEOD waveforms (figure 4.3A) (von der Emde, 1990; von der Emde and Schwarz, 2002). Waveform distortions are a result of capacitive objects acting like a filter on the frequency components of the lEODs, inducing attenuations and phase shifts (von der Emde, 1990).

The amplitude and waveform sensitivity of the mormyromast is based on its special morphology and physiological characteristics. Within the fish skin the organ forms a two-chamber system (schematically shown in figure 4.3B) with an outer and inner sensory chamber (Szabo and Wersäll, 1970). Both are joined via a small canal. The outer chamber is connected to a pore on the skin surface by a plug of loosely packed epidermal cells (Bell et al., 1989). Each sensory chamber contains different types of electroreceptor cells (Szabo and Wersäll, 1970). The so-called A-cells are exposed to the bottom of the outer chamber with only the small tip of their apical membrane (figure 4.3B). The type B sensory cells (B-cells) extend into the inner chamber with a large portion of their apical membrane, which is covered with microvilli (figure 4.3B) (Bell et al., 1989; Szabo and Wersäll, 1970). Both cell types are innervated by nerve fibers, one afferent fiber for all B-cells and two afferent fibers for the A-cells of a mormyromast (Bell et al., 1989; Szabo and Wersäll, 1970). Electrophysiological recordings of the type A and B afferent fibers revealed that A-cells are pure amplitude coders, whereas B-cells code lEOD amplitude and waveform combined (von der Emde and Bleckmann, 1992). In addition, B-cells were found to be tuned to characteristic waveform distortions, as caused by underwater organisms (von der Emde and Bleckmann, 1997).

Suggested by a follow-up modeling study, the functional difference between A- and B-receptors results from their different morphology (mentioned above) and different membrane properties (i.e., capacitance and conductance) (Shuai et al., 1998).

The afferent fibers from all mormyromasts project to the electrosensory lateral line lobe (ELL) in the hindbrain, which is the first central processing stage of electrosensory information (figure 4.3C). This cerebellum-like structure is organized into three separate zones. Only two of them receive mormyromast input. The medial zone exclusively gains amplitude information from A-cell afferents. Combined amplitude and waveform information from B-cell afferents is transmitted to the dorsolateral zone (Bell and Szabo,

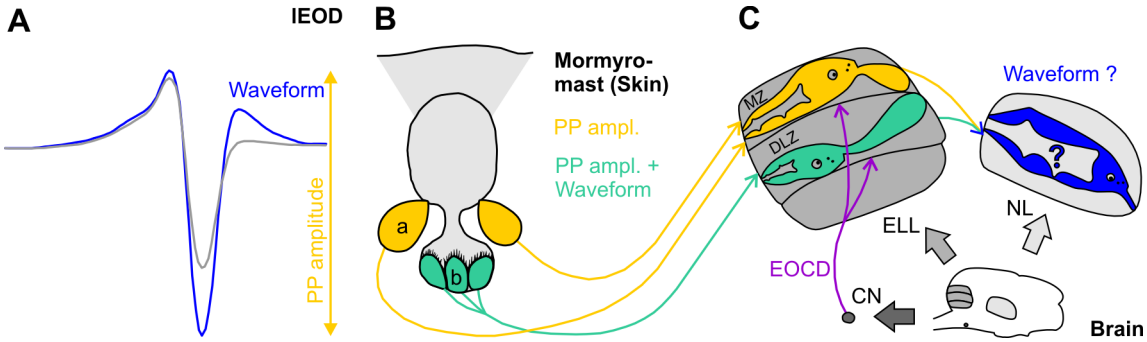

Figure 4.3: Processing of electrosensory information.

(A) Local EOD (gray) at the fish skin, which is modulated in its peak-to-peak (PP) amplitude (yellow) and waveform (blue) by a nearby object. **(B)** Scheme of an electroreceptor organ (mormyromast) in the fish skin. Receptor cells respond to the lEOD's PP amplitude (a, A-cells) or PP amplitude plus waveform (b, B-cells). For further details see main text. **(C)** Early stages of the electrosensory pathway in the fish brain. Somatotopic maps of the fish body (see sketches) are formed by mormyromast amplitude information (yellow) in the medial zone (MZ) or by waveform plus amplitude information (green) in the dorsolateral zone (DLZ) of the electric lateral line lobe (ELL, gray). While a sketch roughly illustrates a map's orientation and the central overrepresentations of certain body parts, it does not reflect that each somatotopic representation fully occupies its respective ELL zone. MZ and DLZ also receive an efference copy of the fish's EOD, called electric organ corollary discharge (EOCD, purple), a neuronal signature relayed from the brains command nucleus (CN, dark gray). EOCD and mormyromast input combined may provide a 'modulation pattern' in both ELL maps. MZ and DLZ inputs join within the Nucleus lateralis (NL, light gray) where another but 'coarser' body map (blue sketch) is formed, which likely contains waveform information. While the sketch roughly indicates the map's orientation, it may not necessarily reflect other anatomical details (most of which are at present unknown). Figure 4.3 was prepared based on the information provided by (Bacelo et al., 2008; Gottwald et al., 2017a; Hollmann et al., 2016; von der Emde et al., 2008; Zeymer et al., 2018).

1986; Bell et al., 1989). Both zones have a somatotopic arrangement (Bell and Russell, 1978; Bell and Szabo, 1986). Thus, their electrosensory input forms a topographic map of the fish's electroreceptive body regions. In both maps, the projections from the chin appendix and the nasal region (the two foveae) occupy disproportionally larger areas than those from the trunk (Bacelo et al., 2008) (figure 4.3C). Such central overrepresentations of foveal sensory areas are also found in other sensory systems, e.g., in the visual system of mammals (e.g., Azzopardi and Cowey, 1993).

In addition to the projections from the fish skin, the ELL network indirectly receives input from the brain's EOD command nucleus (CN), which controls the fish's electric organ. When it signals the electric organ to discharge, a copy of this neuronal signature, termed the electric organ corollary discharge (EOCD), is relayed to the ELL and combined with

the present mormyromast afferent input (Bell, 1986; Bell, 1989) (figure 4.3C).

The EOCD is modified by past electrosensory information (Bell, 1989) and thus might reference to it in the ELL. It therefore can be suggested that the ELL networks might be able to relate the current electrosensory input (e.g., in the presence of an object) to the recent sensory past (e.g., without the object present). Hypothetically, this would provide a 'modulation pattern' within both ELL zones, from which object-evoked electric images could be acquired.

Accordingly, the electric image of a resistive object would form in the ELL medial and dorsolateral zone by the object-evoked amplitude modulations. An electric 'amplitude' image of a capacitive object would be restricted to the medial zone as it receives solely amplitude input instead of the target's combined amplitude and waveform information reaching the dorsolateral zone.

The pure waveform component of the dorsolateral zone's input (and conceived modulation pattern) is not likely decoded at the level of the ELL (von der Emde and Bell, 1994). Even though a somatotopic interconnection of both ELL zones exists and interzonal information processing occurs (Bell et al., 1981; Fechner et al., 2018), this proposedly provides just a contrast enhancement between the two zones' sensory maps.

However, *G. petersii* is able to distinguish between capacitive and purely resistive objects (von der Emde, 1990), which requires an unambiguous determination of the object-evoked waveform distortions/modulations. This ability may result from central computations at a higher stage of the electrosensory pathway (von der Emde and Bell, 1994).

A downstream nucleus to the ELL is the torus semicircularis in the mid brain, which contains the nucleus lateralis (NL). The NL receives projections from both the medial and the dorsolateral zone of the ELL (Bell et al., 1981) (figure 4.3C). A recent anatomical study (Hollmann et al., 2016) shows that information from corresponding areas of those two zones projects to the same area within the NL. This connection might indeed allow for waveform extraction when the information of both channels is 'subtracted' from one another by NL neurons. Presently, this needs to be verified by electrophysiological recordings. The study (Hollmann et al., 2016) further supports a topographic organization of the NL network (Bell et al., 1981). A somatotopic map of the fish body is therefore preserved in the NL (figure 4.3C). It is reported to be quite 'robust' (Hollmann et al., 2016) but can be considered 'coarser' when compared to those of the ELL network. Detailed proportions of this map, i.e., potential overrepresentations of foveal skin regions as it is

found in the ELL, are yet unknown.

In principle, the findings mentioned above allow for the hypothesis that electric 'waveform images' of capacitive objects may be obtained at the level of the mid brain.

Beyond the ELL and NL, further projections to higher processing stations (i.e., the heavily oversized valvula of the cerebellum and the forebrain) do exist. All these circuits of the electrosensory pathway, along with additional feedback loops, create a massive neuronal machinery that is at its higher levels barely understood (Bell and Szabo, 1986; von der Emde, 1999a). It drives the processing of electric images, which is associated with specialized behavioral imaging strategies and computational imaging principles.

4.4 Behavioral imaging strategies

During inspections of novel objects, *G. petersii* usually employs several stereotyped and object-directed scanning motions, i.e., the probing motor acts (PMAs) (Toerring and Moller, 1984). Five basic PMAs (figure 4.4) were identified by Toerring and colleagues based on videotaped object explorations of free-swimming fish in an open field arena. The study also revealed that fish regularized their EOD repetition rate (around 33 Hz) when performing PMAs. PMAs were therefore proposed to be associated with the electric imaging of objects. It was also shown that in electrically silenced *G. petersii*, with an electric organ rendered inoperative by surgery, some PMAs were missing.

A recent study on motor patterns in *G. petersii* (Hofmann et al., 2014) also showed that such movements are linked with the EOD discharge behavior and thus are associated with the acquisition of electrosensory information. These findings imply that *G. petersii* uses PMAs to actively condition the electric images of objects. Here, it takes control of two main aspects of image generation. First, by regulating EOD production, the fish defines the rate of electric images that is needed to scan an object effectively. Second, by movement, it can adjust the distance and alignment of its electrosensory skin surface towards an object. As mentioned in section 4.2, these conditions shape the profiles of electric images. Behavioral and modeling studies suggest that *G. petersii* exploits these motion-derived changes of consecutive electric images as cues for object evaluations (e.g., distance estimation) (Hofmann et al., 2017; Pedraja et al., 2018). Such a use of spatio-temporal information is also found in other sensory systems, for example, in vision (Esch and Burns, 1995; Warren et al., 2001), where it is called optical flow. By analogy, it was called elec-

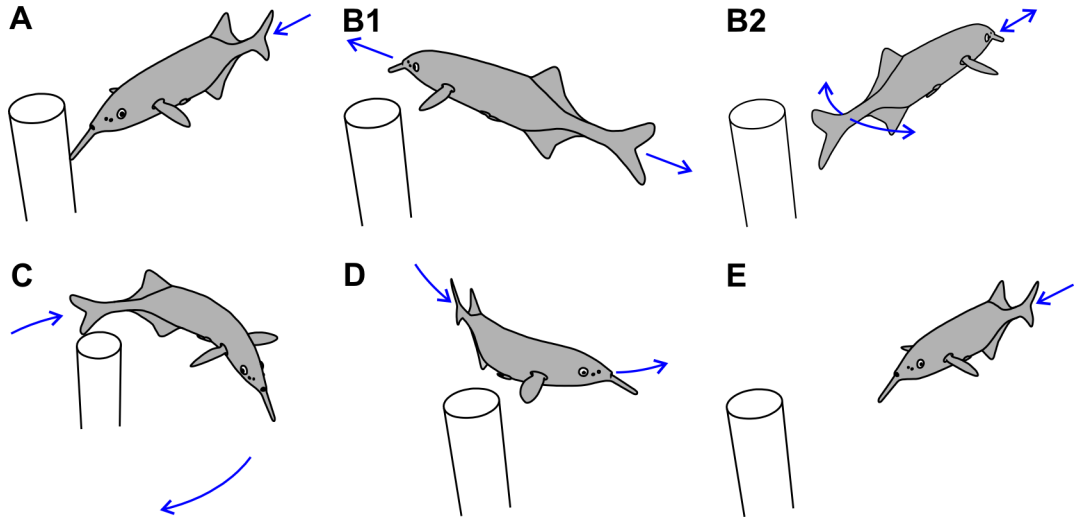

Figure 4.4: Object scanning movements (probing motor acts, PMAs) employed by *G. petersii*.
(A-E) The object under inspection (a metal rod) is shown in white. *G. petersii* is highlighted in gray. The fish's movements and their directions are indicated by blue arrows. Six different PMAs were identified. **(A)** 'chin probing'. **(B1)** 'lateral va-et-vient'. **(B2)** 'radial va-et vient'. **(C)** 'lateral probing'. **(D)** 'tangential probing'. **(E)** 'stationary probing'. Figure 4.4 was prepared based on the information provided by (Toerring and Moller, 1984).

tric flow (e.g., Hofmann et al., 2012; Hofmann et al., 2013) for active electrolocation. Here on, I will term the motion-driven imaging strategies of *G. petersii* dynamic (electric) imaging.

In addition to 'static' electric images (figure 4.2C) that are received when the fish spots an object from a stationary position (i.e., 'static electric imaging'), dynamic electric imaging could provide the animal with another, but 'temporal electric image' (Hofmann et al., 2012). I will refer to this image type as dynamic electric image. Unlike a static image, which is obtained simultaneously by several electroreceptor organs across the fish skin, the dynamic image could be acquired with only a single receptor organ. In doing so, the image is formed from the successive receptor responses as the fish moves past an object. Modeling of such dynamic, one-dimensional images at the animal's trunk showed that they roughly resembled bell-shaped curves as their static image counterparts (Hofmann et al., 2012). In addition, it was shown that dynamic images contained similar information for object analysis (Hofmann et al., 2012) as static images (von der Emde et al., 1998).

4.5 Computational imaging principles

For the analysis of environmental objects, it is suggested that *G. petersii* applies both static and dynamic electric imaging. The profiles of static images (see section 4.2) as well as dynamic images (Hofmann et al., 2012) are influenced in a multi-parametrical fashion by an object under investigation. In other words, if a single attribute of the object (e.g., its distance) changes, many properties of the image profile will change simultaneously (e.g., the modulation magnitude, width and the steepness of the flanks). In addition, different object features (e.g., distance and size) can affect the image in similar ways. Thus, prominent features of its profile such as the peak (i.e., the strongest modulation) in the image center, the steepest slope of the flanks and the image width, which fish can pick for object analysis, are ambiguous (von der Emde and Schwarz, 2002).

To gain information about most object features, *G. petersii* needs to resolve the many interdependencies of object and image parameters. Due to the findings of previous image recording and modeling studies, a basic framework can be established for an object's features and the imaging parameters that are proposed for their determination. The estimation and decoding of spatial/geometrical object properties (i.e., position, distance, size and shape) is summarized in section 4.5.1 Because previous work (e.g., Caputi et al., 1998; Hofmann et al., 2017; Hofmann et al., 2012; Pedraja et al., 2018; von der Emde et al., 1998) focused on the electric imaging of purely resistive objects, it relates exclusively to the processing of amplitude images. Analysis of amplitude images was usually restricted to one-dimensional image profiles in these studies. Estimation and decoding of electrical object properties (resistance, capacitance and derived electrical impedance) is introduced in section 4.5.2 As yet, only very few of the imaging principles, derived from recording and modeling data, have been verified by behavioral experiments.

4.5.1 Estimation and decoding of spatial and geometrical object properties

Probably the easiest cue that can be estimated from an amplitude image is the position of an object within the electric field. It is indicated by the position of the image peak, called peak amplitude, on the fish skin (Caputi et al., 1998) (figure 4.5). For the unambiguous extraction of further object attributes, it is suggested that *G. petersii* has to integrate several image parameters.

Based on image recording and behavioral data, von der Emde and colleges revealed a parameter combination, which effectively depicts electric image blur for distance estimation (von der Emde et al., 1998). Termed the relative slope or slope-to-amplitude ratio (SAR) it is calculated as the ratio of the steepest slope and the peak-amplitude of a static image (figure 4.5). Crucially, the SAR changed only with the distance but not with the size or material (metal or plastic) of tested cube-objects. Hence, fish could accurately determine the distances of those objects in the behavioral experiments. Metal spheres, however, differed in their SARs from those of the cubes, e.g., when located at the same distance, which makes them appear to be farther away. When this 'electrical illusion' was

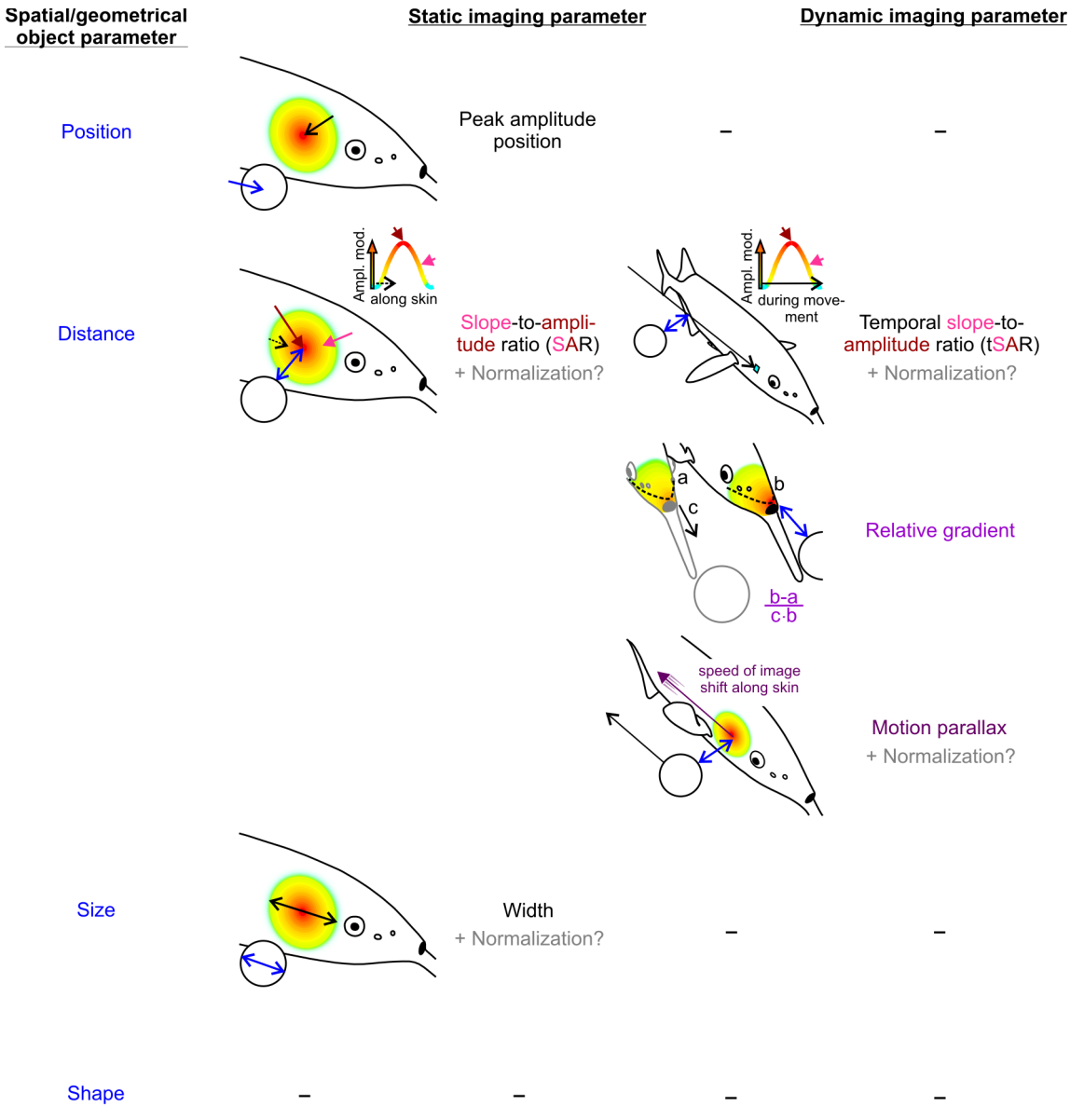

Figure 4.5: (previous page) Spatial and geometrical object properties and electric imaging parameters proposed for their determination.

Object parameters (left) are indicated in blue in the schematic drawings. Static imaging parameters (middle), obtained from an amplitude image in a stationary position to the object (left schemes), are highlighted in black or color-coded. Dynamic imaging parameters (right text and schemes) are indicted by different colors. In the second row, the left inset (bell-shaped curve) depicts a static, 1-D amplitude image (i.e., a transect of the spatial image on the fish skin at mid-height; see dashed black arrows). The right inset (bell-shaped curve) illustrates a dynamic, 1-D amplitude image obtained from a single electroreceptor organ (rectangle on the fish skin) during movement (black arrows). In both image types the peak amplitude and slope are marked. The scheme in the third row shows two consecutive amplitude images obtained during movement towards the object. Cues to be combined according to the indicated formula are an image's modulation magnitude (i.e., here determined by the modulations integrated along the dashed line on the fish skin; a or b) and the distance moved (black arrow; c). In the fourth row the velocity of an amplitude image moving along the fish skin is indicated (purple arrow) as an object passes by (black arrow). All imaging parameters with the gray label 'normalization?' are suggested to or may potentially require some sort of additional standardization to become unambiguous indicators of object features. The label '–' marks as yet unknown imaging parameters. Further descriptions of the depicted imaging parameters are given in the main text. Figure 4.5 was prepared based on the information provided by (Hofmann et al., 2017; Hofmann et al., 2012; Pedraja et al., 2018; von der Emde, 2006; von der Emde et al., 1998).

tested behaviorally, fish indeed estimated cubes to be nearer than spheres. Those findings strongly suggest that *G. petersii* relies on the SAR for distance determination of resistive objects. It was also reported that, over time, fish were able to compensate for their shape-related bias during object distance estimation (Schwarz and von der Emde, 2001) To do so, unambiguous image information about the object shape has to be integrated with the SAR; a mechanism that is as yet unknown.

In a modeling study (Hofmann et al., 2012) it was further proposed that *G. petersii* may not only rely on the SAR for depth perception but may also utilize an analogous parameter from dynamic electric images during probing motor acts. It was termed the temporal SAR (tSAR) (figure 4.5). When modeled for different-sized metal cubes the tSAR conveyed size-invariant information of the objects' distances. Whether it is also independent of the object material or affected in a similar way by object shape than the SAR remains to be tested as well as its actual use by the animal.

Further investigations on dynamic imaging (Hofmann et al., 2017) yielded a novel distance cue based on the 'spatiotemporal blurring' of electric images. This so-called relative

gradient is acquired during an object approach by relating two images from two successive positions (towards the object) with one another. The cue is calculated by combining the change in the images' (modulation) magnitudes with the product of the distance moved and the current image's magnitude as a ratio (figure 4.5). Behavioral investigations of approaches towards different-sized metal cubes showed that fish increased EOD activity, reduced thrust and aligned their posture with closer proximity to the targets. Modeling of such approaches implies that this behavior conditions electric images and their acquisition, promoting computations of relative gradients. Modeling results also showed that the rel. gradient, acquired for different-sized metal cubes and spheres or cubes of varying electrical conductivity, was only scaled by object distance. This suggests a lack of electric illusions for related distance estimations, which, however, needs to be verified by additional behavioral assays.

Most recently, a dynamic distance cue was revealed (Pedraja et al., 2018) that is similar to motion parallax in vision (e.g., Kral, 2003). It arises, e.g., when *G. petersii* moves by electrolocation targets (figure 4.5) and causes the amplitude images evoked by nearby items to move faster across the fish skin than those of distant objects. While it was shown that the cue is involved in centering behavior, it is not known whether electrical illusions potentially occur for motion parallax.

An effective distance estimator, obtained through static or dynamic imaging, is critical to compensate distance dependencies of image parameters that determine other object features. It was thus hypothesized that fish may combine the SAR with the image width to determine object size from a stationary position (von der Emde and Schwarz, 2002). (figure 4.5). Dynamic strategies have so far not been proposed. Even though electric imaging cues for unequivocal size recognition are still missing, behavioral tests with a fish indicated a perception of size constancy, by which the animal could accurately discriminate two different-sized cubes with individually varied distances (von der Emde et al., 2010).

Behavioral experiments further demonstrate that fish can recognize and memorize the shape of resistive objects (i.e., simple geometries: cube, sphere, pyramid and others). Even though *G. petersii* tends to analyze volume differences to discriminate different-shaped metal objects, it also solves shape-discrimination tasks with abstracted/altered versions of such targets (i.e., contour or plastic objects) or with equivolumetric test objects (Haubrich, 2015 and Knechtges, 2018, supervised by M. Gottwald; Schumacher et al., 2017a;

Schumacher et al., 2016a; Schumacher et al., 2016b; von der Emde and Fetz, 2007).
Interestingly, fish were reportedly better in discerning equivolumetric object geometries that likely provided stronger modulations in electric flow (sphere vs. ellipsoid) than others (sphere vs. cube) (Schumacher et al., 2016a). This implies that shape recognition might rather be achieved by dynamic than static electric imaging. However, concrete cues derived from either strategy have not been identified yet for *G. petersii* (figure 4.5).

4.5.2 Estimation and decoding of electrical object properties

An electrolocating *G. petersii* perceives purely resistive items, e.g., experimentally used metal and plastic objects (see section 4.2) or gravel, stones and driftwood in its natural habitats, (Moritz, 2010) by amplitude images. Animals and plants, because of their acellular and cellular (i.e., resistive and capacitive) structures (Meyer, 1982; Schwan, 1963), cause amplitude and, as suggested in section 4.3, waveform images.
By sensing their capacitive properties, *G. petersii* proposedly discerns such animate organisms from the surrounding, inanimate items and backgrounds without capacitance (von der Emde and Schwarz, 2002). It can further be suggested that fish identify a crucial capacitive target, e.g., a prey insect larva mainly by its 'complex' electrical impedance (von der Emde and Bleckmann, 1998; von der Emde and Schwarz, 2002), i.e., its combined resistive and capacitive properties (Meyer, 1982). Accordingly, in behavioral tests it was found that foraging *G. petersii* rejected artificial prey items, which resembled a real chironomid larva in its size, form, color and flavor but not its electrical impedance (von der Emde and Bleckmann, 1998).
Due to the multi-parametrical distortions in electric imaging, varying sizes, distances and positions of electrolocation targets will bias the fish's perception of their electrical properties (von der Emde and Schwarz, 2002). It was therefore suspected that *G. petersii* integrates several static imaging cues to disambiguate its resistance, capacitance and impedance estimations (von der Emde and Schwarz, 2002).
As a potential unequivocal measure for object resistance, the authors proposed a 'calibrated' peak amplitude of an object's amplitude image (figure 4.6). To date, however, no study has specified or experimentally verified the cue's roughly outlined calibration, suggesting some sort of combination with the SAR and with other, yet undetermined features (figure 4.5) decoding spatial and geometrical object properties (von der Emde and

Schwarz, 2002).

While such a calibration, applied to object-evoked waveform modulations, could provide undistorted capacitance sensing (von der Emde and Schwarz, 2002), it has, so far, not been related to a specific waveform image cue (figure 4.6). Although waveform images still need to be investigated in detail and be verified, e.g., via experimental recordings, their calibrated peak modulations may be conceived as a potential capacitance measure.

In principle, a combination of the calibrated amplitude and waveform cue would inform the animal about a target's complex impedance. Interestingly, electrolocating fish were indeed found to perceive object-evoked amplitude and waveform information independently, to weigh them equally and to combine both additively, when discerning artificial test objects that solely differed in complex impedance (von der Emde and Ronacher, 1994). As the fish often displayed probing motor acts during these tasks, dynamic imaging could additionally be involved in obtaining the cues, suggested above, or may provide the animal with other, presently unknown impedance measures (figure 4.6).

Another, static imaging concept for complex-impedance sensing was introduced in a simulation study (Budelli and Caputi, 2000). The authors modeled single, artificial objects

Figure 4.6: (next page) Electrical object properties and electric imaging parameters proposed for their determination.

Object parameters (left) are indicated in blue in the schematic drawings. Profiles of amplitude images are shown in reddish colors. Waveform image profiles are illustrated by bluish colors. Static imaging parameters (middle) are indicated in black or color-coded. As yet unknown imaging parameters are marked by the label '–'. In the first row, the inset (bell-shaped curve) depicts a 1-D amplitude image (as described in the previous figure 4.5) with parameters. The drawing in the last row depicts an amplitude and a waveform image, which are simultaneously 'projected' onto the fish skin by an object of complex impedance. A few modulations of both images (from corresponding positions on the fish skin) are marked (diamond, triangle, circle, square). The inset indicates a proposed linear relationship (purple line) of the amplitude and waveform image modulations when combined in a scattergram (as amplitude-waveform modulation pairs, diamond, triangle, circle, square). The line's slope, depicting this relationship, is termed an electric-color cue (for further details see main text). An 'electric-color line' intersects with the scattergram's axes at a single point, i.e., the basal condition, (black arrow) where the magnitude of amplitude and waveform modulation corresponds to zero. Imaging parameters with the gray label 'normalization?' are suggested to or may potentially require some sort of additional standardization to become unambiguous indicators of object features. Detailed descriptions of the depicted imaging parameters are given in the main text. Figure 4.6 was prepared based on the information provided by (Budelli and Caputi, 2000; von der Emde, 2006; von der Emde and Schwarz, 2002).

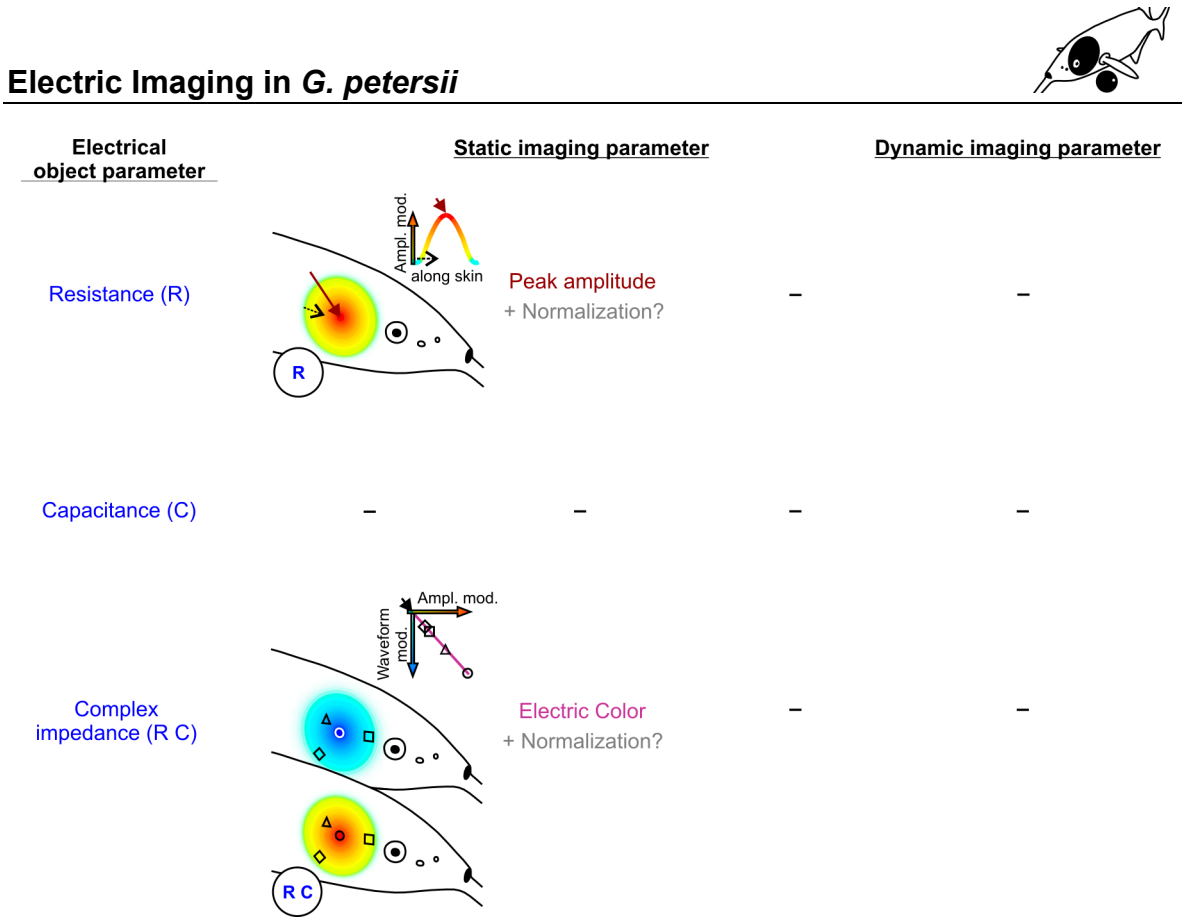

with individual complex impedances close to an electrolocating fish. Each target evoked an amplitude and simultaneously a waveform image, formed by either the amplitude or waveform modulations from across the fish skin facing the target (figure 4.6).

The study showed that the combination of an object's amplitude and waveform image yields a linear relationship between the two images' modulations. Accordingly, plotted against one another in a scattergram, the amplitude and waveform image modulations from corresponding skin positions (amplitude-waveform modulation pairs) fitted a line (figure 4.6). The lines of all targets intersected at a single point of the scattergram at which the magnitude of amplitude and waveform modulation equaled zero (i.e., the basal condition, figure 4.6). It was further shown that their evoked lines divided targets with certain complex impedances into separate groups. Each group contained lines with similar slopes, which differed from those of the other groups' lines. A single object that was also modeled at a farther distance or a slightly different position to the fish provided the same line as before.

Based on these results, Budelli and Caputi suggested that the lines' slopes might be a cue to determine groups or 'families' of complex impedance objects, probably irrespective of object distance or position. As a line's slope depicts the relationship of an amplitude and waveform image, it basically relates the fish's A and B type receptor information, from

which these images derive (see section 4.3). The cue was therefore called an electric color (Budelli and Caputi, 2000) in a loose analogy to visual color, which is determined from the activity ratio of distinct photoreceptor types (e.g., Kelber, 2016).

Due to the perceptual traits suggested above, complex-impedance sensing through electric colors may provide an advantageous strategy for unambiguous, critical object recognitions. This, however, would require individual electric colors to define distinct groups or types of aquatic organisms. Consequently, similar electric colors would have to designate a certain type of organism, e.g., prey insect larvae, selectively and reliably, which means irrespective of their sizes and shapes or their positions and distances to electrolocating fish. If so, electric-color sensing might likely be an adaption for fast object identifications (e.g., during foraging) as it potentially requires less elaborate processing in the brain than impedance estimations by the 'calibrated cues' mentioned previously.

Until now, however, electric-color perception has never been investigated in a natural, behaviorally relevant context such as foraging. In turn, the attempt to demonstrate it, e.g., in conditioning experiments with artificial objects, introduced by (e.g., von der Emde, 1990; von der Emde and Ronacher, 1994), was not successful (Röver, 2012).

Behavioral assays focusing on prey identification may therefore provide a promising alternative to test whether fish rely on electric colors during active electrolocation. Furthermore, the modeling results (Budelli and Caputi, 2000) suggesting electric-color extraction from electric images need to be verified by a complementary approach, i.e., by evaluating experimentally recorded electric images of artificial and natural targets.

4.6 Aims of the studies on electric imaging in *G. petersii*

G. petersii performs close-range inspections of crucial targets, e.g., of prey insect larvae predominantly with its active electric sense (e.g., von der Emde, 1994; von der Emde and Bleckmann, 1998). Active electrolocation (as outlined in sections 4.1-4.5) allows the fish to do so in the dark and without being distracted by murky water or cluttered surroundings. Although considered a key function of the active electric sense, the electric imaging of aquatic organisms (electrical capacitive items with complex impedances) has been scarcely investigated. *G. petersii's* static and/or dynamic imaging strategies to judge them selectively and reliably are unknown. To date, only a few suggestions have been made about the potential mechanisms underlying this ability, i.e., estimation of electric colors or

calibrated impedance estimation, likely achieved through integrations of several electric image parameters (Budelli and Caputi, 2000; von der Emde and Schwarz, 2002, see also section 4.5).

The aim of the studies presented in chapters 5 and 6 of this thesis is to reveal if and how electrolocating *G. petersii* may apply such concepts to probe and identify their most relevant objects of interest (prey and other capacitive organisms). To do so, stimulus recordings and behavioral experiments were conducted, using natural and artificial electrolocation targets. Chapter 5 focuses on investigating the electric images of capacitive objects and the mechanisms of electric-color computation, object distance estimation and 'calibrated' impedance estimation. Chapter 6 deals with the behavioral verification of electric-color sensing and the traits and use of electric color, which are compared to those of color in vision. Visual color provides a reliable percept (e.g., over distance or from different viewing positions), which selectively designates targets and enhances them against their backgrounds (Foster, 2011; Kelber and Jacobs, 2016; Romero et al., 2011). Consequently, many sighted animals rely on color vision for critical object recognitions, e.g., during foraging (e.g., Kelber and Jacobs, 2016). An electrical, color-like cue in *G. petersii*, whose 'computation', traits and use resemble those of visual color (Stevens, 2012), would suggest 'color' perception as a sensory concept beyond vision and passive sensing.

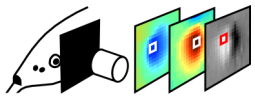

5. Electric imaging principles for the inspection of capacitive objects by weakly electric fish *Gnathonemus petersii*

This chapter is based and expands on the study:

Gottwald, M., Bott, R.A. and von der Emde, G. (2017) Estimation of distance and electric impedance of capacitive objects in the weakly electric fish *Gnathonemus petersii*. *Journal of Experimental Biology* **220,** 3142–3153.

My contribution to the published work included: conceptualization of the research goals/study experiments; development/design of the experimental setup, recording software and analysis scripts; performing and overseeing experiments; analysis/visualization of the study data; preparation/writing of the manuscript; supervision of the thesis contributing to this study:

Bott R.A. (2014). Vermessung und Parametrisierung elektrischer Bilder kapazitiver Objekte bei dem schwach elektrischen Fisch *Gnathonemus petersii*. *Bachelor's thesis*. Zoological Institute, University of Bonn, Bonn.

5.1 Abstract

During active electrolocation, the weakly electric fish *Gnathonemus petersii* judges distance and electrical impedance as crucial cues for object inspection. Nearby capacitive objects, which modulate local amplitude and waveform of the fish's electric probing signals, 'cast' amplitude and waveform images onto the fish's electroreceptive skin. For an unambiguous estimation of an object's impedance and distance, the animal has to deal with multiple dependencies of object and image parameters. Based on experimentally recorded amplitude and waveform images, we investigated possible strategies of the fish to unequivocally determine both the distance and the (complex) impedance of capacitive objects. We show that the 'relative slope' in amplitude images, but not in waveform images, is independent of object impedance and is a measure of object distance. Distance-invariant impedance estimators were obtained by two different analytical strategies. (1) The 'peak modulations' of amplitude and waveform images were calibrated with the amplitude images' relative slopes through a 'dynamic' (motion-based) routine. We suggest that 'calibrated peak modulations', derived from both image types, provide stable impedance measures when combined. (2) A 'static' (non-motion-based) impedance estimator, termed electric color, was evaluated. Our results confirm electric color as a distance-invariant cue for impedance estimation and suggest a simple mechanism, by which fish could reliably derive it from amplitude and waveform images. Our proposed computations of electrolocation cues are principally supported by the structural/functional organization of *G. petersii's* electrosensory neuronal pathways and the fish's behavioral strategies for object inspection.

5.2 Introduction

In active sensory systems, the analysis of scenes but also of a target's specific features often requires compensations of sensory ambiguities (e.g., during echolocation applied by bats (Melcón et al., 2010; Moss and Surlykke, 2010; von der Emde and Schnitzler, 1990). Also, the active electric sense of weakly electric fish *Gnathonemus petersii* (Mormyridae) is an interesting model to study image processing and behavioral strategies for unambiguous extractions of object features. Being nocturnal, the animal employs its active electric sense for short-range orientation and foraging (active electrolocation) (Schumacher

et al., 2017b; von der Emde, 1994; von der Emde and Bleckmann, 1998). During active electrolocation, the fish generates an electric field around its body by emitting biphasic current pulses (electric organ discharges, EODs) with an electric organ (EO) in the tail (Bell et al., 1976; Harder et al., 1964). Electroreceptor organs (mormyromasts) are spread across the fish's back and stomach, and at a higher density at the head and chin appendix (Harder, 1968; von der Emde and Schwarz, 2002). They detect the electric pulses at the fish's skin, which are called local EODs (lEODs).

Two types of receptor cells – A-cells and B-cells – within each mormyromast monitor the peak-to-peak (PP, figure 5.1) amplitude (A-cells) or amplitude and waveform (B-cells) of the lEODs (Szabo and Wersäll, 1970; von der Emde and Bleckmann, 1992). Both parameters are altered by nearby objects with electrical impedances different from that of water. Electrical purely resistive objects (inanimate targets like stones, dead wood or sand) modulate only the lEOD amplitude. Capacitive objects (underwater organisms like other fish, plants or prey insect larvae) also modulate or 'distort' the lEOD waveform (von der Emde and Schwarz, 2002). In such crucial electrolocation targets, with capacitive in addition to resistive electrical components, the electrical impedance is complex (Meyer, 1982; Schwan, 1963). A measure to quantify the lEOD waveform distortion, caused by capacitive items, is the so-called P/N ratio (von der Emde, 1990), which is the absolute ratio of the positive to negative lEOD peaks (figure 5.1). The object-induced lEOD modulations across the fish body form 'electric images'. By modulating the lEOD ampli-

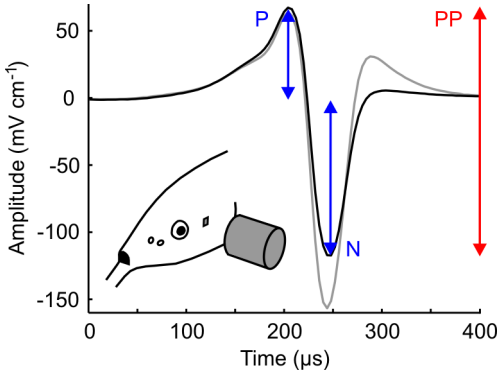

Figure 5.1: Local electric organ discharge (lEOD) and lEOD signal parameters.

Waveforms of two lEODs recorded close to the side of the head (gray rectangle to the right of the eye) of a discharging *Gnathonemus petersii*. Compared with a lEOD without an object (black signal) a capacitive (4 nF) dipole object (gray cylinder) modulates the peak-to-peak (PP) amplitude (red double arrow) and the ratio of the peak amplitudes (blue double arrows) of the positive (P) and negative (N) phase, by distorting the lEOD waveform (gray signal).

tudes and waveforms on the fish skin (Budelli and Caputi, 2000), a capacitive object simultaneously generates an amplitude image and a waveform image. Electric images encode spatial, geometrical and electrical properties of nearby objects.

Over the past years, modeling and recording studies (e.g., Budelli and Caputi, 2000; Caputi et al., 1998; Hofmann et al., 2012; von der Emde et al., 1998), complemented by behavioral data, have revealed many details of electric image profiles and uncovered image features for object inspection. However, almost all of these studies focused solely on amplitude images of purely resistive objects.

Amplitude images have a center-surround organization (or 'Mexican hat' profile) (Caputi et al., 1998). As these image profiles are sculpted by the electrical impedance, size, shape and distance of an object, image features are influenced by many object parameters (von der Emde and Schwarz, 2002). An unambiguous cue for short-range distance estimation, however, is the relative slope of the amplitude image (Caputi et al., 1998; Hofmann et al., 2012; Sicardi et al., 2000; von der Emde et al., 1998). It is defined as the ratio of the steepest slope to the strongest modulation (peak) of the image (von der Emde et al., 1998). Furthermore, the relative slope is hypothesized to be the crucial factor to compensate for distortions, caused by variations in object distance, during estimations of other object features (von der Emde and Schwarz, 2002). The mechanism underlying such a 'calibration' for impedance sensing is as yet unknown.

Another parameter for distance-invariant impedance estimation, which is potentially utilized by *G. petersii*, was introduced in a modeling study (Budelli and Caputi, 2000). It is calculated from the linear relationship of an amplitude and waveform image's modulations as a slope value. Because this cue relates the fish's A and B type receptor information (from which both image types derive), it was termed as electric color (Budelli and Caputi, 2000), in a loose analogy to visual color, which is also attained by relating inputs of at least two different receptor types. So far, there is still a lack of electric image measurements or behavioral assays to complement the simulation results (Budelli and Caputi, 2000) and verify electric-color sensing for *G. petersii*.

In this study, we explored the electric image parameters and computational strategies underlying distance and electrical-impedance estimation of capacitive objects. We present high-resolution, 2-D electric image recordings of artificial ('dipole objects' (von der Emde, 1990)) and natural capacitive objects with different distances to the fish's head. The profiles of amplitude and, for the first time, also of waveform images are analyzed in

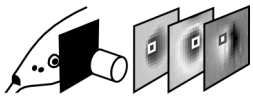

detail. We hypothesize that the relative slopes of amplitude images but also of waveform images mediate short-range distance estimation of capacitive objects. We further hypothesize that a calibration of the electric images' peak modulations with the relative image slopes provides distance-invariant cues for object impedance estimation and propose a detailed calibration routine. Finally, we evaluated the possibility of distance-independent impedance detection through electric color and suggest a mechanism, by which electric color is reliably extracted from electric images.

5.3 Materials and methods

5.3.1 Experimental animals

Electric image data were obtained from three *G. petersii* (length ~15 cm) of unspecified sex and age. The animals were purchased from a local fish dealer (Aquarium Glaser, Rodgau, Hessen, Germany). Fish were housed in separate tanks (60 l) at a water temperature of 26 ± 1 °C and an electrical conductivity of 100 ± 10 µS cm^{-1}, with a 12 h: 12h light: dark cycle.

Experiments were carried out in accordance with the guidelines of German law and with the animal welfare regulations of the University of Bonn. All procedures and methods were approved by the LANUV NRW (Landesamt für Natur, Umwelt und Verbraucherschutz Nordrhein-Westfalen, reference number: 84-02.04.2015.A444).

5.3.2 Recording of lEOD modulations: basic procedure

Prior to recordings, fish received initial anesthesia by Ethomidate (2 mg ml^{-1}, Janssen-Cilag GmbH, Neuss, North Rhine-Westfalia, Germany) using a concentration of 0.6 ml Ethomidate in 1 liter of water. While anesthesia drastically reduced movement of the fish and slowed down EOD emission rate (~1 Hz), EOD amplitude and waveform were unaffected (Engelmann et al., 2006), and fish could still ventilate autonomously.

Immobilized fish were then fixed onto a central Styrofoam holder (6 cm × 9 cm × 2 cm) in the experimental tank (38.5 cm × 28.7 cm × 18.8 cm) using four pairs of wooden sticks and cloth strings (figure 5.2). To sustain anesthesia during experiments, the tank water (26 ± 1 °C; 100 ± 5 µS cm^{-1}) had a concentration of 0.3 ml Ethomidate per liter.

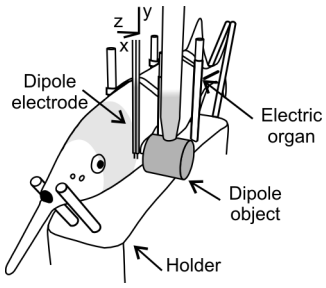

Figure 5.2: Recording of local electric organ discharge (lEOD) modulations.
lEOD modulations evoked by capacitive stimulus objects (e.g., a dipole object indicated in dark gray) were recorded with a dipole electrode (dark gray) close to the skin (light gray) of a fixed *G. petersii*.

Using a micromanipulator, artificial or natural capacitive objects were positioned close to the side of the fish head. lEOD recordings were performed with a self-made carbon dipole electrode (2 mm pole length, 1 mm inter-pole-distance), placed between the object and the fish skin, with the carbon poles orientated perpendicular to the rostro-caudal axis of the fish (figure 5.2). Electrode positioning was achieved using a computer-guided motor system (e.g., Fechler and von der Emde, 2012), allowing precise movements in x (rostro-caudal), y (dorso-ventral) and z (lateral) directions (figure 5.2). Local EODs were amplified (custom-built differential amplifier, × 100), filtered (band-pass: 1 Hz to 100 kHz) and digitized (A/D-converter, resolution: 16-bit, sampling-rate: 250 kHz, NI PCIe 6341, National Instruments, Austin, Texas, USA). A self-designed LabVIEW-program (National Instruments) was used to monitor the recordings, to process lEOD modulations and to visualize and store the data.

To define the object-evoked, lEOD amplitude (PP) and waveform (P/N) modulation close to a particular skin position, lEODs ($n \geq 5$) were recorded in the presence and absence of an object. The PP and P/N modulation was then calculated by dividing the means of the PP or P/N values obtained with the object by those obtained without the object.

In addition, the 'basal PP and P/N condition' at a particular position was determined, which is a baseline of negligible small PP or P/N modulations. During electrolocation, it can either occur when the object-evoked lEOD amplitude or waveform does not considerably differ from those obtained without the object or when amplitude and waveform parameters from two successive lEODs without any object are combined. Here, the basal condition was calculated by dividing the means of PP or P/N values measured in two successive trials in the absence of any object.

During the experiments, two different recording routines were applied for (1) preliminary recordings of dipole objects (see section 5.3.3 below) and (2) electric image recordings of dipole objects and natural capacitive objects (see section 5.3.5).

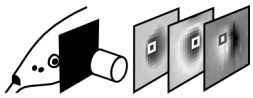

5.3.3 Artificial capacitive objects

A selfmade, cylindrical dipole object (8 mm × 8 mm; volume: 0.4 cm^3) was used to create artificial capacitive objects, with several (complex) impedances, during the experiments. The front and back of the cylinder were made of carbon and the curved surface was coated with electrical insulating varnish. Both carbon poles were internally wired and connected to a variable resistance/capacitance circuit. By changing circuit settings, resistive and capacitive dipole objects were generated, which induce a wide range of lEOD amplitude (PP) and waveform (P/N) modulations, similar to those caused by natural objects (von der Emde, 1990).

A quick experimental assessment of the range of dipole-object-evoked PP and P/N modulations was achieved by performing lEOD recordings at only a single spot close to the fish skin (von der Emde and Ronacher, 1994). Thus, only a single central spot or 'pixel' within the dipole objects' electric images was analyzed. Following this procedure, we quantified PP and P/N modulations of capacitive (n = 11, 0.5 nF to 1000 nF) and resistive dipole objects (n = 9, 0 Ω to 1 MΩ) to select circuit settings for further electric image measurements. Object-evoked modulations were obtained for 5 and 8 mm object distance and for selected circuit settings (4, 30 nF), over a larger range of object-to-fish distances (see figure 5.3A for details). In addition, the basal PP and P/N condition was acquired. For recordings (n = 20 lEODs per object setting), the electrode was positioned between eye and the gill opening at 2 mm distance to the side of the head of a discharging *G. petersii* (figure 5.3A). The dipole cylinder was orientated perpendicular to the electrode and the fish's skin (figure 5.2).

Figure 5.3A shows the PP and P/N modulation (recorded for a given object setting) as PP-P/N modulation pair in a scattergram (with amplitude and waveform modulation on its axis). PP modulations below 1 were obtained when the dipole object had a higher resistance than the surrounding water. PP modulations larger than 1 are caused by dipole objects with a smaller resistance than that of the water. P/N modulations smaller than 1 indicate a distortion of the local EOD waveform. Note that the magnitude of PP and P/N modulations becomes stronger the more they deviate from 1 (basal condition).

PP-P/N modulation pairs obtained for 5 and 8 mm object distances (figure 5.3A) shaped the borders of two so-called physical stimulus spaces (von der Emde and Ronacher, 1994). Such spaces indicate the range of amplitude and waveform modulations, evoked by the

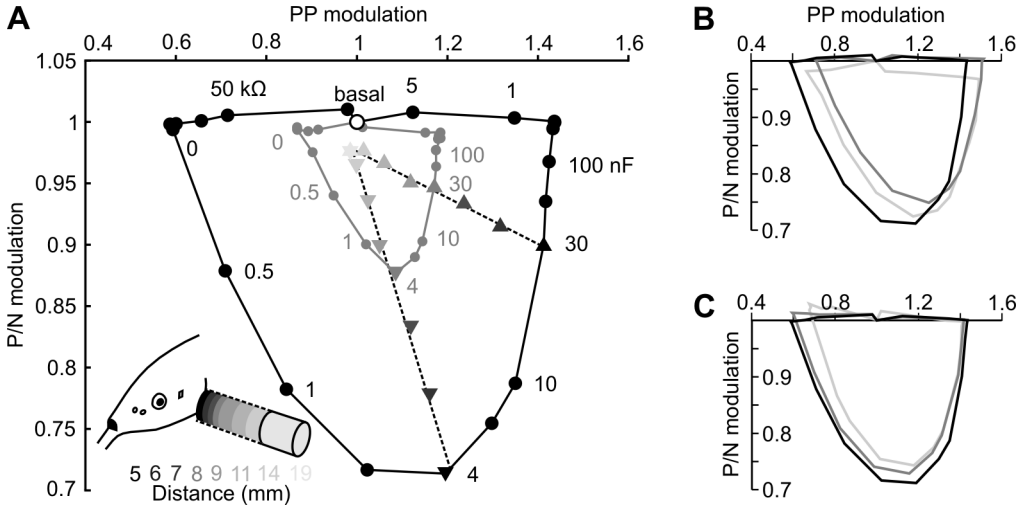

Figure 5.3: Physical stimulus spaces and electric-color lines.

(A) Physical stimulus spaces obtained for a *G. petersii* (recording position is indicated by a gray rectangle to the right of the fish's eye) at 5 mm (black) and 8 mm (gray) object distance. Filled circles indicate PP-P/N modulation pairs induced by capacitive and resistive dipole object settings, some of which are indicated. The basal PP-P/N condition is indicated by an open circle. Filled triangles show PP-P/N modulation pairs of a 4 and 30 nF dipole object obtained over increasing object distance (coded by black to gray shading; see also inset and numbers on the bottom left). All markings (circles, triangles) depict mean values, obtained from several (n = 20) repetitive lEOD recordings per object setting. Each of these two data sets could be fitted with an individual linear function ([dashed] electric-color line). **(B)** Stimulus spaces recorded (at 5 mm object distance) for the three experimental animals (shading indicates different fish). **(C)** Stimulus spaces recorded (at 5 mm object distance) for one fish on three different days (shading indicates different recording days).

dipole object's circuit settings. This range, and so the stimulus space, shrinks with farther object distance. The basal PP-P/N condition (PP mod. ~1 and P/N mod. ~1) can be conceived as a common 'origin' of both stimulus spaces, where the modulation magnitude corresponds to zero.

The PP-P/N modulation pairs of an object (4 or 30 nF, figure 5.3A), recorded at a single skin position for several increasing object distances, formed a distinct linear function ('electric-color line'). In theory (Budelli and Caputi, 2000), all the other PP-P/N modulation pairs of the full amplitude and waveform images, caused by the same dipole object, would also lie on this specific line. Electric-color lines of different objects (4 or 30 nF) converged towards the basal PP-P/N condition (with a slight offset; see the two lines in figure 5.3A). The slope of each line provides a measure 'electric color' to judge the object's impedance, independent of object distance (Budelli and Caputi, 2000; Caputi and Budelli, 2006).

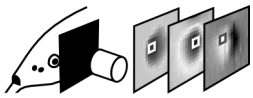

As our preliminary results agreed with earlier findings (Budelli and Caputi, 2000; Caputi and Budelli, 2006; von der Emde and Ronacher, 1994; von der Emde and Schwarz, 2002), we chose four capacitive dipole objects (1, 4, 30, 100 nF; see figure 5.3) for electric image measurements.

To ensure that object-evoked modulations obtained for different fish and recording sessions were comparable, we additionally recorded stimulus spaces for the two other experimental animals and for one fish on two additional days. Because results for different fish (figure 5.3B) and different days (figure 5.3C) revealed no considerable variations, it was appropriate to collect electric image data from different animals over a prolonged period of time.

5.3.4 Natural capacitive objects

As natural capacitive objects, we used a caddis worm (*Anabolia nervosa*, ~2 cm^3), a zebrafish (*Danio rerio*, ~2 cm^3), an aquatic plant stem (*Anubias sp*. ~5 cm^3) and a tomato (~14 cm^3). Compared to the dipole objects, which were made of carbon and partly an insulating cover, the natural objects had a rather homogenous surface. The caddis worm, however, with its protective debris case, soft abdomen and chitinized head, featured a versatile material composition (which is also the case for the dipole objects). Prior to the recordings, the stimulus animals were euthanized by immersion in a solution of 2 mg ml^{-1} Ethomidate (caddis worm) or 2g l^{-1} MS 222 (2g l^{-1}, Acros Organics, Fair Lawn, New Jersey, USA) (zebrafish).

5.3.5 Recording of electric images

For electric image recordings, a 2-D measuring grid was used, which forms a vertical plane (18 mm × 19 mm) close to the side of the fish's head (figure 5.4). Objects were aligned in a middle position with respect to the plane's center (figure 5.4) at various (5, 6.5, 8 mm) object-to-fish distances. The plane's center, located 9 mm caudal from the fish's eye (x position), at the height of the eye (dorso - ventral; y position) and 2 mm from the skin (lateral, z position), was used as a positioning reference for the electrode prior to the measurements. During recordings, the electrode was moved in 1 mm (x direction) and 2 mm (y direction) steps, covering the plane with n = 200 lEOD recording positions (fig-

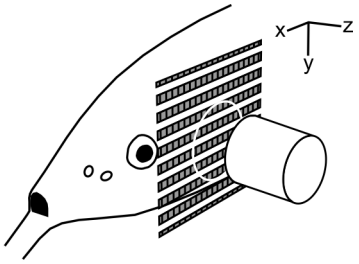

Figure 5.4: Measuring grid for 2-D electric images.
A grid of several (n = 200) lEOD recording positions (gray rectangles) formed a measuring plane close to the head of *G. petersii*. With respect to the plane, an electrolocation target (dipole object, white) was aligned in a central position as indicated by the object's contour (white circle) marked on it.

ure 5.4). The recording of an electric image took several hours (~2.5 - 3 h). The final image resolution was set to 380 (19 × 20) pixels (figure 5.5A) by linear interpolation of the recorded modulations.

5.3.6 Analysis of electric images

Electric image analyses and visualizations were carried out with custom-written MATLAB (MathWorks, Natick, Massachusetts, USA) routines.

The center-surround organization of electric images (figures 5.5A and 5.5B) was analyzed by defining their Mexican hat profiles. Such profiles have a center and a rim of pronounced modulations, which deviate from the basal condition (i.e., the modulation baseline of ~1). Mexican hat profiles can occur in two different configurations. One configuration features central modulations of larger than 1 and rim modulations of smaller than 1. The other configuration yields central modulations of smaller than 1 and rim modulations of larger than 1. An area of negligible small modulations (~1), which can be called a 'basal region', usually separates image center and rim in both configurations.

To identify central, basal and peripheral modulations of an amplitude or waveform image (figure 5.5A), the image's modulations were compared to the basal PP or P/N condition.

In our analysis the basal condition depicted a modulation baseline from across the measuring grid (shown in figure 5.4). It was acquired from nine recordings (three for each fish), performed without any object. Modulation baselines, form across the grid, were averaged for each of the nine measurements. Those means were again averaged to obtain the basal amplitude (PP = 1 ± 0.018) or waveform (P/N = 1 ± 0.005) condition.

The modulations of an object-evoked electric image that fell in the range of twice the standard deviation of the basal condition were determined as the basal region of the image.

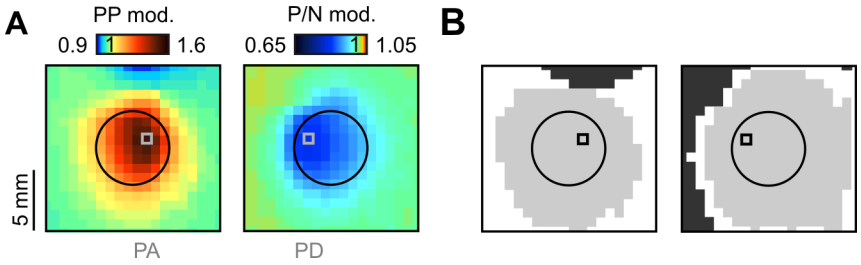

Figure 5.5: Electric image analysis – Mexican hat profiles.

(A) Amplitude (left) and waveform image (right) of a 30 nF dipole object at 5 mm object distance. Image modulations are shown color-coded. The dipole object's optical contour (black circle) is indicated in both images. Peak modulations of the images (i.e., the values with the largest deviation from 1) are marked as gray rectangles and labeled below the image as peak amplitude (PA) or peak distortion (PD). **(B)** Mexican hat profiles of the amplitude (left) and waveform image (right) with image center (light gray), basal area (white) and rim area (dark gray) accentuated. Central regions contain the peak modulations of electric images, whose positions are indicated by black rectangles.

Modulations outside this range were considered to be part of the image center or rim (figure 5.5B). The image center was determined as the area that contained the image pixel with the strongest modulation (i.e., with the largest deviation from 1). This parameter is termed the peak amplitude (PA, for amplitude images) or peak distortion (PD, for waveform images) (figure 5.5). Both parameters are related to an object's impedance but change with the shape, size and distance of the object.

To obtain the relative image slope as a measure for short object distances, the absolute maximal or minimal (rostral) image slope was divided by the peak modulation (PA, PD) of the image center (figure 5.6). The relative image slope is termed the slope-to-amplitude ratio (SAR, for amplitude images) (figure 5.6A) or slope-to-distortion ratio (SDR, for waveform images) (figure 5.6B).

To obtain an electric-color line, the (PP) modulations of an object's amplitude image were plotted against the (P/N) modulations of the object's waveform image in a scattergram. As illustrated in figure 5.7A, the resulting PP-P/N modulation pairs can form a spatial distribution instead of a line (electric-color line). As such distributions lack a clear linear relationship between the amplitude and waveform image modulations a possible color line has to be estimated by further calculations. Thus, we first identified and labeled PP-P/N modulation pairs that might indicate the path of an electric-color line (within a distribution). To do so, we made two assumptions: (1) The scattering of PP-P/N modulation pairs is related to local form differences of the two electric images (amplitude

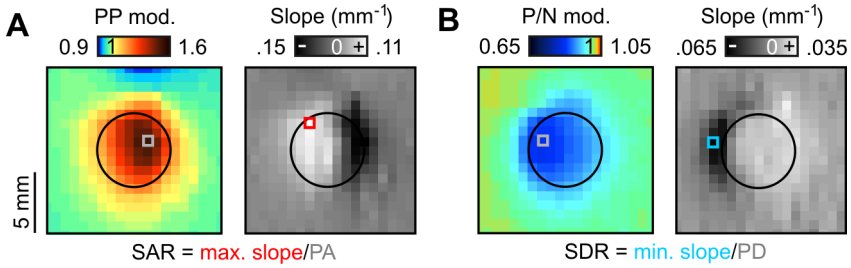

Figure 5.6: Electric image analysis – Relative slopes.

(A) On the left, the amplitude image of the 30 nF dipole object at 5 mm object distance is shown with color-coded modulations. The dipole object's contour (black circle) and the image's peak amplitude (PA, gray rectangle) are indicated. The right image shows the profile of the image's slopes, which were calculated in horizontal direction for each image row. Slopes values are coded by white-to-black shading. The steepest (rostral) slope is indicated (red rectangle). The image's peak amplitude and the steepest image slope combined provide the relative slope or slope-to-amplitude ratio (SAR) as indicated below. **(B)** Waveform image of the 30 nF dipole object (left) and the profile of the image's slopes (right) with the same arrangement and markings as in (A). Through combination of the image's peak distortion (gray rectangle, PD) and the steepest (rostal) slope (blue rectangle) the relative slope, i.e., slope-to-distortion ratio (SDR) is acquired as labeled below.

Figure 5.7: (next page) Electric image analysis – Electric-color lines.

(A) Modulations of the amplitude and waveform image (evoked by the 30 nF dipole object at 5 mm object distance) plotted against one another in a scattergram. Instead of an electric-color line, the object's PP-PN modulation pairs (gray rectangles) yield a spatial distribution. **(B)** Further calculations (see main text) were performed to estimate the pathway of an electric-color line within the distribution shown in (A). The normalized profile (i.e., 'shape') of the amplitude image is depicted leftmost in 2-D and 3-D with color-coded (normalized) modulations. In the 2-D profile the dipole object's contour (black circle) is marked. The shape of the waveform image is shown in the middle in the same manner as the amplitude image's shape with analogous markings. Both forms were compared (see main text) to identify local similarities and differences between them. The rightmost profile indicates equally shaped areas (purple) or differently shaped areas (light gray) of the two electric images. **(C)** Distribution of PP-P/N modulation pairs (as in (A)) with additional markings. PP-P/N modulation pairs were highlighted according to the image areas to which they belong, i.e., either the equally shaped areas (purple) or differently shaped areas (light gray) of the two images. Purple modulation pairs indicate the pathway of an electric-color line within the distribution. Two methods were tested to obtain electric-color lines that match the linear electric-color pathway. (1) A linear fit was applied to the distribution (black, dashed line). (2) The basal PP-P/N condition (open circle) and a 'peak modulation pair' (black rectangle) were marked and connected (black solid line). To acquire the peak modulation pair, the images' peak modulations were combined, irrespective of them originating from corresponding positions within the images or not.

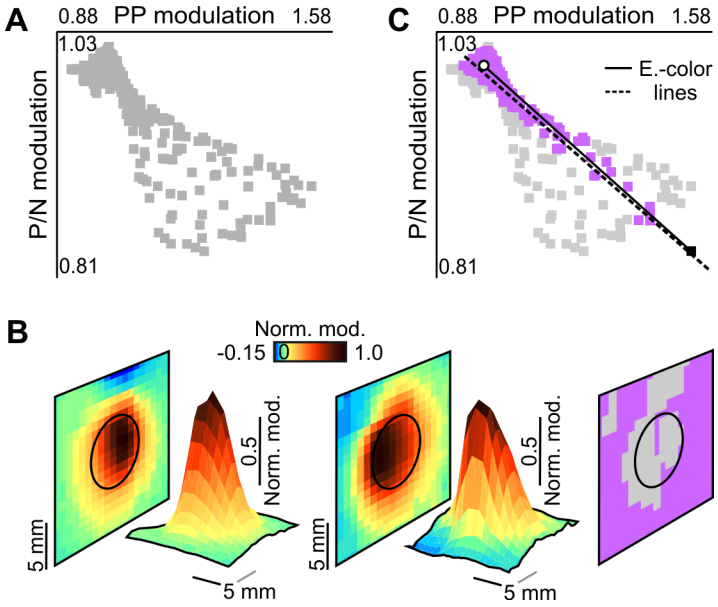

versus waveform); (2) all PP-P/N pairs obtained from equally shaped areas of an amplitude and waveform image indicate the path of the electric-color line.

To analyze the form of an amplitude or waveform image, it is necessary to normalize the image profile (figure 5.7B). Normalization was performed, by setting the peak modulation (PA or PD) of an electric image to 1, the basal condition to 0 and by rescaling all other image modulations with respect to these settings. Local form differences of an amplitude and waveform image were then calculated by subtracting their normalized modulations (PP minus the corresponding P/N image pixel, pixel per pixel). Differences of normalized modulations within a range of ± 0.1 indicated equally shaped image areas and outside this range differently shaped image areas. After identifying equally and differently shaped areas of an amplitude and waveform image (figure 5.7B), this information was used to mark the linear electric-color pathway within the distribution of the images' PP-P/N modulation pairs (figure 5.7C). This was achieved by emphasizing the modulation pairs from the equally shaped image areas.

Note that while the calculations outlined above promote electric-color estimation in our analysis, we consider them as too complex to be performed by *G. petersii*. Thus, to finally add an electric-color line to the distribution simpler methods were used. The distribution was fitted with a line (figure 5.7C). As an alternative, the basal PP-P/N condition and a 'peak modulation pair' were marked in the scattergram and connected by a line (figure 5.7C). The peak modulation (PA-PD) pair was obtained by combining peak amplitude and peak distortion, even though they might originate from different local positions within the

amplitude and waveform image (see figure 5.5).

Both ways of acquiring electric-color lines were evaluated for the distributions of PP-P/N modulation pairs of several eletrolocation targets. The method providing the most accurate alignment of electric-color lines with the electric-color pathways of these distributions was used to extract the electric colors of electrolocation targets (as the lines' slopes).

5.4 Results

5.4.1 Amplitude and waveform images

Electric images of dipole objects (figure 5.8A) and of natural capacitive objects (figure 5.8B) had a center-surround (Mexican hat) profile, as has been reported in other studies for amplitude images of purely resistive objects (e.g., Caputi et al., 1998).

Interestingly, we found that in addition to amplitude images, waveform images also shared this basic electric image organization (figure 5.8). However, for most capacitive objects, the modulation patterns of the two image types differed considerably (figure 5.8: color-coded profiles). Hence, variations in size, shape, number and location of the Mexican hat profiles' central, basal and rim areas occurred (figure 5.8: gray-scale profiles). Variation among Mexican hat profiles of amplitude images was greater than that of waveform images. Note that for some electric image profiles that greatly exceeded the size of the measuring plane (figure 5.8B), possible outer regions (basal or rim areas) could not be

Figure 5.8: (next page) Electric images of dipole and natural objects at 5 mm object distance.

(A) Dipole objects. **(A1)** Schematic drawing indicating the position of a dipole object (gray cylinder) in front of the measuring plane (white), on which the object's contour is marked. Object circuit settings are given below. **(A2)** Amplitude images of each object are shown as a color-coded image indicating the image modulations and as a gray-scale image with accentuated image (Mexican hat) areas – center (light gray), basal area (white) and rim area (dark gray). The images' peak amplitudes (rectangles) and the objects' contours are indicated. **(A3)** Waveform images shown in the same manner as described in (A2) (rectangles mark peak distortions). **(B)** Natural objects. **(B1)** Schematic drawing of the objects in front of the measuring plane (white). The object's contours are marked on it. The contour of the caddis worm indicates its different body sections – (a) debris case, (b) abdomen, (c) head. **(B2)** Amplitude images of the objects shown in the same manner as in A2. **(B3)** Waveform images of the objects arranged as in (A3) with analogous markings.

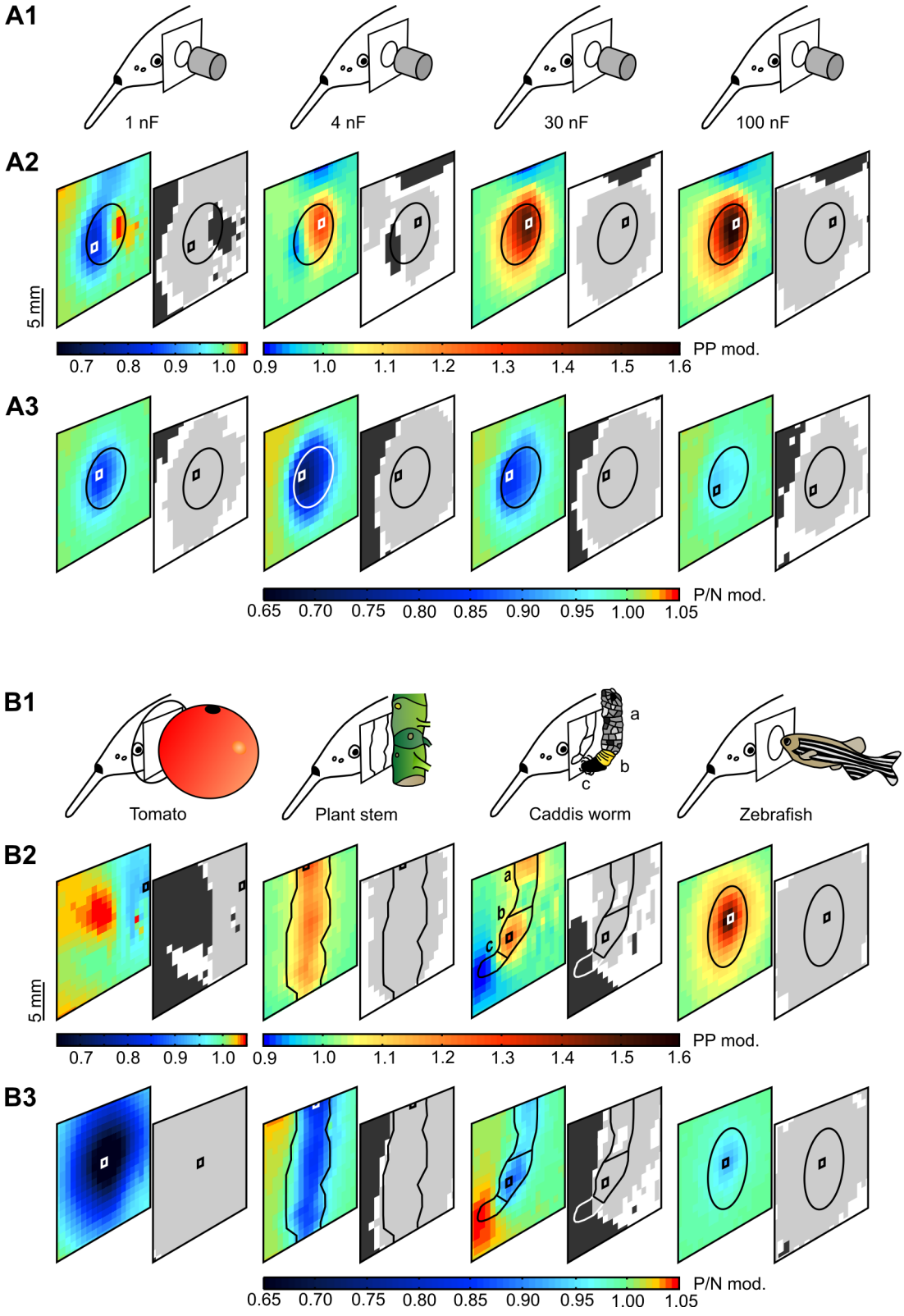

assessed. In almost all amplitude and waveform images (figure 5.8), image centers were obtained near the skin area immediately adjacent to the objects. The peak modulations (PA, PD) within the central regions of an object's amplitude and waveform image often did

not match the same locations. Here, offsets of several (1-9.2) millimeters were observed (except for the peak modulations of the caddis worm's electric images, which showed no offset of positions, figure 5.8B).

5.4.2 Distance estimation of capacitive objects

To evaluate whether short-range distance estimation in *G. petersii* might be mediated by amplitude and waveform images, we recorded electric images of dipole objects at three different object-to-fish distances (5, 6.5, 8 mm).

As different capacitive dipole objects were generated only by changing the circuit settings of the dipole cylinder, size and shape of the objects were constant. Thus, electric images were only influenced by the two object parameters electrical impedance and distance. For four capacitive circuit settings of the dipole object we recorded n = 5 (4, 30 nF) or n = 1 (1,

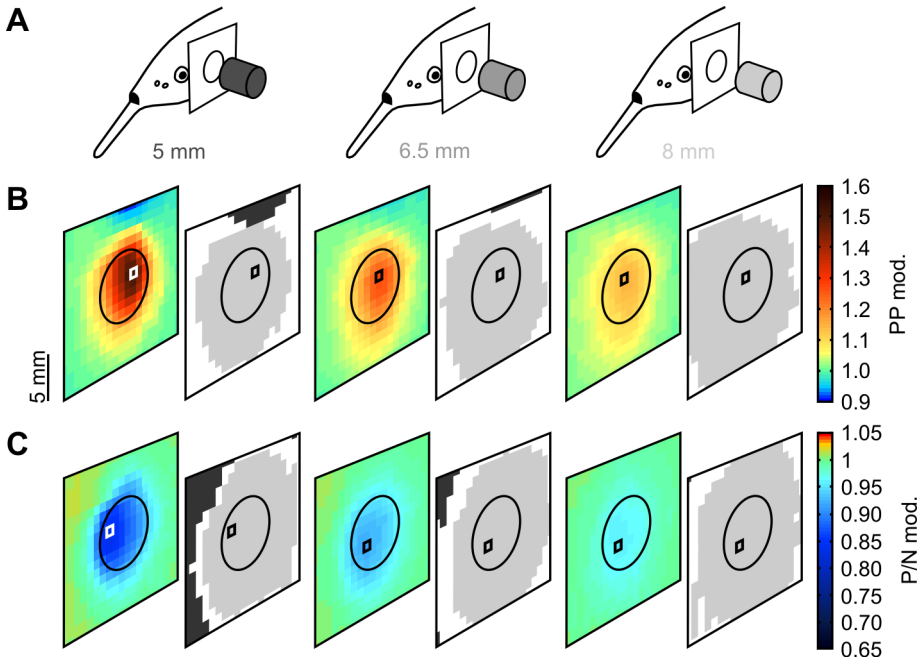

Figure 5.9: Electric images of a 30 nF dipole object at different object distances.

(A) Schematic drawing indicating object distance (by dark to light gray object shading and numbers) and showing an object's position in front of the measuring plane (white). The objects' contours are marked on it. **(B)** Amplitude images shown as color-coded images and as images with the central, basal and rim areas of the Mexican hat profiles indicated by white-to-gray shading as described in figure 5.8. The peak amplitudes (rectangles) of the images and the objects' contours are marked. **(C)** Waveform images arranged as in (B) with analogous markings (rectangles show peak distortions).

100 nF) electric images for each object distance.

With farther object distance, amplitude and waveform images expanded in size but became weaker and showed a lower modulation contrast (example shown in figure 5.9). Thus, over distance, the images' peak modulations (PA and PD) were reduced in magnitude (deviation from 1) and rostral image slopes became less steep (figure 5.10). Both image parameters were also influenced by object impedance that is varied by the individual capacitive object settings (figure 5.10). When image slopes were divided by the peak modulations (to obtain

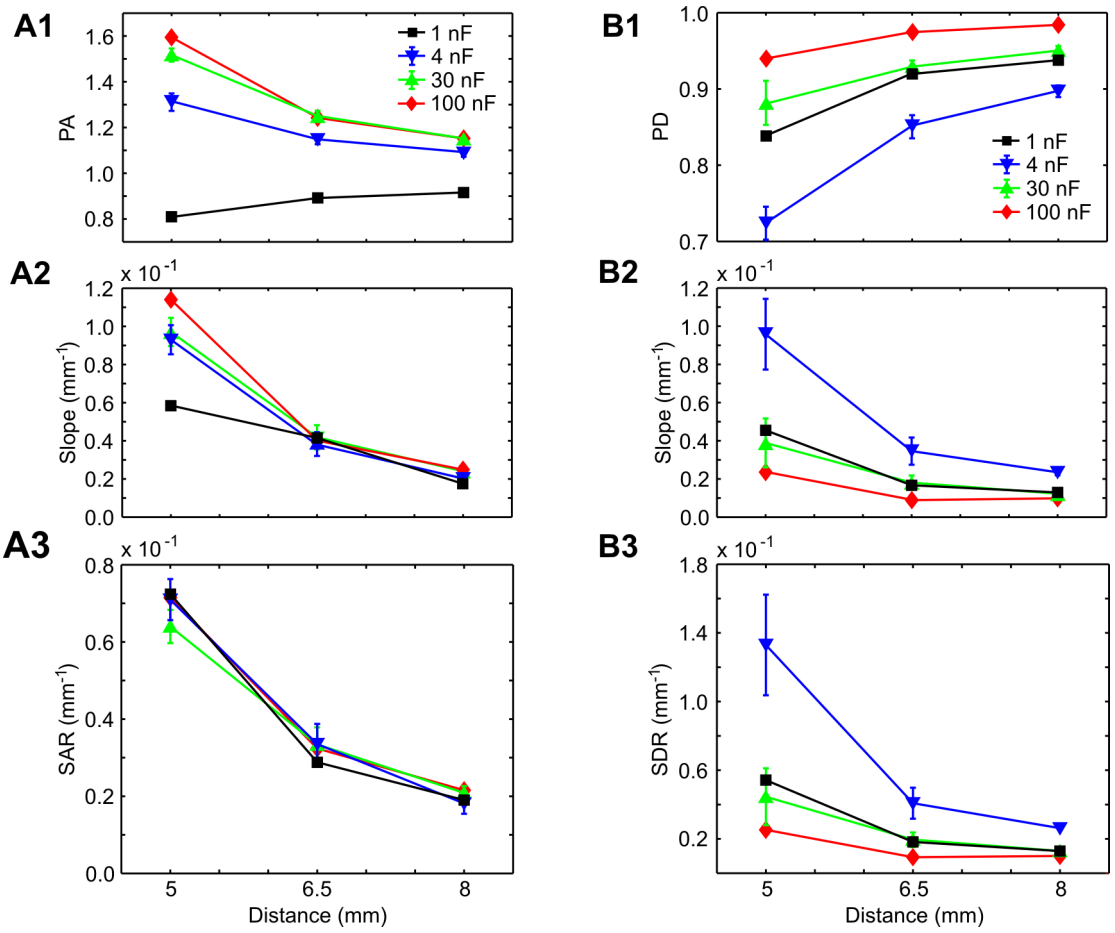

Figure 5.10: Relationship of amplitude and waveform image parameters to object capacitance and distance.

(A) Amplitude image parameters. Values depict either means ± SD of image parameters acquired from several recordings (n = 5) or values result from single recordings. Image parameters obtained for individual capacitive object settings are indicated by symbols/lines of different colors. **(A1)** Peak amplitudes (PA). **(A2)** Steepest, rostral image slopes (absolute values). **(A3)** Relative slopes (slope-to-amplitude ratio, SAR). **(B)** Waveform image parameters shown in the same manner and with analogous markings as described in (A). **(B1)** Peak distortions (PD). **(B2)** Steepest rostral slopes (absolute values). **(B3)** Relative slopes (slope-to-distortion ratio, SDR).

SARs or SDRs) variations due to object impedance were almost cancelled for relative slopes of amplitude images (SARs; see figure 5.10A3). In contrast, SDRs (figure 5.10B3) of waveform images were still altered by distance and the capacitive settings of the dipole object. Thus, only the relative slopes of amplitude images provided unequivocal distance cues independent of object impedance.

5.4.3 Impedance estimation of capacitive objects

Two analytical strategies were suggested that might enable *G. petersii* to judge object impedance irrespective of object distance.

The first strategy we address is the calibration of the peak modulations of amplitude (PA) and waveform images (PD). To do so, we combined both peak modulations with the SAR of amplitude images. SDRs were not used for the calibration routine, as they were not unequivocal distance measures.

For each dipole object setting (1, 4, 30 100 nF) and object distance (5, 6.5, 8 mm) PA and PD were first plotted versus the SAR (figure 5.11A). Over distance, the relationship of PA or PD and SAR revealed distinct linear functions for the object settings. Lines with a close or overlapping alignment (e.g., the two lines of the 30 and 100 nF object in figure 5.11A, uppermost) occurred for dipole objects that generated similar peak modulations (compare PA of the 30 and 100 nF object in figure 5.10A1).

The slopes of the lines provided distance-invariant measures for object resistance ('calibrated PA', figure 5.11B, uppermost) or capacitance ('calibrated PD', figure 5.11B, bottommost). To obtain such slope values, the fish has to relate the SAR and peak modulations (PA, PD), gained by two successive amplitude and waveform images, when approaching an object. In doing so, the distance passed between the acquisitions of consecutive images may vary as a result of the swimming speed and EOD rhythm of the animal. Figure 5.11B shows calibrated peak modulations, acquired for different distance intervals through individual combinations of two respective SAR-PA or SAR-PD pairs from different object distances. These slope values depended on the capacitive settings of the dipole object (and related object impedance) and showed no considerable variation for different distance intervals. The direction (larger or smaller than 1) and relative magnitude (deviation from 1) of the original peak modulations (figure 5.10A.1 and B.1) were preserved by the calibrated peak modulations (figure 5.11B). They are now encoded by the

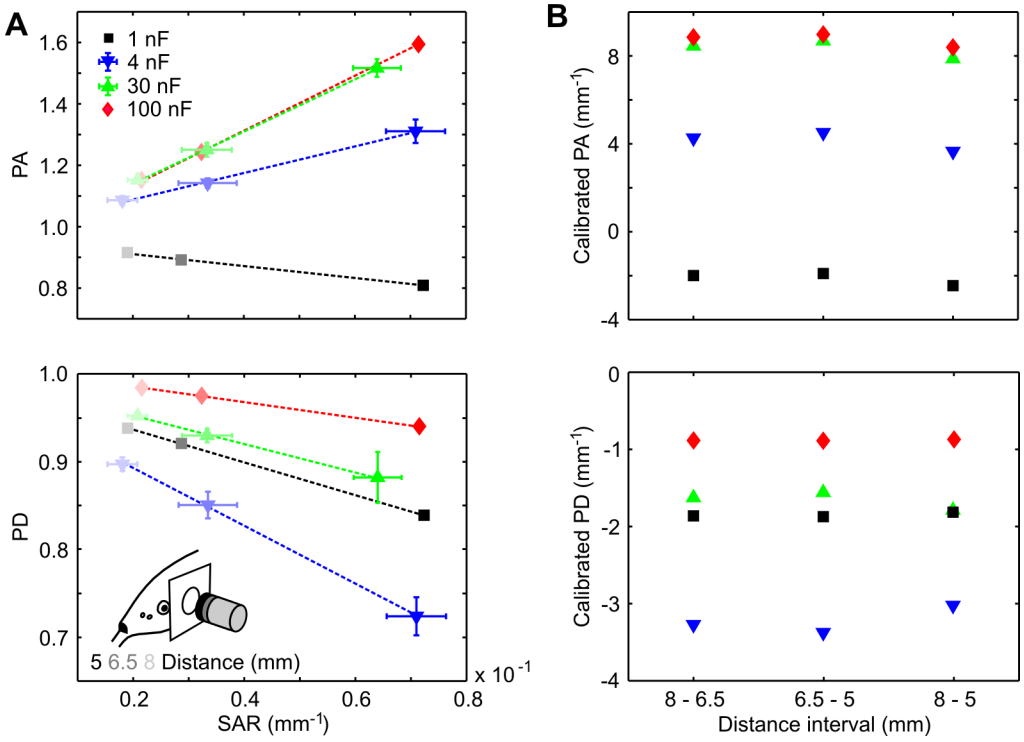

Figure 5.11: Calibrated peak modulations obtained by relating peak modulation and SAR over distance.

(A) Peak modulations: PA (uppermost) and PD (bottommost) as linear functions of the SAR, acquired over distance (5 to 6.5 to 8 mm). Symbols of different colors indicate SAR-PA or SAR-PD pairs obtained for individual capacitive object settings. Values depict either means ± SD of image parameters acquired from several recordings (n = 5) or values result from single recordings. Color intensity of the symbols codes for the three object distances (as illustrated in the inset on the bottom left for the 1 nF object). Linear data fits are shown as dashed lines. Lines are colored according to the corresponding capacitive setting of the dipole object. **(B)** Calibrated peak modulations for PA (top) and PD (bottom). Values were calculated as slopes from the data sets in (A) for different distance intervals (by combining two respective SAR-PA or SAR-PD pairs from different object distances).

direction (positive or negative) and the steepness of these slope values. Both, calibrated PA and PD could enable distance-invariant impedance estimation when combined (added together).

As an alternative to the dynamic (motion-based) calibration mechanism outlined above, we evaluated a second, 'static' strategy for impedance estimation by electric colors. Electric color can proposedly be extracted from the linear relationship between an amplitude and waveform image's modulations at a stationary position to an object (Budelli and Caputi, 2000). Consequently, the amplitude and waveform image modulations should form an

electric-color line when combined in a scattergram as PP-P/N modulation pairs. Figure 5.12 depicts the distributions of PP-P/N modulation pairs for dipole and natural objects (all with 5 mm object distance). Most distributions showed varying amounts of scatter, indicating that, for almost all of the objects tested, PP-P/N modulation pairs did not form a definite electric-color line. However, the PP-P/N modulation pairs from equally shaped areas of an amplitude and waveform image marked a linear pathway, which we propose corresponds to the path of an electric-color line within a distribution. The clearest electric-color pathway was obtained for a distribution that was almost exclusively composed of PP-

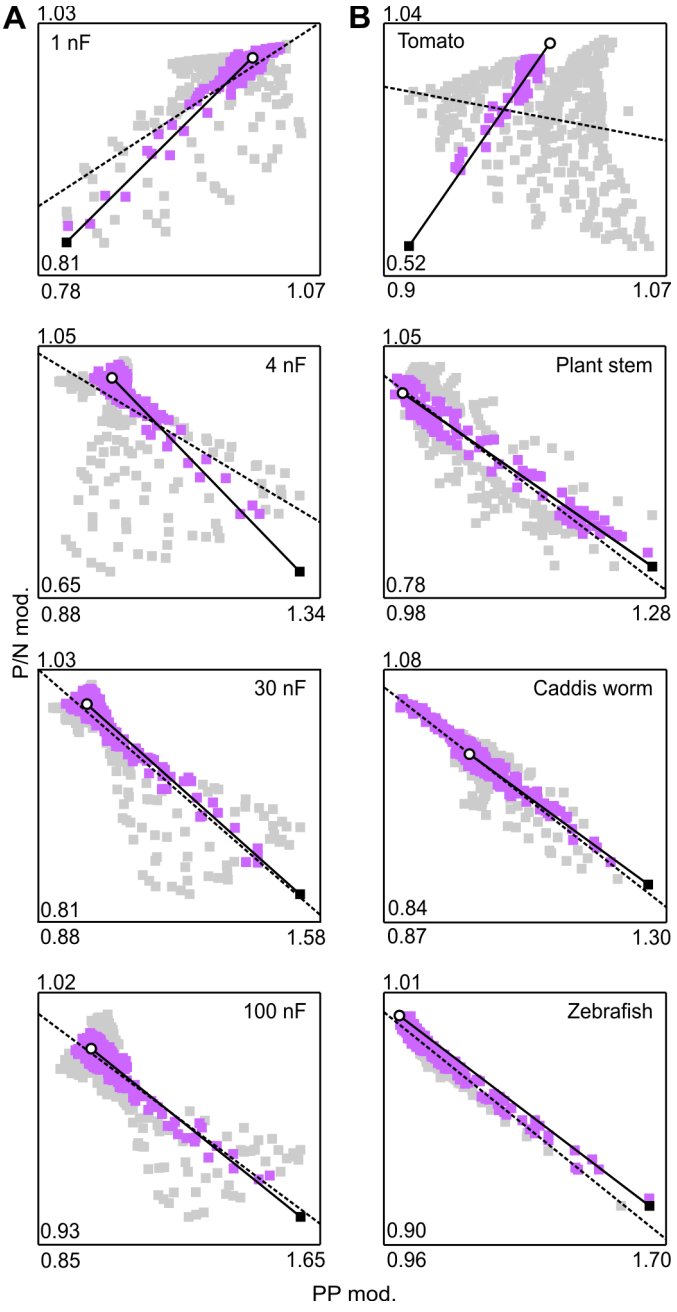

Figure 5.12: Determinations of electric-color lines for objects at 5 mm object distance.

(A) Distributions of PP-P/N modulation pairs (gray and purple rectangles) of dipole-object-evoked electric images. Capacitive object settings are given at the top corners. Purple rectangles indicate PP-P/N modulation pairs acquired from equally shaped amplitude and waveform image areas. They mark the electric-color pathway of a distribution. Open circles indicate the basal PP-PN condition. Black rectangles show peak modulation pairs. Linear fits (electric-color lines) are indicated by black dashed lines (for whole data fits) and by black solid lines (connecting basal condition and peak modulation pair). **(B)** Distributions of PP-P/N modulation pairs of electric images evoked by natural objects. Distributions are arranged as in (A) with analogous markings.

P/N modulation pairs from equally shaped image areas (zebrafish, figure 5.12B, bottommost).

To determine electric-color lines for a distribution of PP-P/N modulation pairs, we applied linear fits to either the whole distribution or only to the peak modulation pair of the distribution and the basal PP-PN condition. Judging the performance of both methods by matching the obtained lines with the electric-color pathway, we found that linear functions due to fitting basal and peak modulation pair had an accurate alignment for all distributions (shown in figure 5.12), whereas lines of whole data fits did not (e.g., tomato, figure 5.12B, uppermost).

Further extraction of electric color (as a line's slope) was therefore limited to the linear functions gained by connecting the peak modulation pair and basal condition.

To evaluate distance invariance of electric color, we analyzed the dipole-object-evoked electric images that were previously used to determine the SAR-based calibration mechanism for impedance estimation. We found that individual electric-color lines occurred for the different dipole object settings (figure 5.13A). Electric-color lines obtained for a given dipole object (1, 4, 30 or 100 nF) showed only slight variations in

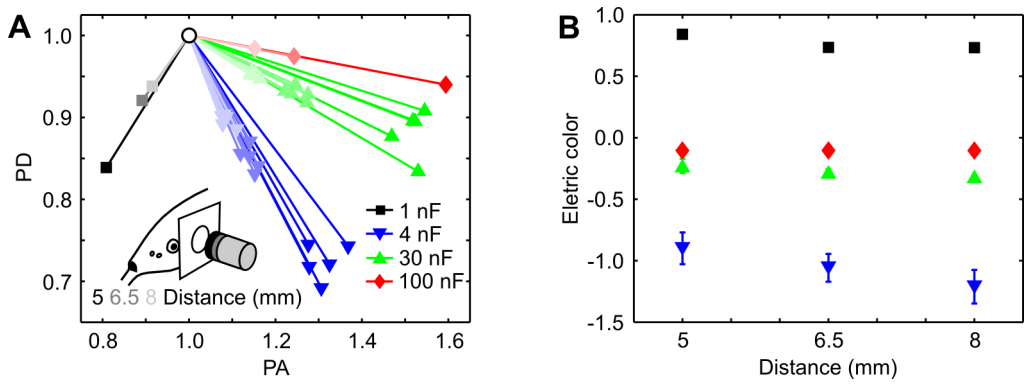

Figure 5.13: Electric colors obtained by relating peak modulation pairs from electric images with the basal condition.

(A) Electric-color lines acquired by several (n = 5) or single image recordings of capacitive dipole objects at different object distances (5, 6.5, 8 mm). Peak modulation (PA-PD) pairs obtained for individual capacitive object settings are indicated by symbols of different colors. Electric-color lines (with corresponding colors) connect a peak modulation pair with the basal condition (open circle). Color intensities (of symbols and lines) code for the three object distances, as illustrated for the 1 nF object in the inset on the bottom left. **(B)** Electric colors calculated as slopes of the lines in (A). They are shown as means ± SD (of n = 5 electric color values) or as single values.

their relative alignment. These variations, as observable in the data with multiple measurements of a dipole object (4 and 30 nF objects), systematically decreased with farther object distance. Electric colors, extracted from these linear functions (figure 5.13B), did not change considerably for different object distances, but were scaled by the capacitive settings of the dipole object (that vary its complex electrical impedance). Thus, in accordance with simulation data from (Budelli and Caputi, 2000), we found electric color to be a distance-invariant impedance estimator. In addition, we could show that extraction of electric color was more accurate by relating just a peak modulation pair to the basal amplitude and waveform condition than incorporating all modulation pairs of an amplitude and waveform image (figure 5.12). Note that, even though the basal condition defines the PP and P/N modulation baseline we did not match it with the actual origin of the scattergram of amplitude and waveform modulations in this study. This, however, can principally be achieved by rescaling the modulations (i.e., by subtracting 1 from all PP and P/N modulations). As a result, an electric-color line, determined by peak modulation (PA-PD) pair and basal condition (figure 5.13), depicts a proportional relationship of PA and PD. Consequently, electric color (i.e., the slope of the line) can be calculated as the ratio of both peak modulations (PD-to-PA ratio). This implies that, during active electrolocation, *G. petersii* could derive the electric color of an object from the peak modulations of the object-evoked amplitude and waveform image simply as a ratio.

5.5 Discussion

In the present study, we addressed the unambiguous analysis of capacitive objects by electrolocating *G. petersii*. In the fish's natural environment capacitive items represent crucial targets (e.g., prey insect larvae), which makes their reliable inspection a critical task. As yet, the computational strategies the fish might use to do so are mainly unknown. Here, we specifically focused on imaging mechanisms enabling estimation of an object's distance and (complex) impedance independent of one another. Electric image types and imaging principles, presented in this study, are discussed with regard to being supported by the structural/functional organization of *G. petersii's* electrosensory neuronal pathways and behavioral electrolocation strategies.

5.5.1 Amplitude and waveform images

To our knowledge, this is the first study on active electrolocation in mormyrid fish providing extensive recordings of high-resolution, 2-D amplitude and waveform images of artificial and natural capacitive objects. In our measurements, electric images were mainly acquired close to the electroreceptive areas of the fish head. The recorded electric images thus appropriately represent the sensory information, which is actually perceived by the animal.

In these fish, the receptor-encoded lEOD amplitude and waveform information is transmitted via afferent fibers to the neuronal network of the electrosensory lateral line lobe (ELL), a cerebellum-like structure in the hindbrain (Bell, 1990a; Meek et al., 1999). Amplitude information is projected to the medial zone of the ELL (by A-cell afferents). Amplitude and waveform information combined is relayed to the dorso-lateral ELL zone (by B-cell afferents). Both zones provide somatotopic maps of the electroreceptive body surface (Maler et al., 1973). The object-evoked excitation pattern within both ELL zones is processed jointly with an efference copy of the fish's EOD, termed electric organ corollary discharge (EOCD) (Bell, 1989). The EOCD is modifiable by previous sensory experience such as the stimuli in the absence of the object (Bell, 1989; Bell et al., 1997). By combining both (the object-evoked and EOCD-evoked) neuronal signatures, the circuitry just mentioned is principally sufficient to provide the modulations, which define an object's electric image. Following this concept, amplitude images will result from the modulation patterns within the ELL medial zone. Determination of waveform images, however, will require a 'subtraction' of both ELL zones' modulation patterns at a higher level (von der Emde and Bell, 1994). Anatomical studies indeed have shown that projections from the two ELL zones converge at the nucleus lateralis in the midbrain (Bell et al., 1981; Hollmann et al., 2016). Moreover, these studies provided evidence of a somatotopic midbrain map, from which waveform images could be acquired. The somatotopic organization at the level of the midbrain, however, was found to be much weaker than in the ELL network (Hollmann et al., 2016).

As we show in this study, not only amplitude but also waveform images have a center-surround organization (Mexican hat profile) (figure 5.8). While such profiles appear to be a general feature of electric images, they occur in different configurations caused by various object-evoked effects on the fish's electric field. These effects depend on the object

resistance (compared to that of the water) and capacitance (Budelli et al., 2002; Caputi et al., 1998). Objects with a lower resistance (e.g., the water plant, figure 5.8B) concentrate electric field lines at a central area on the fish skin. Here, lEOD amplitudes increase, whereas they decrease in the surrounding. An amplitude image with a Mexican hat configuration of central modulations larger 1 and peripheral modulations below 1 is induced. In contrast, targets with a higher resistance (e.g., the tomato, figure 5.8B) have an opposite effect on the fish's electric field and thereby cause the other Mexican hat configuration of amplitude images. Dipole objects with both, high and low resistance parts (i.e., carbon poles vs. insulating cover) exposed to the electric field cause both effects (local concentrations and scatter of field lines). Their amplitude images can therefore be more complex, i.e., feature Mexican hat configurations with a central but divided rim area (especially for object settings where electric field attraction by the object's carbon poles is profoundly reduced [1 nF] or lowered [4 nF], figure 5.8A2).

The capacitive component of the targets reduces lEODs at a central region on the fish skin in their initial phase (charging capacitance), while their second phase (discharging capacitance) grows (Budelli et al., 2002). The lEODs' P/N ratios decrease. An opposite distortion of lEOD waveforms occurs in the surrounding. As a result, only one Mexican hat configuration of central modulations below 1 and rim modulations larger 1 is generated (figure 5.8B3) for waveform images.

5.5.2 Distance estimation of capacitive objects

When object distance increases, amplitude and waveform images undergo multiple changes. As indicated by the local image features peak modulation and rostral image slope in figure 5.10, modulation magnitude and contrast are reduced, while the image profile spreads out, as shown in figure 5.9. Both image features (peak and slope) are also influenced by the (complex) impedance of capacitive objects (figure 5.10). *G. petersii* needs to consider and resolve these multi-parametric effects to obtain a reliable cue for short-range distance estimation. Behavioral, simulation and image recording studies (Hofmann et al., 2012; Sicardi et al., 2000; von der Emde et al., 1998) all suggest that the animals use the relative slope of amplitude images (SAR) as a prominent cue to judge the distance of purely resistive objects. The SAR was shown to be independent of an object's size or particular electrical resistance, whereas certain strong variations in object shape

affected the SAR in addition to object distance (Sicardi et al., 2000; von der Emde et al., 1998). Because capacitive objects (figure 5.8) like purely resistive objects induce amplitude images, the SAR might be a general distance estimator for both types of electrolocation targets. Our results obtained for capacitive dipole objects (figure 5.10A3) support this concept. Having excluded variations of object size and shape in the experiments, we found the SAR to change with distance but not for individual object capacitances (and related complex impedances).

As capacitive objects also induce waveform images (figure 5.8), we hypothesized an analogous mechanism for estimating object distance by SDRs. Such a 'backup cue' could improve object distance estimation in situations when the SAR might be difficult to extract, e.g., in case of capacitive objects causing only very weak and noisy amplitude images. Our results, however, showed that the SDR was affected by the distance and impedance of dipole objects (figure 5.10B3). Thus, waveform images are unlikely to provide reliable distance estimations, which in turn appear to be exclusively possible by amplitude image information.

Accordingly, the areas in the fish brain, associated with amplitude and (proposedly) waveform images, might differ in their structural/functional organization, which enables feature extractions from those images. The small receptive fields (Metzen et al., 2008) of ELL neurons, which process amplitude images are well suited for encoding local image features such as the peak amplitude or rostral image slope ('contrast'). Topographically specific mechanisms of lateral inhibition provided by ELL interneurons (Meek et al., 1999; Meek et al., 2001) might further improve this task by enhancing electric image contrast (von der Emde and Engelmann, 2011). In comparison, the 'weak' somatotopic organization of the midbrain map (Hollmann et al., 2016), which may provide only coarse waveform images, might not enable precise determinations of local image contrasts (or relative image slopes derived from them).

5.5.3 Impedance estimation of capacitive objects

Complex-impedance sensing proposedly enables *G. petersii* to identify capacitive prey items (von der Emde and Bleckmann, 1998) (insect larvae on or within the soil) or to discriminate among other capacitive targets (e.g., other animals, plants etc.). Object impedance is encoded by the two stimulus dimensions lEOD amplitude and waveform

perceived by electrolocating *G. petersii* (von der Emde, 1990; von der Emde and Bleckmann, 1992). Behavioral tests showed that the fish sense amplitude and waveform information independently and weigh them equally for discriminations of capacitive objects (von der Emde and Ronacher, 1994).

The peak modulations of an object's amplitude (PA) and waveform image (PD) might be the most prominent features for object impedance estimation as they represent the strongest change of each stimulus dimension. However, to turn PA and PD into unambiguous impedance estimators, fish need to compensate for the effects of object size, shape and distance, which also influence the peak modulations.

In this study, we introduced a possible mechanism (figure 5.11) to calibrate the peak modulations against variations caused by object distance (figures 5.10A1 and 5.10B1). This calibration routine implies that *G. petersii* relates SAR and PA or PD of consecutive electric images while changing its distance to an object. We showed that calibrated peak modulations acquired by smaller or larger distance changes (intervals) and with different proximities to a target were very similar and thus stable over distance (figure 5.11). To compute calibrated peak modulations, *G. petersii* might simply approach an object or employ object scanning behaviors nearby. Interestingly, fish were indeed observed to perform stereotyped and object-directed movements, so-called probing motor acts (Toerring and Moller, 1984), when discerning dipole objects with different complex impedances (von der Emde and Ronacher, 1994). Dynamic electric imaging, which already is involved in centering behavior (Pedraja et al., 2018) and is suggested for other recognition tasks (Hofmann et al., 2017; Hofmann et al., 2012), might thus also be used for impedance estimations by *G. petersii*. In our mechanism, the calibrated PA encodes resistive and the calibrated PD capacitive electrical properties, both of which define an object's (complex) impedance (Meyer, 1982; Schwan, 1963). Consequently, to judge object impedance, fish would have to 'integrate' (sum) the two cues. Supporting such a strategy, the animals were found to combine amplitude and waveform information (additively) to discriminate between dipole objects of complex impedance (von der Emde and Ronacher, 1994).

Electric-color sensing is another potential strategy the fish may use to evaluate complex impedance targets irrespective of their distance (Budelli and Caputi, 2000). In accordance with previous (simulation) data (Budelli and Caputi, 2000) we confirmed electric color as a stable impedance estimator over short distances (figure 5.13). To compute electric color no

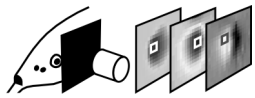

probing motions are required. It is suggested to derive from a clear color line, formed by an amplitude and waveform image's modulations (Budelli and Caputi, 2000). In contrast, our results for different targets (natural and dipole objects) showed that their amplitude and waveform image modulations lacked a definite linear relationship and scattered when combined. Only the modulations combined from equally shaped areas of an amplitude and waveform image revealed the pathway of an electric-color line (figure 5.12). To determine such modulations rather complex image normalization routines were needed (figure 5.7), which we assume *G. petersii* cannot perform. However, we found another, much simpler strategy to depict the amplitude and waveform modulation relationship as defined by the electric-color pathway. Here, the electric-color line was obtained from the peak modulations of electric images (PA, PD) and a modulation baseline (basal condition). Because this color line represents a quasi 'proportional' relationship of both peak modulations, electric color could simply be determined by the ratio of PD and PA.

As yet, there are no behavioral verifications (Röver, 2012) or implications for electric-color sensing that show if and how the fish might do so. Instead, the anatomical/physiological organization of the electrosensory pathway in the fish brain might give a first hint whether our proposed mechanism of electric-color extraction might be applicable. When compared, the topographic organization of the 'amplitude map' (ELL medial zone) appears much more distinct than that of the proposed 'waveform map' (nucleus lateralis) (Hollmann et al., 2016). The latter can be considered 'coarser' in comparison. Because of this difference, it appears unlikely that a precise topographical and 'hardwired' combination of amplitude and waveform image modulations takes place to process electric color. In contrast, the calculation of peak modulations by, for example, the mean activity of a population of neurons (von der Emde and Engelmann, 2011) should be unaffected by the maps' differences mentioned above.

This, in addition to our findings, may suggest that a reliable mechanism for electric-color estimations might be based on the combination of the amplitude and waveform images' peak modulations.

The extraction of electric color (as a simple peak modulation ratio) vs. the more complex, additive combination of calibrated peak modulations would add different qualities to object impedance estimation. As a result, fish could rely on each of the two proposed perceptual mechanisms to different degrees during particular object-recognition tasks. Especially for fast inspections of crucial targets (e.g., prey insect larvae in the soil) electric-color

perception seems more suitable than the more elaborate, motion-based strategy of impedance estimation. Indeed, *G. petersii* do not display the 'rather time-consuming' probing motor acts (Toerring and Moller, 1984) during foraging (von der Emde, 1992; von der Emde et al., 2008).

5.6 Conclusion

This chapter suggests unambiguous active electrolocation strategies, by which weakly electric fish *Gnathonemus petersii* could inspect capacitive objects. To judge object distance and impedance independent of one another, dynamic (motion-based) and/or static electric imaging, as usually performed by these fish, is applicable. It provides electric image cues through very basic calculations, which are principally supported by the structural/functional organization of *G. petersii's* electrosensory neuronal pathways. Reliable distance estimators (relative image slopes) derive from the targets' amplitude images as static cues. Robust impedance estimations, based on the objects' amplitude and waveform images, could be achieved through electric colors (static image cues) or by the images' peak modulations, when calibrated with the distance estimator (as dynamic cues) and combined. Electric-color sensing, as the simpler and thus potentially quicker mechanism, seems suited best for fast recognitions of capacitive targets. It might therefore drive the animal's quick and reliable identification of (capacitive) prey items, which is considered a crucial electrolocation task, but presently hardly understood. To reveal electric-color sensing for *G. petersii*, a follow-up study may define electric colors and color traits for prey/non-prey items (via recordings) and complementarily test the foraging skills of electrolocating fish (via behavioral assays).

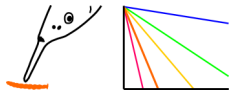

6. Electric-color sensing in weakly electric fish suggests color perception as a sensory concept beyond vision

This chapter is based and expands on the study:

Gottwald, M., Singh, N., Haubrich, A.N., Regett, S. and von der Emde, G. (2018). Electric-Color Sensing in Weakly Electric Fish suggests Color Perception as a Sensory Concept beyond Vision. *Current Biology* **28,** 3648–3658.

My contribution to the published work included: conceptualization of the research goals/study experiments; development/design of the experimental setups, recording software and analysis scripts; performing and overseeing experiments; analysis/visualization of the study data; preparation/writing of the manuscript; supervision of the theses contributing to this study:

Haubrich A.N. (2015). Untersuchung der elektrischen Farbe von natürlichen Objekten bei der aktiven Elektroortung des schwach elektrischen Fisches *Gnathonemus petersii*. *Bachelor's thesis*. Zoological Institute, University of Bonn, Bonn.

Regett S. (2016). Objektdetektion im Substrat beim schwach elektrischen Fisch *Gnathonemus petersii*. *Bachelor's thesis*. Zoological Institute, University of Bonn, Bonn.

Singh N. (2018). Detection of artificial food material by active electrolocation in *Gnathonemus petersii*. *Master's thesis*. Zoological Institute, University of Bonn, Bonn.

6.1 Abstract

Many sighted animals use color as salient and reliable cue to identify conspecifics, predators or food. Similarly, nocturnal weakly electric fish *Gnathonemus petersii* might rely on 'electric colors' for unambiguous, critical object recognitions. These fish identify nearby targets by emitting electric signals and by sensing the object-evoked signal modulations in amplitude and waveform with two types of epidermal electroreceptors (active electrolocation). Electrical capacitive objects (animals, plants) modulate both parameters; purely resistive targets (e.g., rocks) only the signal's amplitude. Ambiguities of electrosensory inputs arise when object size, distance or position vary. While previous reports suggest electrosensory disambiguations when both modulations are combined as electric colors, this concept has never been demonstrated in a natural, behaviorally relevant context. Here, we assessed electric-color perception by (1) recording object-evoked signal modulations and (2) by testing the fishes' behavioral responses to these objects during foraging. We found that modulations caused by aquatic animals or plants provided electric colors when combined as a ratio. Individual electric colors designated crucial targets (electric fish, prey insect larvae or others) irrespective of their size, distance or position. In behavioral tests, electrolocating fish reliably identified prey insect larvae of varying sizes from different distances and did not differentiate between artificial prey items generating similar electric colors. Our results indicate a color-like perceptual cue during active electrolocation, the 'computation', reliability and use of which resemble those of color in vision. This suggests 'color' perception as a sensory concept beyond vision and passive sensing.

6.2 Introduction

Color vision is widespread across the animal kingdom and found in various forms in mollusks, arthropods and vertebrates. To all these animals, color is essential to being able to recognize relevant objects and to judge their properties. During foraging, for example, it can be used to enhance the contrast between food items and the background (Kelber and Jacobs, 2016). Some animals have an innate color preference, which helps them to identify a certain food source or prey (e.g., Kawamura et al., 2017; Lunau and Maier, 1995; Taylor et al., 2014). In addition, some prey animals may indicate or pretend toxicity by warning

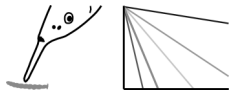

colors, which will be avoided by predators (Rojas et al., 2015). Likewise, the perception of signal colors or color patterns enables the recognition of conspecifics and mate choice (e.g., Couldridge and Alexander, 2002; Detto, 2007; Tamura et al., 2017).

The physical basis of color is the wavelength spectrum of light reflected from an object. Most importantly, perceived color is the result of the brain's neuronal processing, which determines color appearance. At least in non-aquatic environments, it is remarkably stable, e.g., over distance, a wide range of illumination conditions and for different viewing positions (Foster, 2011; Romero et al., 2011). While the neuronal networks of color perception are complex, the basic principle is rather simple: color is encoded by the activity ratio of different photoreceptor types (which is recombined in opponent channels) (Kelber, 2016).

Similar to the many sighted animals, which use color for crucial and reliable object recognitions, the nocturnally active and weakly electric fish *Gnathonemus petersii* might rely on a color-like cue to do so during active electrolocation.

By discharging an electric organ in its tail, the fish emits brief pulses (electric organ discharges, EODs), which generate an electric field around its body (von der Emde and Ruhl, 2015). The fish's back, stomach, head and chin appendix are covered with electroreceptor organs (mormyromasts) (Harder, 1968; von der Emde and Schwarz, 2002). They monitor the local EODs (lEODs) at the fish skin. lEOD alterations, caused by a nearby target disturbing the electric field, are detected by the mormyromasts, at the skin region opposite to the target, with two different types of electroreceptors, termed A- and B-cells (Szabo and Wersäll, 1970; von der Emde and Bleckmann, 1992). This allows *G. petersii* to perceive object-evoked amplitude and waveform modulations of its pulses, which are critical cues for object discrimination (von der Emde, 1990; von der Emde and Ronacher, 1994; von der Emde and Schwarz, 2002). Electrical purely resistive targets (such as rocks, sand or soil) only modulate the lEOD amplitude. Capacitive objects (animals and plants) modulate the lEODs in amplitude and waveform (von der Emde and Schwarz, 2002; Gottwald et al., 2017a, see chapter 5). Object-evoked amplitude or waveform modulations from across the fish skin provide *G. petersii* with a separate 'electric image' of the target (Budelli and Caputi, 2000; Gottwald et al., 2017a). Because amplitude and waveform modulations vary with an object's size, distance and position, amplitude and waveform images are highly ambiguous. However, when combined, the modulations of the two images yield a cue, which is invariant to object distance and might

serve as a 'marker' for individual types or 'families' of capacitive targets (Budelli and Caputi, 2000; Caputi and Budelli, 2006; Gottwald et al., 2017a) (underwater organisms). It was called an electric color as it, partly like visual color, relates the information (here, amplitude and waveform image modulation) derived from distinct receptor types (here, A- and B-cells of the mormyromast) (Budelli and Caputi, 2000), as a ratio (Gottwald et al., 2017a, see chapter 5).

Proposedly acquired by rather simple and quick computations, electric color was hypothesized to enable fast recognitions of electrolocation targets, e.g., of prey (insect larvae in the soil) (Gottwald et al., 2017a). During foraging (and other critical tasks), electric-color sensing might emphasize and reliably designate such items irrespective of their distance and possibly also their sizes and positions.

If so, color sensing during active electrolocation would be based upon similar computational 'goals and strategies' (Stevens, 2012) as color perception in sighted animals. Visual and electric color would share similar aspects of color traits and utility, though originating from different physical inputs and neuronal machineries of an active (electric) vs. passive (visual) sensory system(s). Electric-color sensing, if present in *G. petersii* and matching the criteria mentioned above, would consequently suggest color perception as a sensory concept beyond vision and passive sensing.

So far, electric-color perception by *G. petersii* has not been demonstrated (Röver, 2012) or been tested in a natural, behaviorally relevant context, which is our aim in this study. To do so, we used two complementary approaches (recording and behavioral experiments).

We recorded the amplitude and waveform modulations evoked by *G. petersii's* natural capacitive targets (weakly electric or other fish, prey insect larvae and water plants). This data was used to define electric colors and color traits for targets with different sizes, distances or positions. Recordings were also conducted to select artificial stimulus objects, whose amplitude and waveform modulations either resembled those of prey larvae or not.

In the behavioral experiments, we then tested the foraging skills of electrolocating *G. petersii*. First, we investigated if variations in the size or distance of stimulus objects (buried prey insect larvae vs. plant stems and copper rods) affect the fish's prey recognitions. Changing target size or distance (burial depth) renders object-evoked amplitude or waveform modulations ambiguous for identifications of prey/non-prey items. A correct choice behavior, however, would suggest that the fish use an unequivocal active electrolocation cue to do so. Matching behavioral and recording results may reveal such a

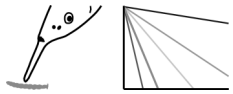

cue as electric color.

In the second behavioral assay, we tested prey identifications with real prey larvae vs. the artificial prey/non-prey items, which lack cues that usually emanate from natural targets (odors, passive electrolocation cues etc.). Passive electric stimuli, for example, arise from bio-chemical processes (such as ion flow across epithelia of body openings) and/or muscle contractions (e.g., respiratory movements etc.) of aquatic organisms (Bedore et al., 2015; Moller, 1995). Like other electroreceptive animals (sharks, rays or platypus), which use passive electrolocation, e.g., during foraging (Collin and Whitehead, 2004; Czech-Damal et al., 2012), also *G. petersii* can perceive passive electric stimuli by epidermal, 'ampullary' organs (e.g., Moller, 1995).

While previous behavioral experiments (von der Emde and Bleckmann, 1998) imply that such additional cues only make a minor contribution to the fish's actual prey choice, a dominant active electrolocation cue for this task has not been identified yet. Comparing *G. petersii's* choices of artificial prey items, providing solely active electrolocation cues, with choices of real prey in our experiments would reveal a potential, dominant electric-color cue for prey identification with respect to the other stimuli evoked by natural prey.

6.3 Materials and methods

6.3.1 Experimental Animals

Seven wild-caught *G. petersii* of unspecified sex and age were obtained from a commercial fish dealer (Aquarium Glaser, Rodgau, Hessen, Germany). Fish were housed in separate tanks (23 cm × 40 cm × 40 cm) with a 12 h:12 h light:dark cycle. Water conductivity (~100 µS cm^{-1}) and temperature (~27 °C) were kept constant. One fish was used for recording experiments. The other six fish participated in behavioral experiments. Other animals, used as experimental stimulus objects (electrolocation targets) during experiments, were either purchased from commercial dealers (non-electric fishes, chironomid larvae, Fressnapf Holding SE, Krefeld, North Rhine-Westfalia, Germany; weakly electric fish, Aquarium Glaser) or collected from a local creek (Nette, various insect larvae). All procedures and methods performed in the recording experiments were approved by the authorities of the State of North Rhine-Westphalia (Landesamt für Natur, Umwelt und Verbraucherschutz Nordrhein-Westfalen, LANUV-NRW), reference number:

84- 02.04.2015.A444. All behavioral experiments were carried out in accordance with the guidelines of German law and with the animal welfare regulations of the University of Bonn.

6.3.2 Recording experiments

To experimentally define electric color of an electrolocation target usually requires the recording of its amplitude and waveform image (i.e., the object-evoked amplitude and waveform modulations from across the fish skin) (Gottwald et al., 2017a).
However, doing so for the many stimulus objects we aimed to evaluate in this study would be too time consuming and thus is not applicable. We therefore used a simpler approach to acquire an object's electric color by recording only the amplitude and waveform modulation from a single, central spot of its electric images. Preliminary tests, as outlined in the appendix (A.1), indicated that this quick, alternative approach yields analogous results to the mechanism suggested for electric-color extraction in the previous study (Gottwald et al., 2017a, see chapter 5).
Amplitude and waveform modulations of several water plants (Fressnapf Holding SE), insect larvae (prey), fish and electric fish (for taxonomic classifications see results section and figure 6.5) were measured close to the chin appendix of a *G. petersii* (figure 6.1). The fish's movable chin appendix is considered to be an 'electroreceptive fovea' (Castelló et al., 2000; von der Emde and Schwarz, 2002), which is used for object inspection and prey recognition (von der Emde and Ruhl, 2015). Prior to recordings, stimulus animals were euthanized in a lethal Etomidat (2 mg ml^{-1}, Janssen-Cilag GmbH, Neuss, North Rhine-Westfalia, Germany) solution (insect larvae) or in a lethal MS 222 (2 g l^{-1}, Acros Organics, Fair Lawn, New Jersey, USA) solution (fish, electric fish).
The *G. petersii* was narcotized in an Etomidat solution (0.6 ml Etomidat in 1 liter of water). It was then fixed onto a plastic holder (9 cm × 1.5 cm × 6 cm) in the center of the experimental tank (28.7 cm × 38.5 cm × 18.8 cm) with cloth strings and wooden sticks (figure 6.1A). The tank water (11 l, 99.3 ± 2.6 µS cm^{-1}, 25.6 ± 0.4 °C) was mixed with 3.3 ml Ethomidat to maintain anesthesia. Under sedation, the animal discharges its electric organ in the tail at a slow and regular rate. 15 lEODs were recorded, 1 mm away from the fish's skin, with a selfmade carbon dipole electrode (pole-length: 2 mm, inter-pole-distance: 1 mm) in the presence and the absence of a stimulus object. In doing so, the elec-

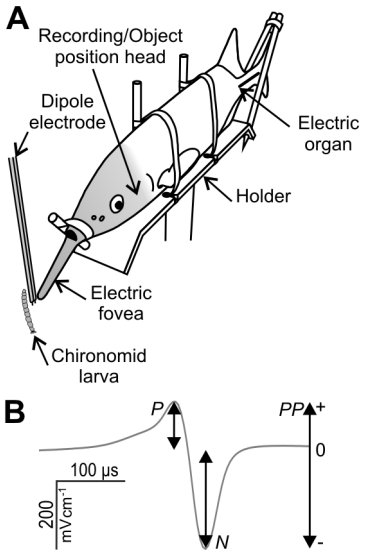

Figure 6.1: Recording of local electric organ discharge (lEOD) modulations.

(A) Insect larvae (or fish, aquatic plants and artificial objects, not shown) were recorded close to the electric fovea (gray) and at the side of the head of a fixed *G. petersii* with a dipole electrode (gray). **(B)** lEOD recorded at the electric fovea (without object). Stimulus objects modulate the lEOD's (peak-to-peak) amplitude (PP, double arrow) and waveform (ratio of the peak amplitude of the positive [P] and negative [N] lEOD phase, double arrows).

trode was placed (at a stationary position) between the object and the fish skin (figure 6.1A). The electrode's two poles were orientated perpendicular to the fish's skin surface. Electrode positioning was achieved by a computer-guided motor system, as used in previous studies (Fechler and von der Emde, 2012; Gottwald et al., 2017a). For object placement we used a micromanipulator.

The biphasic waveforms of the lEODs (figure 6.1B) were amplified (×100, custom-built differential amplifier), filtered (band-pass: 1 Hz to 100 kHz) and digitized (resolution: 16-bit, sampling rate: 250 kHz, A/D converter PCIe 6341, National Instruments, Austin, Texas, USA). lEOD amplitude was defined as peak-to-peak amplitude (PP) of the signal's positive (P) and negative (N) phase and the lEOD waveform was determined by the peak amplitude ratio of the two signal phases (P/N) (figure 6.1B). The amplitude and waveform parameters of the 15 lEODs obtained with and without a stimulus object were each calculated and averaged with a self-designed LabVIEW program (National Instruments).

The object-evoked lEOD amplitude (PP) or waveform (P/N) modulation was then calculated as the ratio between the PP or P/N means, determined for the target present and absent. These ratios were then subtracted with 1. As a result, PP and P/N modulations are indicated by values larger or smaller than 0. They get stronger the more they deviate from 0. In turn, values ~0 show that no (considerable) object-evoked modulation has occurred.

PP and P/N modulations of animals and plants were recorded for several conditions (different object sizes or distances to the recording electrode). The modulations of some individuals were also measured close to the side of the head of the *G. petersii*. Here, stimulus object and electrode were positioned between the eye and the gill opening (figure

6.1A).

Finally, small resistors or capacitors (YAGEO Corp., New Taipei, Taiwan) and self-made carbon or plastic particles (all of equal size: 2 mm × 1.25 mm × 1.25 mm) were recorded close to the fish's fovea. Doing so, we selected artificial stimulus objects that did or did not generate modulations similar to larval prey insects.

6.3.3 Behavioral experiments

Prey identification by *G. petersii* was tested under different foraging conditions. The tanks (23 cm × 40 cm × 40 cm) in which the six fish were housed contained an experimental arena (23 cm × 10 cm). Water conductivity (103 ± 4.7 µS cm^{-1}) and temperature (27.2 ± 1.1 °C) were kept constant during experiments.

6.3.3.1 Tests with different sizes/distances of prey/non-prey items

The experimental arena consisted of a sandbox (20 cm × 10 cm × 3 cm), which was divided into eight feeding areas (2 × 4, with each area sized 5 cm × 5 cm × 3 cm) (figure 6.2). Three *G. petersii* (fish 1-3), which were trained to feed from the sandbox, were tested. Before trials, an opaque plastic divider blocked the access to the sandbox, while a prey (dead chironomid larva) or non-prey item (plant stem: *Hydrocotyle vulgaris* or copper rod) was buried in one of the areas. Presentation of stimulus objects and selection of feeding areas was pseudorandomized during trials. Burial depth (object distance) was either 1 or 5 mm. Object size (length) was either large (~15 mm) or small (~8-10 mm). Buried objects did not provide visual cues for their identification. Burying also attenuated possible odors or passive electrolocation cues. A fish had 30 seconds per trial to search the sandbox for

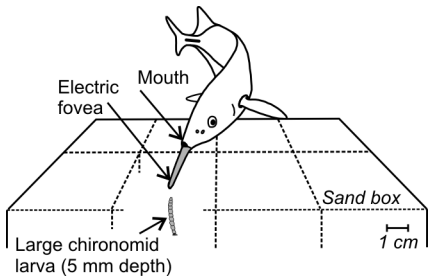

Figure 6.2: Presentation of different-sized stimulus objects at varying distances.
Sandbox with eight feeding areas. Small or large prey (chironomid larvae) or non-prey items (not shown) were buried at two different depths ('distances' of 1 or 5 mm). Foraging fish scanned the sand with their electric fovea (gray). Items identified as prey were sucked in the fish's open mouth.

prey. In doing so, fish scanned the sand with their chin appendix (electroreceptive fovea). After detection, fish dug for the object and when also judged as prey, sucked it into the mouth (intake). Digging was therefore chosen as the criterion that fish had found the object and object intake as the criterion that fish had identified the object as prey item. After every second trial, an interim-trial was conducted with a chironomid larva to keep the fish motivated.

6.3.3.2 Tests with artificial objects

Five *G. petersii* (fish 2-6) were tested. The fish were trained to feed from a plastic table (20 cm × 10 cm × 3 cm, figure 6.3). Capacitors, resistors, plastic and carbon particles were presented. Some of these items electrically resembled prey (chironomid or other insect larvae) or non-prey items (see results section). Small, dead chironomid larvae (8.6 ± 1.7 mm length) were used as a control for natural prey. During object placement, the plastic divider restricted access to the feeding table. A stimulus object was placed pseudo-randomly on the table in one of eight position markers (figure 6.3). Stimulus objects were presented in a pseudorandomized order. In each trial, fish had 30 seconds to electrically probe an object and to suck it in. Trials were conducted at an ambient light level of 113 ± 5.5 lx at which visual object discrimination is no more reliable in *G. petersii* (Schuster and Amtsfeld, 2002). Stimulus objects were also too small to be visually recognized due to the poor spatial resolution of the fish's grouped retina (von der Emde and Ruhl, 2015). Artificial items did also not provide chemical or passive electric stimuli to *G. petersii*. Identification of these objects was therefore restricted to active electrolocation cues. An object was considered found when a fish had approached it very closely (~1 mm) with its chin appendix or had touched it. Object intake was chosen as the criterion that the fish had identified an (artificial) object as a prey item. After every third trial, an interim-trial was

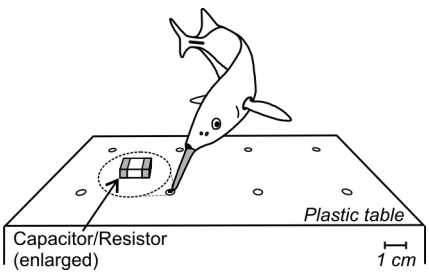

Figure 6.3: Presentation of artificial stimulus objects. Capacitors/resistors (or plastic/carbon particles and chironomid larvae, not shown) were presented on a plastic table. Circles on the table indicate positioning markers for object placement. Foraging fish scanned the table with their electric fovea (gray) and (artificial) items identified as prey were then sucked into the mouth.

conducted with a real chironomid larva to maintain motivation of the fish.

6.3.4 Statistical analysis and quantification

Statistical analyses of the recording and behavioral data were performed using SPSS (IBM Corp., Armonk, New York, USA).

6.4 Results

6.4.1 Electric colors reliably designate relevant environmental targets

Several targets (fish, electric fish, different types of insect larvae and plants) were used to test for electric colors of natural capacitive objects during active electrolocation. The object-evoked lEOD amplitude (PP) and waveform (P/N) modulations (examples shown in figure 6.4) were recorded close to the skin of a *G. petersii* at a fixed position. Measurements were mainly conducted at the fish's chin appendix (electroreceptive fovea). The second object and recording position was at the side of the fish's head (see section 6.3.2 and figure 6.1A). Electric colors were calculated as waveform-to-amplitude

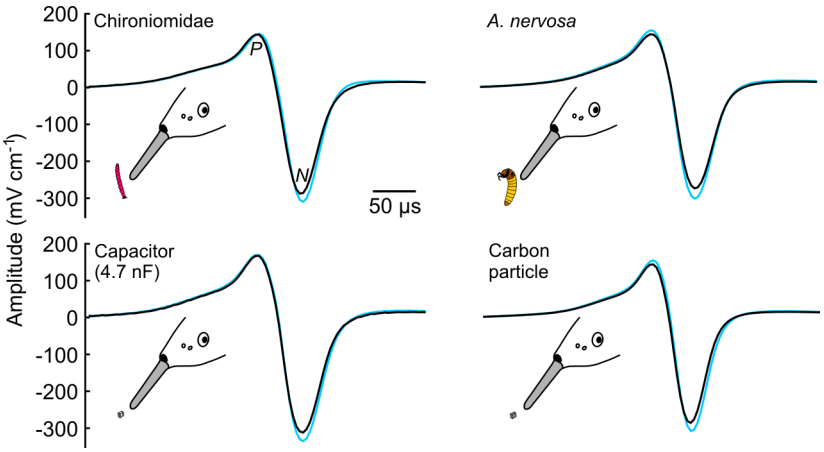

Figure 6.4: Object-evoked lEOD amplitude and waveform modulations.
lEODs recorded at the tip of fish's electric fovea (gray) with stimulus objects (see insets) present (blue signals) and absent (black signals). Electrical capacitive targets (e.g., insect larvae and capacitor) slightly modulate the lEOD (peak-to-peak) amplitude and waveform (ratio of the peak amplitude of the positive [P] and negative [N] phase) by scaling N considerably stronger than P. Purely resistive stimulus objects (e.g., a carbon particle) only cause an amplitude modulation, scaling N relative to P to a much lower extend.

modulation ratios. They were evaluated for different object sizes, different object distances and the two recording positions (figures 6.5A – 6.5C).

For each stimulus object, the PP modulation was plotted versus the P/N modulation in a scattergram, yielding a PP-P/N modulation pair (Budelli and Caputi, 2000; Caputi and Budelli, 2006; Gottwald et al., 2017a; von der Emde and Ronacher, 1994; von der Emde and Schwarz, 2002) (figures 6.5A and 6.5B). In these graphs, PP-P/N modulation pairs

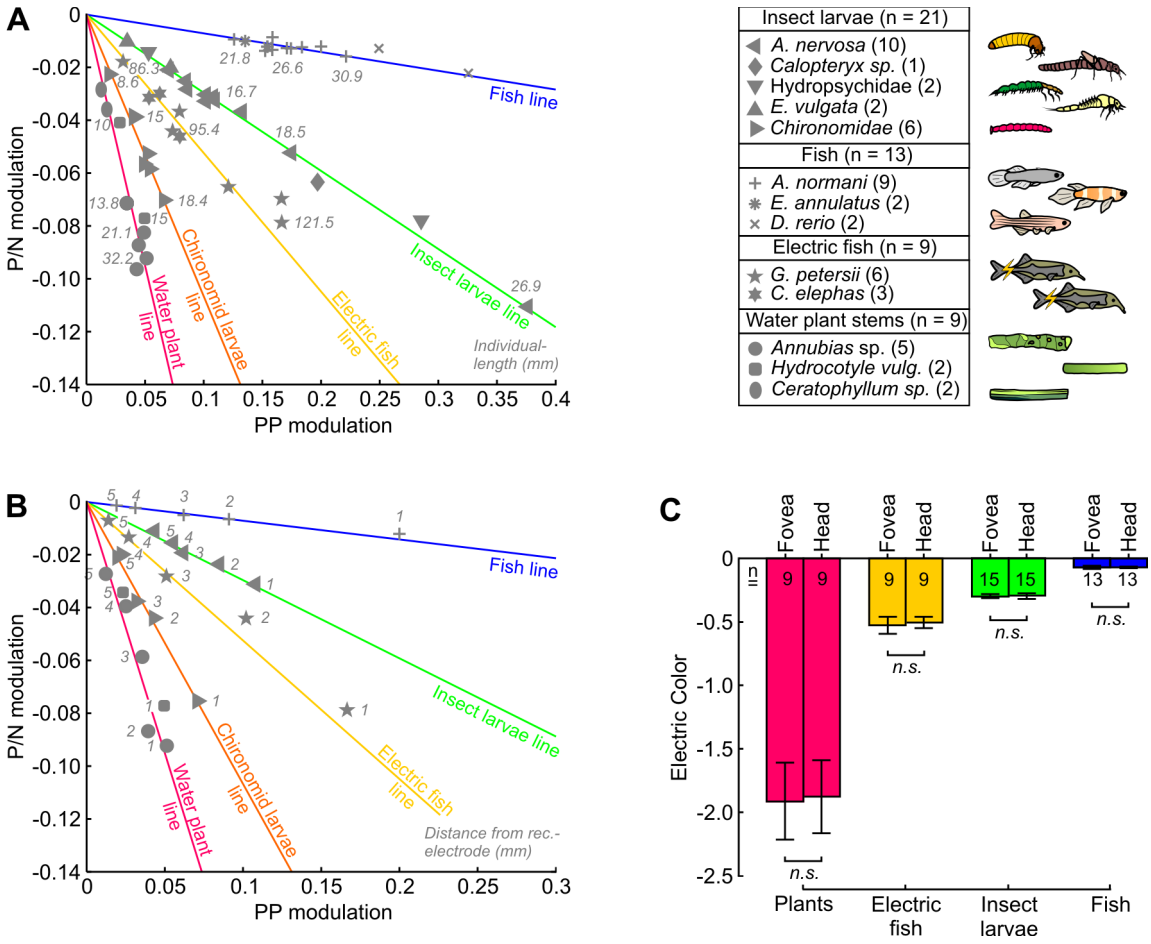

Figure 6.5: Electric colors evoked by natural electrolocation targets.

(A) Recordings of animals and plants of various sizes (lengths) at the electric fovea (1 mm distance from the recording electrode). Object-evoked modulations (PP or P/N) are stronger the more they deviate from 0. The individuals' PP-P/N modulation pairs (gray symbols) with a similar waveform (P/N) -to-amplitude (PP) modulation ratio (electric color) fall onto a linear function (color line). Indicated by the lines labels, electric color defines categories of stimulus objects, irrespective of their sizes. **(B)** PP-P/N modulation pairs of single target items, recorded at different distances to the electric fovea, fall onto their respective color lines obtained from the data in (A). **(C)** Statistical comparison (paired t-test, 2-tailed) of electric colors recorded from the same target items at the fovea (data in A) and at the side of the head (shown as means ± SD). Data had passed Shapiro-Wilk normality test in advance ($p > 0.05$ for all groups).

recorded at the fovea, e.g., for differently sized animals and plants could be aligned with five linear functions (figure 6.5A, colored lines). Each line was obtained only for objects, whose PP-P/N modulation pairs provided a similar waveform-to-amplitude modulation ratio (electric color). As indicated by the line labels, electric colors corresponded to basic categories of natural objects (fish, electric fish, water plants, insect larvae). Interestingly, insect larvae generated two very distinct electric-color lines, one for chironomids and one for all other insect larvae tested. Chironomids are the main food item of *G. petersii* (Nwani et al., 2011), and due to their specific electric color, they clearly stand out among larval prey insects. Because PP-P/N modulation pairs caused by all stimulus objects showed close alignments to their specific color lines irrespective of object size, electric color was size-invariant (figure 6.5A).

When recorded for different object distances from the fovea (figure 6.5B), PP-P/N modulation pairs of stimulus objects fitted the same color lines, which were obtained before for stimulus objects of different types and sizes. This suggests that electric color is also distance-invariant.

Electric colors of stimulus objects, which were recorded successively at the fovea (figure 6.5A) and at the side of the fish's head, showed no significant differences when statistically compared (figure 6.5C). Thus, electric colors were stable for different 'electric viewing' positions (i.e., when an object is inspected with the fovea or the head). Our measurements also showed that PP or P/N modulations alone varied non-systematically for different stimulus objects, distances and sizes (figures 6.5A and 6.5B). Hence, only electric color, i.e., the ratio of waveform-to-amplitude modulations, provided an unambiguous active electrolocation cue for identifying relevant environmental objects, especially larval prey insects.

6.4.2 Electrolocating fish use electric color to reliably identify prey

In behavioral experiments, we tested whether fish might rely on electric-color cues for prey recognition. If so, they should be able to spontaneously identify chironomid larvae and to reject non-prey items, irrespective of their size or distance (i.e., the burial depth within the soil). However, as natural objects might also provide additional cues, e.g., odors for their identification, we also used artificial objects, which possess solely electrical properties (figures 6.4 and 6.6, see also section 6.3.3.2) during the tests. Based on

recordings close to the fovea, we selected small resistors and capacitors, which caused different amplitude and waveform modulations but provided stable electric colors of either a chironomid larva (capacitors) or of the other larval prey insects (resistors) (figure 6.6). Note that, with their metal/plastic enclosure exposed to the fish's electric emissions, resistors had additional weak capacitive properties and thus evoked weak waveform (P/N) modulations. Pure electrical resistors usually do not change the waveform of the fish's electric signal. We additionally used small carbon or plastic particles, which generated only amplitude (PP) modulations and thus did not provide electric colors (figure 6.6).

In the first series of behavioral experiments, three *G. petersii* (fish 1-3) were trained to feed from a sandbox (see section 6.3.3.1 and figure 6.2) containing a single buried chironomid larva or a non-prey item (plant stem or a copper rod). Like the carbon particle (figures 6.4 and 6.6), a copper rod is an electrical conductor (i.e., purely resistive) and causes only amplitude modulations and thus does not generate an electric color. Stimulus items were either large (~15 mm) or small (~8-10 mm) and were presented at a depth of 1 or 5 mm (figure 6.7). During trials, fish electrically scanned the sandbox for food with their chin appendix. Items identified as prey were then sucked into the mouth (intake).

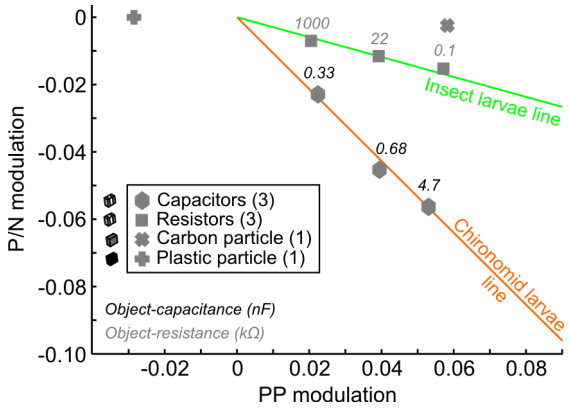

Figure 6.6: Electric colors evoked by artificial electrolocation targets.

Artificial objects recorded at the electric fovea (0.5 mm distance to the recording electrode). Certain capacitors and resistors (values written next to the symbols) generate electric colors of natural prey. Thus, their PP-P/N modulation pairs (gray symbols) fit the color lines, obtained from the data in figure 6.5A. The resistors provided electric colors as a result of a weak additional capacitance evoking amplitude (PP) and waveform (P/N) modulations (refer to main text for details). Carbon and plastic particles, as purely resistive objects, caused amplitude modulations (indicated by values larger or smaller 0) but no (considerable) waveform modulations (indicated by the values ~0). Such objects therefore do not evoke electric colors.

In all three fish, intakes of chironomids reached 100 % (figure 6.7), irrespective of sizes or burial depths. Non-prey items evoked, if at all, only minor intake rates, which were statistically inseparable (figure 6.7). Some plant stems were erroneously judged as chironomid prey only when they were large and deeply buried (5 mm) or when they were small and buried at shallow depth (1 mm). Our recordings revealed that in these perceptual situations, PP-PN modulation pairs evoked by plant stems tended to scatter near the chironomid color line (see *Hydrocotyle vulgaris* with 10 mm length, figure 6.5A, or at 5 mm distance, figure 6.5B). The rare choices of plant stems might have therefore been driven by this minor electric color bias.

The constant choice behavior for chironomid larvae suggests the use of electric color for prey identification in *G. petersii*. We are aware of no other active electrolocation cue, which could have guided prey choice as performed by the fish. While foraging relies mainly on the active electric sense, it probably was assisted by the perception of odor cues and/or passive electrolocation cues (i.e., low frequency electric stimuli) (Engelmann et al., 2010; von der Emde, 1994; von der Emde and Bleckmann, 1998).

However, such additional cues are far less important, especially for triggering prey choice (i.e., intake) (von der Emde and Bleckmann, 1998), and can be considered to be attenuated for our buried stimulus items.

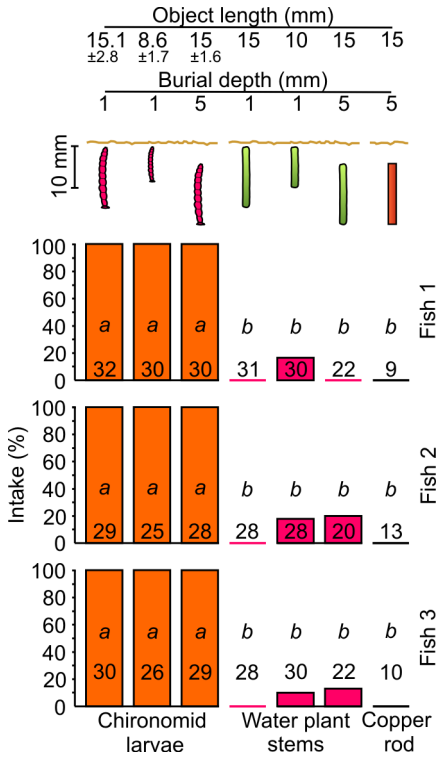

Figure 6.7: Prey recognition for differently sized stimulus objects at varying distances. Relative intake of small and large prey and non-prey items, buried at two different depths ('distances') in the sandbox. Object properties are illustrated by the inset scheme. Three fish were tested. Plant stems belonged to species *Hydrocotyle vulgaris*. For each condition, 32 trials were conducted. The number of detected items is given within or above the bars. An Exact Fisher-test (2-tailed) was used to compare the relative object intake under the different conditions for each fish. Bars, which do not differ significantly ($p > 0.05$) or show constant values, are indicated by the same italic letter. The bar color indicates the electric colors of the objects (see figure 6.5).

In a second series of behavioral experiments, five *G. petersii* (fish 2-6) were offered chironomids or artificial prey or non-prey items (figure 6.8). The artificial items do not generate low frequency stimuli or chemical cues and thus provided only active electrolocation cues for their identification (see section 6.3.3.2). Therefore, artificial prey could only be identified reliably by means of electric color (as indicated in figure 6.6). In all five fish, intake rates of artificial objects having the same electric color did not differ statistically (figure 6.8). In addition, objects that did not generate electric colors (plastic and carbon particles) were completely rejected by the fish (figure 6.8).

Intake rates for capacitors (60-75 %) with the electric color of chironomids or resistors (25-38 %) with the electric color of the insect larvae line (figure 6.6) statistically differed from one another and from intake rates of real chironomid larvae (93-100 %) (figure 6.8). The intake rates of artificial items show that fish rely on electric color to reliably identify prey by means of active electrolocation. Even though different intake rates for chironomids and capacitors suggest a use of additional parameters, e.g., odors or passive electric stimuli (von der Emde and Bleckmann, 1998), the high intake rates for capacitors reveal electric

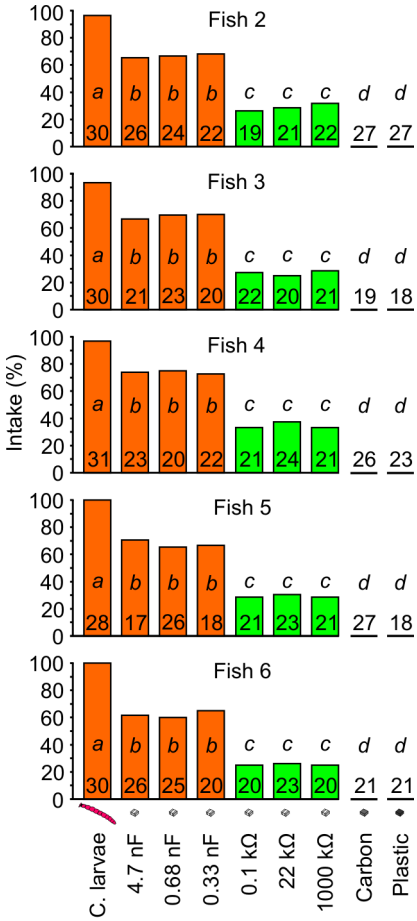

Figure 6.8: Prey recognition for artificial stimulus objects.

Relative intake of artificial objects and chironomid larvae for five fish. For each condition 32 trails were conducted. The number of objects found is given within or above the bars. Exact Fisher-tests (2-tailed) were used to compare the rel. object intake under the different conditions for each fish. Bars, which do not differ significantly ($p > 0.05$) or show constant values, are indicated by the same italic letter. Different italic letters indicate significant differences ($p \leq 0.05$) in intakes. Bar colors indicate the electric colors of the objects (see figures 6.5 and 6.6).

color as the dominant cue for prey identification. The lower intake rates of resistors indicate that the fish recognized them as their 'secondary' insect prey, which is preferred less compared to chironomid larvae (Nwani et al., 2011). Electrical differentiation of primary from secondary prey larvae might be an easy task for *G. petersii* due to the clear difference in their electric color revealed by our recordings (figure 6.5A).

6.5 Discussion

Our results show that the weakly electric fish *G. petersii* uses a color-like perceptual cue to identify crucial environmental objects such as prey. Although vision and the active electric sense rely on different physical stimuli, color perception in the two modalities results from similar aspects of color formation. Electric colors can be represented as distinct lines (color lines) in a two-dimensional space with amplitude and waveform modulation on its axis (figure 6.5) (Budelli and Caputi, 2000; Caputi and Budelli, 2006; Gottwald et al., 2017a) This bears close resemblance to the representation of visual color hues, e.g., in the human visual system, which form distinct color lines within their respective color space (isoluminant plane only). Here, both axes are opponent color channels (e.g., Hansen et al., 2007), which recombine the information from different types of cones (Kelber, 2016) via subtraction.

Also in *G. petersii,* central subtraction of its two electroreceptor channels is required to extract waveform modulations as counterpart to amplitude modulations. Sensory processing at the receptor level only provides amplitude or amplitude and waveform information combined, each of which is transduced by one of the two electroreceptor types (A- or B-cells) of the fish's epidermal sense organs (mormyromasts) (Fechner et al., 2018; Szabo and Wersäll, 1970; von der Emde and Bleckmann, 1992). While both sensory streams project to separate zones in first order central regions, waveform extraction is suggested to take place at higher brain level (Fechner et al., 2018; Hollmann et al., 2016).

Visual and electric colors are advantageous for object detection in a similar way. Compared to pure intensity contrasts, which can be very ambiguous when lightness changes, color enhances the contrast of relevant objects (e.g., fruits, flowers etc.) against their backgrounds more reliably and clearly (Johnson and Mullen, 2016; Kelber and Jacobs, 2016). During active electrolocation, the voltage of the fish's electric emissions varies around the animal (Pusch et al., 2008) and thereby the 'electric illumination' of

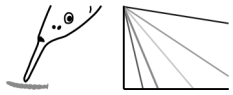

nearby targets. Object-evoked amplitude modulations and contrasts change accordingly (Pusch et al., 2008). In turn, the electric color of capacitive objects makes, e.g., prey items stick out more robust and distinctively from resistive backgrounds (soil, sand, stones), which only cause amplitude modulations (von der Emde and Ruhl, 2015).

Electric colors also render the fish's active electric sense reliable for the identification of relevant objects (prey, other animals, plants). Our recordings revealed that electric colors were remarkably stable, irrespective of an object's size, distance or position (figures 6.5A-6.5C). We thereby verify and extend on previous simulation (Budelli and Caputi, 2000; Caputi and Budelli, 2006) and recording (Gottwald et al., 2017a) results obtained with artificial objects, which suggested electric color as a distance-invariant cue. Without being combined, amplitude or waveform modulations do not provide these qualities mentioned above (figures 6.5A and 6.5B).

Interestingly, horseshoe bats apply a partly reminiscent strategy for identifying prey insects irrespective of position during active echolocation (von der Emde and Schnitzler, 1990). To do so, the prey-evoked amplitude and frequency modulations of their acoustic signals are combined. Unlike *G. petersii*, passive electroreceptive animals such as sharks, rays or platypus (Collin and Whitehead, 2004; Czech-Damal et al., 2012) rely on only a single (i.e., passive) electric cue during foraging that can be varied (i.e., attenuated) when prey freezes, slows breathing or covers its body openings (e.g., Bedore et al., 2015). Our behavioral tests (figures 6.7 and 6.8) suggest that *G. petersii* only minimally uses such passive electric information but mainly benefits from the stability of electric color (i.e., color constancy) during prey identification through active electrolocation.

Also in the visual sense, color constancy is a basic requirement for the functionality of color vision in many animals (e.g., bees, fish, monkeys) and in humans (Hurlbert, 2007). Here, it provides a stable color sensation for different distances (in non-aquatic environments) or positions of an object (Foster, 2011; Romero et al., 2011). To achieve visual color constancy, the brain has to tackle spectral variations caused by changes of the illuminant (e.g., at day or dusk) or by interactions of light and atmospheric particles (e.g., over a larger distance) (Foster, 2011; Romero et al., 2011). Additional compensation is required for variations caused by changes in background reflectance (e.g., when an object is seen against different backgrounds (Brown, 2003)). During active electrolocation, object-to-background interferences also occur (Fechler and von der Emde, 2012). Foraging of actively electrolocating *G. petersii*, however, is only minimally affected by varying

backgrounds (i.e., substrates) (von der Emde, 1994).

The dominant role of active electrolocation during object and especially prey identification might be further explained by another trait of electric color. The electrical properties, which generate the electric colors of natural capacitive objects, depend on their integral cellular and acellular structures (Schwan, 1963). We assume that these, and thus also electric color, cannot be changed easily, e.g., by prey items. In contrast, changes of visual coloration 'only' require the manipulation of pigments, and thus can serve for adaptive concealment against predators (Duarte et al., 2017). As mentioned above, also passive electric cues can be masked by prey animals providing bioelectric crypsis (e.g., Bedore et al., 2015) against passively electrolocating predators (e.g., sharks). Electric color, during active electrolocation, bypasses usual anti-predator behavior of chironomid larvae (e.g., Hölker and Stief, 2005) and does not easily allow prey (and other animals) to camouflage their identity or to blend into the background.

Our recording experiments demonstrate that electric colors indicate categories of environmental capacitive objects to *G. petersii*. This is in line with an earlier suggestion (Budelli and Caputi, 2000) that fish might be able to determine and discriminate 'families' of capacitive objects by recognizing their individual electric colors. Here, we show that two different electric colors divide insect larvae into primary (chironomids) (Nwani et al., 2011) and secondary prey items (other insect larvae). Accordingly, fish did prefer capacitors with the electric color of chironomids over resistors, which have the electric color of 'secondary' prey (figure 6.8).

Because our fish were caught in the wild, we do not know whether these electric-color preferences are innate or were initially learned through sensory experience. However, the fish's quick and almost 'reflex-like' foraging responses to artificial prey items, which also did not change (adapt) throughout the course of the experiments, may suggest an inborn and 'hardwired' choice behavior. Without the need of elaborate processing in the brain, the strategy of electric-color perception might be suited best to capture small and otherwise inconspicuous insect prey. Similarly in color vision, innate color preferences enable an effective response to relevant food sources, e.g., in various insects, in spiders or fish (Kawamura et al., 2017; Kelber and Jacobs, 2016; Lunau and Maier, 1995; Taylor et al., 2014).

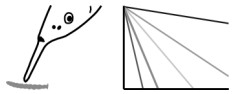

6.6 Conclusion

The study presented in this chapter shows that weakly electric fish *G. petersii* employ a color-like cue to identify relevant items such as prey. As steady markers, electric colors designate those targets selectively and reliably. This makes electric-color sensing a critical adaption of the active electric sense to its specific environment and renders it more robust than (passive) electric sensing in other animals (sharks, platypus etc.). Despite the different physical inputs and neuronal machineries used in vision and active electrolocation, color turns out in both senses as the appropriate percept for enabling crucial, selective and reliable object recognitions (e.g., during foraging). On a broader scope, the similar computational 'goals and strategies' (Stevens, 2012) underlying both types of color sensing and resembling aspects of color traits suggest color perception as sensory concept beyond vision and passive sensing.

III. Electric Imaging in Biomimetic Devices

7. Introduction – Active electrolocation devices

7.1 Active electrolocation sensors for underwater imaging

7.1.1 Motivations for current approaches

The active electric sense allows nocturnal weakly electric fish to orientate and inspect nearby targets in murky and cluttered surroundings. In doing so, electrolocating fish rely on advantageous features, their active electrosensory system provides. The fishes' electric emissions (probing signals) remain stable in particle-rich, turbulent water (e.g., Crampton, 2019; Krahe, 2019). Relevant targets, however, e.g., electrical capacitive objects (like prey), modulate them distinctively (Aguilera and Caputi, 2003; Gottwald et al., 2018; von der Emde, 1990; von der Emde, 1998) and thereby the electric field surrounding the fish with each emission. Furthermore, the electroreceptive fish body, onto which the object-evoked modulations are mapped as electric images, enables an omnidirectional 'electric view' (e.g., Gottwald et al., 2017a; Snyder et al., 2007; Zakon, 1986).

While in nature active electrolocation provides a very effective imaging modality for turbid and dark waters, those commonly used in technical sensor systems (e.g., optical or sonar imaging (e.g., Lu et al., 2015) face several restrictions in such surroundings. Here, absorption, scattering and attenuation effects degrade sonar signals and evoke noise, color-distortions and blurring in optical images (Lu et al., 2015; Richards et al., 1998; Schettini and Corchs, 2010). Additionally, sonar works well in dark and open areas but suffers in confined and shallow waters from multiple acoustic reverberations, whose interpretation is difficult (Zhao et al., 2009). The active electric sense, however, evolved in fish from partly shallow and densely vegetated water bodies (Crampton, 2011; Crampton, 2019; Moritz, 2010) and is thus well adapted to cluttered, confined spaces.

When engineered for aquatic machines, this electrosense could complement their optical and acoustic, long- and medium-range sensors. In vehicles, robots or probes it would enable short-range navigation or explorations, otherwise hardly achieved. Thus, besides techniques improving both conventional imaging modalities for adverse marine/freshwater conditions, as mentioned above, (e.g., Amer et al., 2019; Hung et al., 2016; Liu et al., 2018; Xu et al., 2019; Zhao et al., 2009) some recent biomimetic approaches focus on the construction of active electrolocation sensors (e.g., Bai et al., 2015; Bazeille et al., 2017a;

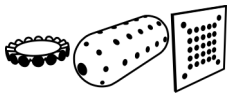

Bazeille et al., 2017b; Servagent et al., 2013; Solberg et al., 2008; Wang et al., 2017; Wolf-Homeyer et al., 2016). Active electrolocation is ideally suited for freshwaters (of ~100 µS cm^{-1} (Moller, 1980)) and works as well in seawater (typically ~43000 µS cm^{-1} (Culkin and Smith, 1980)) with calibrated sensors (see Bazeille et al., 2017a; Servagent et al., 2013; Solberg et al., 2008 and principally also Bai et al., 2015).

7.1.2 Current prototypical sensor systems

Some individual sensor designs (figure 7.1), which have been tested in simulations and experiments with prototypes, are presented below. The sensors feature one or more emitter electrode(s) to surround themselves with an electric field and a few or many receiver electrodes to monitor it. Due to the field perturbations, caused by nearby targets, sensor-based electric images are captured and analyzed for object inspection or navigational tasks.
Figure 7.1A shows a prototype called SensorPod (Bai et al., 2015; Bai et al., 2016; Bai et al., 2012) with a slender, cylindrical body covered with several electrodes. Two separate electrode configurations of the device have been evaluated for electric image acquisition. In their 2015 study, Bai and colleagues used the sensor's two terminal electrodes as emitters and five differential electrode pairs as a horizontal row of receivers, combining electrodes from opposite sensor sides. In the other configuration, the electric field was established with a terminal emitter and grounding electrode and was recorded with just a single, central receiver (electrode pair) (Bai et al., 2012).
In the SensorPod's first configuration a static electric image could be recorded along the receiver array with a stationary target in front of it (figure 7.1A1). The second configuration required an object to be moved along the sensor side, while simultaneously two 'dynamic' electric images were captured through several successive measurements (figure 7.1A2). To compute static or the fist type of dynamic electric images, the Sensor Pods' received (perturbation) signal was 'demodulated' with its output signal, which means both signals were multiplied and then filtered. The second type of dynamic electric images was calculated by demodulating the received signal with a 90° phase-shifted reference of the emitted field signal.
All these electric images yielded biphasic curves, which depending on the electrolocation targtes (e.g., conductive sphere vs. ellipsoid or water plant vs. rock) differed in their shapes, magnitudes and polarity (figures 7.1A1 and 7.1A2). Static images, acquired for

different object-to-sensor alignments and analyzed with, e.g., statistical learning algorithms, identified electrical purely resistive targets (conductors and insulators) along with their spatial and geometrical features (Bai et al., 2015).

The individual profiles of dynamic images allowed the device to differentiate the organic

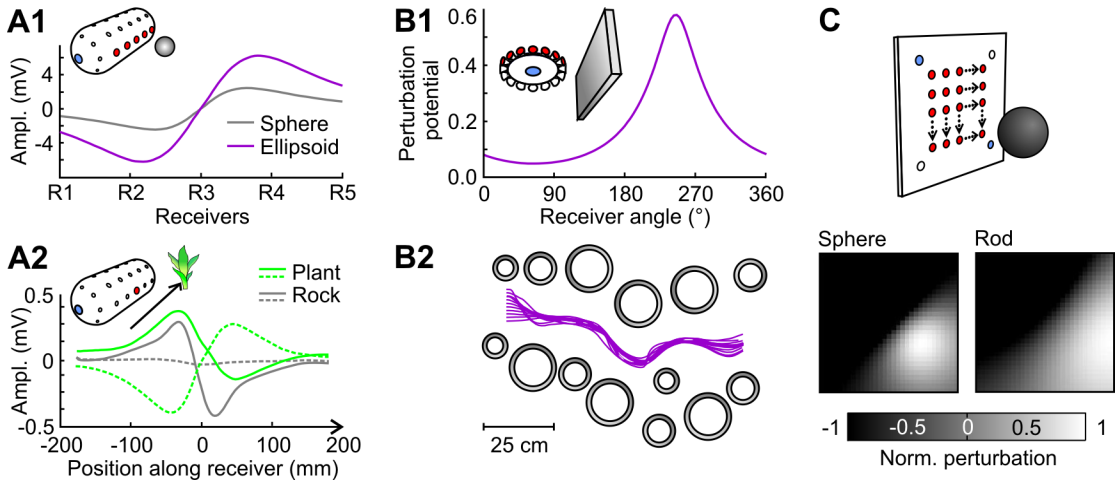

Figure 7.1: Active electrolocation sensors and sensor-based electric images.

(A-C) Three individual sensor prototypes are illustrated schematically. With their emitter (blue) and receiver electrodes (red) the sensors generate and monitor electric fields surrounding them. Based on the field perturbations evoked by nearby items, the sensors acquire the objects' electric images to inspect them or to navigate the surroundings. **(A)** Cylindrical prototype 'SensorPod'. **(A1)** Static electric image of a conductive sphere (gray trace) and ellipsoid (purple trace) captured along the sensor's 1-D receiver array (red). Profiles of *these* 1-D electric images depict biphasic amplitude curves, as a result of the SensorPod's electrode configuration used for electric imaging (see main text). The images were computed via demodulations of the received field perturbations with a reference of the sensor's emitted field signal. **(A2)** Dynamic, 1-D electric images (green and gray biphasic ampl. curves) acquired with a single receiver (red), while an object (a water plant [green] or a rock [not shown]) is moved along the SensorPod (see black arrow). For each target, two types of dynamic images (equally colored solid/dashed curves) are acquired, by demodulations as mentioned above (for solid curves) or (for dashed curves) by demodulating the received perturbations with a phase-shifted reference signal. Figures 7.1A1 and 7.1A2 were redrawn after (Bai et al., 2012; Bai et al., 2015) and modified. **(B)** Disc-shaped prototype. **(B1)** Static, 1-D electric image (purple, bell-shaped curve) of a conductive wall (gray) obtained with the sensor's circular, 1-D receiver array (red). **(B2)** Electric imaging enables the device to pass an area cluttered with metal cylinders (gray circles) in several trials, as indicated by the trajectories of sensor movements (purple traces). Figures 7.1B1 and 7.1B2 were redrawn after (Dimble et al., 2014) and modified. **(C)** Square-shaped prototype. The sensor images nearby targets in front of it, e.g., an insulating sphere (black), with a 2-D receiver array (red), whose electrode density (only roughly illustrated above) varied for different versions of the device (see main text). Normalized, 2-D electric images of an insulating sphere and rod are shown bottommost. Figure 7.1C was modified after (Wang et al., 2017).

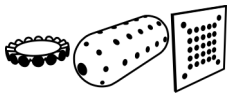

and electrical capacitive target (plant) from the inanimate, purely resistive target (rock) (Bai et al., 2012). To promote such discriminations the SensorPod could judge the phase of the object-evoked field perturbations, in addition to their amplitudes (depicted by the electric images) (Bai et al., 2012).

Another prototypical, but disk-shaped electrolocation sensor (figure 7.1B) was introduced in a study by Dimble and colleagues (Dimble et al., 2014). It featured a central emitter electrode at the bottom and, along its periphery, a circular array of receiver electrodes (figure 7.1B1). As a result of this particular electrode configuration, the device provides a circumferential electric image of its surroundings.

With, a single electrolocation target (e.g., a conductive wall) in the vicinity of the sensor this electric image resembles a bell-shaped curve (figure 7.1B1). More complex image profiles will form with multiple targets present. The acquired electric images were processed with a bio-inspired algorithm, basically a mathematical version of the optical flow analysis performed by insects during navigation (e.g., Humbert and Hyslop, 2010). In doing so, the machine was able to maneuver through confined, cluttered test sites, e.g., composed of conductive or insulating cylinders (figure 7.1B2), and to avoid obstacles in its way.

The prototypes mentioned above use a single, either horizontal or circular row of receivers for electric imaging and thus can capture only 1-D electric images of nearby targets (figures 7.1A and 7.1B). Recently, however, a square-shaped sensor with a 2-D receiver array (figure 7.1C, uppermost) was presented (Wang et al., 2017; Wang et al., 2016). Individual prototypes, i.e., either built or simulated versions of the device, were equipped with two emitter electrodes, in diagonally opposite corners, and different numbers of receivers, e.g., 5 × 5, 16 × 16, 28 × 28 electrodes etc. Object-evoked perturbations of the sensors' electric field were recorded across the array, by combining its receivers as differential electrode pairs. Received perturbations were then demodulated with the emitted field signal and normalized to obtain a target's 2-D electric image (e.g., of an insulating sphere or rod as shown in figure 7.1C, bottommost). These images typically consisted of two diagonally opposite areas of positive vs. negative perturbations. Both areas' perturbation patterns and sizes varied in electric images of insulating targets with individual spatial and geometrical properties (Wang et al., 2017). Electric image analysis, driven by, e.g., a neuronal network for image recognition and other algorithms, enabled the prototypes to recognize such purely resistive targets (e.g., spheres, cubes or rods) and their

positions (Wang et al., 2017; Wang et al., 2016).

Although current active electrolocation sensors successfully mimic electric imaging, they derive electric images partly by other computations than weakly electric fish. These devices (e.g., Bai et al., 2012; Bai et al., 2015; Wang et al., 2017) lack the typical Mexican hat type images perceived by the animals (e.g., Caputi et al., 1998; Gottwald et al., 2017a; Pedraja et al., 2014). 'Natural' electric images, however, provide some efficient yet simple cues for object inspection. Several of them have been revealed specifically for mormyrid fish via electrolocation studies on species *Gnathonemus petersii* (e.g., Budelli and Caputi, 2000; Gottwald et al., 2017a; Gottwald et al., 2018; Hofmann et al., 2017; Pedraja et al., 2018; von der Emde et al., 1998). So far, only one of the fish's analytical cues, i.e., the relative image slope (von der Emde et al., 1998), has been adopted for a prototypical, distance sensor (Schwarz et al., 2001). Determined by just a single, very basic calculation with the device, the parameter principally enabled quick proximity estimations, e.g., of different-sized, conductive and insulating spheres (Schwarz et al., 2001; G. von der Emde, personal communication).

The other cues, intuitively used by electrolocating *G. petersii* (e.g., electric colors as verified in this thesis), may offer electrolocation sensors further analytical strategies that are effective and computationally inexpensive. Hence, future prototypes, applying these principles, could advantageously complement the recent electrolocation devices, which usually rely on rather conventional, more elaborate evaluations of electric images (e.g., statistical learning techniques (Bai et al., 2015; Wang et al., 2017; Wang et al., 2016)) to explore their targets.

7.2 An active electrolocation catheter system for inspection of atherosclerotic plaques

7.2.1 Motivations for the approach

Cardiovascular diseases, i.e., disorders of the heart and blood vessels, are the global leading cause of death (Libby et al., 2019; Roth et al., 2017). The major cause of cardiovascular diseases is a chronic, inflammatory condition of arteries, called atherosclerosis (Gregersen and Halvorsen, 2018; Insull, 2009; Libby et al., 2019). It drives the progression of 'plaques' within the arteries' walls by accumulation of lipids, fibrous

material and other elements (e.g., Gregersen and Halvorsen, 2018; Libby et al., 2019). Plaque buildup within the heart's coronary arteries, provoking coronary artery disease, is the most serious manifestation of this degenerative process (Libby et al., 2019; Sanchis-Gomar et al., 2016; Stone, 2012). By narrowing those arteries, advanced, fibro-fatty plaques ('atheromas') can limit blood flow and evoke 'cardiac ischemia' (e.g., Libby et al., 2019), which triggers chest pain, abnormal heart rhythms and, over time, may lead to heart failure.

In daily clinical practice, coronary plaques are usually assessed by 'angiography'. In this invasive procedure, a catheter is guided to the patient's coronary arteries, into which it injects a contrast medium (figure 7.2) (e.g., Athanasiou et al., 2017). This dye is visible on X-ray images ('angiograms') that are simultaneously captured (around the patient's chest) by a movable X-ray imaging system (Athanasiou et al., 2017). While such angiograms outline the arteries' plaque-evoked narrowings, they cannot specifically indicate plaque conditions that may inflict more dangerous future complications (e.g., Batty et al., 2016; Cheng et al., 2014; Virmani et al., 2000). These fragile, 'high-risk' plaques ('thin-cap

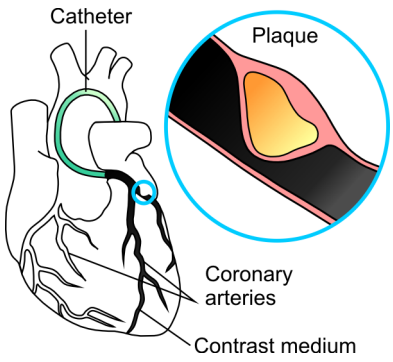

Figure 7.2: Schematic illustration of a coronary angiography.

During invasive angiography, a catheter (green) is inserted into a blood vessel of the arm or groin (not shown) and threaded to the coronary arteries of the patient's heart muscle (white). The device then fills those arteries with dye (contrast medium, black), which is monitored with an external imaging system (not shown) by rapidly capturing X-ray images (angiograms). In the angiograms, the dye depicts the arteries' branches and their plaque-evoked narrowing, which forms a 'dent' (see small blue circle). As indicated in the inset (see large, blue circle), a plaque's structure within the artery wall (light red) is not visualized by the dye (black) running through the artery lumen. As a result, structural features of an advanced plaque (atheroma), i.e., its lipid core (yellow) and underlying fibrous cap (light red) cannot be assessed by angiography. It thus lacks the ability to determine, e.g., rupture-prone 'high-risk' atheromas (i.e., 'thin-cap fibroatheromas'), which feature a large core with a thin and fragile cap underneath (see inset).

fibroatheromas, TCFAs') differ from other atheromas in having a large and necrotic 'lipid core' with an underlying 'cap' of thin, fibrous tissue (figure 7.2) (Virmani et al., 2000; Virmani et al., 2006; Virmani et al., 2002). Their sudden rupture can induce blood clots, completely clogging the arteries, which instantly puts the affected individual at risk for a fatal heart attack or cardiac arrest (e.g., Insull, 2009; Libby et al., 2019; Virmani et al., 2000; Virmani et al., 2006). Rather mild and non-occlusive ruptures of TCFAs, in turn, may heal without inducing life-threatening events (e.g., Burke et al., 2001; Insull, 2009; Virmani et al., 2000).

High-risk TCFAs can partly be identified via optical or ultrasound catheters (e.g., Athanasiou et al., 2017; Batty et al., 2016; Benedek et al., 2016; Cheng et al., 2014). Such diagnostic tools, however, are not routinely used in addition to angiography, primarily due to cost-containment in daily clinical practice (Bourantas et al., 2016; Koskinas et al., 2018; Koskinas et al., 2016; Li et al., 2018). More cost-effective catheter systems, with the ability to efficiently determine lower- and high-risk coronary plaques, could help overcome this shortcoming. Such devices might be obtained via improvements of the above-mentioned catheter systems (e.g., Bourantas et al., 2016; Koskinas et al., 2018) or when using other diagnostic modalities for plaque inspections that require less complex catheters, hardware and algorithms.

An electrical evaluation of plaques, for example, can be performed with simple sensors, featuring just a few electrodes and wires. Several of such 'electric impedance spectroscopy' approaches revealed (in experiments/simulations) that individual plaque types display distinct electrical properties (resistance/capacitance and electrical impedance) as a result of their specific integral structures (e.g., lipids, fibrous and other materials/elements). Here, a plaque is probed with a weak, alternating current at various frequencies. In doing so, the sensors' electrodes either touch a small area of the plaque (Stiles and Oakley, 2003; Streitner et al., 2009; Yu et al., 2011; Yu et al., 2010; Zhang et al., 2015) or small circumferential spots of the plaque and artery wall (Packard et al., 2017). For catheter-based plaque inspections (Packard et al., 2017; Stiles and Oakley, 2003; Streitner et al., 2009), impedance spectroscopy sensors are usually mounted on so-called balloon-catheters that can be inflated towards the vessel wall.

The studies above imply that electrical plaque analysis could principally yield a cost-efficient future diagnostic procedure to determine low-to-high-risk plaque conditions. Impedance spectroscopy, however, disadvantageously relies on flexible, rather 'elaborate'

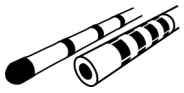

catheters, the inflations of which interrupt blood flow. In addition, in most studies (Stiles and Oakley, 2002; Streitner et al., 2009; Yu et al., 2010; Yu et al., 2011; Zhang et al., 2015), it allowed only small portions of a plaque to be investigated. Conversely, a non-contact imaging modality that could analyze whole plaques with plain catheters would make electrical plaque evaluations more effective, less obstructive and cheaper.

In order to achieve these goals, a recent biomimetic project of our lab and the Research Center Jülich focused on adapting active electrolocation for catheter-based plaque inspections. By applying the electrolocation strategies of weakly electric fish *G. petersii*, such bio-inspired catheters may be able to capture electric images of close by low-to-high-risk plaques and identify them via combinations of simple image cues. So far, we have tested two early, prototypical versions of the catheter system (i.e., a ring- or multi-electrode electrolocation catheter) with first, promising results.

7.2.2 Ring-electrode electrolocation catheter

The catheter system's initial version (Gottwald, 2010; Gottwald and von der Emde, 2013; Gottwald et al., 2011; Metzen et al., 2012) mainly combines a standard 4-ring-electrode catheter, a custom, electrolocation software (controlling this device) and routines to process plaque-evoked electric images. We used it in several basic experiments, i.e., catheterizations of synthetic (coronary) arteries with plaques, to explore active electrolocation principles for plaque diagnostics.

As simplified, experimental substitutes, our synthetic arteries and plaques predominantly mimicked the approximate electrical conductivity of real ones (e.g., Stiles and Oakley, 2002; Stiles and Oakley, 2003) and were oversized in comparison. Each 'artery' was made of a conductive agar tube. A synthetic plaque, within the top wall of a tube's central section, featured a pork-lard core surrounded by a thin, conductive agarose cap.

In the experiments, several plaques of four (P1-4) (Gottwald et al., 2011) or five different types (Gottwald, 2010; Gottwald and von der Emde, 2013; Metzen et al., 2012), which increased in core volume (from 1-268 mm^3) and represented small-to-large synthetic atheromas, were inspected. To do so, the catheter was manually moved stepwise through a tube, emitting, at each step, weak *G. petersii* pulses from its tip electrode (sender, S). The signals were recorded with a particular of (Gottwald et al., 2011) or all of the catheter's other electrodes (receivers, R1-3) (Gottwald, 2010; Gottwald and von der Emde, 2013;

Metzen et al., 2012). These settings provided different catheter configurations (S–R1, S–R2 or S–R3) for 'dynamic' (motion-based) electric image acquisitions.

'Dynamic modulation profiles' of a synthetic artery, which contained an electric image of its plaque, were gained by processing the pulses' artery- and plaque-evoked modulations. In doing so, modulations of two individual signal parameters were evaluated, i.e., of the pulses' (peak-to-peak) amplitudes and their phase-shifts to the output signals of the catheter. Amplitude modulations resulted from the resistive electrical properties of the electrolocation targets and phase-shift modulations from their (presumably faint) capacitances.

As an example, figure 7.3 depicts an amplitude mod. profile (figure 7.3A) and phase-shift mod. profile (figure 7.3B) with their respective electric images that were captured of an 'artery' with a P4 plaque by catheter configuration S–R1. Both profiles show a modulation

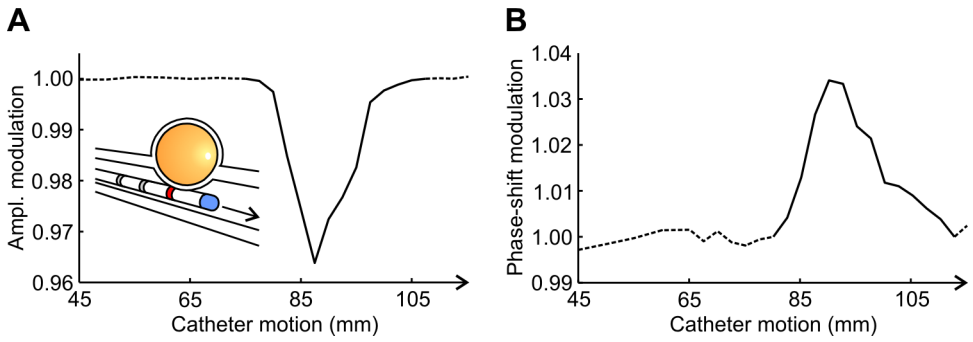

Figure 7.3: Ring-electrode electrolocation catheter and catheter-based electric images.

(A) The schematic drawing illustrates the catheterization of a synthetic agarose artery (white tube) with a fatty 'P4-type' agar plaque (white ball with yellowish fat core). Advancing through the artery, the ring-electrode catheter (white) emits/receives weak electric signals (not shown), the artery-evoked modulations of which yield a dynamic (i.e., catheter-motion-dependent) 'modulation profile' (dashed/solid black trace). Within the profile, signal modulations caused by the artery's plaque provide a 'dynamic electric image' ('v-shaped' curve; solid black line) for plaque inspection. This 'amplitude mod. profile' and its 'amplitude image' derive from (peak-to-peak) amplitude modulations of the electric signals, acquired by catheter configuration S–R1. The S-R1 setting combines the sender (S, blue) with just the first (R1, red) of the catheter's receivers (the second [R2] and third [R3] of which are indicated in gray). **(B)** Phase-shift modulation profile (dashed/solid black trace) with an electric phase-shift image (inverted 'v-shaped' curve; black line), obtained from the same artery and plaque as in (A) by the same catheter configuration (S–R1). This second type of mod. profile/electric image is gained from the artery/plaque-evoked modulations of the phase-shifts between the catheter's generated and received electric signals. Detailed descriptions of the mod. profiles and electric images (shown in A and B) are given in the main text. Figures 7.3A and 7.3B were redrawn after (Gottwald et al., 2011) and modified.

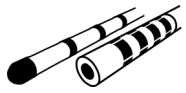

baseline of ~1 in their peripheral regions, whereas their central, plaque-evoked electric image features pronounced modulations of smaller than 1 (in the amplitude image) or larger 1 (in the phase-shift image) (figures 7.3A and B). The two image types depict roughly 'v-shaped' curves with opposite directions. Image modulations in each direction (i.e., larger or smaller 1) become stronger the more they deviate from 1.

The profiles of catheter-based electric images depend on the catheter configuration they were computed for and the investigated plaque type. For catheter configurations with a sender-to-receiver distance that is wider than the inspected plaque (e.g., when using the S–R3 configuration on plaque type P4) 'w-shaped' amplitude vs. inverted 'w-shaped' phase-shift images are gained instead of the above-mentioned 'v-shaped' ones (e.g., Gottwald et al., 2011). From small-to-large plaques (P1-to-P4 and beyond), electric images increase in their magnitude (deviation from 1) and become steeper and wider (Gottwald, 2010; Gottwald and von der Emde, 2013; Gottwald et al., 2011; Metzen et al., 2012).

For plaque discrimination, we extracted and evaluated two features from amplitude and phase-shift images, i.e., their peak modulations (with the largest deviation from 1) and their widths. These image cues could be used to discern most of (Gottwald, 2010; Metzen et al., 2012) or all of the synthetic plaque types from one another (Gottwald et al., 2011).

So far, the above-mentioned results imply that our active electrolocation catheter may principally be suitable to differentiate small-to-large atheromas of coronary arteries. Additional experiments, however, are needed to test whether it might potentially be able to identify 'low-to-high-risk' conditions of such plaques.

Highly dangerous plaque conditions, like thin-cap fibroatheromas (TCFAs) or other advanced 'lipid core plaques (LCPs)', have critical cap and core sizes (e.g., a cap thickness below 65 µm and rel. core area above 10% for TCFAs) (e.g., Gardner et al., 2008; Virmani et al., 2006; Virmani et al., 2002). Those structural features basically separate them from lower-risk plaques.

By adopting TCFA and LCP thresholds (of cap and core sizes) for our synthetic atheromas, artificial versions of low-to-high-risk plaque conditions can be determined as electrolocation targets. Their catheter-based identification requires electric image cues that predominately relate to the plaques' cap and core dimensions. For accurate discriminations of the plaques' conditions, those 'key image features' would have to distinguish them in the same way as the thresholds of the plaques' structural features.

Besides investigating plaque classifications, as mentioned above, future experiments with

the ring-electrode electrolocation catheter shall focus on making the device more versatile for plaque inspections. Hence, other types of electric images need to be explored. While we rely on amplitude and phase-shift images to evaluate synthetic plaques in our recent studies (Gottwald and von der Emde, 2013; Gottwald et al., 2011; Metzen et al., 2012), preliminary tests imply that also electric 'waveform images' could be used to do so (Gottwald, 2010), providing, in principle, a computationally less expensive alternative to phase-shift images. Waveform images derive from modulations of the peak amplitude ratio of the catheter's pulses (Gottwald, 2010), i.e., a very simple parameter. Due to their computational benefits over phase-shift images, waveform images and their parameters will be examined for plaque classifications, in addition to those of amplitude images, in our follow-up study.

7.2.3 Multi-electrode electrolocation catheter

In the second version of our catheter system a custom-build multi-electrode catheter (Mayekar et al., 2011; Mayekar et al., 2012) is applied for plaque investigations. It features a frontal sender and four electrode rings, each of which has four separate receivers pointing either to the top, bottom, left or right. Individual electrode settings of the device (e.g., with several or one of its receivers being used in combination with the sender) can enable different strategies of electric imaging. So far, only a few of them were tested via catheterizations of oversized and electrically very oversimplified synthetic arteries and plaques, i.e., small Plexiglas tubes with different-sized metal or plastic balls (Mayekar et al., 2012). To probe these targets (in experiments/simulations), the catheter emits and receives weak, sinusoidal electric signals, during its stepwise motions through the tubes.
Based on the signals' amplitude modulations, evoked by the 'arteries' and their synthetic plaques, amplitude modulation profiles with amplitude images were captured with the device (Mayekar et al., 2012). When using the sender and just a single, upper receiver of the catheter to do so, dynamic modulation profiles with electric images are obtained, which form linear traces similar to those acquired by the ring-electrode electrolocation catheter (example shown in figure 7.4).
As yet not fully developed (Mayekar et al., 2011) or untested strategies of electric imaging, however, may provide modulation profiles/electric images as 2-D maps, instead of linear traces, which would improve plaque detection/localization. For example, with all four re-

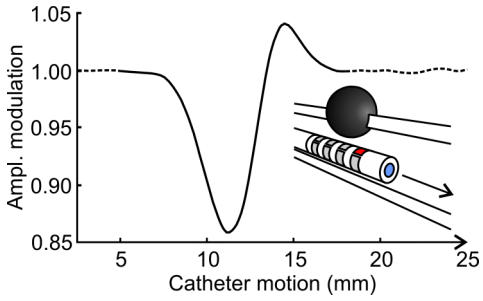

Figure 7.4: Multi-electrode electrolocation catheter and catheter-based electric image.
The schematic drawing illustrates a simulated catheterization of a synthetic Plexiglas artery (white tube) with a plastic plaque (black ball). To probe them with weak electric signals (not shown), the catheter (white) applies its sender (blue) together with the top receiver (red) from the first of its electrode rings (highlighted in gray). The signal's amplitude modulations, acquired from along the artery via catheter motion, provide a dynamic amplitude modulation profile (dashed/solid black trace). The profile's roughly v-shaped, but slightly biphasic curve (solid black line) depicts the electric image (i.e., dynamic amplitude image) of the artery's synthetic plaque. Figure 7.4 was redrawn after (Mayekar et al., 2012) and modified.

ceivers of an electrode ring being used in combination with the catheter's sender, a synthetic artery's dynamic but 2-D modulation profile could be acquired. Such a 2-D map may depict the top, bottom, left and right wall of the catheterized arterial section by color-coded modulations. A dynamic electric image within this profile would not only locate a plaque along the artery but also convey its circumferential position within the artery wall.
In addition to dynamic electric imaging, plaques could be inspected by static electric imaging, i.e., with the catheter placed in a stationary position below the plaque. The modulations, from across all four of the catheter's electrode rings, would then form a 2-D, color-coded map (i.e., a 'static electric image'), indicating the plaque with respect to the top, bottom left and right artery wall.
In our next study, experiments with the multi-electrode catheter will thus focus on dynamic/static acquisitions of 2-D amplitude and waveform images and their potential benefits for plaque detections. For these tests, it is necessary to change the catheter's probing signal to a weak *G. petersii*-type pulse, whose specific, biphasic waveform allows for determinations of waveform images in addition to amplitude images. Furthermore, the simple electrolocation targets, used so far (Mayekar et al., 2011; Mayekar et al., 2012), need to and will be replaced by ones that resemble the complex electrical properties of real arteries and plaques (e.g., Stiles and Oakley, 2002; Streitner et al., 2009; Yu et al., 2010; Yu et al., 2011; Zhang et al., 2015) more closely.

As a first example of such targets, a synthetic TCFA (with an arterial tissue cap and plastic core) will be catheterized, which is embedded in a coronary artery explant from a pig heart.

7.3 Aims of the studies on electric imaging in biomimetic devices

Currently, active electrolocation, as performed by weakly electric fish, is implemented for several aquatic sensors/robots (e.g., Bai et al., 2012; Bai et al., 2015; Dimble et al., 2014; Wang et al., 2017 and others). In murky, cluttered waters, being adverse to other sensors, it enables these bio-inspired prototypes to navigate or inspect nearby targets (as outlined in section 7.1). Similar to the fish the sensors receive and analyze electric images in doing so. Often, however, the image processing/analytical strategies of the devices are different and more elaborate than those of the fish, which make active electrolocation so efficient in nature.

The aim of the study presented in chapter 8 of this thesis is to design and test a biomimetic active electrolocation camera. This prototype specifically applies the electric imaging principles of weakly electric fish *G. petersii* (as investigated in chapters 5 and 6) for effective, yet computationally inexpensive object explorations in murky waters. Its ability to identify electrolocation targets via electric-color estimations, to assess their distance based on electric image blurring and to acquire their 'electric outlines' (as a novel image feature) was examined by inspecting artificial items or natural targets with the device. The 'electric camera' could provide an advantageous alternative to optical underwater sensors (e.g., close-range cameras), which suffer from multiple visual disturbances in murky surroundings (e.g., Lu et al., 2015; Schettini and Corchs, 2010). Object exploration skills of the device, acquired through novel cues such as electric outlines, might also help to explain similar, yet barely understood electrolocation skills of the fish ('reverse biomimetics').

The other biomimetic, but medical approach focused on in this thesis is an active electrolocation catheter system (as introduced in section 7.2). It aims at providing critical and cost-efficient inspections of atherosclerotic plaques in coronary arteries. In daily clinical practice, such catheter-based evaluations of potential high-risk plaques are limited foremost by high costs of the existing (optical or ultrasound) devices (e.g., Benedek et al., 2016; Koskinas et al., 2016; Koskinas et al., 2018).

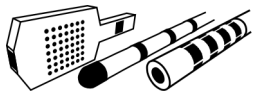

The goal of the final study, presented in chapter 9, is to refine the two current prototypes of the electrolocation catheter system towards detections/discriminations of low-to-high-risk plaque conditions. Both catheters were tested by electrolocating synthetic plaques via catheter-based electric images, whose parameters were examined for plaque diagnostics. The images' cues, i.e., their peaks, relative slopes and widths were either inspired by the research on electrolocating *G. petersii* in chapter 5 or adopted from former catheter studies (e.g., Gottwald, 2010; Gottwald et al., 2011). Successful identifications of synthetic low-to-high-risk plaques would imply critical plaque inspections to be principally possible with simple electrolocation catheters and a prospective low-cost catheter system (based on such devices). It could promote more frequent and preventive diagnoses of coronary high-risk plaques, which provoke fatal complications of coronary artery disease (Libby et al., 2019; Stone, 2012; Virmani et al., 2006).

8. A bio-inspired electric camera for short-range object inspection in murky waters

This chapter is based and expands on the study:

Gottwald, M., Herzog, H. and von der Emde, G. (2019). A bio-inspired electric camera for short-range object inspection in murky waters. *Bioinspiration & Biomimetics.* **14**, 035002–1–10.

My contribution to the published work included: conceptualization of the research goals/study experiments; development/design of the experimental setup, recording software and analysis scripts; performing the experiments; analysis/visualization of the study data; preparation/writing of the manuscript.

8.1 Abstract

Underwater object inspection by optical sensors is usually unreliable in turbid or dark environments. Here, we designed a biomimetic 'electric camera', inspired by weakly electric fish *Gnathonemus petersii*, which successfully use active electrolocation for this task. The device probed nearby objects with a weak electric field and captured 'electric images' of the targets by processing the object-evoked field modulations. The camera-based electric images strongly resembled those available to *G. petersii*. Furthermore, by extracting the fish's analytical cues from these images, close objects could be reliably analyzed. Based on the level of 'image blurring' short distances of electrolocation targets, spheres of different sizes and material, were estimated. Natural targets, fish or plants, were identified irrespective of their size or distance by their two individual 'electric colors' derived from electric images. Furthermore, we introduce an image cue, called the electric outline, which provided information resembling a target's optical contour. Our results indicate that bio-inspired electric imaging principles provide promising cues for sensor-based, short-range object inspections in murky waters. By resembling the electric imaging applied by *G. petersii*, our device can also be used for 'reverse biomimetics', revealing imaging cues that so far have not been considered for weakly electric fish.

8.2 Introduction

Turbid and dark surroundings challenge sensors (cameras), which rely on visual information for underwater imaging (Lu et al., 2015). Optical images, which in principal provide reliable features for object recognition (e.g., colors or contours), suffer from absorption, attenuation and scattering effects in turbid waters. As a result, visual noise, blurring and color-distortions can occur (Lu et al., 2015; Schettini and Corchs, 2010). In addition to improving optical imaging for such adverse conditions (e.g., Amer et al., 2019; Hung et al., 2016; Liu et al., 2018 and others), also alternative, bio-inspired sensory modalities may increase the performance of aquatic imaging devices.

Nocturnally active weakly electric fish *Gnathonemus petersii*, which inhabit murky freshwater habitats in tropical Africa, rely on electric imaging of their surroundings through active electrolocation (Moritz, 2010; von der Emde and Schwarz, 2002). To do so, they generate current pulses (electric organ discharges, EODs) with an electric organ in the

tail, which establishes an electric field around the animals (Bell et al., 1976; Harder et al., 1964). Emitted EODs are separated by pauses that are varied, e.g., shortened when fish increase their EOD repetition rate (up to ~80 Hz) during object inspection (von der Emde and Schwarz, 2001).

Crucially, EODs are not distorted by the particle-rich and noisy water but modified by larger nearby objects. The fish monitor their EODs by electroreceptor organs, which are densely distributed across the skin (Hollmann et al., 2008; Szabo and Wersäll, 1970) and thereby form an 'electroreceptive screen'. Local EOD (lEOD) modulations, caused by objects, are especially strong at the skin region opposite the object, where fish obtain a so-called electric image. Electrical purely resistive items (e.g., stones, wood) modulate the amplitude of lEODs (von der Emde and Schwarz, 2002). Capacitive items (e.g., fish, plants) evoke lEOD amplitude and waveform modulations (von der Emde and Schwarz, 2002). Accordingly, object-evoked amplitude and waveform images occur (Budelli and Caputi, 2000; Gottwald et al., 2017a). Compared to optical images, electric images have coarse and distorted profiles with a center-surround organization (termed a Mexican hat profile) (Caputi et al., 1998; Gottwald et al., 2017a). They are shaped in a multi-parametrical fashion by several object features (e.g., distance, size, shape, electrical resistance/capacitance, complex electrical impedance and others) (Gottwald et al., 2017a; von der Emde, 1999b; von der Emde and Schwarz, 2002; von der Emde et al., 1998). Analytical image cues, however, which can disambiguate object feature extraction (e.g., for distance (von der Emde et al., 1998) or electric impedance estimation (Budelli and Caputi, 2000; Gottwald et al., 2017a)) can be obtained from electric images.

Through combination of an amplitude and waveform image's modulations the so-called electric color can be calculated (Budelli and Caputi, 2000; Gottwald et al., 2017a). This linear relationship of amplitude and waveform modulations provides a distance-invariant impedance estimator to identify electrical capacitive objects (Budelli and Caputi, 2000; Gottwald et al., 2017a). Recently, it was shown that through electric-color sensing *G. petersii* can reliably identify crucial capacitive items, e.g., prey of various sizes from different distances (Gottwald et al., 2018).

Object distance can be inferred from the level of 'image blur', determined by the so-called slope-to-amplitude ratio (SAR) of amplitude images (Gottwald et al., 2017a; von der Emde et al., 1998). The SAR is defined as the ratio of the steepest slope and the strongest modulation (peak) of the image.

Here, we tested a first prototype of a multi-electrode sensor for short-range electric imaging in turbid and dark waters, which closely mimics the active electrosensory system of the fish. As our device was used to capture 2-D electric images of several nearby targets, we call it an 'electric camera'. Amplitude and waveform images of capacitive items (loaches and plant stems) and amplitude images of purely resistive objects (wood, plastic rod, aluminum or plastic spheres) were examined. Electrolocation targets were evaluated by calculating the image features mentioned above (i.e., electric color and SAR). Amplitude images were also processed with a common edge detection algorithm to derive an 'electric outline', which similarly to an object's optical contour may provide a valuable cue for object identification. Our results are discussed with regard to active electrolocation in *G. petersii* and to electric imaging applied in other technical underwater sensors (Bai et al., 2012; Bai et al., 2015; Bai et al., 2016; Bazeille et al., 2017b; Schwarz et al., 2001; Servagent et al., 2013; Wang et al., 2017; Wang et al., 2016), inspired by weakly electric fish.

8.3 Materials and methods

8.3.1 Electric image recordings

Electric images of capacitive objects (loaches [*Gyrinocheilus aymonieri*], non-aquatic plant stems [*Zamioculas zamiifolia*]) and of resistive objects (aluminum [Al]-spheres, plastic sphere, plastic rod, wood) were recorded. Prior to the measurements, stimulus animals (loaches) were euthanized by a lethal MS 222 solution (2 g l^{-1}, Acros Organics, Fair Lawn, New Jersey, USA). The electric camera was fixed onto a custom-made stand outside the experimental tank (28.7 cm × 38.5 cm × 18.8 cm). It was then placed underwater (11 l, 103.5 ± 3.1 µS cm^{-1}, 25.5 ± 0.3 °C) in the tank's center at a distance of 6 cm to the bottom.

The custom-build camera body (1 cm × 4.5 cm × 12.5 cm; Micromotive GmbH, Mainz, Rhineland-Palatinate, Germany) provided a set of gold electrodes (figure 8.1A). The front section featured a grounding electrode (1 cm^2) at the tip and two arrays (3.2 cm × 3.2 cm) of 49 receivers (3.1 mm^2/electrode) on both sides. The thin, elongated back was equipped with a movable sender consisting of two electrodes (1 cm^2/electrode), one on the left and right side. The sender was fixed at a distance of 2 cm from the camera's back end.

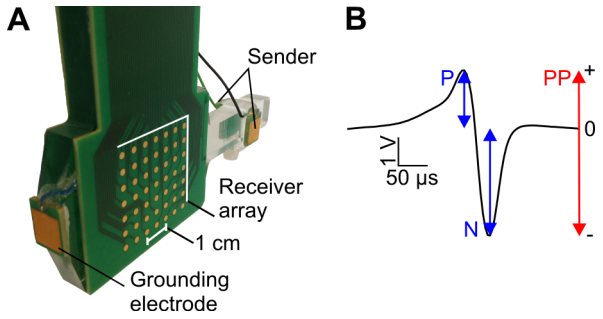

Figure 8.1: Electric camera and signal.

(A) Overview of the electric camera and its electrode setting (sender, grounding electrode and receiver array) for recordings. **(B)** The electric signal's (EOD's) peak-to-peak amplitude (PP, red double-headed arrow) and the peak amplitude of the positive (P) and negative (N) phase (blue double-headed arrows) are indicated. The EOD's peak amplitude ratio (P/N ratio) defined the EOD waveform. Based on the object-evoked modulations of the two signal parameters (PP or P/N ratio), electric amplitude or waveform images were acquired.

During electric image recordings, a *G. petersii* EOD signal (6 V PP, 400 µs, figure 8.1B) was generated by a custom-written LabVIEW program (National Instruments, Austin, Texas, USA) and emitted (PCIe 6341, BNC 2120, National Instruments) simultaneously at the two electrodes of the camera's sender. The EOD repetition rate was set to 1 Hz. The grounded tip electrode of the camera was used to drag the EOD-evoked electric field to the camera's front section with its 2-D receiver arrays (input impedance = 47 kΩ/electrode).

Note that while both arrays may provide valuable information for object inspection, our setup currently does not allow for simultaneous measurements from both sides of the device. Electric images were therefore recorded from only one receiver array (figure 8.1A). To do so, a particular object was placed in front of the array using a micromanipulator.

For a single image recording, 10 EODs were sampled locally at each of the array's electrodes in the presence as well as the absence of the object (for one electrode after another using a custom-made multiplexer circuit). These local EODs (lEODs) were amplified (×60, custom-build amplifiers), filtered (band-pass: 8 Hz to 100 kHz) and digitized (resolution: 16-bit, sampling rate: 250 kHz, PCIe 6341, BNC 2120, National Instruments). The lEODs' peak-to-peak amplitudes (PP) and the peak amplitude ratios of the positive (P) and negative (N) lEOD phase (P/N ratios) were calculated by a custom-written LabVIEW program (Gottwald et al., 2017a). PP defined the lEOD amplitude and P/N the lEOD waveform. Each of those parameters, i.e., 10 PP or P/N values obtained per receiver electrode with and without object, was averaged.

Eventually, by dividing the two conditions 'with object' and 'without object' for PP or P/N and by subtracting 1 from these ratios, the lEOD amplitude or waveform modulation was obtained for each electrode of the receiver array. The modulations from across the receiver array formed an amplitude image (PP modulations) or a waveform image (P/N modulations).

8.3.2 Electric image analysis

Electric image analyses and visualizations were carried out with custom-written or standard MATLAB (MathWorks, Natick, Massachusetts, USA) routines. Amplitude and waveform images (3.2 cm × 3.2 cm) had an initial resolution of 49 (7 × 7) pixels. The final image resolution was set to 169 (13 × 13) pixels by linear interpolation (examples of both image types are shown in figure 8.2A).

The center-surround organization of electric images was analyzed by defining their Mexican hat profile. It is shaped by an image's positive vs. negative (i.e., reverse) modulations, which form a central vs. peripheral area. Two configurations of Mexican hat profiles can occur. They either feature a negative center and positive rim (figure 8.2A) or a positive center and negative rim. In between center and rim usually lies a region, of negligible small modulations (i.e., positive or negative values close to 0), which is called a basal area. Image modulations irrespective of their sign (+ or -) become more pronounced (stronger) the more they deviate from 0. Here, we used a threshold from -0.01 to 0.01, which defines modulations within threshold range as part of the basal image region. In turn, pronounced image modulations outside threshold range form the center and rim of an image (as indicated in figure 8.2B).

Further analysis was performed to extract several features from electric images. The peak modulation of electric images (figure 8.2C) was determined as the value with the largest deviation from 0 irrespective of its sign (+ or -). It is called peak amplitude (PA) for amplitude and peak distortion (PD) for waveform images. The peak modulation occurs within the central region of electric images (figure 8.2C). PA and PD, of an object's amplitude and waveform image, were combined as PA-PD pair in a scattergram to derive electric color (figure 8.2C). Electric color was determined by the linear, proportional relationship of PA and PD and depicted by an 'electric-color line' (figure 8.2C). Such lines may provide the identification of different capacitive electrolocation targets.

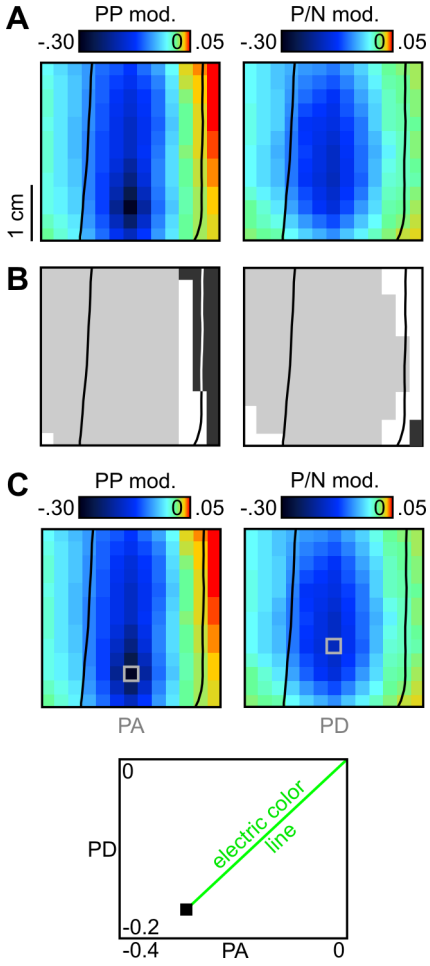

Figure 8.2: Electric image analysis – Mexican hat profiles and electric color.
(A) Electric amplitude (left) and waveform image (right) evoked by a plant stem at 5 mm object distance. Image modulations are shown color-coded. The plant's optical contour (black lines) is marked on both images. **(B)** Separate regions in electric images, i.e., image center (light gray), basal area (white) and rim area (dark gray) define the images' center-surround organization, called a Mexican hat profile. **(C)** The peak modulation (i.e., the value with the largest deviation from 0) is marked (gray rectangle) within and indicated below each image, i.e., peak amplitude (PA) for the amplitude and peak distortion (PD) for the waveform image. The lower graph illustrates the combination of both peak modulations (as PA-PD pair) in a scattergram. The linear, proportional relationship of PA and PD (i.e., electric color) is indicated by an 'electric-color line' (green).

For object distance estimation, the SAR was determined from the object-evoked amplitude image (figure 8.3A). The parameters defining the SAR were successively extracted (figure 8.3B). First, the peak amplitude of the image was selected. Second, the steepest slope of the image was calculated. To do so, only a subsection of the image was evaluated. It covered the left image side until the position of the peak amplitude (providing the subsection's right border). Within this area image slopes were calculated in horizontal direction separately for each image row (figure 8.3B). The overall steepest value from all rows was selected. Eventually, the SAR was calculated dividing the steepest image slope by the peak amplitude (figure 8.3B).

To evaluate an object's electric outline, amplitude images were processed with the so-called Canny edge detector algorithm (Canny, 1986). Thereby, a trace of edges ('outline') was computed within the image (figure 8.3C). Basically, this multi-stage algorithm combined horizontal and vertical image gradients as 'edges'. By taking edge strength and direction into account, while applying thresholding and hysteresis, edges were tracked and

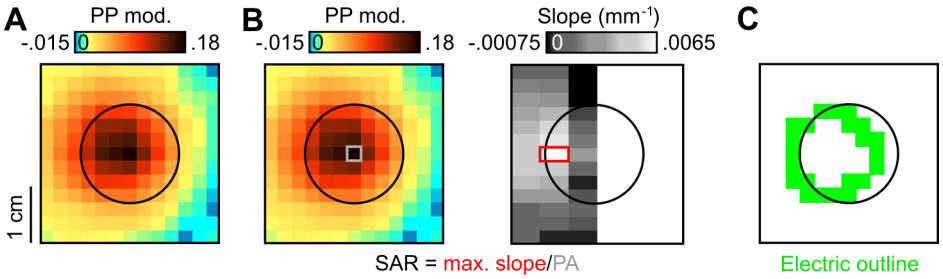

Figure 8.3: Electric image analysis – Slope-to-amplitude ratio and electric outline.
(A) Electric amplitude image evoked by an aluminum (Al) sphere (2.9 cm^3) at 5 mm object distance. Image modulations are shown color-coded. The sphere's optical contour (black circle) is marked on the image. **(B)** On the left, the amplitude image is shown with indicated peak amplitude (gray rectangle). The right image shows the image slopes, calculated in horizontal direction, for a subsection of the amplitude image. The steepest slope is marked (red rectangle). Both image features combined provide the slope-to-amplitude ratio (SAR) as indicated below. **(C)** Electric outline of the sphere, defined by the amplitude image's edge pixels (green), computed by the Canny edge detector algorithm.

connected.

8.3.3 Ethical statement

Experiments on animal subjects were conducted in accordance with German law and the guidelines and animal welfare regulations of the relevant authorities including the University of Bonn. Experimental protocols were approved by the Amt für Veterinärdienste Bundesstadt Bonn (reference number: 56.2).

8.4 Results

Amplitude and waveform images were captured for several electrolocation targets (capacitive and resistive items) and the basic image organization was assessed. To determine effects of variations in object size, distance or orientation on electric images, simple resistive objects were used and their amplitude images were examined. Electric color was evaluated as an identifier for capacitive objects. The SAR was assessed as a short-range distance estimator for simple resistive targets. The electric outline was evaluated for capacitive and resistive items of different sizes, distances or orientations.

8.4.1 Amplitude and waveform images

At a close distance (5 mm), both capacitive items (loach, plant, figure 8.4A) and purely resistive objects (wood, Al-sphere, figure 8.4A) evoked distinct amplitude images (figure 8.4B). The images showed a center-surround (Mexican hat) organization with central, basal and rim area(s) (figure 8.4B). The image centers were the most prominent regions of the Mexican hat profiles and the largest in size. Within the 'electric screen', defined by the camera's receiver array, image centers were obtained at the region immediately opposite to an object. However, image centers were usually larger than an item's actual size and expanded beyond the objects limits on the electric screen (figure 8.4B). This is especially seen in the amplitude image of the loach, where the center occupied almost the whole profile so that the rim region was not visible (figure 8.4B).

In addition to the amplitude images, the capacitive items evoked waveform images (figure 8.4C). These images were also divided into a central, basal and rim area, which defined them as Mexican hat profiles. Like the centers of amplitude images, waveform image centers were acquired at the portion of the electric screen right in front of the target (figure 8.4C), and they could also reach beyond that area.

The individual electrical, spatial and geometrical features of the electrolocation targets shaped the modulation patterns of both image types. Thus, modulations of different magnitudes and contrasts were acquired in the different image profiles (figures 8.4B and 8.4C). As a result, basic image features such as peak amplitudes and slopes (in amplitude images) or peak distortions (in waveform images) varied. The electrical object properties (i.e., a higher or lower resistance compared to that of the water or an additional capacitance) also defined the basic configuration of electric images (figures 8.4B and 8.4C). Amplitude images either showed a Mexican hat profile with positive central and negative peripheral modulations (for low resistance objects) or an opposite profile with negative central and positive rim modulations (for high resistance objects). For waveform images of capacitive objects only the second configuration with negative central and positive peripheral modulations occurred.

In turn, purely resistive objects provided only a basal area of negligible small waveform modulations (figure 8.4C) instead of a pronounced and true waveform image.

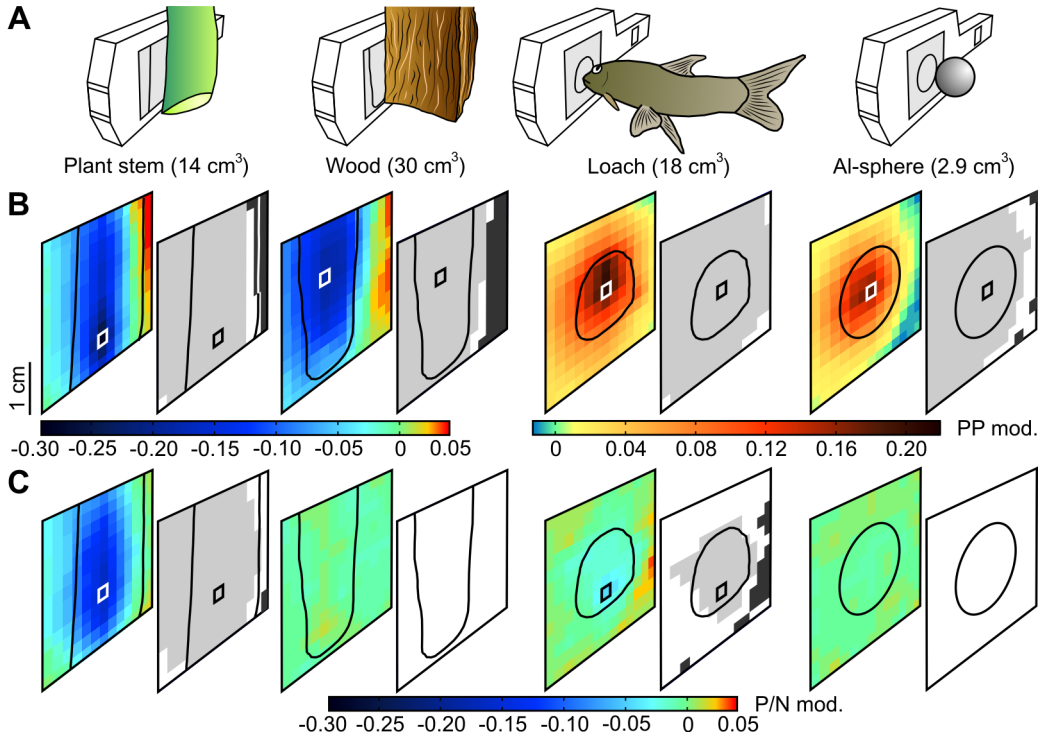

Figure 8.4: Electric images of resistive and capacitive objects at 5 mm object distance.
(A) Schematic drawing indicating an object's position in front of the electric camera. The camera's receiver array is highlighted in gray with the object's contour marked on it. **(B)** The amplitude images of each object are shown as a color-coded image indicating the image modulations and as a gray-scale image with accentuated image (Mexican hat) areas – center (light gray), basal area (white) and rim area (dark gray). The images' peak amplitudes (rectangles) and the objects' optical contours (black lines) are marked. **(C)** Waveform images of the objects with the same arrangement and markings as in (B). Rectangles mark peak distortions. Note that the profiles obtained for the wood and Al-sphere only consist of a basal area (indicated in green or white) and thus do not provide waveform images (Mexican hat profiles).

8.4.2 Amplitude images – effects of object size and distance

Depending on size or distance of an object different amplitude images were acquired (examples are shown for amplitude images of Al-spheres in figure 8.5).
A large sphere (figure 8.5A, leftmost) evoked an image with strong modulations and a clear center-surround organization, i.e., with central, basal and rim areas (figure 8.5B, leftmost). A smaller sphere at the same distance (5 mm) caused an image with weaker modulations and with a less pronounced Mexican hat profile (figures 8.5A and 8.5B, middle), lacking a rim region. Both objects' amplitude images differed in the sizes of their central regions. In comparison, the center of the small sphere's image was smaller than

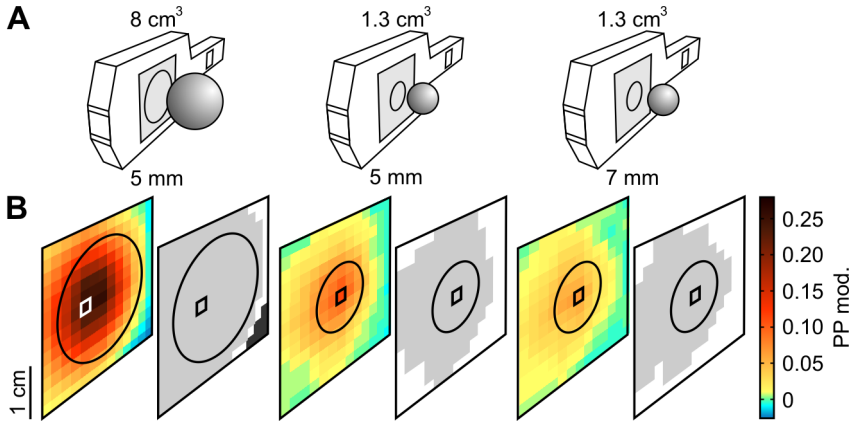

Figure 8.5: Electric images of Al-spheres of different sizes and distances.

(A) Schematic drawing of the Al-spheres in front of the electric camera's receiver array (gray). The spheres' contours are marked on it. Sphere volumes are given at the top and their distances at the bottom. **(B)** Amplitude images shown as color-coded images and as images with the central, basal and rim areas of the Mexican hat profiles indicated by white-to-gray shading as described in figure 8.4. Peak amplitudes (rectangles) of the images and the spheres' optical contours are marked.

that of the large sphere's image. The lower magnitudes in image modulations, which occurred with a smaller object size, affected two basic features of the amplitude image simultaneously. In the weaker image, the peak amplitude was degraded and, as a result of a lower modulation contrast, the image slope was less steep. When the distance of the small sphere (figure 8.5A, rightmost) was increased (from 5 to 7 mm), the modulations and contrast of the image profile were further reduced (figure 8.5B, rightmost). Thus, similar to the decline in object size, a farther object distance decreased peak modulation (PA) and image slope.

Even though variations in sphere size or distance shaped amplitude images in similar ways, particular combinations of these features will not result in equal electric images.

For example, at some farther distance (> 7 mm) the large sphere will evoke an image with a peak modulation that matches that from the image of the small sphere at close distance (e.g., 5 mm). These two images, however, will still differ in the sizes of their central regions and in the steepness of the image slopes (i.e., local modulation contrast).

8.4.3 Amplitude images – effects of object orientation

Variations in amplitude images were obtained when the orientation of an object in front of the electric camera was changed (examples are shown in figure 8.6 for amplitude images

of a plastic rod). Three different orientations of the rod were captured (figure 8.6A). The amplitude images all showed Mexican hat profiles with central, basal and rim regions present (figure 8.6B). Depending on the rods particular orientation, the image regions varied in modulation magnitudes and in size. When the long and curved side of the rod was facing the camera (in horizontal-parallel or vertical position), images with stronger modulations and contrasts were acquired than when the plain and small frontal section of the rod was captured (in horizontal-perpendicular position). Basic image features such as the peak amplitude and image slope were thus modified by different object orientations.

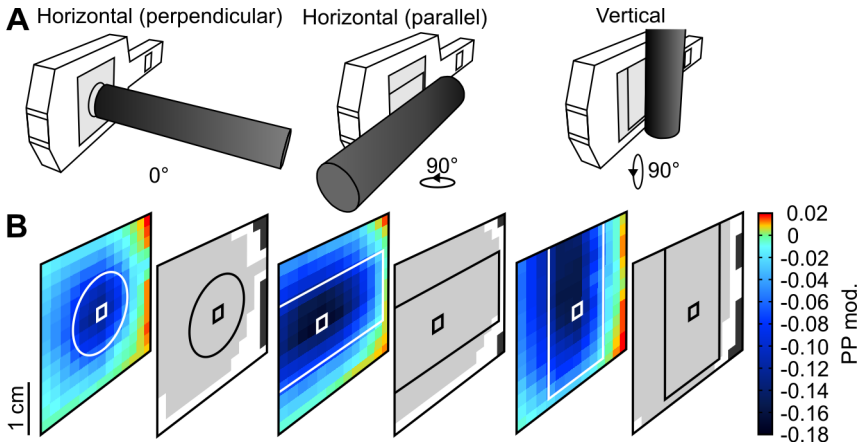

Figure 8.6: Electric images of a plastic rod with different orientations.

(A) Schematic drawing indicating the rod's three orientations in front of the electric camera. Rotation angles between orientations are indicated below. Object distance for all orientations was 5 mm. The camera's receiver array is highlighted in gray with the rod's contour marked on it. **(B)** Amplitude images shown as color-coded images and as images with the Mexican hat areas indicated by white-to-gray shading as described in previous figures. Peak amplitudes (rectangles) of the images and the rod's optical contours are indicated.

8.4.4 Electric color and SAR

To identify capacitive objects (loaches or plant stems of different distances and sizes) we evaluated their electric colors. To do so, the peak modulations of their amplitude and waveform images (PA, PD) were plotted against one another in a scattergram.

As indicated in figure 8.7A, PAs and PDs were scaled by various object properties (size, distance and electrical impedance). A reduction in object size or distance caused weaker peak modulations (with values closer to 0). Corresponding PA-PD pairs were then

positioned closer to the origin of the scattergram. PA-PD pairs of plants (i.e., combinations of negative modulations) were located in a different quadrant of the scattergram than those evoked by loaches (i.e., combinations of positive and negative modulations). These individual combinations (of positive and/or negative peak modulations) result from the different electrical impedances of plants and loaches.

Based on their specific distributions, mentioned above, PA-PD pairs fitted two distinct linear functions, i.e., electric-color lines with a characteristic positive or negative slope (figure 8.7A). The linear, proportional relationship of PA and PD depicted by each line's slope represents a different electric color for loaches and plant stems. From the individual PA-PD pair (evoked by an object) this electric color can simply be estimated as the PD-to-PA ratio. Electric colors may serve as reliable identifiers for different types of capacitive objects, due to their electrical impedance, as shown here for different-sized loaches and plants at close range.

Using the SAR of amplitude images, short distances of electrical resistive spheres (of different sizes or material, aluminum or plastic) were evaluated. The SARs of the different spheres showed close alignments and were scaled by object distance (figure 8.7B). The SAR could therefore be used to assess short distances of resistive targets irrespective of object size or material.

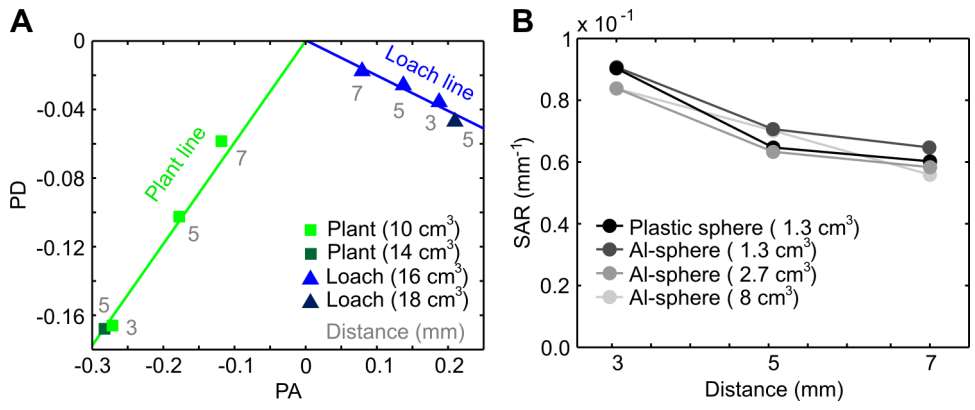

Figure 8.7: Bio-inspired electric image parameters.

(A) Electric color. Two 'electric-color lines' (green and blue line) fit the pairs of peak modulations (from amplitude [PA] and waveform images [PD]) evoked by capacitive objects of different distances or sizes. Due to their distinct linear relationships (i.e., electric colors), color lines indicate plants or loaches (as labeled aside). **(B)** Slope-to-amplitude ratio (SAR) of amplitude images. SARs of spheres of different sizes or materials at three object distances. The SARs showed close alignments and scaled with distance.

8.4.5 Electric outline

To obtain a contour-like feature from amplitude images their electric outlines were assessed. Figure 8.8 shows the electric outlines and the optical contours of several capacitive or resistive targets. Some of these items had different sizes and were recorded at different distances or with varying orientations (for details see also figures 8.4-8.6). Their electric outlines roughly resembled the optical object contours. Targets with circular or oval contours (e.g., Al-spheres, loach) were represented by roundish electric outlines (figure 8.8A), whereas objects with long contours (e.g., plant stems, wood) evoked elongated electric outlines (figure 8.8B). Similar to the contour in an optical image the electric outline may therefore provide information on the orientation and geometry of a nearby electrolocation target.

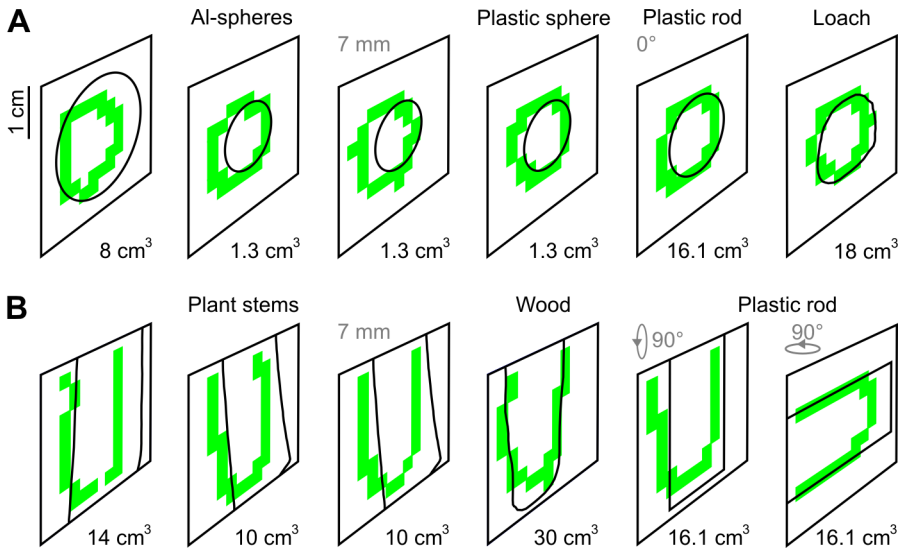

Figure 8.8: Electric outlines.

(A) Roundish electric outlines (shown in green) derived from amplitude images of different targets (labeled at the top) with circular or oval optical contours (marked in black). Object sizes (volumes) are indicated at the bottom. For some items, additional information on their distance or angle is indicated in gray above the images. The distance of the other targets was 5 mm. **(B)** Elongated electric outlines (green) evoked by objects with long optical contours. Labels, markings and arrangements are analogous to those in (A).

8.5 Discussion

In the present study we applied a bio-inspired electric camera for short-range imaging and inspection of underwater targets. The images captured with the electric camera offered some similar features for object recognition (electric colors and outlines) as those obtained with optical cameras (colors and contours). Unlike most optical imaging systems, however, which work only very poorly in turbid or dark waters, an electric camera may still provide reliable cues for short-range object inspection and thereby offer promising imaging strategies for underwater machines. It might also be used to reveal cues that are principally available from electric images but so far have not been considered during object imaging in weakly electric fish (reverse biomimetics) or in other technical active electric sensor systems.

8.5.1 Electric images

Electric image generation with the electric camera basically resembled the electric imaging of objects by *G. petersii* (Budelli and Caputi, 2000; Gottwald et al., 2017a), i.e., purely resistive items caused only amplitude images, whereas capacitive objects additionally evoked waveform images (figure 8.4). Based on waveform information, fish can detect capacitive objects and differentiate them from resistive items (von der Emde, 1990). Representing animate objects such as other fish, plants or prey insect larvae, capacitive objects are crucial targets for *G. petersii* (Gottwald et al., 2017a; von der Emde and Ronacher, 1994; von der Emde and Schwarz, 2002). In the fish's environment they electrically stand out from typical background items (von der Emde and Schwarz, 2002), such as rocks, roots or the soil, all of which are merely resistive. The electric camera also allowed detection and separation of capacitive and resistive items based on amplitude and waveform images. This enables general, short-range localizations of capacitive objects (e.g., fish or plants, figure 8.4) suitable even for turbid or low light underwater surroundings like aquacultures. Here, the device could also be used to spot potentially obstructive or unwanted low resistance items (e.g., pieces of metal etc.). For such targets, amplitude images clearly differed from those of natural background objects with a high resistance (compare the amplitude images of the Al-sphere and wood in figure 8.4).
In accordance with the electric images reported for *G. petersii* (Caputi et al., 1998;

Gottwald et al., 2017a), the camera-based electric images showed Mexican hat profiles with central, basal and peripheral areas (figures 8.4-8.6). Furthermore, as available to the fish (Budelli et al., 2002; Gottwald et al., 2017a; von der Emde, 1999b) two basic configurations of amplitude images (with positive or negative central modulations) versus one for waveform images (with negative central modulations) were acquired by our device (figure 8.4). For *G. petersii* (Budelli et al., 2002; Gottwald et al., 2017a; Gómez-Sena et al., 2014) and in our biomimetic approach (figures 8.4-8.6), electric images constitute coarse and ambiguous object representations and are shaped by the target's spatial, geometrical and electrical properties. Interdependencies of object features and the image profile that were revealed for electrolocating fish (von der Emde, 1999b; von der Emde and Schwarz, 2002; von der Emde et al., 1998) matched those of the camera-based electric images (e.g., object size and distance both influenced the modulation and contrast in amplitude images, figure 8.5). In addition, different orientations can change the electric image profiles in modulation and contrast for most electrolocation targets, except spheres. For *G. petersii*, this was shown for amplitude images of simple resistive items, such as ellipsoids or cubes (Gómez-Sena et al., 2014), and it was also depicted by the amplitude images of a rod for the electric camera (figure 8.6). Despite the many variations that occur in electric images, the animals successfully perform several object recognition tasks (distance, size, shape, electrical impedance estimation etc.) (Schumacher et al., 2016a; von der Emde, 1990; von der Emde and Fetz, 2007; von der Emde and Ronacher, 1994; von der Emde et al., 1998; von der Emde et al., 2010). To do so, the fish most likely combine basic image features, e.g., peak modulation and image slope, to compensate for multi-parametrical dependencies, e.g., in distance estimation (von der Emde et al., 1998), which we also adapted for the electric camera.

In former technical studies, other biomimetic electrolocation devices were developed, which also applied electric imaging. In most cases, they partially differed from the biological model used, often due to sensor design. Typical prototypes featured a slender, cylindrical body with one or more emitter(s) at the end(s) and a single or several receiver(s), which were aligned in a row and may point in different circumferential directions (Bai et al., 2012; Bai et al., 2015; Bai et al., 2016; Bazeille et al., 2017b; Servagent et al., 2013). The sensors could therefore acquire only 1-D electric images by static imaging (Bai et al., 2015) or mandatorily via sensor movements (Bai et al., 2012; Bai et al., 2016; Bazeille et al., 2017b; Servagent et al., 2013). Weakly electric fish, with their

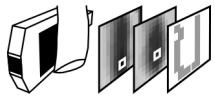

spatial receptor distribution (Zakon, 1986), receive electric images across an electroreceptive surface, e.g., when spotting an object from a stationary position. To explore advantages of spatial electric imaging for electrolocation devices, a planar prototype with a 2-D receiver array was introduced recently (Wang et al., 2017; Wang et al., 2016). However, as a result of their individual recording circuitry and image processing, the electric images acquired by the sensors mentioned above (Bai et al., 2015; Bai et al., 2016; Wang et al., 2017) could differ from those obtained by the fish. In turn, by providing electric images similar to those available to the fish, our electric camera adds to the ensemble of established sensors, offering imaging strategies closely linked to those of the biological model.

8.5.2 Object inspection by electric image features

We successfully adapted the bio-inspired image cues electric color and SAR for camera-based object inspections.

In our experiments, electric color served as a distance- and size-invariant impedance estimator, indicating certain capacitive objects. Thus, as recently reported for electric colors available to *G. petersii* (Gottwald et al., 2018, see chapter 6), also electric colors obtained with the electric camera may indicate several categories of natural environmental objects irrespective of their sizes, distances and potentially also their positions. Supporting the findings of another study with electrolocating fish (Gottwald et al., 2017a, see chapter 5) we also showed that electric color could be extracted by the combination of the electric image peaks (PA and PD) (figure 8.7A).

Distance perception in *G. petersii* is achieved through the SAR depicting the 'image blur' of amplitude images (Gottwald et al., 2017a; von der Emde et al., 1998). Electric image recordings (von der Emde et al., 1998) revealed that SARs of simple resistive metal or plastic objects (cubes or spheres) were scaled by object distance and shape, but not affected by material or size. As a result, the animals' distance discriminations were biased by object shape when judging the distance of cubes versus spheres in behavioral experiments (von der Emde et al., 1998). Fish were, however, able to compensate for this 'electrical illusion' through learning to arrive at an accurate distance discrimination over time (Schwarz and von der Emde, 2001). In accordance with the biological findings, SARs of Al- or plastic spheres obtained with the electric camera indicated object distance,

irrespective of material or size (figure 8.7B). Our results also verify and extend on preliminary tests with an early sensor prototype, indicating SAR-based distance estimations, via 1-D electric images, to be principally possible (Schwarz et al., 2001; G. von der Emde, personal communication).

In contrast to the fish, which can perform object inspections up to a distance of several centimeters (Schumacher et al., 2016a; von der Emde et al., 1998; von der Emde et al., 2010), the electric camera currently has a much smaller working range (see figure 8.7). This may be improved by reducing the sender-to-receiver distance, by increasing the power of the senders and by refining the recording circuitry of the device.

With the electric outline, we introduce a novel electric image cue for object analysis. This contour-like feature was provided by the edge information of 2-D amplitude images. Because amplitude images were distorted and coarse representations of electrolocation targets (figures 8.4B, 8.5B, 8.6B), their electric outlines roughly matched the objects' contours (figure 8.8). However, to indicate a certain target, its electric outline does not necessarily need to resemble the optical contour. Simply, a unique and unambiguous electric outline would make a reliable identification mark of an object, e.g., a sphere. Even though amplitude images of spheres were modified by object size, distance (figure 8.5B) and material, their electric outlines remained very stable (figure 8.8A). Individual objects, however, yielded similar electric outlines as spheres when captured in certain orientations (compare, e.g., spheres and rod in figure 8.8A).

As shown for the rod in figure 8.8B, other object orientations did further change the electric outline, which then clearly differed from those of the spheres. These results imply that electric outlines from several 'electric viewpoints' need to be combined for unequivocal object identification. Such a strategy bears interesting similarities to the object scanning behavior of *G. petersii*. The fish use stereotyped probing motions (so-called probing motor acts) to investigate novel objects from various directions (Toerring and Moller, 1984). Object-directed scanning motions also occurred during object shape discriminations (Schumacher et al., 2016a; von der Emde and Fetz, 2007). Here, two objects that proposedly provided large differences in their electric images when explored from different orientations, were reliably discerned by the fish (Schumacher et al., 2016a). Furthermore, fish were able to recognize an object's shape irrespective of the object material (von der Emde and Fetz, 2007). These findings suggest that the electric outline may also be a potential cue for shape estimation in our biological model.

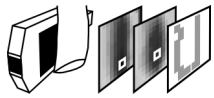

Compared to our electric camera, other technical sensor systems relied on more complex electric imaging and processing methodologies, which involved neuronal networks (Wang et al., 2017; Wang et al., 2016), statistical learning algorithms (Bai et al., 2015) and others to perform similar object inspection tasks. In doing so, these devices were able to locate or identify geometrical objects (cubes, spheres, ellipsoids) of different resistive materials (metal vs. plastic), some of which had several orientations, different sizes and distances (Bai et al., 2015; Bazeille et al., 2017b; Servagent et al., 2013). Based on 2-D electric images, resistive objects such as a sphere, cube or rod could be identified (Wang et al., 2017). In addition, a natural capacitive object (water plant) could be differentiated from a purely resistive object (rock) (Bai et al., 2012). In contrast, our results show that also simple cues, directly adapted from those used by weakly electric fish and based on very basic calculations (electric color and SAR), provide efficient object inspection strategies for active electric sensor systems, which in addition are computationally inexpensive.

8.6 Conclusion

The electric camera, presented here, depicts our first prototype of a murky-water imaging device. It closely mimics electric imaging and corresponding cues used by the weakly electric fish *G. petersii*. It thus offers object inspection abilities similar to those of the fish, i.e., electrical close-range determinations of object distance (via image blurring) or object impedance (through electric colors) but also of electric outlines as a novel feature. Principally, this allows for localization and categorization of several types of underwater targets even in turbid, polluted or dark surroundings, which is hardly achieved by other, e.g., optical underwater sensors.

In follow-up studies, the electric camera prototype may be refined towards a robotic application, which requires improving its range, circuitry and the implementation of additional algorithms to automate its object inspections. Further experiments may also focus on simulating object inspections as applied by weakly electric fish with the device to uncover potential, unknown electric imaging skills of these animals. Examples of such skills may be the determination of electric outlines of objects as presented in this study for the electric camera.

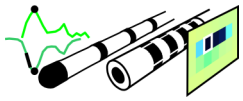

9. Bio-inspired active electrolocation catheters for plaque inspection in coronary arteries

This chapter is a modified and expanded version of the study:

Gottwald, M., Matuschek, A. and von der Emde, G. (2017). An active electrolocation catheter system for imaging and analysis of coronary plaques. *Bioinspiration & Biomimetics* **12**, 015002, 1–17.

My contribution to the published work included: conceptualization of the research goals/study experiments; development/design of the experimental setup, recording software and analysis scripts; performing and overseeing experiments; analysis/visualization of the study data; preparation/writing of the manuscript; supervision of the thesis contributing to this study:

Matuschek A. (2014). Entwicklung und Vermessung eines biologischen arteriosklerotischen Korrelats mit Hilfe eines bionischen Elektroortungs-Katheters. *Bachelor's thesis*. Zoological Institute, University of Bonn, Bonn.

9.1 Abstract

Coronary artery disease – globally a leading cause of death – develops when 'plaques' within the heart's (coronary) arteries evolve from low-to-high-risk conditions, which limit or inhibit blood supply. Although some invasive, state-of-the-art catheter systems can partly identify high-risk plaques, foremost their high costs restrict a use in daily clinical practice. Here, we present a prototypical and prospective low-cost catheter system, which is bio-inspired by weakly electric fish *Gnathonemus petersii* and applies 'active electrolocation' for plaque diagnostics. Two versions of this system, i.e., with a ring- or multi-electrode catheter, were tested, by analyzing synthetic plaques with the devices. The catheters probed them with weak electric pulses, whose plaque-evoked modulations in amplitude and waveform caused electric amplitude and waveform images. With the ring-catheter these images were acquired in synthetic arteries through catheter motion. The multi-electrode catheter captured them via motion or for a stationary position in a coronary artery explant (from a pig heart). Based on *G. petersii's* analytical cues, derived from these images, synthetic plaques could be reliably investigated. Individual plaque conditions of synthetic arteries, mimicking low-to-high-risk plaques, were identified with a combination of 'key image features', i.e., the 'peaks' of amplitude and waveform images and the amplitude images' 'relative slopes'. 2-D electric images, acquired with the multi-electrode catheter, allowed the localization of a synthetic high-risk plaque. Our results indicate that electric imaging principles, applied by a biomimetic and rather inexpensive catheter system, provide promising cues for critical plaque inspections in coronary arteries.

9.2 Introduction

At present, coronary artery disease is one of the most frequent causes of death (Libby et al., 2019; Sanchis-Gomar et al., 2016). Predominantly elicited by fibro-fatty deposits within the walls of coronary arteries, called plaques or atheromas, it impairs the heart's perfusion (Libby et al., 2019; Stone, 2012). The limited blood flow, due to mature plaques narrowing these arteries, provokes chest pain (angina) and eventually can lead to heart failure (e.g., Libby et al., 2019). Sudden, high-risk events such as heart attack or cardiac arrest mainly result from a complete arterial blockage after plaque rupture (e.g., Libby et al., 2019; Virmani et al., 2006).

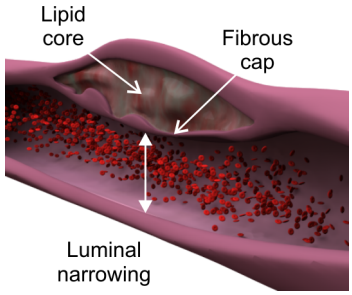

Figure 9.1: Illustration of a rupture-prone plaque.
The illustration depicts a view within a coronary artery, the top wall of which contains a rupture-prone high-risk plaque ('thin-cap fibroatheroma', TCFA). The plaque's critical, structural features are indicated along with the plaque-evoked narrowing of the artery lumen (white double-headed arrow).

While a plaque-evoked arterial narrowing is usually assessed in a catheter-based angiography, the plaque's condition, based upon its structure, cannot be evaluated by this procedure (e.g., Batty et al., 2016). Rupture-prone 'high-risk' plaques, so-called thin-cap fibroatheromas (TCFAs), feature a large and necrotic 'lipid core', covered by a fragile 'cap' of thin, fibrous tissue (figure 9.1) (Virmani et al., 2006; Virmani et al., 2002; Virmani et al., 2000). Although some current ultrasound or optical catheters can partly indicate such critical, structural features, they are not used for routine plaque inspections, primarily due to cost containment (Batty et al., 2016; Benedek et al., 2016; Koskinas et al., 2016; Koskinas et al., 2018; Li et al., 2018). Hence, in daily clinical practice, there is still a need for more cost-effective catheters, which can identify low-to-high-risk plaque conditions (complementary to angiography).

Interestingly, an electric imaging modality found in weakly electric fish *Gnathonemus petersii* may enable such a device when adapted for a biomimetic, 'active electrolocation catheter' (e.g., von der Emde et al., 2009). The nocturnally active *G. petersii* uses active electrolocation to identify prey and other aquatic organisms in particle-rich and turbulent waters (Gottwald et al., 2018; Moritz, 2010; von der Emde and Schwarz, 2002). To do so, the fish surrounds itself with a weak electric field, by emitting a short, biphasic pulse (electric organ discharge, EOD) from an electric organ in the tail (Bell et al., 1976; Harder et al., 1964). Electroreceptor organs, by which the animals sense their EODs, tightly cover the fish skin (e.g., Hollmann et al., 2008).

An object under inspection alters the electric field and thereby the local EODs (lEODs) at the skin region opposite to it. The object-evoked lEOD modulations from across the skin provide the fish with an 'electric image'. Aquatic organisms with complex impedances, due to their resistive and capacitive electrical properties, cause LEOD modulations in amplitude and waveform (Gottwald et al., 2017a; von der Emde and Schwarz, 2002). As a result, they simultaneously evoke electric 'amplitude' and 'waveform' images (Budelli and

Caputi, 2000; Gottwald et al., 2017a).

Besides such 'static images', acquired from a stationary position, the fish often perform probing motions towards an object of interest and may thereby derive a 'dynamic electric image' (Hofmann et al., 2012; Toerring and Moller, 1984). In theory, this image type could form via the successive responses of (just a single or few) electroreceptor organ(s) when the animal moves past the object (Hofmann et al., 2012).

Based on an object's electric image(s), *G. petersii* can judge spatial, geometrical and electrical object properties to locate and identify its targets. In doing so, the fish proposedly computes quite simple parameters, like an image's peak, slope, width etc., and individually combines them to compensate for initial, multi-parametrical relationships of image and object cues (e.g., Gottwald et al., 2017a; Hofmann et al., 2012; von der Emde and Schwarz, 2002; von der Emde et al., 1998).

Beyond biology, active electrolocation could principally enable a medical catheter to determine and discriminate coronary plaques electrically. So far, other electrical procedures such as electrical/electrochemical impedance spectroscopy yielded promising results for plaque identification (in basic experiments/simulations) (e.g., Stiles and Oakley, 2003; Streitner et al., 2009; Yu et al., 2010; Yu et al., 2011; Zhang et al., 2015). *G. petersii's* simple electrolocation principles could provide computationally inexpensive strategies for this task. Furthermore, to apply them, only plain catheters (with few wires and electrodes) along with standard recording/processing hardware would be needed. This makes an active electrolocation catheter system a potential 'low-cost' device. In our previous studies, two prototypical versions of this system (with either a ring- or multi-electrode catheter) successfully investigated different types of simplified, synthetic arteries with plaques (Gottwald and von der Emde, 2013; Gottwald et al., 2011; Mayekar et al., 2011; Mayekar et al., 2012; Metzen et al., 2012).

Here, we report further tests and improvements of the devices. Using the ring-electrode electrolocation catheter, motion-derived (i.e., 'dynamic') amplitude and waveform images were captured of synthetic atheromas mimicking low-to-high-risk plaques. We determined the relationships of bio-inspired image parameters and the plaques' structure to identify those features of electric images, which predominately relate to 'critical' structural cues of the plaques. In combination, such key image features may allow for a classification of 'low-to-high-risk' plaque conditions. The custom multi-electrode electrolocation catheter was used to localize a synthetic high-risk plaque (TCFA) in a pig coronary artery by 2-D

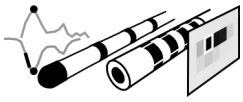

electric images. To do so, we acquired amplitude and waveform images via catheter motion (dynamic electric images) or for a stationary catheter position below the plaque (i.e., static images) and analyzed them.

9.3 Materials and methods

9.3.1 Plaque inspection with a ring-electrode electrolocation catheter

9.3.1.1 Ring-electrode electrolocation catheter

For plaque inspections in synthetic arteries, we used a commercial catheter (Finder 6F, ∅ = 2 mm, Dr. Osypka GmbH, Rheinfelden-Herten, Baden-Wuerttemberg, Germany) with four platinum ring electrodes (figure 9.2A). A custom-written LabVIEW program (National Instruments, Austin, Texas, USA) controlled the catheter's (basic) electrolocation functions, i.e., to establish an EOD-evoked electric field (around the electrodes) and to monitor it. Generated by the program, a weak *G. petersii* EOD signal (1V PP; 499 µs figure 9.2B) was emitted (NI 6251-USB, BNC 2129, National Instruments) at the tip electrode (length = 2 mm), i.e., the sender (S) of the catheter. The other ring electrodes (length = 1 mm/electrode) served as receivers (input impedance = 1 kΩ/electrode), the first (R1) and third (R3) of which were used for local EOD recordings, respectively (figure

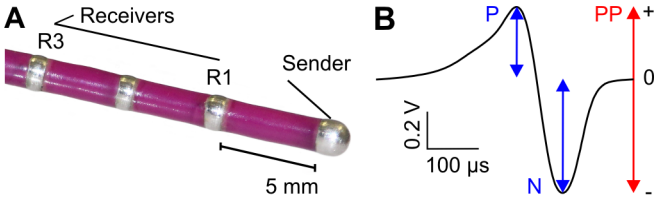

Figure 9.2: Ring-electrode electrolocation catheter and electric signal.

(A) Overview of the ring-electrode catheter and its electrode setting (sender and receivers) for active electrolocation. Either the first (R1) or third receiver (R3) was used along with the sender (S) for electric imaging of synthetic plaques, providing the catheter's S–R1 or S–R3 configuration. **(B)** EOD signal emitted by the catheter's sender. The EOD's peak-to-peak amplitude (PP, red double-headed arrow) and the peak amplitude of the positive (P) and negative (N) phase (blue double headed arrows) are marked. The peak amplitude ratio (P/N ratio) served as a measure of the signal's waveform. Amplitude (PP) and waveform (P/N) modulations, evoked by synthetic plaques, were used to compute electric amplitude and waveform images.

9.2A). We call the catheter's two configurations, defined by these settings, S–R1 and S–R3. Local EODs (lEODs), acquired with the S–R1 or S–R3 configuration, were digitized (resolution: 16-bit, sampling rate: 480 kHz, NI6251-USB, BNC 2120, National Instruments) and analyzed by the LabVIEW program. To determine the lEODs' amplitude, the peak-to-peak amplitude of the signals was computed and to quantify their waveform the peak amplitude ratio of the positive (P) and negative (N) lEOD phase (P/N ratio) was calculated (figure 9.2B). Based on plaque-evoked modulations of the catheter's electric field and lEODs, electric amplitude and waveform images were obtained.

9.3.1.2 Synthetic arteries with plaques

The synthetic coronary arteries, used in the experiments, were transparent and electrical conductive agarose tubes (Gottwald et al., 2011; Metzen et al., 2012) with an inner diameter of 5 mm, a wall thickness of 2 mm and a length of 300 mm. Their conductivity was set to 0.57 S m^{-1}, i.e., the approximate conductivity of a natural artery (e.g., Stiles and Oakley, 2002; Stiles and Oakley, 2003). At their center, the tubes featured a fatty, synthetic plaque (atheroma) within the top wall (figure 9.3). The synthetic plaques consisted of an electrically insulating core, made form pig fat (lard), which was encapsulated by a conductive agarose cap (0.57 S m^{-1}). Four basic plaque types (P1-4), each with a different core volume (1 [P1], 5 [P2], 113.5 [P3], 268.1 [P4] mm^3), were prepared. Their core shapes were either hemispheric/ellipsoidal (for P1-2) or spherical (for P3-4). In total we

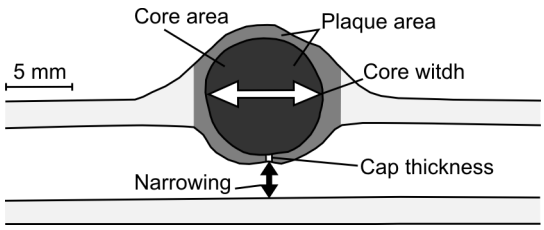

Figure 9.3: Side view of a synthetic plaque with indicated plaque parameters.
This schematic side view of a P4 plaque was redrawn from a photograph, which was captured through the transparent synthetic artery. The artery lumen is indicated in white and the artery wall in light gray. The synthetic plaque is located in the center of the upper wall. Several plaque features are marked, which have been determined (from the original photograph) using Image J software (W. Rasband, National Institute of health, Maryland, USA). In addition to these features, a plaque's rel. core area was calculated as the percentage ratio of the core area (dark gray) and total plaque area (dark gray and gray areas).

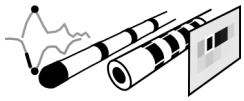

used 12 plaques, i.e., three versions of each plaque type.

Based on side view photos of the plaques (captured through the transparent tubes), we defined the plaques' individual structural characteristics (e.g., their relative core area [rca], cap thickness [ct] and others) as well as the plaque-evoked narrowing of the tubes (see figure 9.3 and table A.2 in the appendix for details).

Medical (histopathological) studies imply that real low-to-high-risk plaques can principally be determined through the dimensions of both structural features mentioned above (e.g., Virmani et al., 2006; Virmani et al., 2002). In thin-cap fibroatheromas, they reach critical thresholds (of rca > 10% and ct < 65µm) (e.g., Virmani et al., 2006). Other advanced 'lipid core plaques', putting patients at risk, have thicker caps, defined, e.g., as < 450µm (Gardner et al., 2008; Schlett et al., 2013; Virmani et al., 2006).

Here, we adopted the thresholds of 450 µm for cap thickness and 10% for rel. core area to determine separate conditions of our synthetic atheromas. Four conditions (C1-to-C4), indicating 'low-risk' (C1) to 'high-risk' (C4) synthetic plaques (table A.2), were defined (rca < 10% and ct > 450µm [C1]; rca < 10% and ct < 450µm [C2]; rca > 10% and ct > 450µm [C3], rca > 10% and ct < 450µm [C4]).

Even though our synthetic arteries and plaques partly resemble features of real ones, they are oversized in comparison and electrically simplified, e.g., by not specifically mimicking capacitive electrical properties of arterial tissue and plaques (e.g., Stiles and Oakley, 2002; Stiles and Oakley, 2003). Nonetheless, catheter-based electric imaging of such basic experimental substitutes can give a first hint whether active electrolocation cues could principally indicate low-to-high-risk plaques in coronary arteries.

9.3.1.3 Acquisition and analysis of dynamic electric images

Catheterizations of synthetic arteries with plaques were performed in an experimental tank (48.4 cm × 18.4 cm × 14.5 cm) with a clear salt solution (25 °C). The fluid's electrical conductivity was set to 0.7 S m^{-1}, i.e., the approximate conductivity of human blood (e.g., Stiles and Oakley, 2002; Stiles and Oakley, 2003).

Prior to electric image acquisitions, synthetic arteries (agarose tubes) were fixed onto a custom-made Styrofoam holder (35 cm × 2 cm × 1.5 cm) in the center of the tank (figure 9.4). The holder featured several positioning markers, which defined a grid for a stepwise catheter motion through the tubes. The grid's increments at the outer sections of the tubes

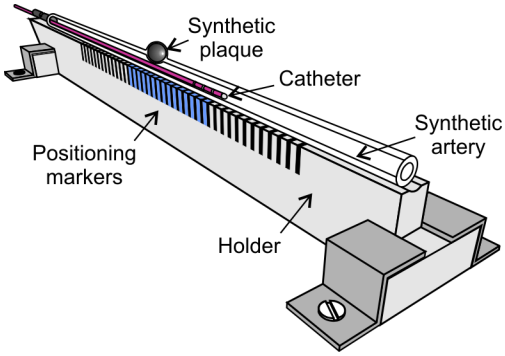

Figure 9.4: Catheterization of synthetic arteries with plaque.

A custom holder (light gray) was used to fixate a synthetic artery (white) with plaque (black) during catheterization. Positioning markers (black and blue stripes) on the holder guide the manual, stepwise motion of the catheter (purple) trough the 'artery'.

(step size = 5 mm) were larger than at the tubes' central region (step size = 2.5 mm), where the synthetic plaque was located (figure 9.4).

For a single catheterization, the catheter was moved, by hand, stepwise through a tube and either its S–R1 or S–R3 configuration was set. At each position the catheter emitted a burst of 100 EOD signals, with a delay of 80 ms between each EOD. Simultaneously, lEODs were sampled (either by catheter receiver R1 or R3) and their amplitudes (PP) and waveforms (P/N) were calculated, averaged and stored by the LabVIEW program.

Based on the obtained PP or P/N trace, we determined a tube's 'amplitude or waveform modulation profile' with a plaque's electric image in its center (figure 9.5). To do so, we used custom-written Matlab (MathWorks, Natick, Massachusetts, USA) routines. Their individual processing steps are summarized in brief below and outlined in detail in appendix A.2 (figure A.2.1). Basically, these multi-stage algorithms defined the traces' plaque-evoked central section and calculated the PP or P/N modulations within the central and outer sections of the traces. To compute these modulations, the PP or P/N values of a trace were divided by expectancy values of PP or P/N that would have been obtained in the tube without a plaque present. Consequently, expectancy values were similar to the PP or P/N values, recorded in the tubes peripheral regions (without plaque) and differed from those obtained in the tubes central region (with the plaque). As a result, amplitude or waveform mod. profiles featured peripheral regions of negligible small, i.e., 'basal' modulations of ~1 (figures 9.5A and 9.5B). Their central electric image, in turn, yields pronounced modulations (of either larger or smaller than 1) (figures 9.5A and 9.5B). Image modulations in both directions (larger or smaller 1) become stronger the more they deviate from 1.

Depending on the plaques' electrical and spatial properties as well as the catheter's configuration, electric amplitude images provide characteristic profiles (Gottwald and von

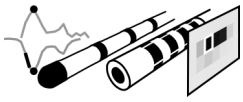

der Emde, 2013; Gottwald et al., 2011; Metzen et al., 2012). Acquired with configuration S–R3, the plaque's amplitude images yield 'w-shaped' curves (example shown in figure 9.5A). In turn, when the catheter's sender-to-receiver distance is shorter than the plaque under inspection, i.e., when using configuration S–R1 for electric imaging of P3-4 plaques, amplitude images will have a 'v-shaped' profile (e.g., Gottwald and von der Emde, 2013; Gottwald et al., 2011). The first half of each image profile results from sender-plaque interaction, whereas the second half is generated when the catheter receiver is moved past

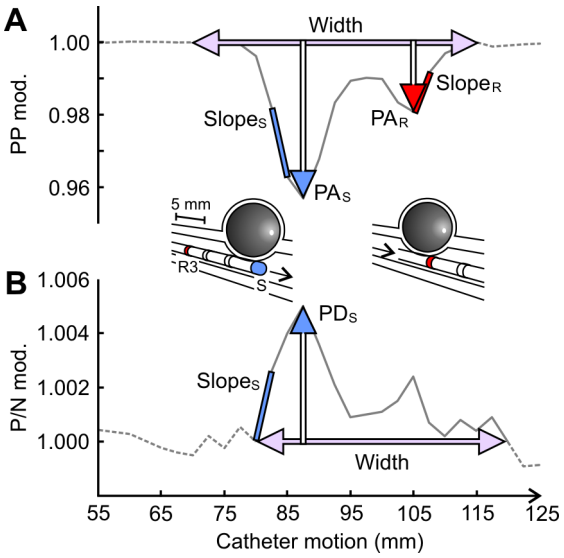

Figure 9.5: Analyzes of plaque-evoked dynamic electric images.

(A) Amplitude image of a P4 plaque (solid gray line) within a synthetic artery's amplitude (PP) modulation profile, acquired with catheter configuration S–R3 (i.e., a combination of the device's sender [S] and third receiver [R3]). Only small fractions of the profile's peripheral regions, (dashed gray lines) adjacent to the electric image, are shown. Electric image parameters of the first image half, which is generated (left scheme) when the catheter's sender (blue) moves past the plaque (black/white), are marked in blue and indexed with an 'S', i.e., the steepest slope$_{(s)}$ and peak amplitude (PA$_S$). The magnitude (i.e., deviation from 1) of the peak amplitude (blue arrowhead) is indicated by the arrow length. Both parameters are combined to obtain the slope-to-amplitude ratio (SAR$_S$, not shown). Only in amplitude images, captured with the catheter's S–R3 configuration, additional features were extracted from the second image half, which is induced when the receiver (R3, red) passes the plaque (rightmost scheme). These parameters are marked in red and carry the index 'R'. Like image features of the first image half, the image width (light purple, double-headed arrow) was determined for all amplitude images (captured with the S–R3 or S–R1 configuration). **(B)** Plaque-evoked waveform image within the synthetic artery's waveform (P/N) modulation profile, both arranged as in (A) with analogous markings. Image features extracted from waveform images (acquired with S–R1 [not shown] and S–R3 [above]) are the steepest slope$_{(s)}$, the peak distortion (PD$_S$) and the slope-to-distortion ratio (SDR$_S$, not shown) of the first image half and the image width.

the plaque (figure 9.5A). Catheter-plaque interactions, as mentioned above, also shaped the profiles of waveform images (example shown in figure 9.5B).

Several bio-inspired features were derived from both image types. Of the images' first half, we determined the steepest slope$_{(S)}$ and the strongest modulation (peak), which is termed peak amplitude (PA_S) for amplitude images and peak distortion (PD_S) for waveform images (figure 9.5). The cues' index 'S' indicates them to be evoked by sender-plaque interactions during electric imaging.

By dividing the image slope by the peak modulation we obtained the electric images' relative slopes, i.e., the amplitude images' 'slope-to-amplitude ratio' (SAR_S) or the waveform images' 'slope-to-distortion ratio' (SDR_S) (figure 9.5).

For amplitude images, acquired by catheter configuration S–R3, we also extracted image features from the second half of their 'w-shaped' profiles, i.e., PA_R, image slope$_{(R)}$ and SAR_R (figure 9.5A). Resulting from receiver-plaque interactions during electric imaging, these cues were labeled with the index 'R'.

Eventually, the width of amplitude and waveform images was defined (figure 9.5).

9.3.1.4 Statistical analysis and quantification

Based on the obtained amplitude and waveform images and their parameters, we evaluated the plaque detection performance of the ring-electrode electrolocation catheter and its ability to indicate 'low-to-high-risk' conditions (C1-to-C4) of synthetic plaques (atheromas). In doing so, we performed statistical analyzes of the electric image and plaque parameters (i.e., a correlation and cluster analysis) using SPSS (IBM Corp., Armonk, New York, USA).

9.3.2 Plaque inspection with a multi-electrode electrolocation catheter

9.3.2.1 Multi-electrode electrolocation catheter

Plaque detection in a pig coronary artery was performed with a custom-build multi-electrode catheter (⌀ = 2 mm, Micromotive GmbH, Mainz, Rhineland-Palatinate, Germany) (Mayekar et al., 2011; Mayekar et al., 2012). It featured 17 gold electrodes, i.e., a sender (0.79 mm^2) at its tip and four electrode rings (Er1-4), each composed of four (R1-

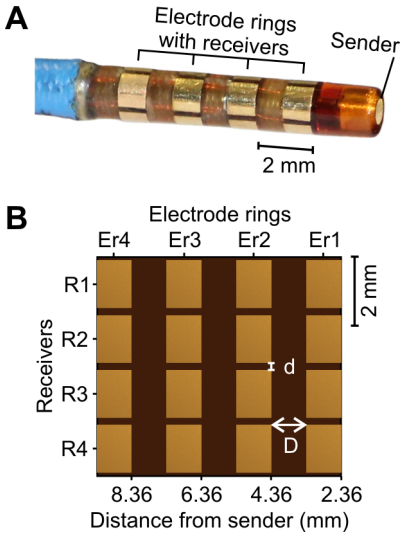

Figure 9.6: Multi-electrode electrolocation catheter.

(A) Overview of the custom 17-electrode catheter and its electrode setting (sender and electrode rings with individual receivers) for active electrolocation. **(B)** In-detail illustration of the catheter's electrode rings (Er1-4) and their four receivers (R1-4), shown as an 'unfolded' 2-D map. The spacing between a ring's electrodes (d) is 0.2 mm; between the individual electrode rings (D) it is 1 mm.

4) individual receivers (1.37 mm^2/electrode, input impedance = 10 kΩ/electrode) (figures 9.6A and 9.6B).

During active electrolocation, a weak and shortened version of a *G. petersii* EOD (150 mV PP; 141 µs) was generated by a custom LabVIEW program and emitted (NI PXI-5412, National Instruments) at the catheter's sender. The modified EOD signal contained a peak frequency of 10 kHz, which as an operating frequency in impedance spectroscopy studies (e.g., Yu et al., 2010; Yu et al., 2011) was well suited to electrically discriminate plaques from normal arterial tissue. Furthermore, the EOD's low voltage/power should prevent irritations of the artery wall. lEODs were sampled simultaneously across the catheter's 16 receivers and digitized (resolution: 12-bit, sampling rate: 60 MHz, NI PXI-5105, National Instruments). The LabVIEW program stored the lEODs, which were further processed by custom-written Matlab routines to determine the artery's amplitude (PP) and waveform (P/N) mod. profiles and the plaque's electric images.

9.3.2.2 Coronary artery with synthetic plaque

Prior to the experiment, a coronary artery was equipped with a synthetic plaque. To do so, a block of cardiac tissue (7.3 cm × 1 cm × 1.2 cm), containing the artery segment (length = 7.3 cm; inner ∅ ~ 3 mm), was harvested from a fresh pig heart and placed in a custom Plexiglas chamber (12 cm × 1.5 cm × 1.5 cm, figure 9.7A). Entry and exit of the artery were glued (Sekundenkleber-blitzschnell, UHU GmbH & Co KG, Bühl, Baden-Wuerttemberg, Germany) to the chamber's 'connectors' (figure 9.7A). At the block's center,

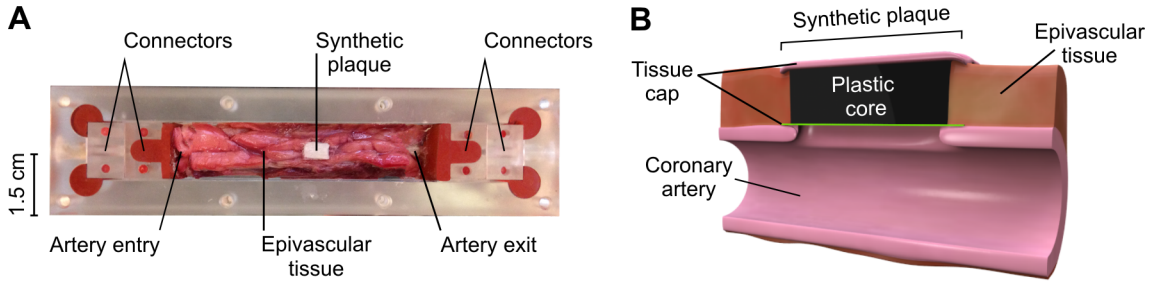

Figure 9.7: Coronary artery and synthetic plaque.

(A) Coronary artery segment with synthetic plaque – contained in a block of cardiac tissue – and fixed within a custom-made Plexiglas chamber. Both ends of the tissue block as well as the artery's entry and exit are glued to connectors of the chamber. **(B)** The illustration depicts a view inside the center of the tissue block and coronary artery, showing the synthetic plaque and its components (plastic core and arterial tissue caps) in different colors. Embedded within the epivascular tissue on top of the artery the plaque covers and seals a cut out of the upper artery wall.

we made a small cut out (6 mm × 3 mm) in the epivascular tissue and upper artery wall, within which the synthetic plaque was carefully fixed with glue (figure 9.7A). The rectangular-shaped plaque featured a plastic core (6 mm × 1.87 mm × 3 mm), whose top and bottom had been glued to a thin cap of arterial tissue (figure 9.7B). Both tissue layers had been prepared with a cryostat (CM1850, Leica Microsystems, Wetzlar, Hessen, Germany) from excerpts of the inner wall of a second, separate coronary artery segment. The upper cap was thicker (259 µm) than the plaque's bottom cap (50 µm), which was exposed to the artery's lumen.

Due to its bottom cap's thickness below 65 µm and a rel. core area > 10%, the plaque was termed a synthetic version of a thin-cap fibroatheroma. With its electrical insulating core overlaid by thin arterial tissue, we assume it to partly mimic basic resistive and capacitive properties of such (rupture-prone) plaques. However, as the synthetic plaque is oversized compared to real plaques and will not cover their complex electrical properties (e.g., Stiles and Oakley, 2003; Streitner et al., 2009; Yu et al., 2010; Yu et al., 2011; Zhang et al., 2015) in detail, it has to be considered a simplified, artificial version of a high-risk plaque.

9.3.2.3 Acquisition and analysis of dynamic/static electric images

Prior to the catheterization experiment, the Plexiglas chamber, containing the tissue block with artery and plaque, was sealed with a lid. It was then attached to an outer Plexiglas

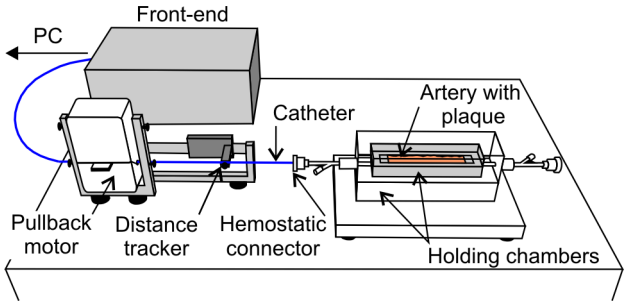

Figure 9.8: Catheterization of the coronary artery with synthetic plaque.

The chamber (gray), holding the tissue block (orange) with artery and plaque, is housed in another Plexiglas chamber with heamostatic connectors (white). Via the frontal connector the catheter (blue) is inserted and then pushed close to the artery's end. During catheterization, the catheter is withdrawn automatically with a pullback motor (white), while its stepwise movement through the artery is measured with a distance tracker (dark gray). A front-end (gray), defining the catheter's input impedance, connects the device to the computer and LabVIEW program, which controls the catheter's electrolocation functions and the other devices, providing/tracking catheter motion.

chamber, equipped with 'hemostatic connectors' at the front and back (figure 9.8). Through the chamber's frontal connector, the artery was filled with a salt solution (37 °C) that matched the conductivity (0.67 S m^{-1}) of blood with a hematocrit level of 43.6% (Matuschek, 2014). The connector was also used to insert the catheter (figure 9.8), which was pushed 6.4 cm into the artery segment. The catheter's receivers (R1-4) of each electrode ring (Er1-4) either faced the top (R2), the bottom (R4), the left (R1) or the right portion (R3) of the artery wall. The catheter was mounted in a pullback motor (Track Back® II, Volcano Corp., San Diego, California, USA) and self-made distance tracker (figure 9.8). This fixation ensured the orientation of the catheter receivers (as mentioned above) not to change throughout the catheterization of the artery and plaque. The pullback motor and distance tracker were both connected to (NI 6251-USB, National Instruments) and monitored by the LabVIEW program, which also controlled the electrolocation functions of the catheter. During the experiment, the catheter was withdrawn stepwise via the pullback motor and its motion through the artery (i.e., 24 positions with a step size of -1.54 ± 0.63 mm) was recorded with the distance tracker. At each position the catheter emitted 100 EODs with a delay of 200 µs between each signal. lEODs were sampled across the catheter's receivers and saved by the LabVIEW program. A custom-written Matlab routine was used to filter the signals (band-pass: 50 Hz to 200 kHz) and to screen them, deleting lEODs with vertical offsets > 10 mV. Amplitudes (PP) and waveforms

(P/N) of the retained lEODs (n ≥ 71 per catheter receiver at each position) were determined and averaged (for each catheter receiver at each position).

The artery's dynamic amplitude or waveform mod. profiles with a central, plaque-evoked electric image were derived from the PP or P/N traces of either the catheter's first or third electrode ring (Er1 or Er3). We call these two catheter configurations (for which dynamic mod. profiles and electric images were calculated) S–Er1 and S–Er3, indicating them as a combination of the respective electrode ring (Er1 or Er3) and the catheter's sender (S).

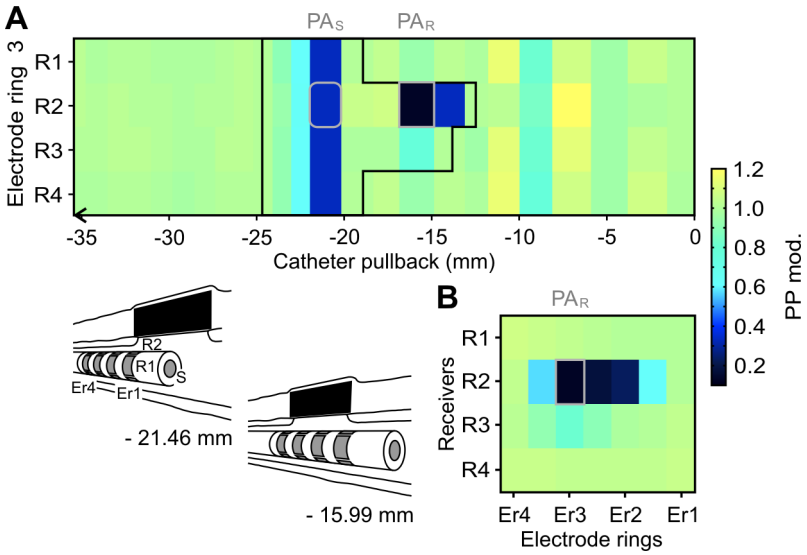

Figure 9.9: Analyzes of plaque-evoked dynamic and static electric images.

(A) Dynamic amplitude (PP) modulation profile acquired along the artery for catheter configuration S–Er3 (which combines the catheters's sender [S] and third electrode ring [Er3] of four receivers [R1-4]). The center of the profile contains the plaque's 2-D amplitude image (framed by a black line). It features two peak amplitudes, i.e., its two strongest modulations (with the largest deviations from 1). One of them, labeled as PA_R above and marked by a gray rectangle within the image, occurs at catheter pullback position -15.99 mm, where Er3 is below the plaque (black/white), as illustrated in the schematic drawing at the bottom. The other peak amplitude, indicated by a gray, rounded rectangle within the image and marked as PA_S above, emerges at pullback position -21.46 mm, where the catheter's sender faces the plaque, as shown in the leftmost sketch. In addition this inset indicates the catheter's electrodes, i.e., the sender (S, gray) and the direction of the electrode rings (Er1-4) and their receivers (R1-4, gray). Besides catheter configuration S–Er3, described above, dynamic electric images were also acquired for the catheter configuration S–Er1 (not shown). **(B)** Static, 2-D amplitude image of the plaque acquired for catheter pullback position -15.99 mm by amplitude modulations from all electrode rings of the catheter and their receivers (R1-4 of Er1-4). The image's peak amplitude is marked by a gray rectangle and labeled as PA_R. While not depicted in this figure, also static/dynamic waveform images of the plaque and their peak distortions, i.e., PD_S and/or PD_R, were evaluated in this study.

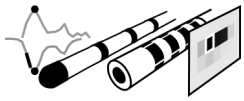

Each electrode ring (Er1 or Er3) provides four traces of PP or P/N, acquired with its individual receivers (R1-4) along the artery. Using custom-written Matlab routines, each trace was analyzed by identifying its central and outer sections and by calculating their (PP or P/N) modulations. A detailed description of these analytical steps is given in appendix A.2 (figure A.2.2). Eventually, the four modulation traces (of PP or P/N) of an electrode ring (Er1 or Er3) were combined as a 2-D, color-coded map (example shown in figure 9.9A) with a resolution of 96 pixels (i.e., the modulations of R1-4 × 24 pullback positions). Another Matlab routine (explicated in detail in appendix A.2, figure A.2.3) was used to compute static amplitude or waveform images.

Such images were composed of the PP or P/N modulations of all 16 catheter receivers (R1-4 of Er1-4) at a single pullback position with the catheter's electrode rings centrally placed underneath the plaque. To compute the images' modulations, PP or P/N data, acquired below the plaque, was divided by PP or P/N catheter data from the artery's peripheral regions (without plaque). The resulting electric images were depicted as color-coded, 2-D maps (example shown in figure 9.9B). Their initial resolution of 16 modulation pixels (for R1-4 × Er1-4) was increased to 28 (4 × 7) pixels by linear interpolation.

Both, dynamic and static electric images were evaluated whether they can indicate the plaque's position within the artery wall. To do so, their peak modulations were determined, which either result from interactions of the catheter's receivers with the plaque, i.e., PA_R, PD_R (in static/dynamic images) or from sender-plaque interactions, i.e., PA_S, PD_S (in dynamic electric images).

9.4 Results and discussion

9.4.1 Plaque inspection with a ring-electrode electrolocation catheter

9.4.1.1 Plaque detection by dynamic electric images

Twelve synthetic plaques, i.e., three versions of each plaque type (P1-4), were tested to determine the plaque detection performance of the ring-electrode electrolocation catheter. By either using catheter configuration S–R1 or S–R3 each artery with plaque was inspected three times (repetitively). Thus, 36 dynamic amplitude and waveform mod. profiles with plaque-evoked electric images could potentially be acquired for each

configuration.

All the synthetic arteries' amplitude mod. profiles, for S–R1 and S–R3, provided amplitude images of synthetic plaques. In turn, plaque-evoked waveform images could only be derived from 67% (for S–R1) or from 72% (for S–R3) of the waveform mod. profiles. Here, all larger plaque types (P3-4) yielded pronounced waveform images. For most smaller plaques (P1-2) waveform images were successfully computed either from none of or not each of the plaques' three modulation profiles (per catheter configuration). Hence, amplitude images were more reliable plaque indicators than waveform images.

In our previous catheter studies, amplitude images provided the same, high accuracy for plaque detection (Gottwald and von der Emde, 2013; Gottwald et al., 2011; Metzen et al., 2012). The pronounced amplitude images, we obtained here (example shown in figure 9.5A in the materials and methods section) and in the earlier studies, result from the considerable higher resistance of the synthetic atheromas (fatty agar plaques) compared to those of the synthetic arteries (conductive agar tubes).

The weak waveform images (example shown in figure 9.5B) indicate faint capacitive properties of synthetic plaques, which provoked only slight modulations of the catheter's electric field and received lEOD waveforms. Similar waveform images (of low magnitudes) were acquired in preliminary tests, when inspecting synthetic plaques with an earlier version of the ring-electrode electrolocation catheter (Gottwald, 2010).

In these tests (Gottwald, 2010) and a follow-up study (Gottwald et al., 2011), synthetic plaques had also been located, due to their capacitive properties, by so-called phase-shift images. To do so, the phase-shifts of the catheter's received lEODs and its output EODs had been computed, the plaque-evoked modulations of which formed the electric images. While in the initial experiments (Gottwald, 2010) phase-shift images were absent for some of the smaller (e.g., P1, P2 type) plaques, pronounced images could be captured for all plaques (P1-4) in the latter tests (Gottwald et al., 2011) with a modified version of the electrolocation catheter. Similarly, further modifications of our current device may improve its plaque detection by waveform images. This may be achieved, e.g., by refining the (Matlab) routine for waveform image extractions to better acquire the weaker images of small plaques.

Ring-catheter-based electric images designate synthetic plaques but are much wider compared to them (Gottwald and von der Emde, 2013; Gottwald et al., 2011; Metzen et al., 2012) (figures 9.5A and 9.5B; table A.2). Hence, for more precise estimations of a plaque's

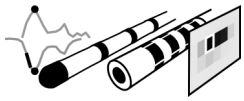

position, particular image features may be used instead of the whole image profile. In accordance with our earlier studies (Gottwald and von der Emde, 2013; Gottwald et al., 2011; Metzen et al., 2012), we suggest that the plaque position could be inferred from the positions of the peak amplitudes (PA_S or PA_R) in amplitude images (example shown in figure 9.5A). Also peak distortions (PD_S) in waveform images could be used to do so (example shown in figure 9.5B). As these peak modulations were acquired by either sender- or receiver-plaque interactions, a potential strategy to determine plaque locations would involve tracking the catheter's sender and/or receiver electrode during catheterization. Electrode positions at which peak modulations of electric images occur would then convey a plaque's position within the artery.

9.4.1.2 Associations of electric image and plaque parameters

For the analysis of synthetic plaques, several bio-inspired parameters were extracted from a plaque's amplitude ($n = 3$) and waveform images ($n \leq 3$), i.e., their peak modulations, relative slopes and widths (examples shown in figure 9.5). They were then averaged to acquire the parameters' means for each plaque. Amplitude image features were evaluated for all twelve synthetic plaques, whereas waveform image parameters could only be determined for 10 plaques.

Based on a correlation analysis, we evaluated the interdependencies of the image parameters and the individual features of synthetic plaques (table 9.1). In doing so, key features of electric images could be identified, which predominantly relate to the plaques' rel. core area or cap thickness, i.e., the critical cues defining 'low-to-high-risk' plaque conditions (C1-to-C4). The analysis showed that peak modulations of amplitude images (PA_S, PA_R) and of waveform images (PD_S) provided the strongest correlations to the rel. core areas of synthetic plaques (see correlation coefficients/significance levels highlighted in bold and blue in table 9.1). As further indicated by the correlation coefficients and significance levels in table 9.1 (bold, blue), the relative slopes of amplitude images (SAR_S, SAR_R) showed the strongest associations to the cap thickness. As a result of their predominant dependencies to the plaques' critical features, these key image parameters may, in combination, designate the 'low-to-high-risk' conditions (C1-to-C4) of synthetic plaques. We further assume the relations of key image features to the plaques' other parameters (e.g., rel. narrowing, core width etc., table 9.1) not to interfere with this task.

Table 9.1: Associations between electric image parameters and plaque parameters.

The table depicts correlation coefficients and significance levels for the correlations of electric image and plaque parameters (Spearman 2-tailed). Both are highlighted in bold and blue for parameters of amplitude images and waveform images (italic), which provide the strongest associations to either the rel. core area or the cap thickness of synthetic plaques. Correlation analyzes were based on n = 12 amplitude image and plaque parameters (of 12 synthetic plaques) or n = 10 waveform image and plaque parameters (of 10 synthetic plaques), respectively.

	Plaque parameters					
Image parameters	Rel. narrowing	Plaque area	Core width	C. area	Rel. c. area	Cap thickness
PA_S [a]	-0.615 [c]	-0.860 [d]	-0.895 [d]	-0.867 [d]	**-0.902** [d]	0.587 [c]
PA_S [b]	-0.615 [c]	-0.860 [d]	-0.895 [d]	-0.867 [d]	**-0.902** [d]	0.587 [c]
PA_R [b]	-0.601 [c]	-0.888 [d]	-0.902 [d]	-0.895 [d]	**-0.923** [d]	0.678 [c]
SAR_S [a]	0.322	0.685 [c]	0.615 [c]	0.699 [c]	0.734 [d]	**-0.853** [d]
SAR_S [b]	0.221	0.697 [c]	0.644 [c]	0.732 [d]	0.697 [c]	**-0.942** [d]
SAR_R [b]	0.343	0.706 [c]	0.657 [c]	0.713 [d]	0.727 [c]	**-0.839** [d]
Width [a]	0.595 [c]	0.914 [d]	0.921 [d]	0.862 [d]	0.830 [d]	-0.557
Width [b]	0.740 [d]	0.877 [d]	0.916 [d]	0.898 [d]	0.905 [d]	-0.446
PD_S [a]	0.588	0.879 [d]	0.879 [d]	0.867 [d]	**0.915** [d]	-0.394
PD_S [b]	0.711 [c]	0.851 [d]	0.863 [d]	0.875 [d]	**0.936** [d]	-0.286
SDR_S [a]	0.527	0.624	0.527	0.636 [c]	0.709 [c]	-0.358
SDR_S [b]	0.697 [c]	0.455	0.382	0.467	0.733 [c]	-0.212
Width [a]	0.430	0.345	0.479	0.273	0.152	-0.564
Width [b]	0.640 [c]	0.732 [c]	0.768 [d]	0.701 [c]	0.750 [c]	-0.372

[a] Acquired by catheter configuration: S–R1

[b] Acquired by catheter configuration: S–R3

[c] Correlation is significant at the 0.05 level.

[d] Correlation is significant at the 0.01 level.

These (additional) correlations were often considerably weaker than those of a key image feature and its related critical plaque parameter (table 9.1). Stronger correlations of a key image parameter (PA_S, PA_R, PD_S) only occurred with other plaque parameters (plaque area, core area/width) that were related to the relevant and critical plaque feature (rel. core area) (table 9.1).

Figure 9.10 depicts an overview of the relationships of the key image features (acquired by catheter configuration S–R1 or S–R3) and the critical plaque parameters. The distributions of PA_S, PD_S and SAR_S showed only slight variations when obtained by the individual configurations of the catheter (compare the left and right graphs in figures 9.10A - 9.10C).

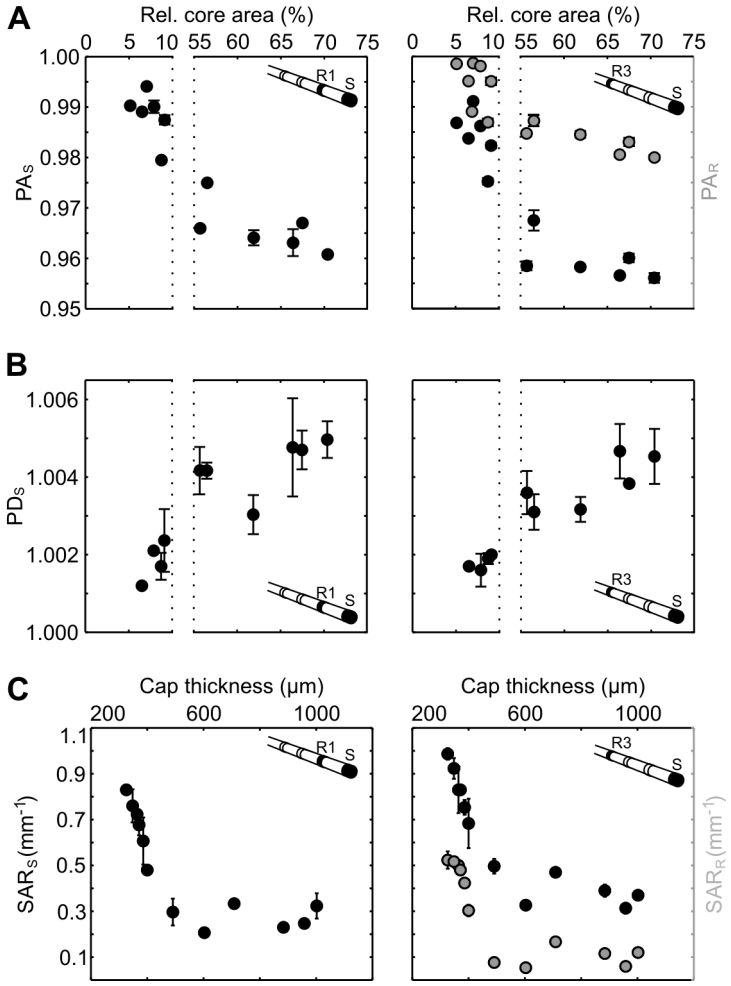

Figure 9.10: Relationship of the amplitude and waveform images' key features to the rel. core area or cap thickness of synthetic plaques.

Values depict either means ± SD of image parameters acquired from several (n = 3 or n = 2) electric images of a synthetic plaque or result from a single electric image. Amplitude image parameters for n = 12 synthetic plaques and waveform image parameters for n = 10 synthetic plaques are shown. **(A)** Peak amplitudes (PA) of amplitude images – plotted versus the plaques' rel. core areas – were acquired by catheter configuration S–R1 (leftmost graph and inset) or S–R3 (rightmost graph and inset). PA_S in both graphs (black circles) result from interactions of the catheter's sender (S) and the plaque during electric imaging. PA_R of the rightmost graph (gray circles) result from receiver (R) - plaque interactions. Note that for a better visualization of the data, both graphs are split in two separate parts yielding a gap (dashed lines) of the x-axis' scaling in between. **(B)** Peak distortions (PD_S) of waveform images plotted against the plaques' rel. core areas. Image parameters are shown in the same manner, with analogous markings, index, shading and organizations of the graphs as described in (A). **(C)** Slope-to-amplitude ratios (SAR_S and SAR_R) plotted versus the cap thickness of synthetic plaques. Both parameters are shown with analogous markings, indices and shading as described in (A).

Key image features acquired via S–R3 and due to the interactions of plaques and the catheter's receiver (PA_R and SAR_R) turned out to be weaker than those caused by sender-plaque interactions (PA_S and SAR_S) (figures 9.10A and 9.10C, black vs. gray distributions). As a result of the parameters' different magnitudes (compare PA_S and PA_R or SAR_S and SAR_R, figures 9.10A and 9.10C rightmost), their distributions were vertically shifted against one another. However, besides being shifted, the distributions basically resembled each other.

The findings mentioned above imply that key image features, gained by each catheter configuration and either related to sender- or receiver-plaque interactions (during electric imaging), may be suitable for 'low-to-high-risk' classifications of synthetic plaques and may potentially provide similar results when used to do so.

9.4.1.3 Identification of 'low-to-high-risk' plaque conditions

In order to determine 'low-to-high-risk' conditions of synthetic plaques (C1-to-C4), key image features were combined as PA-PD-SAR pairs for each of the two catheter-configurations (for S–R1 see figure 9.11A; for S–R3 see figure 9.11B). Since we did not derive PD_R parameters from electric waveform images, only plaque-evoked PA_S-PD_S-SAR_S pairs could be investigated in this study. In addition, they could only be evaluated for the 10 synthetic plaques for which waveform image cues were acquired.

To test whether these combinations of key image features provide accurate classifications of the plaques' conditions, we performed a hierarchical cluster analysis for each of the two data sets mentioned above. For both data sets, PA_S-PD_S-SAR_S pairs formed four individual clusters (figures 9.11A and 9.11B). Each cluster represented an individual plaque condition (figure 9.11). Both results confirm that the combinations of key image features can identify 'low-to-high-risk' conditions of synthetic plaques (atheromas). We thereby extend on previous findings, which so far indicated that small-to-large synthetic atheromas (e.g., P1-to-P4 and beyond) could be differentiated via PA parameters and/or widths of amplitude images (Gottwald et al., 2011; Metzen et al., 2012) or via the peak modulations and widths of phase-shift images (Gottwald et al., 2011). While our recent tests ruled out electric image widths as key image features for 'low-to-high-risk' plaque classifications, peak modulations of phase-shift images (Gottwald et al., 2011) may likely provide a potential alternative or additional cue to the peak distortions used here and may thus be evaluated,

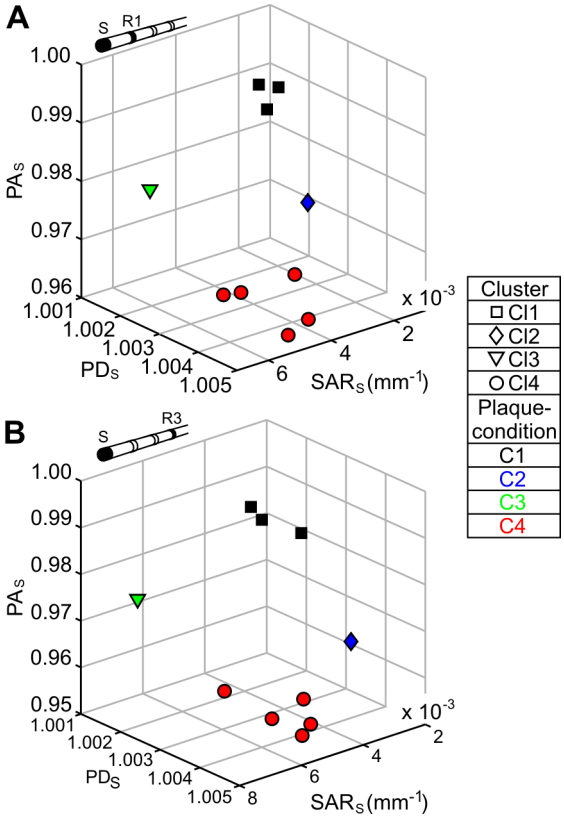

Figure 9.11: Classification of 'low-to-high-risk' plaque conditions (C1-to-C4) via combinations of key image features.

(A) Hierarchical cluster analysis of PA_S, PD_S and SAR_S parameters, acquired by catheter configuration S–R1 (see top left inset). Different symbols indicate four potential clusters (Cl1-4) that could form during the analysis and did so by the PA_S-PD_S-SAR_S pairs (n = 10). Individual symbol colors designate the plaque condition (C1, C2, C3 or C4) that corresponds to a particular PA_S-PD_S-SAR_S pair of a cluster. The distinct colorations of the clusters indicate PA_S-PD_S-SAR_S pairs to clearly designate 'low-to-high-risk' conditions (C1-to-C4) of synthetic plaques (n = 10). **(B)** Plaque classification via PA_S-PD_S-SAR_S pairs (n = 10), acquired by catheter configuration S–R3 (see the top left inset). The analysis yields a similar clustering as described in (A), which is depicted in the same manner, with analogous markings and coloration as in (A).

besides PA_R, PD_R and SAR_R parameters, in future studies.

9.4.2 Plaque inspection with a multi-electrode electrolocation catheter

9.4.2.1 Plaque detection by 2-D, dynamic and static electric images

We used our custom catheter to electrolocate a synthetic high-risk plaque (thin-cap fibroatheroma) in a pig coronary artery with a single catheterization (individual catheter pullback positions along the plaque are illustrated in figure 9.12A).

In a first strategy for plaque inspection, we determined the plaque-evoked dynamic electric images within the artery's 2-D amplitude (figure 9.12B) and waveform mod. profiles (figure 9.12C). The profiles were computed either for the S–Er1 configuration (figures 9.12B and 9.12C, uppermost) or the S–Er3 configuration of the catheter (figures 9.12B and 9.12C bottommost).

While the artery's modulation profiles almost exclusively showed negligible small

modulations (i.e., basal modulations ~ 1), their amplitude or waveform images also featured pronounced modulations (below 1) (figures 9.12B and 9.12C). They were caused by the plaque's higher electrical resistance and (presumably) lower capacitance compared to those of the artery wall. Catheter configuration S–Er3 provided the largest electric images with the highest modulation magnitudes (i.e., the largest deviations from 1).

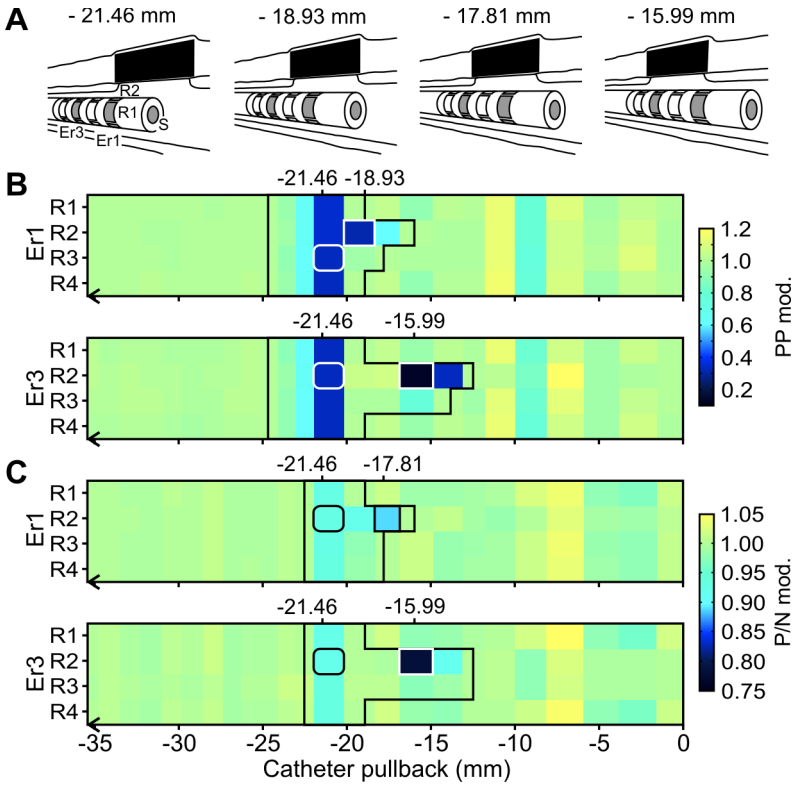

Figure 9.12: 2-D, dynamic amplitude and waveform modulation profiles of the artery with plaque-evoked electric images.

(A) Schematic drawings showing the catheter below the synthetic plaque (white/black) at individual catheter pullback positions (mm) along the artery (white). Catheter electrodes, i.e., the sender (S), individual electrode rings (Er1, Er3) and their receivers (R1-4) are indicated in detail in the leftmost drawing and highlighted in gray in all the drawings. **(B)** Color-coded amplitude mod. profiles acquired for catheter configuration S–Er1 (uppermost profile) or configuration S–Er3 (bottommost profile). Within the profiles a black line frames the plaque's amplitude image. The image's peak amplitudes are marked either by a rounded (PA_S) or regular (white) rectangle (PA_R). The catheter pullback positions (mm) at which both parameters occur are indicated above and are illustrated in (A). **(C)** Color-coded waveform mod. profiles with plaque-evoked waveform image, acquired by the catheter's two configurations (S–R1 or S–R3). Modulation profiles and their electric images are shown in the same manner as described in (B). Peak distortions of the images are marked by rounded (PD_S) or regular (white/black) rectangles (PD_R), with their (pullback) positions given above and illustrated in (A).

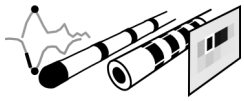

The strongest (peak) modulations in electric images occurred due to receiver-plaque interactions during catheterization. These PA_R and PD_R parameters (figures 9.12B and 9.12C) were acquired from catheter pullback positions, where either the first (Er1) or third (Er3) electrode ring of the device was situated below the plaque (figure 9.12A). Along the electrode rings' receivers (R1-4), the peak modulations emerged at R2, which had pointed towards the plaque (figure 9.12A). In most electric images (except in the amplitude image of the S–Er1 configuration, figure 9.12B uppermost) also PA_S or PD_S parameters, related to sender-plaque interactions, were obtained at catheter receiver R2 (figures 9.12B and 9.12C). Interestingly, sender-plaque interactions also caused strong modulations at the other catheter receivers (R1, R3, R4), which resembled the magnitudes of PA_S or PD_S (figures 9.12B and 9.12C) and resulted from a 'global distortion' of the catheter's electric field.

Together with the information on the catheter's electrode positions (tracking data) and orientations along the artery (figure 9.12A), the electric images' peak modulations could determine the plaque's position.

As an alternative to dynamic electric images, we evaluated static electric images (figure 9.13) for plaque inspections. They were captured for a single pullback position, at which the catheter's electrode rings were centrally placed below the synthetic plaque (figure 9.13A). The plaque's (static) amplitude (figure 9.13B) and waveform image (figure 9.13C) were computed as a 2-D, interpolated profile, based on the amplitude or waveform modulations from across all catheter receivers (R1-4 of Er1-4).

Both images showed similar modulation patterns with mainly basal modulations (~ 1) in their periphery and pronounced modulations (below 1) in their center (figures 9.13B and 9.13C). The central modulations of the amplitude image were much stronger than those of the waveform image (providing larger deviations from 1). They were obtained from the R2 receivers of the catheter's electrode rings, which had directly faced the plaque during catheterization (figure 9.13A). Consequently, the central modulations of amplitude and waveform images indicated the plaque's location within the upper artery wall and they roughly showed its 'width'. Besides depicting the plaque's position, the images' peak modulations, i.e., PA_R in the amplitude image (figure 9.13B) or PD_R in the waveform image (figure 9.13C), also marked the plaque's approximate center.

Bio-inspired dynamic and static electric imaging, as performed in this study, substantially improved the multi-electrode electrolocation catheter with regard to its previous genera-

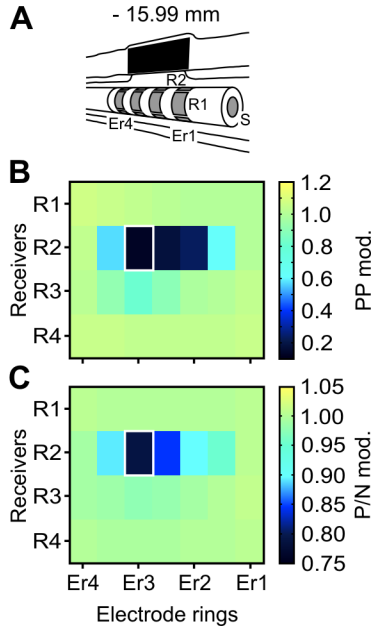

Figure 9.13: 2-D, static amplitude and waveform images of the synthetic plaque.
(A) Schematic drawing illustrating the catheter below the synthetic plaque (white/black) at catheter pullback position -15.99 mm within the artery (white). The catheter's electrodes, i.e., the sender (S), the electrode rings (Er1-4) and their receivers (R1-4) are labeled and all highlighted in gray. **(B)** Color-coded amplitude image, acquired across all electrode rings (as depicted above in (A)) by receiver-plaque interactions. The image's peak amplitude PA_R is marked by a white rectangle. **(C)** Color-coded waveform image, shown in the same manner as described in (A) (the white rectangle indicates the image's peak distortion, PD_R).

tions (Mayekar et al., 2011; Mayekar et al., 2012). So far, these earlier versions of the device had only been tested by real/simulated catheterizations of considerably oversimplified experimental substitutes of arteries and plaques (i.e., small glass/Plexiglas tubes equipped with metal or plastic balls (Mayekar et al., 2011) of different sizes (Mayekar et al., 2012). To probe them, just a sinusoidal electric signal (of 1V and 1kHz) had been used instead of an EOD pulse, while moving the catheter through the tubes. In doing so, 'voltage profiles' (Mayekar et al., 2011) and later electric amplitude images (Mayekar et al., 2012) had been acquired for individual electrode configurations of the device, e.g., for S–Er1-to-S–Er4 (Mayekar et al., 2011), or when using only a single receiver and the sender (Mayekar et al., 2012). These basic experiments/simulations showed that the catheter could detect simple targets as mentioned above and which types of catheter configurations might potentially be useful for future plaque inspections.

Our current findings imply that the improved version of the electrolocation catheter may principally be suitable to detect thin-cap fibroatheromas and thus rupture-prone high-risk plaques of coronary arteries. To further evaluate the plaque detection performance of the device, more catheterizations of coronary arteries with synthetic high-risk plaques may be carried out in follow-up experiments.

9.4.3 Future directions

Here, we evaluated two biomimetic electrolocation catheters for plaque diagnostics. We showed that several catheter configurations, electric imaging strategies, image types and image features were applicable to locate/classify synthetic plaques. These findings provide some interesting implications for enhancing the catheter system beyond its current versions.

A first step to do so, is to focus on plaque inspections via 2-D, dynamic and static electric images, captured with the multi-electrode catheter. Such (amplitude and waveform) images can designate a plaque along the artery wall and advantageously at different circumferential portions of it (see figures 9.12 and 9.13). They also might enable critical plaque classifications by key image features, analogous to those acquired with the ring-electrode catheter (PA, PD and SAR, figures 9.10 and 9.11). Electric phase-shift images, tested in previous studies (Gottwald, 2010; Gottwald et al., 2011), could provide further cues for this task.

In a second step, modified catheter models may be used to promote the electric imaging strategies proposed above. Figure 9.14 shows a new device (a multi-/ring-electrode catheter), whose frontal ring electrode (sender) and adjacent first electrode ring (of 7 re-

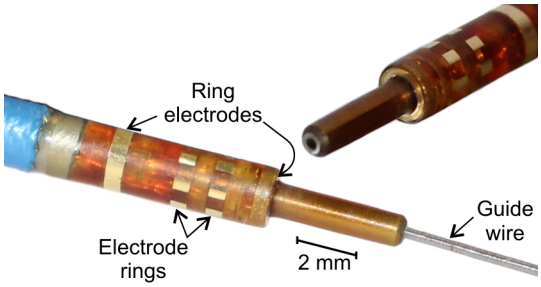

Figure 9.14: Multi-/ring-electrode catheter.

Overview of a new catheter model (designed by M. Gottwald and manufactured by Micromotive GmbH) with two golden electrode rings and ring electrodes. The electrode rings feature 7 receivers (0.2 mm^2/electrode), respectively. The spacing between a ring's receivers and between both electrode rings is 0.5 mm. Each ring electrode (frontal electrode = 0.3 mm height, rear electrode = 0.5 mm length) is 1.5 mm apart from the adjacent receivers. The frontal electrode, surrounding the catheter's elongated tip (see top right inset), serves as an emitter (sender), whereas the rear electrode can be used as a current sink. A detailed description of individual catheter configurations for electric imaging, due to particular electrode combinations, is given in the main text. During catheterization, the device will be fed over a 'guide wire' (silver), which supports and directs the catheter's movements.

ceivers) will enable acquisitions of dynamic electric images of high resolution. During plaque inspections, the catheter will be passed over a so-called guide wire (e.g., Tóth et al., 2015) (figure 9.14), which supports and directs the catheter's motions.

Besides purely bio-inspired strategies of electric image acquisition, the device may also perform others, i.e., 'impedance mappings' of plaques, to capture electric images in future studies. In doing so, its frontal sender would emit chirp signals, whereas the catheter's rear ring-electrode would act as a current sink and its two electrode rings' receivers as differential electrode pairs monitoring the electric emissions. Recent preliminary tests, in which our multi-electrode catheter had been used for impedance mappings of two (pig) coronary arteries with synthetic plaques or two (human) femoral artery explants with either heavy or no plaque burden, yielded distinctive plaque-evoked impedance patterns (Rau, 2013, in cooperation with M. Gottwald, J. Remig [St. Petrus community hospital Bonn] and D. Goltz [University hospital Bonn], unpublished data). Bio-inspired processing of such patterns (as electric images) may provide simple analytical cues for plaque inspections, which could be used in addition to those of amplitude, waveform and phase-shift images.

9.5 Conclusion

The study presented in this chapter suggests an electrolocation catheter system for critical inspections of plaques in coronary arteries. It applies dynamic (motion-based) and static electric imaging, bio-inspired by weakly electric fish *G. petersii*. Testing two prototypical versions of this system (by investigating synthetic plaques) showed a first proof of concept.

Dynamic electric imaging yields key image features that may principally be suitable for detections/classifications of low-to-high-risk plaques and did so for synthetic versions of such plaques. These simple cues (i.e., peak modulations of electric amplitude and waveform images and the amplitude images' relative slopes) rendered plaque analysis a computationally inexpensive task. Electric imaging of plaques was further improved by dynamic or static acquisitions of 2-D amplitude and waveform images, which indicate a plaque at individual portions of the artery wall (top, bottom, left or right). A future version of our catheter system may integrate the electric imaging principles mentioned above, i.e.,

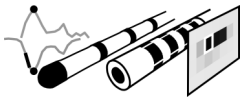

capture 2-D, dynamic/static electric images of (synthetic/real) plaques and identify their conditions by key image features (in follow-up studies).

Because our biomimetic catheter system basically requires just plain catheters and standard hardware, it has the potential to eventually provide a very cost-effective medical tool. It may thereby help to increase (catheter-based) determinations of low-to-high-risk plaque conditions in daily clinical practice, which is limited foremost by the high costs of current (ultrasound or optical) catheters (Benedek et al., 2016; Koskinas et al., 2016; Koskinas et al., 2018).

IV. General Discussion

10. Sensory ecology of the active electric sense

The active electric sense allows weakly electric fish to communicate, orient and forage without getting distracted by the murky, cluttered or rapid waters they inhabit (Crampton, 2019; Krahe, 2019). In addition, by operating in the absence of light, it enables the animals to lead a nocturnal life, hidden from diurnal predators (Crampton, 2019; Lissmann, 1963). From a general perspective, the adaptive advantages of the active electrosensory system are thus well understood. The specific perceptual mechanisms, however, that optimize it for the tasks above, are largely unknown.

One of the animals' most fundamental, yet unresolved, electrolocation skills, i.e., to judge other aquatic organisms by their complex electrical impedances, was investigated in this thesis via studies on species *G. petersii* (chapter 5, Gottwald et al., 2017a; chapter 6, Gottwald et al., 2018). They showed that, in doing so, these fish perceive electric colors (Budelli and Caputi, 2000), which they use to identify invertebrate prey (insect larvae) and, most likely, their further living targets. As almost all other weakly electric fish are also nocturnal invertebrate feeders (e.g., Crampton, 2019; Marrero and Winnemiller, 1993; Winemiller and Adite, 1997), they too may rely on electric-color sensing to occupy this ecological niche and solve similar electrolocation tasks as *G. petersii*. Although the skill has, so far, not been verified in other species, several indications for it can be inferred from previous studies. It is further supported by new analyses I conducted on the published data. Together, these findings are discussed, with respect to *G. petersii's* electric-color estimations, in section 10.1.

By sensing electric colors, actively electrolocating *G. petersii* employ a perceptual mechanism akin to color vision and, as outlined in section 10.2, they use several others (e.g., Hofmann et al., 2017; Pedraja et al., 2018; von der Emde et al., 1998) resembling visual ones. These examples suggest that active (electric) and passive (visual) sensing is optimally shaped by a variaty of similar perceptual strategies.

10.1 Electric-color sensing in and beyond *G. petersii*

Electric-color sensing, as shown in this thesis, enbales weakly electric fish *G. petersii* to find its prey (Gottwald et al., 2017a; Gottwald et al., 2018). Several of its perceptual advantages optimize the fish's active electric sense for prey recognitions and explain its

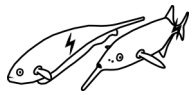

dominant role during foraging (Gottwald et al., 2018; von der Emde and Bleckmann, 1998).

Crucially, while scanning the soil, rocks or woody debris with its chin appendix (electroreceptive fovea) *G. petersii's* electric-color sensations are merely evoked by the capacitive prey insect larvae, hidden insight them, which, unlike their suddoundings, possess complex electrical impedances (Gottwald et al., 2018; Marrero and Winnemiller, 1993; Pinder, 1986; von der Emde and Schwarz, 2002). In addition, due to its unique electric color, the fish's primary prey (chironomids) clearly stands out from other, alltogether 'uniformly colored', secondary targets (ephemeropteran and trichopteran species) (Gottwald et al., 2018; Nwani et al., 2011). Unintentionally exposed by and (most likely) unable to manipulate their 'color-generating' electrical impedances the larvae hardly evade an electrolocating *G. petersii* nearby (Gottwald et al., 2018).

Besides prey insect larvae, electric colors also designate other types of animals *G. petersii* usually encounters, like fish (food competitors), weakly electric fish (potential mates/opponents) and also plants (usual hideouts) (Gottwald et al., 2017a; Gottwald et al., 2018). Hence, in addition to foraging, many situations may occur, where electric colors drive or promote the fish's actions (e.g., seeking shelter from bullies or predators, chasing off competitors, etc.).

Since most other African species (mormyirds) feature active electrosensory systems similar to *G. petersii's* (Bell et al., 1981; Caputi, 2017; Fortune and Chacron, 2011; Harder, 1968; McNamara et al., 2005), they too might rely on electric-color sensing for critical, instant detections of nearby organisms. Previous behavioral experiments already suggest mormyrids, with individual electrolocation pulses, to recognize insect larvae, plants and fishes by their complex (capacitive) impedances (Heiligenberg, 1973; von der Emde and Ringer, 1992). To do so, they capture the electric amplitude and waveform images capacitive objects evoke by modulating the pulses' amplitudes and waveforms locally across the electroreceptive fish skin. While both image types together convey a target's (complex) impedance, each of them is also shaped by the object's size, distance and position, i.e., its spatial features (Budelli and Caputi, 2000; Gottwald et al., 2017a; Gottwald et al., 2018, see chapters 5 and 6).

Because such properties vary for aquatic organisms, e.g., indiviudal prey larvae under inspection, their electric images are highly ambiguous. Consequently, fast and precise electrolocations of them could only be achieved with an impedance estimator that is easily

and unequivocally extracted from these images.

Electric color, as perceived by *G.petersii* (and which would be sensed by other pulse mormyrids the same way) provides all these qualities. It is already acquired by just one amplitude and waveform image *G. petersii* quickly obtains from a nearby position to its target. Furthermore, our findings suggest that, to calculate electric color, the fish merely combines the two images' peak modulations as a ratio. This simple routine accords with the structural/functional organization of the mormyrid brain (Bell et al., 1981; Fechner et al., 2018; Hollmann et al., 2016; McNamara et al., 2005; von der Emde and Engelmann, 2011) and demands, in principle, no elaborate central processing (Gottwald et al., 2017a). Most importantly, however, it yields electric colors as unambiguous impedance cues, designating basic types of aquatic organisms (prey larvae, [electric] fish, plants) irrespective of their spatial properties (chapters 5 and 6, Gottwald et al., 2017a; Gottwald et al., 2018). Electric-color sensing thereby exclusively matches the quick, selective and reliable identification responses of electrolocating *G. petersii* (Gottwald et al., 2018; von der Emde and Bleckmann, 1998) and other pulse mormyrids, seen, e.g., during foraging (personal observation from the lab; von der Emde, 1992).

Beyond Mormyrids, several South American fisches (gymnotids) might also perceive electric colors but with a convergent and more complex pulse-type electrosensory system (Caputi, 2017; Fortune and Chacron, 2011). Unlike their African counterparts, they generate electric signals by electric organs that are not restricted to their tails and activated region-wise and sequentially (e.g., Caputi, 1999). As a result, their pulses change in both amplitude and waveform along the fish skin, whereas, e.g., *G. petersii's* electric signal solely varies in its local amplitudes (Bastian, 1977; Caputi, 1999; Pusch et al., 2008). *G. petersii* also has just one type of epidermal electroreceptor organ for amplitude and waveform image acquisitions (Gottwald et al., 2017a; von der Emde and Bleckmann, 1992); pulse-type gymnotids several types and subtypes (Bastian, 1976; Bastian, 1977; Watson and Bastian, 1979), as extensively explored in species *Gymnotus omarorum* (Caputi and Aguilera, 2019; Caputi et al., 2008; Cilleruelo and Caputi, 2012; Rodríguez-Cattáneo et al., 2017). In further contrast to *G. petersii*, which aquires electric colors (unequivocally) from various target-to-skin positions (chapter 6, Gottwald et al., 2018), *G. omarorum* might do so merely with its electroreceptive fovea (snout region) (Aguilera et al., 2001; Caputi et al., 2008; Castelló et al., 2000; Sanguinetti-Scheck et al., 2011). Yet, the similar electrolocation characteristics of both fishes' foveal regions (Aguilera et al.,

2001; Castelló et al., 2000; Pusch et al., 2008) imply that potential electric colors perceived by *G. omarorum* (and its relatives) could serve as quick, simple and distinctive identifiers of invertebrate prey (and other organisms) as in *G. petersii* (Gottwald et al., 2018). Accordingly, pulse gymnotids lack complex electrolocation behaviours such as prey-directed scanning motions just like *G. petersii* (Nanjappa et al., 2010; von der Emde, 1992), which instead identifies prey larvae via electric colors.

Electric-color perception, however, appears not to be limited to pulse-type fish. New findings, (introduced below), suggest 'wave-type' fishes (Caputi, 2017; Fortune and Chacron, 2011), like the gymnotiform *Eigenmannias*, might employ an equivalent electrolocation strategy. During active electrolocation, they generate a continuous electric signal and obtain its local amplitude and phase (timing) with individual epidermal electroreceptor organs (Assad et al., 1998; Kashimori et al., 1996; Scheich et al., 1973; von der Emde, 1998). Both parameters are considerably modulated by capacitive targets (e.g., von der Emde, 1998), similar to local amplitudes and waveforms in pulse gymnotids or mormyrids. Thereby, roughly the same range of capacitive objects as in *G. omarorum* (Aguilera and Caputi, 2003; Caputi et al., 2008; Rodríguez-Cattáneo et al., 2017) or *G. petersii* (Gottwald et al., 2017a; von der Emde, 1990) elicits electric images in *Eigenmannia* (Fujita and Kashimori, 2010; von der Emde, 1998). Fujita's and Kaschimori's (2010) modeling study depicted such amplitude and phase images for the first (and yet only) time (see figure A.3.1A in appendix A.3 for examples).

To explore whether *Eigenmannia* would be able to extract electric-color cues off these images, I further analyzed the published image data (for details refer to figures A.3.1B and C). In line with electric-color estimations in *G. petersii*, the peak modulation ratios of the targets' two image types yielded electric colors, by which the objects could easily be distinguished. The analyses further showed that the electric color of a capacitive object, which is scaled either in its distance to the fish or its size, remains very stable. *Eigenmannia* species could therefore principally use this cue to unambiguously electrolocate their capacitive, most relevant targets.

In conclusion, the findings discussed in this section imply that African mormyrids (besides *G. petersii*) and South American gymnotids might selectively and reliably recognize invertebrate prey and other capacitive organisms by electric colors. While the fish use individual (i.e., pulse- or wave-type) and independently evolved electrolocation systems (Caputi, 2017; Crampton, 2019; Fortune and Chacron, 2011; Lavoué et al., 2012) to

perform these critical tasks, analogous and convergent mechanisms of electric-color perception seemingly allow them to do so most efficiently. No other electrolocation strategy, known so far, matches or would likewise enable the fishes' fast, precise prey indentifications and let them occupy their nocturnal invertivore niche.

To fully verify electric-color sensing as a common trait among weakly electric fish and understand its central, neuronal underpinnings, additional electric image recordings, behavioral assays and physiological experiments are needed. Novel approaches, e.g., for faster and more extensive electric image recordings (as suggested in the appendix, figure A.3.2) may further help to explore the skill in several mormyrid and gymnotid species.

10.2 Parallels of active electric and visual sensing strategies

Electric-color sensing in *G. petersii* resembles color perceptions of visually guided animals in serveal ways. Like them (e.g., Kelber et al., 2003), the fish acquires its 'color' cues by relating the information of individual receptor types as a ratio (chapters 5 and 6, Gottwald et al., 2017a; Gottwald et al., 2018). *G. petersii* thereby proposedly divides the peaks of amplitude and waveform images, it captures with its A and B type electroreceptors (Gottwald et al., 2017a; Gottwald et al., 2018). Similar to hues, e.g., in human color vision (e.g., Hansen et al., 2007), individual electric colors are defined, within their respective color space, as distinct color lines (Gottwald et al., 2018). Furthermore, like colors in visual detection tasks (Brown, 2003; Foster, 2011; Johnson and Mullen, 2016; Kelber and Jacobs, 2016; Romero et al., 2011), they selectively and reliably designate individual targets against their backgrounds, over distance and from various positions (around the fish), at which (electric) illuminations (by *G. petersii's* electric signals) vary (chapter 6, Gottwald et al., 2018).

While electric colors allow for fast and distinctive identifications of prey and, principally also, other types of relevant capacitive targets (i.e., plant hideouts, electric vs. non-electric fish), (Gottwald et al., 2018), they are not *G. petersii's* only impedance cues during active electrolocation. Interrestingly, when discriminating experimentally used dipole objects, the fish peforms object-directed scanning motions (von der Emde, 1992; von der Emde and Ronacher, 1994), in which it seems to additively combine the amplitude and waveform imformation of the received electric images (von der Emde and Ronacher, 1994).

The dynamic (i.e., motion-based) routine for object impedance evaluations presented in

this thesis (chapter 5, Gottwald et al., 2017a) matches *G. petersii's* electrolocation behavior above and could explain why the fish employs, situationally, another impedance-related cue to judge its capacitive targets. Briefly stated, the routine yields a 'calibrated' and thereby distance-invariant version of the peaks of an object's amplitude and waveform images (see chapter 5 for details). Added together they would provide an impedance estimator, which further depends on the object's size and shape (Gottwald et al., 2017a). Electric colors, on the other hand, already identify aquatic organisms and dipole objects, of characteristic shapes (or 'habiti'), unequivocally due to their complex impedances (Gottwald et al., 2017a; Gottwald et al., 2018). Hence, fish may rely on electric colors to recognize (natural) capacitive targets and on the other cue to further assess their impedances with respect to their sizes. This way, e.g., larger nearby fishes (potential opponents) appear electrically 'brighter' than smaller ones, which would label them as possible threats. Likewise, a certain plant, *G. petersii* might have choosen as home shelter, could be selected, among others of the same electric color, by its individual 'electric brightness'. Dipole objects, whose electric colors often differ from those of typical aquatic organisms (personal observation), seem to be recognized (von der Emde and Ronacher, 1994) primarily by this 'brightness' cue.

Also during vision, several animals rely on brightness information to find sufficient dwellings or to judge unfavorable or potentially risky targets (intruders and others). Herbivorous insects, for instance, use it for occupying feeding/housing sites of their plant hosts (Bian et al., 2020; Prokopy, 1983); prawns for choosing inconspicuous shelters (da Costa et al., 2020). Birds and insects show wariness and aversions towards bright and unpalatable prey (with a high luminance contrast) and noxious animals such as frogs or wasps seemingly convey stonger toxicity levels via brighter warning signs to predators (e.g., Halpin et al., 2021; Maan and Cummings, 2012; Prudic et al., 2006; Vidal-Cordero et al., 2012). Furthermore, the brightness of ornaments and other markings or collorations can indicate an opponent's quality and threat status to fishes, birds and monkeys (e.g., Lehtonen et al., 2015; Mateos and Carranza, 1997; Setchell and Wickings, 2005).

While brightness cues are usually perceived with a single type of photoreceptor (e.g., by bees, flies and proposedly birds and fishes), primates and humans do so by adding the inputs of two cone classes (in broad daylight) (e.g., Olsson et al., 2018; Osorio and Vorobyev, 2005). Similarly, as suggested above, *G. petersii's* electric-brightness sensations depend on summations of its A and B type electroreceptor information (i.e., the peaks of

amplitude and waveform images).

Besides its object recognitions, also the fish's electric depth perceptions resemble visual ones to various degrees. To judge object distance, e.g., from a nearby position, *G. petersii* determines the relative slope of a target's amplitude image (chapter 5, Gottwald et al., 2017a; von der Emde et al., 1998). During object approaches, the fish seems to further rely on the relative gradient between successive images as an additional depth estimator (Hofmann et al., 2017). Both cues effectively depict the 'blurring' of amplitude images, which increases the farther the targets evoking them are located from the fish. Since *G. petersii's* active electrosensory system does not have a focussing mechanism (e.g., von der Emde, 2006), electric images never get 'sharp' (even for very close targets).

In contrast, in several visual systems objects under fixation are sharply focused by a lense (Lazareva, 2017b). Targets out of the focal plane, however, appear blurred and become fuzzier with further distance from it (Lazareva, 2017b). Various animals and also humans utilize this 'defocus blur' in their depth sensations. To us humans it makes them more precise (far off fixation) (Held et al., 2012; Mather, 1997; Read, 2012). Jumping spiders and young oval squids deduce it as the relative 'fuzziness' from (blurry-to-sharp) target images to gauge the range to their prey (Chung and Marshall, 2014; Nagata et al., 2012). This is actually quite similar to *G. petersii's* estimations of rel. gradients from successively less and less blurred (electric) images when swimming towards a particular object. The squids also perform movements to gather their differently focused images (from separate retinal regions) (Chung and Marshall, 2014). Jumping spiders sense them, without motion, by consecutive retinal layers (at varying focal depths) (Nagata et al., 2012).

In addition to electric image blurring, also the speed by which electric images (of objects passed) move across *G. petersii's* electroreceptive skin is important for depth perceptions (Pedraja et al., 2018). It is faster for nearby than for more remote obstacles and assessed by the fish, e.g., for maintaining sufficient distances to them (i.e., centering behavior) (Pedraja et al., 2018).

Also humans and other sighted animals experience this 'motion-parallax' during vision. Here, it makes object images shift more rapidly (across the retina) the closer the objects are to (the focal plane of) the observer's eye (Kral, 2003; Lazareva, 2017a; Nawrot and Joyce, 2006). Visual parallax information is gatheterd (via head or full-body movements and eye motion [if applicable]), e.g., by birds and insects to judge proximities of landing sites, by insects maneuvering obstacles, in human depth sensations and likely those of further

animals (e.g., Kral, 2003; Lazareva, 2017a; Nawrot and Joyce, 2006; Srinivasan, 2011).
In conclusion, *G. petersii's* electric object recognitions (shown in this thesis) and electrical depth perceptions closely resemble visual ones. It detects food items by 'color' cues, judges particular targets (also) by their 'brightness' and determines proximities to objects of interest or obstacles via 'blur and parallax' estimations, like various sighted animals. This implies their visual and *G. petersii's* active electrosensory system(s) rely on similar 'computational strategies (e.g., Stevens, 2012)' to optimally solve analogous critical tasks. Given these examples, also other active versus passive senses may (in spite of different 'inputs, hardwares and algorithms (Stevens, 2012)') be shaped more broadly by such 'comprehensive' sensory concepts, as outlined in this section.

11. Biomimetics: The potential of active electrolocation devices

In recent years, active electrolocation of weakly electric fish has inspired several underwater machines, designed in biomimetic approaches (e.g., Bai et al., 2012; Bai et al., 2015; Dimble et al., 2014; Schwarz et al., 2001; Wang et al., 2017 etc.). These prototypes can principally conduct (short-range) maneuvers or object inspections, otherwise hardly attained with acoustic or optical sensors of robots and vehicles, especially in confined, cluttered or murky waters. Most of them, however, do not exactly mimic the fishes' electrolocation strategies, which, when fully understood and closely adapted, should render such devices more efficient and advantageous for a variety of applications.
In this thesis, active electrolocation cues of species *G. petersii* were investigated (chapters 5 and 6) and implemented into a prototypical 'electric camera' (chapter 8, Gottwald et al., 2019). Like the fish, it acquires simple analytical parameters from the electric images it captures of its targets, i.e., amplitude images of electrically merely resistive items (e.g., made of wood, metal and plastic) or amplitude and waveform images, evoked by capacitive aquatic organisms. Electric colors, derived from them, designate basic types of organisms, such as fish or plants (and certainly others), while inanimate objects (as mentioned above) lack these cues (Gottwald et al., 2019). Distances of objects, on the other hand, can be inferred by (amplitude) image blurring and their basic shapes by electric outlines, i.e., a novel image feature (Gottwald et al., 2019), which might also be used by *G. petersii* to gauge a target's contours, geometry and orientation (chapter 8). Given its object inspection abilities above, verified in this thesis' initial proof of concept (chapter 8), a fully

developed and automated (fresh or seawater) version of the electric camera could help improve challenging underwater operations and augment others.

In marine fish farms, for instance, regular monitoring of net cages is critical. Net holes account for partly major fish escapes, causing considerable economic costs, but also notable environmental issues, as escapees might transmit pathogens or parasites to feral fishes and disrupt wild gene pools (Atalah and Sanchez-Jerez, 2020; Jensen et al., 2010; Yeates et al., 2014). While often performed by divers, net inspections are getting transferred, more and more, to remotely operated or autonomous vehicles with (optical) cameras (e.g., Bjelland et al., 2015; Capocci et al., 2017; Paspalakis et al., 2020; Tao et al., 2018; Telfer et al., 2019).

Poor lighting conditions and murkier water (Price et al., 2015; Thorvaldsen et al., 2015), however, may impede such devices as well as visually guided divers and, situationally, require the use of additional light sources during inspections. This, in turn, stresses nearby fishes, which avoid human divers and bright aquatic machines (Kruusmaa et al., 2020). Since active electrolocation, as performed by the electric camera (Gottwald et al., 2019), works in clear-to-murky waters and the absence of light, a mature electric-camera robot would be able to reliably monitor a farm's net cages without disturbing the cultivated fish. The nettings, typically made of electrically insulating nylon or polyethylene (Reyes et al., 2020), should yield a strong electrical contrast to the conductive seawater (Culkin and Smith, 1980) and therefore holes within them effectively be captured and assed by electric (amplitude) images and their parameters (electric outlines and others). In addition, the device could detect entangled fish and attached, adverse fouling organisms (e.g., Reyes et al., 2020) as they by evoking electric colors would clearly stick out from regular net panels that appear electrically 'colorless' instead.

Beyond aquaculture inspections, a customized electric-camera sensor could also promote difficult and dangerous search operations such as finding diving victims in confined and murky caves (e.g., Buzzacott et al., 2017). Here, it would electrolocate a person simply by his/her diving gear, whose metallic (and conductive) components electrically contrast with the rocky (insulating) surroundings, as well as electric colors it should receive from the victim's partly exposed body parts. Further future uses cases may include explorations of radioactively (or otherwise) contaminated aquatic environments, in which active elctrolocation sensors could operate without getting impaired (Boyer and Lebastard, 2018; von der Emde, 2007).

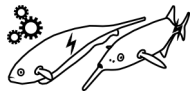

The other equipment refined in this thesis by mimicking *G. petersii's* electric imaging principles (chapters 5 and 6) is a medical catheter system (chapter 9, Gottwald et al., 2017b) to diagnose atherosclerotic plaques in the heart's coronary arteries (Libby et al., 2019; Virmani et al., 2006). The successful detections/identifications of synthetic 'low-to-high-risk' plaques performed with its prototypical electrolocation catheters (chapter 9) suggest it to be principally suitable for estimating coronary plaque conditions. To do so, it evaluates just few simple features of the plaque-evoked electric (amplitude and waveform) images it captures, i.e., their peaks plus (the amplitude images') relative slopes. Other computationally inexpensive analytical routines, recently explored (Gottwald et al., 2011; Rau, 2013), may further add to its current functions. Along with its plain catheters, optimized for extensive (motion-based) or quick (and stationary) plaque assessments (chapter 9, Gottwald et al., 2017b), this biomimetic approach has the potential to provide an effective, versatile and very cost-efficient diagnostic tool. Crucially, such a low-cost device could enhance especially high-risk plaque (Libby et al., 2019; Virmani et al., 2006) recognitions, which, in daily clinical practice, are not adequately achieved by usual angiography and limited foremost by the high costs of contemporary (optical or ultrasound) catheters (Batty et al., 2016; Benedek et al., 2016; Koskinas et al., 2016; Koskinas et al., 2018). With the ability to determine (and monitor) such plaques more frequently sudden and fatal cardiac arrests or heart attacks, as their most severe complications (Insull, 2009; Libby et al., 2019; Virmani et al., 2006), might be prevented in several patients (Koskinas et al., 2016; Koskinas et al., 2018).

Currently, also two other cardiovascular devices, loosely inspired by weakly electric fish, are either in development (Fuerst et al., 2016) or already clinically used (Stein et al., 2019), as outlined below. Fuerst and colleagues proposed a novel guidance system for catheter positioning, which could help reduce the amount of X-ray imaging performed for such tasks (Fuerst et al., 2016; Sutton et al., 2020). In their approach, bloodvessels to be passed during a catheterization get imaged, in advance, via computerized tomography (CT) to determine their inverse cross-sectional areas. These metrics, from along the vessels, depict traces with characteristic peaks or valleys due to each vessel's individual narrowings, widenings and bifurcations. In the (follow-up) intervention, a guiding instrument would be moved through the blood vessel tree, constantly scanning it with a weak electric signal and acquiring a voltage profile that, when matched to the traces above, determines the instrument's location, allowing to navigate it to desired positions a catheter should

subsequently be placed. The system has successfully been tested in simplified, synthetic blood vessels, porcine vessel explants and, in-vivo, in a swine (Fuerst et al., 2016; Sutton, 2017; Sutton et al., 2020). While in these exepriments mainly ordinary electrophysiology catheters served as the system's prototypical guiding instruments, it is now getting optimized for guide wires (Sutton, 2017), along which catheters are commonly directed and positioned during endovascular procedures (e.g., Tóth et al., 2015).

Most recently, Boston Scientific and its partners introduced a new ablation catheter to better treat heart rhythm disorders ('arrythmias'), caused by abnormal myocardial tissue (e.g., Stein et al., 2019; Wakilli, 2018). While such tissue gets lesioned and neutralized during ablation through catheter-based radio-frequency heating, ensuring a suffictient catheter-tissue contact and lesion creation can be challenging (Sulkin et al., 2018; Wakilli, 2018). To monitor these critical factors more precisely, Boston Scientific's catheter generates and senses a weak electric signal with several electrodes and thereby determines the local impedance of its surroundings (e.g., Sulkin et al., 2018). Preclinical experiments conducted with the device showed that it can convey reliable couplings with the myocardium, through higher measured impedances, but also formations of lager lesions, due to greater impedance drops it acquires in the ablation process (Garrott et al., 2020; Sulkin et al., 2018). Particular impedance changes may thus predict effective ablation and lesion progression, whereas values beyond that range should provide thresholds against adverse overablations (Garrott et al., 2020; Sulkin et al., 2018). Several clinical trials (e.g., Das et al., 2021; Martin et al., 2018; Münkler et al., 2020; Sasaki et al., 2020) currently help to determine these predictive markers (e.g., absolute or percentage impedance drops) to make future ablations more efficient and safer.

In conclusion, the biomimetic projects conducted in this thesis and by other research groups or companies, technically adapting active elelctrolocation of weakly electric fish, may provide advantageous and possibly transformative tools for industrial, medical and further tasks. With their potential to improve, e.g., diagnoses/treatments of cardiovascular diseases, the leading cause of (human) deaths worldwide (AHA, 2021; WHO, 2017), or to secure fish stocks in aquacutrures, the world's fastest growing food-production sector (FAO, 2018), future electrolocation devices (like the electric camera, catheter systems etc.) could have a positive and strong impact on society in various ways.

V. References

References

Aguilera, P. A. and Caputi, A. A. (2003). Electroreception in *G. carapo*: detection of changes in waveform of the electrosensory signals. *J. Exp. Biol.* **206**, 989-998.

Aguilera, P. A., Castelló, M. E. and Caputi, A. A. (2001). Electroreception in *Gymnotus Carapo*: Differences between self-generated and conspecific-generated signal carriers. *J. Exp. Biol.* **204**, 185–198.

AHA, American Heart Association (2021). 2021 Heart Disease and Stroke Statistics Update Fact Sheet - At-a-Glance. *Fact Sheet*.

Amer, K. O., Elbouz, M., Alfalou, A., Brosseau, C. and Hajjami, J. (2019). Enhancing underwater optical imaging by using a low-pass polarization filter. *Opt. Express* **27**, 621-643.

Amey-Özel, M. (2018). Das Schnauzenorgan des schwach elektrischen Fischs *Gnathonemus petersii*: Anatomie, neuronale Innervation und senso-motorische Integration. *PhD thesis,* Zoological Institute, University of Bonn, Bonn.

Assad, C., Rasnow, B. and Stoddard, P. K. (1999). Electric organ discharges and electric images during electrolocation. *J. Exp. Biol.* **202**, 1185–1193.

Assad, C., Rasnow, B., Stoddard, P. K. and Bower, J. M. (1998). The electric organ discharges of the gymnotiform fishes: II. *Eigenmannia*. *J. Comp. Physiol. A* **183**, 419–432.

Atalah, J. and Sanchez-Jerez, P. (2020). Global assessment of ecological risks associated with farmed fish escapes. *Glob. Ecol. Conserv.* **21**, e00842–1–10.

Athanasiou, L. S., Dimitrios, I. F. and Lampros, K. M. (2017). *Atherosclerotic Plaque Characterization Methods Based on Coronary Imaging*. London, UK: Elsevier Inc.

Azzopardi, P. and Cowey, A. (1993). Preferential representation of the fovea in the primary visual cortex. *Nature* **361**, 719–721.

Babineau, D., Lewis, J. E. and Longtin, A. (2007). Spatial acuity and prey detection in weakly electric fish. *PLoS Comput. Biol.* **3**, e38–402–411.

Bacelo, J., Engelmann, J., Hollmann, M., von der Emde, G. and Grant, K. (2008). Functional foveae in an electrosensory system. *J. Comp. Neurol.* **511**, 342–359.

Bai, Y., Neveln, I. D., Peshkin, M. and MacIver, M. A. (2016). Enhanced detection performance in electrosense through capacitive sensing. *Bioinspir. & Biomim.* **11**, 055001–1–11.

Bai, Y., Snyder, J. B., Peshkin, M. and MacIver, M. A. (2015). Finding and identifying simple objects underwater with active electrosense. *Int. J. Robot. Res.* **34**, 1255–1277.

Bai, Y., Snyder, J., Silverman, Y., Peshkin, M. and MacIver, M. A. (2012). Sensing capacitance of underwater objects in bio-inspired electrosense. *Proc. IEEE/RSJ Int. Conf. on Intelligent Robots and Systems (IROS) (Vilamoura, Portugal)* pp. 1467-1472.

Bar-Cohen, Y. (2005). Biomimetics: mimicking and inspired-by biology. *Proc. SPIE, Smart Structures and Materials 2005: Electroactive Polymer Actuators and Devices (EAPAD)* **5759**, 1–8.

Barthlott, W. and Neinhuis, C. (1997). Purity of the sacred lotus, or escape from contamination in biological surfaces. *Planta* **202**, 1–8.

Bass, A. H. (1986). Electric organs revisited. In *Electroreception* (eds. Bullock, T. H. and Heiligenberg, W.), pp. 13–70. New York: John Wiley & Sons Inc.

Bastian, J. (1976). Frequency response characteristics of electroreceptors in weakly electric fish (Gymnotoidei) with a pulse discharge. *J. Comp. Physiol. A* **112**, 165–180.

Bastian, J. (1977). Variations in the Frequency Response of Electroreceptors Dependent on Receptor Location in Weakly Electric Fish (Gymnotoidei) with a Pulse Discharge. *J. Comp. Physiol. A* **121**, 53–64.

Batty, J. A., Subba, S., Luke, P., Gigi, L. W. C., Sinclair, H. and Kunadian, V. (2016). Intracoronary Imaging in the Detection of Vulnerable Plaques. *Curr. Cardiol. Rep.* **18**, 28–1–12.

Bazeille, S., Lebastard, V. and Boyer, F. (2017a). Underwater Robots Equipped with Artificial Electric Sense for the Exploration of Unconventional Aquatic Niches. In *Marine Robotics and Applications* (eds. Jaulin, L., Caiti, A., Carreras, M., Creuze, V., Plumet, F., Zerr, B., and Billon-Coat, A.), pp. 29–50. Cham: Springer.

Bazeille, S., Lebastard, V., Lanneau, S. and Boyer, A. F. (2017b). Model based object localization and shape estimation using electric sense on underwater robots. *IFAC-PapersOnLine* **50**, 5047–5054.

Bedore, C. N., Kajiura, S. M. and Johnsen, S. (2015). Freezing behaviour facilitates bioelectric crypsis in cuttlefish faced with predation risk. *Proc. R. Soc. B* **282**, 20151886–1–8.

Bell, C. C. (1986). Electroreception in mormyrid fish: Central Physiology. In *Electroreception* (eds. Bullock, T. H. and Heiligenberg, W.), pp. 423–464. New York: John Wiley & Sons, Inc.

Bell, C. C. (1989). Sensory coding and corollary discharge effects in mormyrid electric fish. *J. Exp. Biol.* **146**, 229–253.

Bell, C. C. (1990a). Mormyromast electroreceptor organs and their afferent fibers in mormyrid fish. II. Intra-axonal recordings show initial stages of central processing. *J. Neurophysiol.* **63**, 303–318.

Bell, C. C. (1990b). Mormyromast electroreceptor organs and their afferent fibers in mormyrid fish. III. Physiological differences between two morphological types of fibers. *J. Neurophysiol.* **63**, 319–332.

References

Bell, C. C. and Russell, C. J. (1978). Termination of electroreceptor and mechanical lateral line afferents in the mormyrid acousticolateral area. *J. Comp. Neurol.* **182**, 367–382.

Bell, C. C. and Szabo, T. (1986). Electroreception in mormyrid fish: Central Anatomy. In *Electroreception* (eds. Bullock, T. H. and Heiligenberg, W.), pp. 375–421. New York: John Wiley & Sons, Inc.

Bell, C. C., Caputi, A. and Grant, K. (1997). Physiology and plasticity of morphologically identified cells in the mormyrid electrosensory lobe. *J. Neurosci.* **17**, 6409–6423.

Bell, C. C., Finger, T. E. and Russell, C. J. (1981). Central connections of the posterior lateral line lobe in mormyrid fish. *Exp. Brain. Res.* **42**, 9–22.

Bell, C. C., Zakon, H. and Finger, T. E. (1989). Mormyromast electroreceptor organs and their afferent fibers in mormyrid fish: I. Morphology. *J. Comp. Neurol.* **286**, 391–407.

Bell, C., Bradbury, J. and Russell, C. (1976). The electric organ of a mormyrid as a current and voltage source. *J. Comp. Physiol. A* **110**, 65–88.

Benda, J., Grewe, J. and Krahe, R. (2013). Neural Noise in Electrocommunication: From Burden to Benefits. In *Animal Communication and Noise* (ed. Brumm, H.), pp. 331–372. Berlin, Heidelberg: Springer Berlin Heidelberg.

Benedek, T., Mester, A., Benedek, A., Rat, N., Opincariu, D. and Chițu, M. (2016). Assessment of Coronary Plaque Vulnerability in Acute Coronary Syndromes using Optical Coherence Tomography and Intravascular Ultrasound. A Systematic Review. *J. C. E.* **2**, 173–184.

Bennett, M. V. L. (1971a). Electric organs. In *Fish Physiology, vol. V* (eds. Hoar, W. S. and Randal, D. J.), pp. 346–491. New York: Academic Press.

Bennett, M. V. L. (1971b). Electroreception. In *Fish Physiology, vol. V* (eds. Hoar, W. S. and Randall, D. J.), pp. 493–574. New York: Academic Press.

Bian, L., Cai, X. M., Luo, Z. X., Li, Z. Q. and Chen, Z. M. (2020). Foliage Intensity is an Important Cue of Habitat Location for *Empoasca onukii*. *Insects* **11**, 426–1–16.

Bjelland, H. V., Føre, M., Lader, P., Kristiansen, D., Holmen, I. M., Fredheim, A., Grøtli, E. I., Fathi, D. E., Oppedal, F., Utne, I. B., et al. (2015). Exposed aquaculture in Norway: Technologies for robust operations in rough conditions. *Proc. OCEANS 2015 MTS/IEEE Washington (OCEANS) (Washington, DC, USA) pp.* 1–10.

Bott, R. (2014). Vermessung und Parametrisierung elektrischer Bilder an unterschiedlichen Hautregionen von *Gnathonemus petersii*. *Projektarbeit,* Zoological Institute, University of Bonn, Bonn.

Bourantas, C. V., Garcia-Garcia, H. M., Torii, R., Zhang, Y.-J., Westwood, M., Crake, T. and Serruys, P. W. (2016). Vulnerable plaque detection: an unrealistic quest or a feasible objective with a clinical value? *Heart* **102**, 581–589.

Boyer, F. and Lebastard, V. (2018). Electric sensing for underwater navigation. In *Living Mashines: A handbook of research in biomimetics and biohybrid systems* (eds. Prescott, T. J., Lepora, N., and Verschure, P. F. M. J.) , pp. 176–181. Oxford: Oxford University Press.

Bringmann, A. (2019). Structure and function of the bird fovea. *Anat. Histol. Embryol.* **101**, 2611–2624.

Brown, R. (2003). Background and illuminants: The yin and yang of colour constancy. In *Colour perception: Mind and the physical world* (eds. Mausfeld, R. and Heyer, D.), pp. 247–272. Oxford: Oxford University Press.

Bruns (1971). Elektrisches Organ von *Gnathonemus (Mormyridae)*. *Cell Tissue Res.* **122**, 538–563.

Budelli, R. and Caputi, A. A. (2000). The electric image in weakly electric fish: perception of objects of complex impedance. *J. Exp. Biol.* **203**, 481–492.

Budelli, R., Caputi, A., Gomez, L., Rother, D. and Grant, K. (2002). The electric image in *Gnathonemus petersii*. *J. Physiol. Paris* **96**, 421–429.

Burke, A. P., Kolodgie, F. D., Farb, A., Weber, D. K., Malcom, G. T., Smialek, J. and Virmani, R. (2001). Healed plaque ruptures and sudden coronary death: evidence that subclinical rupture has a role in plaque progression. *Arterioscler. Thromb. Vasc. Biol.* **103**, 934–940.

Buzzacott, P., Nelson, C., Hill, K. and Hires, L. (2017). Recovery of deceased scuba divers from within flooded subterranean caves. *Forensic. Sci. Int.* **275**, 167–170.

Canny, J. (1986). A computational approach to edge detection. *IEEE Trans. Pattern Anal. Mach. Intell.* **8**, 679–698.

Capocci, R., Dooly, G., Omerdić, E., Coleman, J., Newe, T. and Toal, D. (2017). Inspection-Class Remotely Operated Vehicles—A Review. *J. Mar. Sci. Eng.* **5**, 13–1–32.

Caputi, A. A. (1999). The electric organ discharge of pulse gymnotiforms: the transformation of a simple impulse into a complex spatio-temporal electromotor pattern. *J. Exp. Biol.* **202**, 1229–1241.

Caputi, A. A. (2017). Active Electroreception in Weakly Electric Fish. *Oxford research enceclopedias: Neuroscience,* pp. 1-29. Oxford University Press.

Caputi, A. A. and Aguilera, P. A. (2019). Encoding phase spectrum for evaluating "electric qualia." *J. Exp. Biol.* **222**, 1–10.

References

Caputi, A. A. and Budelli, R. (2006). Peripheral electrosensory imaging by weakly electric fish. *J. Comp. Physiol. A* **192**, 587–600.

Caputi, A. A., Aguilera, P. A. and Pereira, A. C. (2011). Active Electric Imaging: Body-Object Interplay and Object's 'Electric Texture'. *PLoS ONE* **6**, e22793–1–11.

Caputi, A. A., Budelli, R., Grant, K. and Bell, C. C. (1998). The electric image in weakly electric fish: physical images of resistive objects in *Gnathonemus petersii*. *J. Exp. Biol.* **201**, 2115–2128.

Caputi, A. A., Castelló, M. E., Aguilera, P. A., Pereira, C., Nogueira, J., Rodríguez-Cattáneo, A. and Lezcano, C. (2008). Active electroreception in *Gymnotus omari*: Imaging, object discrimination, and early processing of actively generated signals. *J. Physiol. Paris* **102**, 256–271.

Caputi, A. A., Castelló, M. E., Aguilera, P. and Trujillo-Cenóz, O. (2002). Electrolocation and electrocommunication in pulse gymnotids: signal carriers, pre-receptor mechanisms and the electrosensory mosaic. *J. Physiol. Paris* **96**, 493–505.

Castelló, M. E., Aguilera, P. A., Trujillo-Cenóz, O. and Caputi, A. A. (2000). Electroreception in *Gymnotus carapo*: Pre-receptor processing and the distribution of electroreceptor types. *J. Exp. Biol.* **203**, 3279–3287.

Chen, L., House, J. L., Krahe, R. D. and Nelson, M. E. (2004). Modeling signal and background components of electrosensory scenes. *J. Comp. Physiol. A* **191**, 331–345.

Cheng, J. M., Garcia-Garcia, H. M., de Boer, S. P. M., Kardys, I., Heo, J. H., Akkerhuis, K. M., Oemrawsingh, R. M., van Domburg, R. T., Ligthart, J., Witberg, K. T., et al. (2014). In vivo detection of high-risk coronary plaques by radiofrequency intravascular ultrasound and cardiovascular outcome: results of the ATHEROREMO-IVUS study. *Eur. Heart J.* **35**, 639–647.

Chung, W.-S. and Marshall, J. (2014). Range-finding in squid using retinal deformation and image blur. *Curr. Biol.* **24**, R64–R65.

Cilleruelo, E. R. and Caputi, A. A. (2012). Encoding electric signals by *Gymnotus omarorum*: Heuristic modeling of tuberous electroreceptor organs. *Brain Res.* **1434**, 102–114.

Collin, S. P. and Whitehead, D. (2004). The functional roles of passive electroreception in non-electric fishes. *Animal Biol.* **54**, 1–25.

Couldridge, V. and Alexander, G. J. (2002). Color patterns and species recognition in four closely related species of Lake Malawi cichlid. *Behav. Ecol.* **13**, 59–64.

Covey, E. (2005). Neurobiological specializations in echolocating bats. *Anat. Rec. A Discov. Mol. Cell Evol. Biol.* **287**, 1103–1116.

Crampton, W. G. R. (2011). An Ecological Perspective on Diversity and Distributions. In *Historical Biogeography of Neotropical Freshwater Fishes* (eds. Albert, J. S. and Reis, R. E.), pp. 165–189. California: University of California Press, Ltd.

Crampton, W. G. R. (2019). Electroreception, electrogenesis and electric signal evolution. *J. Fish Biol.* **95**, 92–134.

Cronin, T. W. and Bok, M. J. (2016). Photoreception and vision in the ultraviolet. *J. Exp. Biol.* **219**, 2790–2801.

Cronin, T. W., Johnsen, S., Marshall, N. J. and Warrant, E. J. (2014). *Visual Ecology*. Princeton, USA: Princeton University Press.

Culkin, F. and Smith, N. (1980) Determination of the concentration of potassium chloride solution having the same electrical con- ductivity, at 15 °C and infinite frequency, as standard seawater of salinity 35.0000‰ (Chlorinity 19.37394‰). *IEEE J. Ocean. Eng.* **5,** 22–23.

Czech-Damal, N. U., Dehnhardt, G., Manger, P. and Hanke, W. (2012). Passive electroreception in aquatic mammals. *J. Comp. Physiol. A* **199**, 555–563.

da Costa, F. P., Arruda, M. F., Ribeiro, K. and Pessoa, D. M. A. (2020). Influence of color and brightness on ontogenetic shelter preference by prawns (Macrobrachium rosenbergii). *bioRxiv* doi: 10.1101/2020.11.05.368035.

Das, M., Luik, A., Shepherd, E., Sulkin, M., Laughner, J., Oesterlein, T., Duffy, E., Meyer, C., Jais, P., Duchateau, J., et al. (2021). Local catheter impedance drop during pulmonary vein isolation predicts acute conduction block in patients with paroxysmal atrial fibrillation: initial results of the LOCALIZE clinical trial. *Europace* **22**, 664–11–10.

Derbin, C. (1974). Ultrastructure of the ampullary receptor organs in a mormyrid fish, *Gnathonemus petersii*. III. *J. Ultrastruct. Res.* **46**, 254–267.

Derbin, C. and Szabo, T. (1968). Ultrastructure of an Electroreceptor (Knollenorgan) in the Mormyrid Fish *Gnathonemus petersii*. I. *J. Ultrastruct. Res.* **22**, 469–484.

Detto, T. (2007). The fiddler crab *Uca mjoebergi* uses colour vision in mate choice. *Proc. R. Soc. B* **274**, 2785–2790.

Dimble, K. D., Faddy, J. M. and Humbert, J. S. (2014). Electrolocation-based underwater obstacle avoidance using wide-field integration methods. *Bioinspir. & Biomim.* **9**, 016012–1–13.

Duarte, R. C., Flores, A. A. V. and Stevens, M. (2017). Camouflage through colour change: mechanisms, adaptive value and ecological significance. *Philos. Trans. R. Soc. B Biol. Sci.* **372**, 20160342–1–8.

Engelmann, J., Bacelo, J., van den Burg, E. and Grant, K. (2006). Sensory and motor effects of etomidate anesthesia. *J. Neurophysiol.* **95**, 1231–1243.

Engelmann, J., Gertz, S., Goulet, J., Schuh, A. and von der Emde, G. (2010). Coding of Stimuli by Ampullary Afferents in *Gnathonemus petersii*. *J. Neurophysiol.* **104**, 1955–1968.

Esch, H. E. and Burns, J. E. (1995). Honeybees use optic flow to measure the distance of a food source. *Naturwissenschaften* **82**, 38–40.

FAO, Food and Agriculture Organization of the United Nations (2018). The State of World Fisheries and Aquaculture 2018 - Meeting the Sustainable Developement Goals. *Periodical*.

Fechler, K. (2016). Die Analyse komplexer Szenen während der aktiven Elektroortung bei *Gnathonemus Petersii*: Objekterkennung, räumliches Auflösungsvermögen und lokomotorisches Verhalten. *PhD thesis,* Zoological Institute, University of Bonn, Bonn.

Fechler, K. and von der Emde, G. (2012). Figure-ground separation during active electrolocation in the weakly electric fish, *Gnathonemus petersii*. *J. Physiol. Paris* **107**, 72–83.

Fechler, K., Holtkamp, D., Neusel, G., Sanguinetti-Scheck, J. I., Budelli, R. and von der Emde, G. (2012). Mind the gap: the minimal detectable separation distance between two objects during active electrolocation. *J. Fish Biol.* **81**, 2255–2276.

Fechner, S., Grant, K., von der Emde, G. and Engelmann, J. (2018). Physiological evidence of sensory integration in the electrosensory lateral line lobe of *Gnathonemus petersii*. *PLoS ONE* **13**, e0194347–1–17.

Fortune, E. S. and Chacron, M. J. (2011). Physiology of Tuberous Electrosensory Systems. In *Encyclopedia of fish physiology: from genome to environment* (ed. Farrell, A. P.), pp. 366–374. San Diego: Academic press.

Foster, D. H. (2011). Color constancy. *Vision Res.* **51**, 674–700.

Fuerst, B., Sutton, E. E., Ghotbi, R., Cowan, N. J. and Navab, N. (2016). Bioelectric navigation: A new paradigm for intravascular device guidance. *Proc. Int. Conf. on Medical Image Computing and Computer-Assisted Intervention (MICCAI) (Athens, Greece)* pp. 474–481.

Fujita, K. and Kashimori, Y. (2010). Modeling the electric image produced by objects with complex impedance in weakly electric fish. *Biol. Cybern.* **103**, 105–118.

Fujita, K. and Kashimori, Y. (2019). Representation of object's shape by multiple electric images in electrolocation. *Biol. Cybern.* **113**, 239–255.

Gardner, C., Tan, H., Hull, E., Lisauskas, J., Sum, S., Meese, T., Jiang, C., Madden, S., Caplan, J. and Burke, A. (2008). Detection of Lipid Core Coronary Plaques in Autopsy Specimens With a Novel Catheter-Based Near-Infrared Spectroscopy System. *JACC Cardiovasc. Imaging* **1**, 638–648.

Garrott, K. E., Lehn, L., Gams, A. and Hamann, J. (2020). Intra-lesion temperature rise and local impedance drop predictive of lesion growth on RF ablation catheter with mini electrodes. *Heart Rhythm **17**,* S192-S193.

Gebhardt, K., Böhme, M. and von der Emde, G. (2012). Electrocommunication behaviour during social interactions in two species of pulse-type weakly electric fishes (Mormyridae). *J. Fish Biol.* **81**, 2235–2254.

Gottwald, M. (2010). Katheterbasierte Vermessung elektrischer Bilder im Arteriosklerosemodell. *Diploma Thesis,* Zoological Institute, University of Bonn, Bonn.

Gottwald, M. and von der Emde, G. (2013). Bio-Inspired Active Electrolocation Sensors for Inspection of Tube Systems. *Adv. Sci. Technol.* **84**, 45–50.

Gottwald, M., Bott, R. A. and von der Emde, G. (2017a). Estimation of distance and electric impedance of capacitive objects in the weakly electric fish *Gnathonemus petersii*. *J. Exp. Biol.* **220**, 3142–3153.

Gottwald, M., Herzog, H. and von der Emde, G. (2019). A bio-inspired electric camera for short-range object inspection in murky waters. *Bioinspir. & Biomim.* **14**, 035002–1–10.

Gottwald, M., Matuschek, A. and von der Emde, G. (2017b). An active electrolocation catheter system for imaging and analysis of coronary plaques. *Bioinspir. & Biomim.* **12**, 015002–1–17.

Gottwald, M., Mayekar, K., Reiswich, V., Bousack, H., Damalla, D., Biswas, S., Metzen, M. G. and von der Emde, G. (2011). Inspection and analysis of the walls of fluid filled tubes by active electrolocation: a biomimetic approach. *Proc. SPIE, Bioinspiration, Biomimetics, and Bioreplication* **7975**, 797510–1–15.

Gottwald, M., Singh, N., Haubrich, A. N., Regett, S. and von der Emde, G. (2018). Electric-Color Sensing in Weakly Electric Fish Suggests Color Perception as a Sensory Concept beyond Vision. *Curr. Biol.* **28**, 3648–3658.

Gómez-Sena, L., Pedraja, F., Sanguinetti-Scheck, J. I. and Budelli, R. (2014). Computational modeling of electric imaging in weakly electric fish: Insights for physiology, behavior and evolution. *J. Physiol. Paris* **108**, 112–128.

Gregersen, I. and Halvorsen, B. (2018). Inflammatory Mechanisms in Atherosclerosis. In *Atherosclerosis - Yesterday, Today and Tomorrow* (ed. Gianturco, L.), pp. 31–45. London: IntechOpen.

Grzesiak, A., Becker, R. and Verl, A. (2011). The bionic handling assistant: a success story of additive manufacturing. *Assembly Autom.* **31**, 329–333.

Halpin, C. G., Penacchio, O., Lovell, P. G., Cuthill, I. C., Harris, J. M., Skelhorn, J. and Rowe, C. (2021). Pattern contrast influences wariness in naïve predators towards aposematic patterns. *Sci. Rep.* **10**, 9246–1–8.

Hansen, T., Walter, S. and Gegenfurtner, K. R. (2007). Effects of spatial and temporal context on color categories and color constancy. *J. Vis.* **7**, 1–15.

Harder, W. (1968). Die Beziehungen zwischen Elektrorezeptoren, Elektrischem Organ, Seitenlinienorganen und Nervensystem bei den Mormyridae (Teleostei, Pisces). *J. Vergl. Physiol.* **59**, 272–318.

Harder, W., Schief, A. and Uhlemann, H. (1964). Zur Funktion des elektrischen Organs von *Gnathonemus petersii* (Gthr. 1862)(Mormyriformes, Teleostei). *J. Comp. Physiol. A* **48**, 302–331.

Harkness, J. M. (2002). In Appreciation – A Lifetime of Connections: Otto Herbert Schmitt, 1913 – 1998. *Phys. Perspect.* **4**, 456–490.

Haubrich, A. N. (2015). Formerkennung in der aktiven Elektroortung bei *G. petersii*. *Projektarbeit,* Zoological Institute, University of Bonn, Bonn.

Heiligenberg, W. (1973). Electrolocation of objects in the electric fish *Eigenmannia* (Rhamphichthyidae, Gymnotoidei). *J. Comp. Physiol. A* **87**, 137–164.

Heiligenberg, W. (1975). Theoretical and experimental approaches to spatial aspects of electrolocation. *J. Comp. Physiol. A* **103**, 247–272.

Held, R. T., Cooper, E. A. and Banks, M. S. (2012). Blur and disparity are complementary cues to depth. *Curr. Biol.* **22**, 426–431.

Henninger, J., Krahe, R., Kirschbaum, F., Grewe, J. and Benda, J. (2018). Statistics of Natural Communication Signals Observed in the Wild Identify Important Yet Neglected Stimulus Regimes in Weakly Electric Fish. *J. Neurosci.* **38**, 5456–5465.

Hofmann, V., Geurten, B. R. H., Sanguinetti-Scheck, J. I., Gómez-Senna, L. and Engelmann, J. (2014). Motor patterns during active electrosensory acquisition. *Front. Behav. Neurosci.* 00186–1–13.

Hofmann, V., Sanguinetti-Scheck, J. I., Gómez-Sena, L. and Engelmann, J. (2017). Sensory flow as a basis for a novel distance cue in freely behaving electric fish. *J. Neurosci.* **37**, 302–312.

Hofmann, V., Sanguinetti-Scheck, J. I., Gómez-Sena, L. and Engelmann, J. (2012). From static electric images to electric flow: Towards dynamic perceptual cues in active electroreception. *J. Physiol. Paris* **107**, 95–106.

Hofmann, V., Sanguinetti-Scheck, J. I., Künzel, S., Geurten, B., Gómez-Sena, L. and Engelmann, J. (2013). Sensory flow shaped by active sensing: sensorimotor strategies in electric fish. *J. Exp. Biol.* **216**, 2487–2500.

Hollmann, M., Engelmann, J. and von der Emde, G. (2008). Distribution, density and morphology of electroreceptor organs in mormyrid weakly electric fish: anatomical investigations of a receptor mosaic. *J. Zool.* **276**, 149–158.

Hollmann, V., Hofmann, V. and Engelmann, J. (2016). Somatotopic map of the active electrosensory sense in the midbrain of the mormyrid *Gnathonemus petersii*. *J. Comp. Neurol.* **524**, 2479–2491.

Hopkins, C. D. (1988). Neuroethology of electric communication. *Annu. Rev. Neurosci.* **11**, 497–535.

Hölker, F. and Stief, P. (2005). Adaptive behaviour of chironomid larvae (*Chironomus riparius*) in response to chemical stimuli from predators and resource density. *Behav. Ecol. Sociobiol.* **58**, 256–263.

Humbert, J. S. and Hyslop, A. M. (2010). Bioinspired Visuomotor Convergence. *IEEE Trans. Robot.* **26**, 121–130.

Hung, C.-C., Tsao, S.-C., Huang, K.-H., Jang, J.-P., Chang, H.-K. and Dobbs, F. C. (2016). A highly sensitive underwater video system for use in turbid aquaculture ponds. *Sci. Rep.* **6**, 31810–1–7.

Hurlbert, A. (2007). Colour constancy. *Curr. Biol.* **17**, R906–R907.

Hwang, J., Jeong, Y., Park, J. M., Lee, K. H., Hong, J. W. and Choi, J. (2015). Biomimetics: forecasting the future of science, engineering, and medicine. *Int. J. Nanomed.* **10**, 5701–5713.

Insull, W. (2009). The Pathology of Atherosclerosis: Plaque Development and Plaque Responses to Medical Treatment. *Am. J. Med* **122**, S3–14.

Jensen, Ø., Dempster, T., Thorstad, E. B., Uglem, I. and Fredheim, A. (2010). Escapes of fishes from Norwegian sea-cage aquaculture: causes, consequences and prevention. *Aquac. Environ. Interact.* **1**, 71–83.

Johnson, E. N. and Mullen, K. T. (2016). Color in the Cortex. In *Human Color Vision* (eds. Kremers, J., Baraas, R. C., and Marshall, N. J.), pp. 189–217. New York: Springer.

Kashimori, Y., Goto, M. and Kambara, T. (1996). Model of P- and T-Electroreceptors of Weakly Electric Fish. *Biophys. J.* **70**, 2513–2526.

Kawamura, G., Bagarinao, T. U., Asmad, M. F. B. and Lim, L.-S. (2017). Food colour preference of hatchery-reared juveniles of African catfish *Clarias gariepinus*. *Appl. Anim. Behav. Sci.* **196**, 119–122.

Kelber, A. (2016). Colour in the eye of the beholder: receptor sensitivities and neural circuits underlying colour opponency and colour perception. *Curr. Opin. Neurobiol.* **41**, 106–112.

Kelber, A. and Jacobs, G. H. (2016). Evolution of Color Vision. In *Human Color Vision* (eds. Kremers, J., Baraas, R. C., and Marshall, N. J.), pp. 317–354. New York: Springer.

Kelber, A., Vorobyev, M. and Osorio, D. (2003). Animal colour vision - behavioural tests and physiological concepts. *Biol. Rev.* **78**, 81–118.

Knechtges, L. (2018). Shape discrimination in weakly electric fish: local or global cues? *Master's thesis,* Zoological Institute, University of Bonn, Bonn.

References

Knudsen, E. I. (1975). Spatial aspects of the electric fields generated by weakly electric fish. *J. Comp. Physiol. A* **99**, 103–118.

Koskinas, K. C., Nakamura, M., Räber, L., Colleran, R., Kadota, K., Capodanno, D., Wijns, W., Akasaka, T., Valgimigli, M., Guagliumi, G., et al. (2018). Current Use of Intracoronary Imaging in Interventional Practice — Results of a European Association of Percutaneous Cardiovascular Interventions (EAPCI) and Japanese Association of Cardiovascular Interventions and Therapeutics (CVIT) Clinical Practice Survey —. *Circ. J.* **82**, 1360–1368.

Koskinas, K. C., Ughi, G. J., Windecker, S., Tearney, G. J. and Räber, L. (2016). Intracoronary imaging of coronary atherosclerosis: validation for diagnosis, prognosis and treatment. *Eur. Heart J.* **37**, 524–535.

Krahe, R. (2019). Evolutionary Drivers of Electric Signal Diversity. In *Electroreception Fundamental Insights from Comparative Approaches (Springer Handbook of Auditory Research)*(eds. Carlson, B. A., Sisneros, J. A., Popper, A. N., and Fay, R. R.), pp. 191–226. New York: Springer.

Kral, K. (2003). Behavioural–analytical studies of the role of head movements in depth perception in insects, birds and mammals. *Behav. Process.* **64**, 1–12.

Kreysing, M., Pusch, R., Haverkate, D., Landsberger, M., Engelmann, J., Ruiter, J., Mora-Ferrer, C., Ulbricht, E., Grosche, J., Franze, K., et al. (2012). Photonic crystal light collectors in fish retina improve vision in turbid water. *Science* **336**, 1700–1703.

Kruusmaa, M., Gkliva, R., Tuhtan, J. A., Tuvikene, A. and Alfredsen, J. A. (2020). Salmon behavioural response to robots in an aquaculture sea cage. *R. Soc. Open Sci.* **7**, 191220–1–14.

Lavoué, S., Miya, M., Arnegard, M. E., Sullivan, J. P., Hopkins, C. D. and Nishida, M. (2012). Comparable Ages for the Independent Origins of Electrogenesis in African and South American Weakly Electric Fishes. *PLoS ONE* **7**, e36287–1–18.

Lazareva, O. (2017a). Motion Parallax. In *Encyclopedia of evolutionary psychological science* (eds. Shackelford, T. K. and Weekes-Shackelford, V. A.), pp. 1–3. New York: Springer.

Lazareva, O. (2017b). Depth Perception. In *Encyclopedia of evolutionary psychological science* (eds. Shackelford, T. K. and Weekes-Shackelford, V. A.), pp. 1–6. New York: Springer.

Lehtonen, T. K., Sowersby, W., Gagnon, K. and Wong, B. B. M. (2015). Cichlid Fish Use Coloration as a Cue to Assess the Threat Status of Heterospecific Intruders. *Am. Nat.* **186**, 547–552.

Li, M. E., Wa, K. and Gerber, T. (2018). Contemporary Use of Intracoronary Imaging in Percutaneous Coronary Intervention. *EMJ Cardiol.* **6**, 64–74.

Libby, P., Buring, J. E., Badimon, L., Hansson, G. K., Deanfield, J., Bittencourt, M. S., Tokgözoğlu, L. and Lewis, E. F. (2019). Atherosclerosis. *Nat. Rev. Dis. Primers* **5**, 56–1–18.

Lissmann, H. W. (1958). On the function and evolution of electric organs in fish. *J. Exp. Biol.* **35**, 156–191.

Lissmann, H. W. (1963). Electric Location by Fishes. *Scient. Am.* **208**, 50–59.

Lissmann, H. W. and Machin, K. E. (1958). The Mechanism of Object Location in *Gymnarchus Niloticus* and Similar Fish. *J. Exp. Biol.* **35**, 451–486.

Liu, F., Han, P., Wei, Y., Yang, K., Huang, S., Li, X., Zhang, G., Bai, L. and Shao, X. (2018). Deeply seeing through highly turbid water by active polarization imaging. *Opt. Lett.* **43**, 4903-4906.

Lu, H., Li, Y., Zhang, L. and Serikawa, S. (2015). Contrast enhancement for images in turbid water. *J. Opt. Soc. Am. A* **32**, 886–893.

Lunau, K. and Maier, E. J. (1995). Innate colour preferences of flower visitors. *J. Comp. Physiol. A* **177**, 1–19.

Maan, M. E. and Cummings, M. E. (2012). Poison Frog Colors Are Honest Signals of Toxicity, Particularly for Bird Predators. *Am. Nat.* **179**, E1–14.

Maler, L., Karten, H. J. and Bennett, M. V. (1973). The central connections of the posterior lateral line nerve of *Gnathonemus petersii*. *J. Comp. Neurol.* **151**, 57–66.

Marrero, C. and Winnemiller, K. O. (1993). Tube-snouted gymnotiform and mormyriform fishes: convergence of a specialized foraging mode in teleosts. *Environ. Biol. Fisch.* **38**, 209–309.

Marshall, J. and Cronin, T. W. (2011). Polarisation vision. *Curr. Biol.* **21**, R101–R105.

Martin, C. A., Martin, R., Gajendragadkar, P. R., Maury, P., Takigawa, M., Cheniti, G., Frontera, A., Kitamura, T., Duchateau, J., Vlachos, K., et al. (2018). First clinical use of novel ablation catheter incorporating local impedance data. *J. Cardiovasc. Electrophysiol.* **29**, 1197–1206.

Mateos, C. and Carranza, J. (1997). The role of bright plumage in male-male interactions in the ring-necked pheasant. *Anim. Behav.* **54**, 1205–1214.

Mather, G. (1997). The use of image blur as a depth cue. *Perception* **26**, 1147–1158.

Matuschek, A. (2014). Entwicklung und Vermessung eines biologischen arteriosklerotischen Korrelats mit Hilfe eines bionischen Elektroortungs-Katheters. *Bachelor's thesis.* Zoological Institute, University of Bonn, Bonn.

Mayekar, K., Damalla, D., Gottwald, M., Bousack, H. and von der Emde, G. (2011). Characterization of a Bionic Electrolocation Sensor using Finite Element Modeling. *IEEE Sensors 2011 Conf. (Limerick, Ireland)* pp. 978–981.

Mayekar, K., Damalla, D., Gottwald, M., Bousack, H. and von der Emde, G. (2012). A multi-electrode biomimetic electrolocation sensor. *Proc. SPIE, Bioinspiration, Biomimetics, and Bioreplication* **8339**, 83390A–1–11.

McNamara, A. M., Denizot, J.-P. and Hopkins, C. D. (2005). Comparative anatomy of the electrosensory lateral line lobe of mormyrids: the mystery of the missing map in the genus Stomatorhinus (family: Mormyridae). *Brain Behav. Evol.* **65**, 188–201.

Meek, J., Grant, K. and Bell, C. (1999). Structural organization of the mormyrid electrosensory lateral line lobe. *J. Exp. Biol.* **202**, 1291–1300.

Meek, J., Hafmans, T. G., Han, V., Bell, C. C. and Grant, K. (2001). Myelinated dendrites in the mormyrid electrosensory lobe. *J. Comp. Neurol.* **431**, 255–275.

Melcón, M. L., Yovel, Y., Denzinger, A. and Schnitzler, H. U. (2010). How greater mouse-eared bats deal with ambiguous echoic scenes. *J. Comp. Physiol. A* **197**, 505–514.

Metzen, M. G., Engelmann, J., Bacelo, J., Grant, K. and von der Emde, G. (2008). Receptive field properties of neurons in the electrosensory lateral line lobe of the weakly electric fish, *Gnathonemus petersii*. *J. Comp. Physiol. A* **194**, 1063–1075.

Metzen, M., Biswas, S., Bousack, H., Gottwald, M., Mayekar, K. and von der Emde, G. (2012). A biomimetic active electrolocation sensor for detection of atherosclerotic lesions in blood vessels. *IEEE Sensors J.* **12**, 325–331.

Meyer, J. H. (1982). Behavioral responses of weakly electric fish to complex impedances. *J. Comp. Physiol. A* **145**, 459–470.

Migliaro, A., Caputi, A. A. and Budelli, R. (2005). Theoretical analysis of pre-receptor image conditioning in weakly electric fish. *PLoS Comput. Biol.* **1**, e16–123–131.

Moller, P. (1995). *Electric fishes. History and behavior.* London, UK: Chapman & Hall.

Moller, P. (1980). Electroreception and the behaviour of mormyrid electric fish. *Trends Neurosci.* **3**, 105–109.

Moritz, T. (2010). Fishes of Iguidi River—a small forest stream in South-East Benin. *Ichthyol. Explor. Freshwaters* **21**, 9–26.

Moss, C.F. and Surlykke, A. (2010). Probing the natural scene by echolocation in bats. *Front. Behav. Neurosci.* **4**, 00033–1–16.

Münkler, P., Gunawardene, M. A., Jungen, C., Klatt, N., Schwarzl, J. M., Akbulak, R. Ö., Dinshaw, L., Hartmann, J., Jularic, M., Kahle, A.-K., et al. (2020). Local impedance guides catheter ablation in patients with ventricular tachycardia. *J. Cardiovasc. Electrophysiol.* **31**, 61–69.

Nagata, T., Koyanagi, M., Tsukamoto, H., Saeki, S., Isono, K., Shichida, Y., Tokunaga, F., Kinoshita, M., Arikawa, K. and Terakita, A. (2012). Depth perception from image defocus in a jumping spider. *Science* **335**, 469–471.

Nanjappa, P., Brand, L. and Lannoo, M. J. (2010). Swimming Patterns Associated with Foraging in Phylogenetically and Ecologically Diverse American Weakly Electric Teleosts (Gymnotiformes). *Env. Biol. Fish.* **58**, 97–104.

Nawrot, M. and Joyce, L. (2006). The pursuit theory of motion parallax. *Vision Res.* **46**, 4709–4725.

Nelson, M. E. and MacIver, M. A. (1999). Prey capture in the weakly electric fish *Apteronotus albifrons*: sensory acquisition strategies and electrosensory consequences. *J. Exp. Biol.* **202**, 1195–1203.

Nelson, M. E. and MacIver, M. A. (2006). Sensory acquisition in active sensing systems. *J. Comp. Physiol. A* **192**, 573–586.

Nelson, M. E., MacIver, M. A. and Coombs, S. (2002). Modeling electrosensory and mechanosensory images during the predatory behavior of weakly electric fish. *Brain Behav. Evol.* **59**, 199–210.

Nwani, C. D., Odoh, G. E., Ude, E. F. and Okogwu, O. I. (2011). Food and feeding habits of *Gnathonemus petersii* (Osteichthyes: Mormyridae) in Anambra River, Nigeria. *Int. Aquat. Res.* **3**, 45–51.

Ogbeibu, A. E. and Ezeunara, P. U. (2002). Ecological impact of brewery effluent on the Ikpoba river, Nigeria, using the fish communities as bio-indicators. *J. Aquatic Sci.* **17**, 35–44.

Ogbeibu, A. E. and Ezeunara, P. U. (2005). Studies on the food composition and feeding pattern of fish communities in the Ikpoba river, southern nigeria. *J. Aquatic Sci.* **20**, 117–129.

Olsson, P., Lind, O. and Kelber, A. (2018). Chromatic and achromatic vision: parameter choice and limitations for reliable model predictions. *Behav. Ecol.* **29**, 273–282.

Osorio, D. and Vorobyev, M. (2005). Photoreceptor spectral sensitivities in terrestrial animals: adaptations for luminance and colour vision. *Proc. R. Soc. B* **272**, 1745–1752.

Packard, R. R. S., Luo, Y., Abiri, P., Jen, N., Aksoy, O., Suh, W. M., Tai, Y.-C. and Hsiai, T. K. (2017). 3-D Electrochemical Impedance Spectroscopy Mapping of Arteries to Detect Metabolically Active but Angiographically Invisible Atherosclerotic Lesions. *Theranostics* **7**, 2431–2442.

Paspalakis, S., Moirogiorgou, K., Papandroulakis, N., Giakos, G. and Zervakis, M. (2020). Automated fish cage net inspection using image processing techniques. *IET Image Process.* **14**, 2028–2034.

Pedraja, F., Aguilera, P., Caputi, A. A. and Budelli, R. (2014). Electric Imaging through Evolution, a Modeling Study of Commonalities and Differences. *PLoS Comput. Biol.* **10**, e1003722–1–14.

References

Pedraja, F., Hofmann, V., Goulet, J. and Engelmann, J. (2020). Task-Related Sensorimotor Adjustments Increase the Sensory Range in Electrolocation. *J. Neurosci.* **40**, 1097–1109.

Pedraja, F., Hofmann, V., Lucas, K. M., Young, C., Engelmann, J. and Lewis, J. E. (2018). Motion parallax in electric sensing. *Proc. Natl. Acad. Sci. USA* **115**, 573–577.

Pettigrew, J. D. and Frost, B. J. (1985). A Tactile Fovea in the *Scolopacidae*. *Brain Behav. Evol.* **26**, 185–195.

Pinder, L. C. V. (1986). Biology of Freshwater Chironomidae. *Ann. Rev. Entomol.* **31**, 1–23.

Price, C., Black, K. D., Hargrave, B. T. and Morris, J. A., Jr (2015). Marine cage culture and the environment: effects on water quality and primary production. *Aquac. Environ. Interact.* **6**, 151–174.

Prokopy, R. J. (1983). Visual detection of plants by herbivorous insects. *Annu. Rev. Entomol.* **28**, 337–364.

Prudic, K. L., Skemp, A. K. and Papaj, D. R. (2006). Aposematic coloration, luminance contrast, and the benefits of conspicuousness. *Behav. Ecol.* **18**, 41–46.

Pusch, R., Kassing, V., Riemer, U., Wagner, H.-J., von der Emde, G. and Engelmann, J. (2012). A grouped retina provides high temporal resolution in the weakly electric fish *Gnathonemus petersii*. *J. Physiol. Paris* **107**, 84–94.

Pusch, R., von der Emde, G., Hollmann, M., Bacelo, J., Nobel, S., Grant, K. and Engelmann, J. (2008). Active sensing in a mormyrid fish: electric images and peripheral modifications of the signal carrier give evidence of dual foveation. *J. Exp. Biol.* **211**, 921–934.

Rasnow, B. (1996). The effects of simple objects on the electric field of *Apteronotus*. *J. Comp. Physiol. A* **178**, 397–411.

Rau, S. (2013). Bildgebende Verfahren zur Lokalisierung von atherosklerotischen Plaques mittels Methoden der elektrischen Impedanzspektroskopie. *Master's thesis,* FernUniversität Hagen, Hagen.

Read, J. C. A. (2012). Visual Perception: Understanding Visual Cues to Depth. *Curr. Biol.* **22**, R163–R165.

Reyes, R., del Norte Campos, A., Añasco, N. C. and Santander-de Leon, S. M. S. (2020). Biofouling development in marine fish farm influenced by net colour, immersion period and environmental conditions. *Aquac. Res.* **51**, 3129–3138.

Richards, S. D., Brown, N. R. and Leighton, T. G. (1998). Turbidity in future high-frequency sonar performance models. *J. Acoust. Soc. Am.* **103**, 1349–1350.

Rodríguez-Cattáneo, A., Aguilera, P. A. and Caputi, A. A. (2017). Waveform sensitivity of electroreceptors in the pulse-type weakly electric fish *Gymnotus omarorum*. *J. Exp. Biol.* **220**, 1663–1673.

Rojas, B., Valkonen, J. and Nokelainen, O. (2015). Aposematism. *Curr. Biol.* **25**, R350–R351.

Romero, J., Luzón-González, R., Nieves, J. L. and Hernández-Andrés, J. (2011). Color changes in objects in natural scenes as a function of observation distance and weather conditions. *Appl. Opt.* **50**, F112–F120.

Roth, G. A., Johnson, C., Abajobir, A., Abd-Allah, F., Abera, S. F., Abyu, G., Ahmed, M., Aksut, B., Alam, T., Alam, K., et al. (2017). Global, Regional, and National Burden of Cardiovascular Diseases for 10 Causes, 1990 to 2015. *J. Am. Coll. Cardiol.* **70**, 1–25.

Rother, D., Migliaro, A., Canetti, R., Gómez, L., Caputi, A. and Budelli, R. (2003). Electric images of two low resistance objects in weakly electric fish. *Biosystems* **71**, 169–177.

Röver, T. (2012). Die Erkennung von Eigenschaften und Kontrasten virtueller Objekte bei *Gnathonemus Petersii*. *PhD thesis,* Zoological Institute, University of Bonn, Bonn.

Sanchis-Gomar, F., Perez-Quilis, C., Leischik, R. and Lucia, A. (2016). Epidemiology of coronary heart disease and acute coronary syndrome. *Ann. Transl. Med.* **4**, 256–1–12.

Sanguinetti-Scheck, J. I., Pedraja, E. F., Cilleruelo, E., Migliaro, A., Aguilera, P., Caputi, A. A. and Budelli, R. (2011). Fish Geometry and Electric Organ Discharge Determine Functional Organization of the Electrosensory Epithelium. *PLoS ONE* **6**, e27470–1–10.

Sasaki, T., Nakamura, K., Inoue, M., Minami, K., Miki, Y., Goto, K., Take, Y., Kaseno, K., Yamashita, E., Koyama, K., et al. (2020). Optimal local impedance drops for an effective radiofrequency ablation during cavo-tricuspid isthmus ablation. *J. Arrhythm.* **36**, 905–911.

Scheich, H., Bullock, T. H. and Hamstra, R. H. J. (1973). Coding properties of two classes of afferent nerve fibers: high-frequency electroreceptors in the electric fish, *Eigenmannia*. *J. Neurophysiol.* **36**, 39–60.

Schettini, R. and Corchs, S. (2010). Underwater Image Processing: State of the Art of Restoration and Image Enhancement Methods. *EURASIP J. Adv. Signal Process.* **2010**, 52–67.

Schlett, C. L., Maurovich-Horvat, P., Ferencik, M., Alkadhi, H., Stolzmann, P., Scheffel, H., Seifarth, H., Nakano, M., Do, S., Vorpahl, M., et al. (2013). Histogram analysis of lipid-core plaques in coronary computed tomographic angiography: ex vivo validation against histology. *Invest. Radiol.* **48**, 646–653.

Schmitt, O. (1969). Some interesting and useful biomimetic transforms. *Proc. 3rd Int. Biophysics Congress (Boston, USA)* p. 297.

Schumacher, S., Burt de Perera, T. and von der Emde, G. (2016a). Object discrimination through active electrolocation: Shape recognition and the influence of electrical noise. *J. Physiol. Paris* **110**, 151–163.

Schumacher, S., Burt de Perera, T. and von der Emde, G. (2017a). Electrosensory capture during multisensory discrimination of nearby objects in the weakly electric fish *Gnathonemus petersii*. *Sci. Rep.* **7**, 43665–1–11.

Schumacher, S., Burt de Perera, T., Thenert, J. and von der Emde, G. (2016b). Cross-modal object recognition and dynamic weighting of sensory inputs in a fish. *Proc. Natl. Acad. Sci. USA* **113**, 7638–7643.

Schumacher, S., von der Emde, G. and Burt de Perera, T. (2017b). Sensory influence on navigation in the weakly electric fish *Gnathonemus petersii*. *Anim. Behav.* **132**, 1–12.

Schuster, S. and Amtsfeld, S. (2002). Template-matching describes visual pattern-recognition tasks in the weakly electric fish *Gnathonemus petersii*. *J. Exp. Biol.* **205**, 549–557.

Schwan, H. P. (1963). Determination of biological impedances. In *Physical techniques in biological research, vol. VI* (ed. Nastuk, W. L.), pp. 323–406. London: Academic Press.

Schwarz, S. and von der Emde, G. (2001). Distance discrimination during active electrolocation in the weakly electric fish *Gnathonemus petersii*. *J. Comp. Physiol. A* **186**, 1185–1197.

Schwarz, S., Hofmann, M. H. and von der Emde, G. (2001). Weakly electric fish as a natural model for industrial sensors. *BionaReport* **15**, 142–157.

Servagent, N., Jawad, B., Bouvier, S., Boyer, F., Girin, A., Gomez, F., Lebastard, V., Stefanini, C. and Gossiaux, P.-B. (2013). Electrolocation Sensors in Conducting Water Bio-Inspired by Electric Fish. *IEEE Sensors J.* **13**, 1865–1882.

Setchell, J. M. and Wickings, E. J. (2005). Dominance, Status Signals and Coloration in Male Mandrills (*Mandrillus sphinx*). *Ethology* **111**, 25–50.

Shuai, J., Kashimori, Y. and Kambara, T. (1998). Electroreceptor model of the weakly electric fish *Gnathonemus petersii*. I. The model and the origin of differences between A- and B-receptors. *Biophys. J.* **75**, 1712–1726.

Sicardi, E. A., Caputi, A. A. and Budelli, R. (2000). Physical basis of distance discrimination in weakly electric fish. *Physica A* **283**, 86–93.

Sim, M. and Kim, D. (2011). Electrolocation based on tail-bending movements in weakly electric fish. *J. Exp. Biol.* **214**, 2443–2450.

Sim, M. and Kim, D. (2012). Electrolocation of multiple objects based on temporal sweep motions. *Adapt. Behav.* **20**, 146–158.

Snyder, J. B., Nelson, M. E., Burdick, J. W. and MacIver, M. A. (2007). Omnidirectional sensory and motor volumes in electric fish. *PLoS Biol.* **5**, e301–2671–2683.

Solberg, J. R., Lynch, K. M. and MacIver, M. A. (2008). Active Electrolocation for Underwater Target Localization. *Int. J. Robot. Res.* **27**, 529–548.

Speck, T. and Speck, O. (2008). Process sequences in biomimetic research. In *Design and Nature IV Comparing Design in Nature with Science and Engineering* (ed. Brebbia, C. A.), pp. 3–11. Southampton: WIT Press.

Srinivasan, M. V. (2011). Visual control of navigation in insects and its relevance for robotics. *Curr. Opin. Neurobiol.* **21**, 535–543.

Stein, K. M., Sulkin, M. S. and Stivland, T. M. (2019). Advancing electrophysiology: partnerships achieve meaningful innovation. *Europace* **21**, iii29–iii31.

Stevens, K. A. (2012). The vision of David Marr. *Perception* **41**, 1061–1072.

Stevens, M. (2013). *Sensory Ecology, Behaviour, and Evolution*. Oxford, UK: Oxford University Press.

Stiles, D. K. and Oakley, B. (2002). Simulation of electrode impedance and current densities near an atherosclerotic lesion. *Proc. Int. Special Topic Conf. Microtechnologies in Medicine and Biology (IEEE-EMBS) (Madison, USA)* pp. 57–61.

Stiles, D. K. and Oakley, B. (2003). Simulated characterization of atherosclerotic lesions in the coronary arteries by measurement of bioimpedance. *IEEE Trans. Biomed. Eng.* **50**, 916–921.

Stone, J. R. (2012). Pathology of myocardial infarction, coronary artery disease, plaque disruption, and the vulnerable atherosclerotic plaque. *Diagn. Histopathol.* **18**, 478–483.

Streitner, I., Goldhofer, M., Cho, S., Thielecke, H., Kinscherf, R., Streitner, F., Metz, J., Haase, K. K., Borggrefe, M. and Suselbeck, T. (2009). Electric impedance spectroscopy of human atherosclerotic lesions. *Atherosclerosis* **206**, 464–468.

Sulkin, M. S., Laughner, J. I., Hilbert, S., Kapa, S., Kosiuk, J., Younan, P., Romero, I., Shuros, A., Hamann, J. J., Hindricks, G., et al. (2018). Novel Measure of Local Impedance Predicts Catheter-Tissue Contact and Lesion Formation. *Circ. Arrhythm. Electrophysiol.* **11**, e005831–1–11.

Sutton, E. E. (2017). Bioelectric Sensing and Navigation: Multimodal Control in Electric Fish and Endovascular Device Guidance. *PhD thesis,* Department of Mechanical Engineering, Johns Hopkins University, Baltimore.

Sutton, E. E., Fuerst, B., Ghotbi, R., Cowan, N. J. and Navab, N. (2020). Biologically Inspired Catheter for Endovascular Sensing and Navigation. *Sci. Rep.* **10**, 5643–1–10.

Szabo, T. and Wersäll, J. (1970). Ultrastructure of an electroreceptor (mormyromast) in a mormyrid fish, *Gnathonemus petersii*. II. *J. Ultrastruct. Res.* **30**, 473–490.

Tamura, N., Fujii, Y., Boonkhaw, P., Prayoon, U. and Kanchanasaka, B. (2017). Colour vision in Finlayson's squirrel (*Callosciurus finlaysonii*): is conspicuous pelage colour useful for species recognition? *Trop. Zool.* **30**, 110–124.

Tao, Q., Huang, K., Qin, C., Guo, B., Lam, R. and Zhang, F. (2018). Omnidirectional surface vehicle for fish cage inspection. *Proc. OCEANS 2018 MTS/IEEE Charleston (OCEANS) (Charleston, USA)* pp. 1–6.

Taylor, L. A., Maier, E. B., Byrne, K. J., Amin, Z. and Morehouse, N. I. (2014). Colour use by tiny predators: jumping spiders show colour biases during foraging. *Anim. Behav.* **90**, 149–157.

Telfer, T., Ntoumas, M., Tsapakis, M., Papandroulakis, N., Chalkiadakis, V. and Laanen, M. (2019). *Automatic in-situ measurement systems report. Deliverable D7.6 of the TAPAS project funded under the European Union's Horizon 2020 research and innovation programme* GA No: 678396.

Thorvaldsen, T., Holmen, I. M. and Moe, H. K. (2015). The escape of fish from Norwegian fish farms: Causes, risks and the influence of organisational aspects. *Mar. Policy* **55**, 33–38.

Toerring, M. J. and Belbenoit, P. (1979). Motor Programs and Electroreception in Mormyrid Fish. *Behav. Ecol. Sociobiol.* **4**, 369–379.

Toerring, M. J. and Moller, P. (1984). Locomotor and electric displays associated with electrolocation during exploratory behavior in mormyrid fish. *Behav. Brain Res.* **12**, 291–306.

Tóth, G. G., Yamane, M. and Heyndrickx, G. R. (2015). How to select a guidewire: technical features and key characteristics. *Heart* **101**, 645–652.

Vidal-Cordero, J. M., Moreno-Rueda, G., López-Orta, A., Marfil-Daza, C., Ros-Santaella, J. L. and Ortiz-Sánchez, F. J. (2012). Brighter-colored paper wasps (*Polistes dominula*) have larger poison glands. *Front. Zool.* **9**, 20–1–5.

Virmani, R., Burke, A. P., Farb, A. and Kolodgie, F. D. (2006). Pathology of the vulnerable plaque. *J. Am. Coll. Cardiol.* **47**, C13–C18.

Virmani, R., Burke, A. P., Kolodgie, F. D. and Farb, A. (2002). Vulnerable plaque: the pathology of unstable coronary lesions. *J. Interv. Cardiol.* **15**, 439–446.

Virmani, R., Kolodgie, F. D., Burke, A. P., Farb, A. and Schwartz, S. M. (2000). Lessons from sudden coronary death: a comprehensive morphological classification scheme for atherosclerotic lesions. *Arterioscler. Thromb. Vasc. Biol.* **20**, 1262–1275.

von der Emde, G. (1990). Discrimination of objects through electrolocation in the weakly electric fish, *Gnathonemus petersii*. *J. Comp. Physiol. A* **167**, 413–421.

von der Emde, G. (1992). Electrolocation of Capacitive Objects in Four Species of Pulse-type Weakly Electric Fish II. Electric Signalling Behaviour. *Ethology* **92**, 177–192.

von der Emde, G. (1994). Active electrolocation helps *Gnathonemus petersii* to find its prey. *Naturwissenschaften* **81**, 367–369.

von der Emde, G. (1998). Capacitance detection in the wave-type electric fish *Eigenmannia* during active electrolocation. *J. Comp. Physiol. A* **182**, 217–224.

von der Emde, G. (1999a). Electroreception. In *The Physiology of Fisches* (ed. Evans, D. H.), pp. 313–344. Boca Raton: CRC Press.

von der Emde, G. (1999b). Active electrolocation of objects in weakly electric fish. *J. Exp. Biol.* **202**, 1205–1215.

von der Emde, G. (2006). Non-visual environmental imaging and object detection through active electrolocation in weakly electric fish. *J. Comp. Physiol. A* **192**, 601–612.

von der Emde, G. (2007). Biomimetic sensors: Active electrolocation of weakly electric fish as a model for active sensing in technical systems. *J. Bionic. Eng.* **4**, 85–90.

von der Emde, G. and Bell, C. (1994). Responses of cells in the mormyrid electrosensory lobe to EODs with distorted waveforms: implications for capacitance detection. *J. Comp. Physiol. A* **175**, 83–93.

von der Emde, G. and Bleckmann, H. (1992). Differential responses of two types of electroreceptive afferents to signal distortions may permit capacitance measurement in a weakly electric fish, *Gnathonemus petersii*. *J. Comp. Physiol. A* **171**, 683–694.

von der Emde, G. and Bleckmann, H. (1997). Waveform tuning of electroreceptor cells in the weakly electric fish, *Gnathonemus petersii*. *J. Comp. Physiol. A* **181**, 511–524.

von der Emde, G. and Bleckmann, H. (1998). Finding Food: Senses involved in Foraging for Insect Larvae in the Electric Fish *Gnathonemus Petersii*. *J. Exp.Biol.* **201**, 969–980.

von der Emde, G. and Engelmann, J. (2011). Active Electrolocation. In *Encyclopedia of fish physiology: from genome to environment* (ed. Farrell, A. P.), pp. 375–386. San Diego: Academic press.

von der Emde, G. and Fetz, S. (2007). Distance, shape and more: recognition of object features during active electrolocation in a weakly electric fish. *J. Exp. Biol.* **210**, 3082–3095.

References

von der Emde, G. and Ringer, T. (1992). Electrolocation of Capacitive Objects in Four Species of Pulse-type Weakly Electric Fish I. Discrimination Performance. *Ethology* **91**, 326–338.

von der Emde, G. and Ronacher, B. (1994). Perception of electric properties of objects in electrolocating weakly electric fish: two-dimensional similarity scaling reveals a City-Block metric. *J. Comp. Physiol. A* **175**, 801–812.

von der Emde, G. and Ruhl, T. (2015). Matched Filtering in African Weakly Electric Fish: Two Senses with Complementary Filters. In *The Ecology of Animal Senses* (eds. von der Emde, G. and Warrant, E.), pp. 237–263. Switzerland: Springer.

von der Emde, G. and Schnitzler, H. U. (1990). Classification of Insects by Echolocating Greater Horseshoe Bats. *J. Comp. Physiol. A* **167**, 423–430.

von der Emde, G. and Schwarz, S. (2001). How the electric fish brain controls the production and analysis of electric signals during active electrolocation. *Zoology* **103**, 112–124.

von der Emde, G. and Schwarz, S. (2002). Imaging of Objects through active electrolocation in *Gnathonemus petersii*. *J. Physiol. Paris* **96**, 431–444.

von der Emde, G., Amey, M., Engelmann, J., Fetz, S., Folde, C., Hollmann, M., Metzen, M. and Pusch, R. (2008). Active electrolocation in *Gnathonemus petersii*: Behaviour, sensory performance, and receptor systems. *J. Physiol. Paris* **102**, 279–290.

von der Emde, G., Behr, K., Bouton, B., Engelmann, J., Fetz, J. and Folde, C. (2010). 3-Dimensional scene perception during active electrolocation in a weakly electric pulse fish. *Front. Behav. Neurosci.* **4**, 00026–1–13.

von der Emde, G., Bousack, H., Huck, C., Mayekar, K., Pabst, M. and Zhang, Y. (2009). Electric fish as natural models for technical sensor systems. *Proc. SPIE Bioengineered and Bioinspired Systems IV* **7365**, 73650B–1–11.

von der Emde, G., Schwarz, S., Gomez, L., Budelli, R. and Grant, K. (1998). Electric fish measure distance in the dark. *Nature* **395**, 890–894.

Wakilli, R. (2018). Elektrofischkatheter: Ein Fisch revolutioniert die Therapie von Herzrythmusstörungen. *kma - Klinik Management aktuell **23**, 84-87.*

Walton, A. G. and Moller, P. (2010). Maze Learning and Recall in a Weakly Electric Fish, *Mormyrus rume proboscirostris* Boulenger (Mormyridae, Teleostei). *Ethology* **116**, 904–919.

Wang, K., Cui, L. and Do, K. D. (2016). An underwater electrosensory membrane bio-inspired by weakly electric fish. *Proc. IEEE/RSJ Int. Conf. on Intelligent Robots and Systems (IROS) (Daejeon, Korea)* pp. 4951–4956.

Wang, K., Do, K. D. and Cui, L. (2017). An Underwater Electrosensor for Identifying Objects of Similar Volume and Aspect Ratio Using Convolutional Neural Network. *Proc. IEEE/RSJ Int. Conf. on Intelligent Robots and Systems (IROS) (Vancouver, Canada)* pp. 4963–4968.

Warrant, E. J. and Locket, N. A. (1999). Vision in the deep sea. *Biol. Rev.* **79**, 671–712.

Warren, W. H., Kay, B. A., Zosh, W. D., Duchon, A. P. and Sahuc, S. (2001). Optic flow is used to control human walking. *Nat. Neurosci.* **4**, 213–216.

Watson, D. and Bastian, J. (1979). Frequency Response Characteristics of Electroreceptors in the Weakly Electric Fish, *Gymnotus carapo*. *J. Comp. Physiol. A* **134**, 191–202.

Westby, G. W. (1984). Electroreception and communication in electric fish. *Sci. Prog.* **69**, 291–313.

WHO, World Health Organization (2017). Cardiovascular diseases (CVDs). *Fact Sheet*.

Winemiller, K. O. and Adite, A. (1997). Convergent evolution of weakly electric fishes from floodplain habitats in Africa and South America. *Environ. Biol. Fish.* **49**, 175–186.

Wolf-Homeyer, S., Engelmann, J. and Schneider, A. (2016). Electrolocation of objects in fluids by means of active sensor movements based on discrete EEVs. *Bioinspir. & Biomim.* **11**, 055002–1–12.

Xu, Y., Zhao, G., Wang, M. and Liang, S. (2019). Application of Dual-frequency Identification Sonar to detection of visible damages of underwater hydraulic structures. *IOP Conf. Ser.: Earth Environ. Sci.* **237**, 032029–1–8.

Yeates, S. E., Einum, S., Fleming, I. A., Holt, W. V. and Gage, M. J. (2014). Assessing risks of invasion through gamete performance: farm Atlantic salmon sperm and eggs show equivalence in function, fertility, compatibility and competitiveness to wild Atlantic salmon. *Evol. Appl.* **7**, 493–505.

Yu, F., Dai, X., Beebe, T. and Hsiai, T. (2011). Electrochemical impedance spectroscopy to characterize inflammatory atherosclerotic plaques. *Biosens. Bioelectron.* **30**, 165–173.

Yu, F., Li, R., Ai, L., Edington, C., Yu, H., Barr, M., Kim, E. S. and Hsiai, T. K. (2010). Electrochemical Impedance Spectroscopy to Assess Vascular Oxidative Stress. *Ann. Biomed. Eng.* **39**, 287–296.

Zakon, H. H. (1986). The Electroreceptive Periphery. In *Electroreception* (eds. Bullock, T. H. and Heiligenberg, W.), pp. 103–156. New York: John Wiley & Sons, Inc.

Zeymer, M., von der Emde, G. and Wullimann, M. F. (2018). The Mormyrid Optic Tectum Is a Topographic Interface for Active Electrolocation and Visual Sensing. *Front. Neuroanat.* **12**, 00079–1–24.

References

Zhang, X., Xu, L., Lee, J., Li, R., Liu, Y. and Shapero, A. (2015). Flexible micro sensor for intravascular vulnerable plaque diagnostic with electrical impedance spectroscopy. *Proc. IEEE Int. Conf. on Nano/Micro Engineered and Molecular Systems (IEEE-NEMS 2015) (Xi'an, China)* pp. 243–247.

Zhao, S., Lu, T.-F. and Anvar, A. (2009). Automatic object detection for AUV navigation using imaging sonar within confined environments. *Proc. IEEE Conf. on Industrial Electronics and Applications (ICIEA) (Xi'an, China)* pp. 3648–3653.

VI. Appendix

A.1 Electric-color acquisition from the central spot of electric images (related to chapter 6)

A.1.1 Background

During active electrolocation, the weakly electric fish *Gnathonemus petersii* recognizes nearby targets through the electric images they 'cast' onto the animal's electroreceptive body surface (e.g., von der Emde and Schwarz, 2002). An electric image is formed by the object-evoked modulations of the fish's electric emissions (electric organ discharges, EODs), which spread locally across the fish skin (lEOD modulations). Aquatic organisms usually cause lEOD amplitude and waveform modulations and thereby an electric amplitude and waveform image (Gottwald et al., 2017a, see chapter 5).

In chapter 5, it is suggested that *G. petersii* may acquire an electric-color cue (Budelli and Caputi, 2000), by combining the strongest modulation of an amplitude and waveform image (peak modulations). Electric colors may serve electrolocating fish as individual and reliable markers to identify different types of aquatic organisms.

So far, this hypothesis has not been tested, which is the aim of the study presented in chapter 6. In this study, potential electric colors of several electrolocation targets (fish, insect larvae, water plants etc.) shall be evaluated. For electric-color acquisition, recordings of the object-evoked lEOD amplitude and waveform modulations at the head and chin appendix of *G. petersii* shall be conducted. In principle, acquisition of electric color, as suggested above, requires (1) measurements of an amplitude and waveform image's modulations (from across the fish skin) and (2) the identification and combination of the images' peak modulations. However, an electric image recording, e.g., at the side of the fish head takes several hours (see chapter 5, section 5.3.5). This renders corresponding electric-color acquisition a very time consuming procedure, which cannot be carried out in reasonable time for a large number of electrolocation targets, aimed at in the follow-up study (in chapter 6). Thus, the recording of full electric images needs to be replaced by a quicker recording routine to obtain amplitude and waveform modulations for electric-color computation. This may be achieved by recording modulations from just a single position close to the fish skin, which defines the central spot of the electric images.

In the preliminary experiments, reported here, I tested whether electric color assessed by

such image modulations could sufficiently depict electric color as obtained by the amplitude and waveform images' peak modulations. To do so, I recorded electric images of a zebrafish (*Danio rerio*), a caddis worm (*Anabolia nervosa*) and a water plant (*Anubias sp.*) at the side of the fish head and the chin appendix.

So far, electric-color extraction, as proposed above, has only been evaluated for electric images from the fish head (see chapter 5). However, as the electric image of a target varies according to the body region onto which it is 'projected' (Pusch et al., 2008; Bott, 2014, supervised by M. Gottwald), this variability might affect electric-color extraction from electric images. The preliminary experiments will thus help to potentially improve experimental acquisition of electric color but also to verify previous findings on electric-color extraction (see chapter 5) for electric images from different body regions of *G. petersii*, i.e., the head and chin appendix.

A.1.2 Methodology

A.1.2.1 Recording of electric images

Recording experiments were conducted with a single *G. petersii*. The fish was anaesthetized in an Etomidat (Janssen-Cilag GmbH, Neuss, North Rhine-Westfalia, Germany) solution (0.6 ml Etomidat in 1 liter of water). It was then fixed on a central plastic holder (9 cm × 1.5 cm × 6 cm) in the experimental tank (28.7 cm × 38.5 cm × 18.8 cm) by wooden sticks and cloth strings. To sustain anesthesia during experiments, the tank water (11 l, 99.8 ± 2.1 µS cm^{-1}, 25.5 ± 0.3 °C) was mixed with 3.3 ml Ethomidat. Prior to recordings, stimulus animals were euthanized by a lethal MS 222 solution (2 g l^{-1}, Acros Organics, Fair Lawn, New Jersey, USA) (zebrafish) or by a lethal Ethomidate solution (2 mg ml^{-1}) (caddis worm). Using a micromanipulator, a stimulus animal or plant was placed close to the fish skin, i.e., either the side of the head or the chin appendix (figure A.1.1).

lEOD recordings were performed with a carbon dipole electrode (Gottwald et al., 2017a). Its two poles were orientated either perpendicular to the rostro-caudal fish axis (for recordings at the fish head) or to the lateral fish axis (for recordings at the chin appendix). A computer-guided motor system, which allowed electrode movements in x (rostro-caudal), y (dorso-ventral) and z (lateral) directions (e.g., Fechler and von der Emde, 2012), was used to place the electrode between stimulus object and fish skin. The electrode was

then moved to several positions (figure A.1.1), which formed a two-dimensional grid (at the head) or spatial grid (at the chin appendix) for electric image recordings. The grid at the side of the head covers a vertical plane by 1mm (x direction) and 2 mm (y direction) recording steps (figure A.1.1A). It additionally contains a central recording position, which corresponds to the central spot of the acquired electric image. At the chin appendix, the grid consists of a vertical plane in front of the tip and further recording positions along the back of the appendix (figure A.1.1B). Recording steps at the tip were 0.5 mm (in y and z directions). Steps of 1 mm (x direction) and 0.5 mm (y direction) were used between the other grid positions. The frontal measuring plane included the central recording position (providing the central image spot). As indicated in figure A.1.1, a stimulus object was always aligned in a mid position with respect to the electric images' central spot.

At each grid position, lEODs ($n \geq 5$) were recorded in the presence and absence of a stimulus object. The biphasic lEOD waveforms were amplified (×100, custom-built differential amplifier), filtered (band-pass: 1Hz to 100 Hz) and digitized (resolution: 16-bit, sampling rate: 250 kHz, A/D converter PCIe 6341, National Instruments, Austin, Texas, USA). The lEODs' peak-to-peak amplitudes (PP) and the peak amplitude ratios of the positive (P) and negative (N) lEOD phase (P/N ratios) were calculated by a custom-written LabVIEW (National Instruments) program (Gottwald et al., 2017a, see chapter 5). PP determined the lEOD amplitude and P/N the lEOD waveform. The lEOD amplitude or

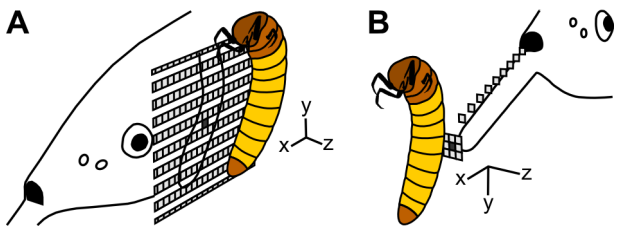

Figure A.1.1: Measuring grids to obtain electric images at different body regions of *G. petersii*.
(A) At the side of the fish head, several lEOD recording positions (n = 200, gray rectangles) form a vertical plane for the acquisition of 2-D electric images. The recording position in the plane's center (dark gray rectangle) provides an electric image's central spot. With respect to this central recording position a close target (caddis worm) is aligned in a mid position as indicated by the target's contour (black line) marked on the grid. **(B)** At the fish's chin appendix lEOD recording positions (n = 18, gray rectangles) provide a spatial grid to obtain electric images. The central position of the grid, which is also the central spot of the obtained spatial image, is marked in dark gray. The caddis worm is placed in a mid position in front of the grid and its central position.

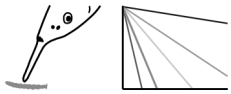

waveform modulation at a grid position was calculated by dividing the means of the PP or P/N values obtained with object by those obtained without the object and by subtracting 1 from these ratios. The modulations from across a grid formed the amplitude image (PP modulations) or the waveform image (P/N modulations) of a stimulus object.
For electric images from the fish head the original resolution of 201 (recorded) modulations was increased by linear interpolation (to 380).

A.1.2.2 Electric-color extraction from electric images

Based on the electric image data of the stimulus objects (caddis worm, zebrafish and plant stem), mechanisms for electric-color extraction are investigated. Besides testing a potential approach for quick electric-color recordings also previous findings, outlined in detail in chapter 5 and summarized in brief below, are evaluated.
The previous study showed that electric color, usually acquired by pairing an amplitude and waveform image's modulations in a scattergramm (Budelli and Caputi, 2000), could only be depicted by modulation pairs from 'equally shaped' areas of both image types. These pairs indicated a linear relationship of amplitude (PP) and waveform (P/N) modulations (i.e., electric color) by forming the path of an electric-color line. It was further demonstrated that the electric-color pathway was accurately fitted by a line, connecting the images' peak modulation pair with the basal condition (i.e., a spot of no or 'zero' modulation within the scattergram). Proposedly, such an electric-color line represents a quasi 'proportional' relationship of both peak modulations. Thus electric color, calculated as the line's slope, could principally be determined by combining the peak modulation of a waveform and amplitude image as a ratio.
According to the procedures conducted in chapter 5, the modulations of a stimulus object's amplitude and waveform image are plotted against one another in a scattergram. Modulation pairs from equally shaped image areas are identified. The algorithm to do so (Gottwald et al., 2017a) is described in detail in chapter 5 and briefly outlined below. It basically requires the amplitude and waveform image to be normalized for defining their shapes, which then are subtracted, while applying 'thresholding'. Differences of normalized modulations within threshold range indicate equally shaped areas of the two images. Modulation pairs from those areas are then emphasized in the scattergram of amplitude and waveform modulations to mark the path of an electric-color line. Eventually, electric-color

lines are defined using two different approaches. A line is added by connecting the peak modulation pair and the basal condition. The other line is acquired by connecting a pair of modulations from the central image spots and the basal condition. Both lines and their slopes are compared with one another and with respect to matching the predefined electric-color pathway.

A.1.3 Findings

A.1.3.1 Electric images

The stimulus objects' electric images obtained from the fish head (figure A.1.2A) are shown in figures A.1.2B and A.1.2C. Due to the individual electrical, spatial and geometrical attributes of the plant stem, zebrafish and caddis worm, their electric images differed from one another. Hence, amplitude and waveform images provided individual patterns of positive and negative modulations with various magnitudes (deviations from 0) (figures A.1.2B and A.1.2C). Within the images an area of pronounced modulations occurred in a region immediately opposite to the stimulus object, i.e., the image center. Image centers contained the central image spot and the images' peak modulation (i.e., the value with the largest deviation from 0). In most of the electric images evoked at the fish

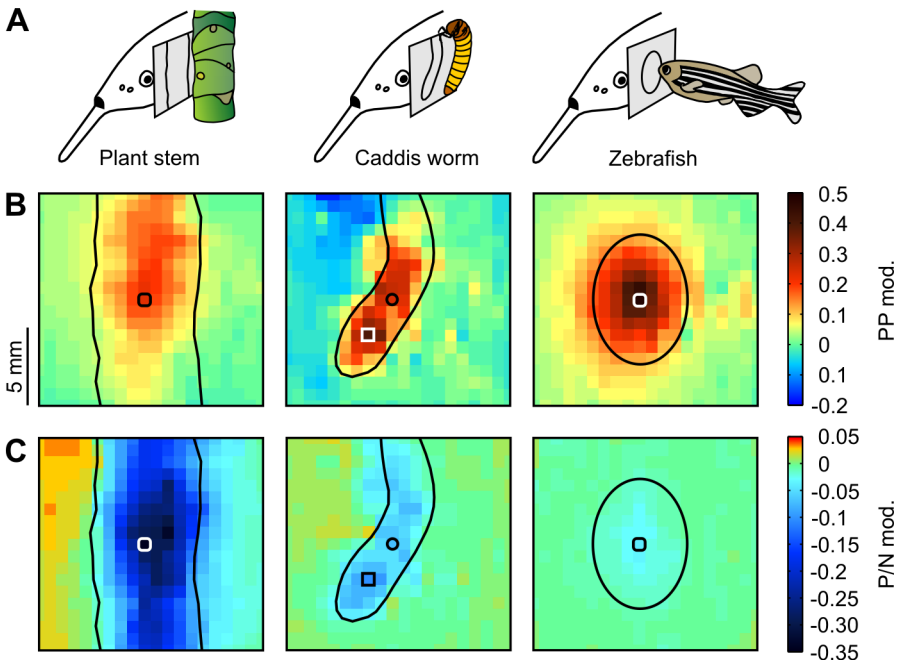

Figure A.1.2: (previous page) Electric images of stimulus objects (aquatic organisms) at the side of the fish head.

(A) Schematic drawing indicating the stimulus objects' positions in front of the measuring plane (gray), on which the object contour is marked (in black). Object-to-fish distances were 5 mm. **(B)** Color-coded amplitude images with the object contour marked on them. A circle indicates the images' central spot and a rectangle the images' peak modulation (i.e., peak amplitude [PA]). When the PA occurred at the central image spot both were indicated by a single rounded rectangle (leftmost and rightmost image). **(C)** Color-coded waveform images. The images are arranged as in (B) and show the same markings indicating the object contour, the central image spot (circle), the peak modulation (i.e., peak distortions [PD]) (rectangle) or both combined (rounded rectangle).

head the peak modulation originated from the central image spot (figures A.1.2B and A.1.2C, leftmost and rightmost).

The amplitude and waveform images acquired from the chin appendix (figures A.1.3A-C) differed considerably from those obtained at the fish head. In comparison, the images had

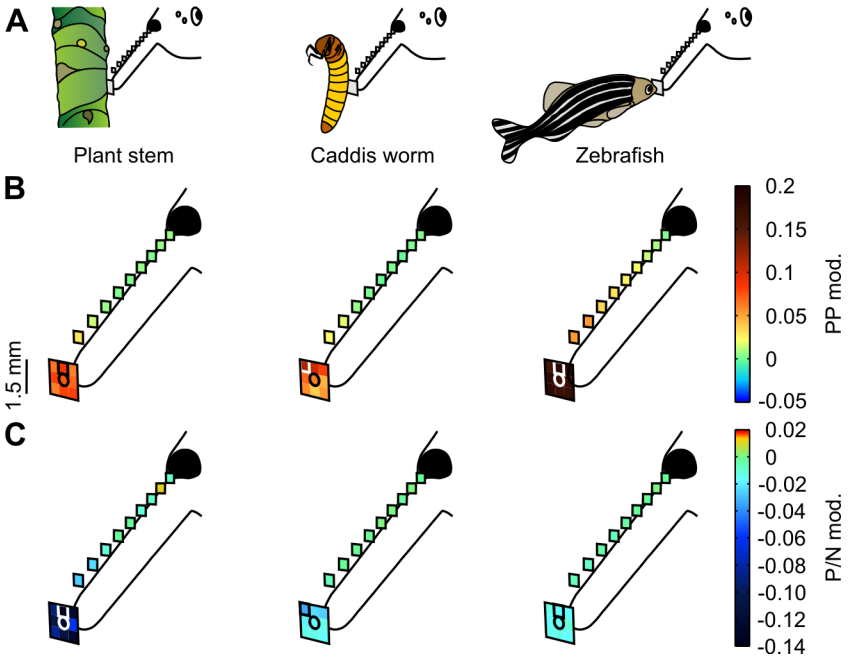

Figure A.1.3: Electric images of stimulus objects (aquatic organisms) at the chin appendix.

(A) Schematic drawing indicating the stimulus objects' position in front of the recording area (gray). Object distances to the chin's tip were 5 mm **(B)** Color-coded amplitude images. Central image spots are marked by circles. The images' peak modulations are indicated by rectangles. **(C)** Color-coded waveform images arranged as in (B) with analogous markings.

weaker modulations and provided rather simple modulation patterns. These patterns varied in their modulation magnitude for the different stimulus objects, (figures A.1.3B and A.1.3C) as previously shown for the patterns of the other electric images (figures A.1.2B and A.1.2C). Similar as in the images from the fish head, an area of pronounced modulations emerged at the image region right in front of an electrolocation target at the chin appendix. The peak modulation in these areas (image centers) did not occur at the central image spot (figures A.1.3B and A.1.3C).

A.1.3.2 Electric-color extractions

To evaluate electric-color extractions from electric images, the amplitude image's (PP) modulations were plotted versus the waveform image's (P/N) modulations in separate scattergrams for all stimulus objects (figure A.1.4).

The distributions of PP-P/N modulation pairs, resulting from electric images from the fish head (figure A.1.4A) and the chin appendix (figure A.1.4B), showed different amounts of scatter. Within these distributions only the modulation pairs from equally shaped areas of an amplitude and waveform image indicated the path of an electric-color line. Similar results have been obtained for electric images from the fish head in the previous study presented in chapter 5. In this study, it has also been shown that an electric-color line, matching a distribution's electric-color pathway, is acquired by fitting the peak modulation pair and basal condition.

The same routine was used to add an electric-color line to the distributions shown in figure A.1.4. All these color lines accurately fitted the distributions' electric-color pathways.

Alternatively, an electric-color line was obtained by connecting the modulation pair from the central image spots and the basal condition. When such lines were added to the distributions they accurately matched the electric-color pathways but also showed close alignments with the other color lines added previously (figures A.1.4A and A.1.4B). Both approaches, mentioned above, yielded exactly the same electric-color line (figure A.1.4A, leftmost and rightmost) when the peak modulations of electric images originated from the central image spots (figure A.1.2, leftmost and rightmost).

These results indicate that electric colors (i.e., the slopes of the lines) do not differ considerably for the two methods of electric-color acquisition. Both accurately depict the electric color of an electrolocation target. The color lines' slopes can simply be calculated

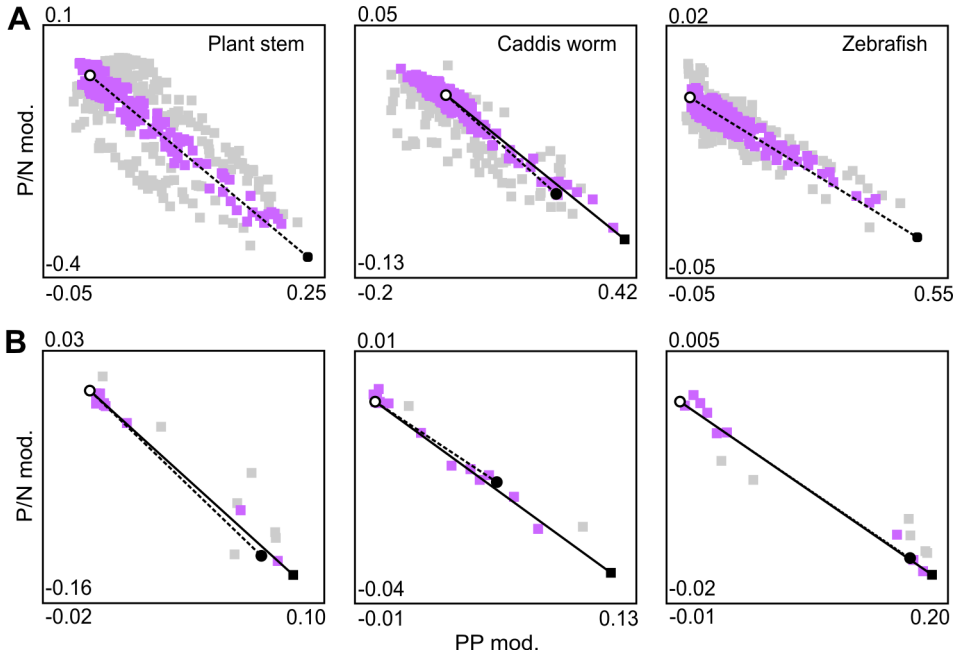

Figure A.1.4: Determinations of electric-color lines from electric image modulations.

(A) Extraction of electric-color lines from the electric images acquired at the fish head. For each stimulus object amplitude and waveform image modulations are plotted in a scattergram as PP-P/N modulation pairs (gray and purple rectangles). Purple rectangles indicate modulation pairs acquired from equally shaped areas of an amplitude and waveform image. They depict a linear electric-color pathway within the distribution of PP-P/N modulation pairs. Open circles mark the origin of the scattergram, i.e., the basal condition (of zero modulation). Filled, black circles indicate the modulation pair acquired from the central image spots ('central modulation pair'). Black rectangles show the modulation pair obtained through combination of an amplitude and waveform image's peak modulation. Note that this is the only modulation pair combining modulations, which may originate from different local positions within both image types. If the peak modulations originate from the central spots of an amplitude and waveform image their modulation pair is marked by a rounded rectangle. Solid lines indicate electric-color lines added by connecting peak modulation pair and basal condition. Dashed lines show electric-color lines connecting the central modulation pair or a peak modulation pair obtained at the central image spots with the basal condition. **(B)** Extraction of electric-color lines from the stimulus objects' electric images acquired at the chin appendix. Distributions of PP-P/N modulation pairs are shown in the same manner and with the same markings as in (A). Electric-color lines were acquired and illustrated as explained in (A).

as either the ratio of the amplitude and waveform modulations forming the peak modulation pair (in the first approach) or of those combined for the central modulation pair (in the second approach).

While electric-color extraction by the peak modulation ratios of electric images is suggested to be applied by *G. petersii* (see also chapter 5), the alternative approach, tested

here, provides advantages for experimental electric-color acquisitions. Unlike the images' peak modulations, which can only be identified after the full electric images have been recorded, the modulations from the central image spots can quickly be acquired from the predefined central recording position close to the fish skin (figure A.1.1). This approach eliminates the need for elaborate and time-consuming measurements to define an object's electric color and allows for electric-color acquisitions of a large number of electrolocation targets in reasonable time. It was used to do so in the study presented in chapter 6.

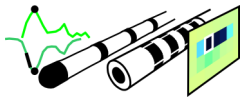

A.2 Supplemental information (related to chapter 9)

Table A.2: Plaque parameters and conditions obtained for synthetic plaque types P1-4 (n = 12).

	Plaque parameters					
Plaque types	Rel. narrowing (%)	Plaque area (mm^2)	Core width (mm)	Core area (mm^2)	Rel. core area (%)	Cap thickness (µm)
P1[a]	22.64	17.06	1.88	1.20	7.04	603
P1[a]	46.18	25.37	2.77	2.00	7.88	491
P1[a]	35.80	23.34	2.33	1.20	5.13	958
P2[a]	54.42	18.61	2.62	1.69	9.10	1002
P2[a]	46.62	26.19	3.66	1.71	6.51	884
P2[b]	20.38	35.89	3.02	3.13	8.73	326
P3[c]	60.00	66.48	6.59	37.57	56.51	709
P3[d]	50.18	48.86	6.41	30.23	61.89	364
P3[d]	49.94	62.71	6.43	34.92	55.69	400
P4[d]	58.58	81.53	7.92	55.04	67.51	348
P4[d]	54.60	71.93	8.06	50.66	70.44	371
P4[d]	51.98	97.94	8.14	65.06	66.43	386

[a] Plaque condition C1 with rel. core area < 10% and cap thickness > 450 µm.

[b] Plaque condition C2 with rel. core area < 10% and cap thickness < 450 µm.

[c] Plaque condition C3 with rel. core area > 10% and cap thickness > 450 µm.

[d] Plaque condition C4 with rel. core area > 10% and cap thickness < 450 µm.

Figure A.2.1: (next page) Routine to compute a synthetic artery's dynamic amplitude and waveform modulation profile with plaque-evoked electric image.

(A) PP amplitude trace (black), acquired with the ring-electrode electrolocation catheter along a synthetic artery (white) with a P4 plaque (white/black) as illustrated in the bottom left inset. The catheter's sender (S) and R3-receiver are marked in black, indicating catheter configuration S–R3, which was used for the recording. Each position of the amplitude trace depicts the mean ± SD of 100 PP values. **(B)** Waveform (P/N) trace (black), obtained during the catheterization. The trace's positions are means ± SD of 100 P/N values, respectively. **(C)** Multi-stage algorithm (custom Matlab [MathWorks, Natick, Massachusetts, USA] routine) for computing an artery's dynamic mod. profile with plaque-evoked electric image. The routine and its individual processing steps are explicated/illustrated with the amplitude trace as input. While not depicted in this figure, the routine works in an analogous way to determine waveform mod. profiles and images. In the two initial processing steps, the amplitude trace's plaque-evoked central section is located by detecting the lowest PP value (marked by an orange dot [step 1]) and the minimal and maximal slope of the trace (marked in yellow [step 2]). The following steps, 3 and 4, of the routine then define the expansion of trace's ('w-shaped') central section. First, a group of five slope values (marked in green), lying ten positions in front of the min. slope and ten positions behind the max. slope of the trace, were selected and averaged respectively (step 3). Each mean and its corresponding standard deviation was then used to z-score the trace's slopes (turquoise lines) that were framed by the group of slopes from which the mean was derived and the adjacent maximum or minimum slope (step 4). Their (absolute) z-scores are depicted color-coded within the two blue-framed arrows above the PP trace. z-scores larger than 1.96 are indicated in red, whereas scores below 1.96 are marked in white. The z-values (z1 and z2) with a score above 1.96, which were closest to the arrow tips, then marked (black arrows) the left (L) and right (R) rim (black) of the amplitude trace's central region. Note that in cases where no z-values above 1.96 did occur, the two outermost z-values (of the arrows) were chosen instead to determine the rims of a trace's central region. In the final step (5), the trace's peripheral regions are each fitted with a line (dashed blue lines). The central region is also fitted with a line (blue solid line), connecting its rims. Each line provides expectancy values of PP amplitudes that would have been acquired in the synthetic artery without a plaque present. Expectancy and recorded values are then divided by one another to obtain amplitude modulations. **(D)** Dynamic amplitude mod. profile with plaque-evoked electric image resulting from the multi-stage algorithm. The profile's peripheral regions (black, dashed lines) only show negligible small modulations, i.e., basal modulations close to 1. The central electric image (black solid line) provides pronounced modulations (below 1). **(E)** Dynamic waveform mod. profile of the synthetic artery with a central plaque-evoked electric image, shown in the same manner as in (D).

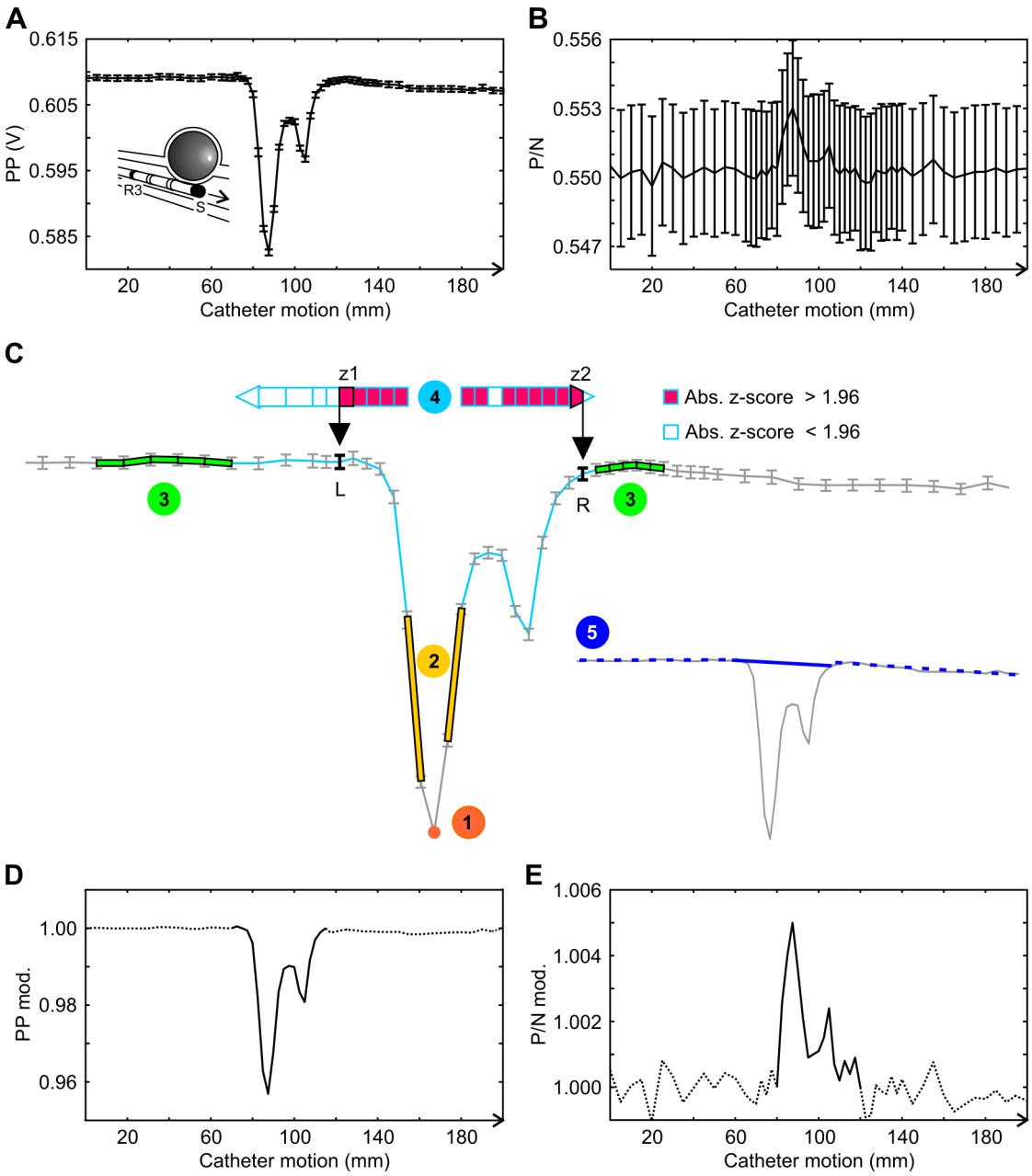
A
0.615
0.605
0.595
0.585
PP (V)
R3
S
20
60
100
140
180
Catheter motion (mm)
B
0.556
0.553
0.550
0.547
P/N
20
60
100
140
180
Catheter motion (mm)
C
z1
z2
4
Abs. z-score > 1.96
Abs. z-score < 1.96
3
L
R
3
2
5
1
D
1.00
0.98
0.96
PP mod.
20
60
100
140
180
Catheter motion (mm)
E
1.006
1.004
1.002
1.000
P/N mod.
20
60
100
140
180
Catheter motion (mm)

Figure A.2.2: (next page) Routine to compute an artery's 2-D, dynamic amplitude and waveform modulation profile with plaque-evoked electric image.

(A) Four PP amplitude traces (light-dark gray) were acquired with the multi-electrode electrolocation catheter via pullback through a (pig) coronary artery (white) with synthetic plaque (white/black), as illustrated in the bottom left inset. The four receivers (R1-4) of the catheter's third electrode ring (Er3), with which the amplitude traces were obtained, as well as the catheter's sender (S) are highlighted in black, indicating catheter configuration S–Er3. Each position of the amplitude traces represents the mean ± SD of n ≥ 71 PP values. **(B-C)** Multi-stage algorithm (custom Matlab routine) for computing an artery's 2-D, dynamic mod. profile with plaque-evoked electric image. The routine and its processing steps are illustrated and explicated with the amplitude trace of catheter receiver R2 as input. The processing of the other catheter receivers' amplitude traces works in the same way and is thus not shown in this figure. Waveform mod. profiles and images, which are also not depicted in this figure, are obtained by analogous computations of the algorithm. **(B)** In the routine's first processing step the peripheral sections of the amplitude trace are estimated. To do so, the trace's slopes were ranked from low to high (absolute) values. Then a group of 'baseline' slopes (circles with green outlines) was selected by excluding the eight steepest slopes of the trace (i.e., a cut off of 35 % of the data). Baseline slopes were then used to reference the trace's peripheral sections in further computations. **(C)** The following steps, 2 and 3 (of the routine), served to locate the trace's plaque-evoked central section and to define its width. First, the group of baseline slopes (n = 23) was averaged. Their mean and corresponding standard deviation was then used to z-score all slopes (light blue lines) of the amplitude trace (step 2). The slopes' (absolute) z-scores are depicted color-coded within the blue-framed boxes above the PP trace. z-scores larger than 1.96 are marked in red, whereas scores below 1.96 are indicated in white. The trace's central section is then located (step 3) by detecting the lowest PP value of the trace (indicated by an orange dot). Starting from this position, the expansion of the central section to the left and right (as indicated by the uppermost orange arrows) was determined by taking the z-scores of the trace's slopes and the slopes' directions (+ or -, as labelled below the z-scores) into account (step 3). The central section's left rim (L, black) is marked (black arrow) by the leftmost z-value (z1), which belonged to a negative slope, had a z-score above 1.96 and marked the end of a row of z values above 1.96, which may include a single value below 1.96. The central section's right rim (R, black) is indicated (black arrow) by the rightmost z-value (z2), which belonged to a positive slope and accords to the rules mentioned above. Eventually, in step 4, a linear fit (dashed blue line) or third degree polynomial fit (dashed blue curve) is applied to the peripheral sections of the amplitude trace, whereas its plaque-evoked central section is fitted with a line (solid blue line). The fits (lines and curve) provide PP expectancy values, which would have been obtained in the artery without a synthetic plaque present. By dividing expectancy and recorded values a trace of amplitude modulations is obtained. **(D)** Combined as a color-coded map, the amplitude mod. traces of R1-4 form the 2-D, dynamic amplitude mod. profile of the artery with the electric image (framed by a black line) in its center. The profile's peripheral sections provide almost entirely basal modulations (~1), whereas the plaque-evoked electric image also shows pronounced modulations (below 1).

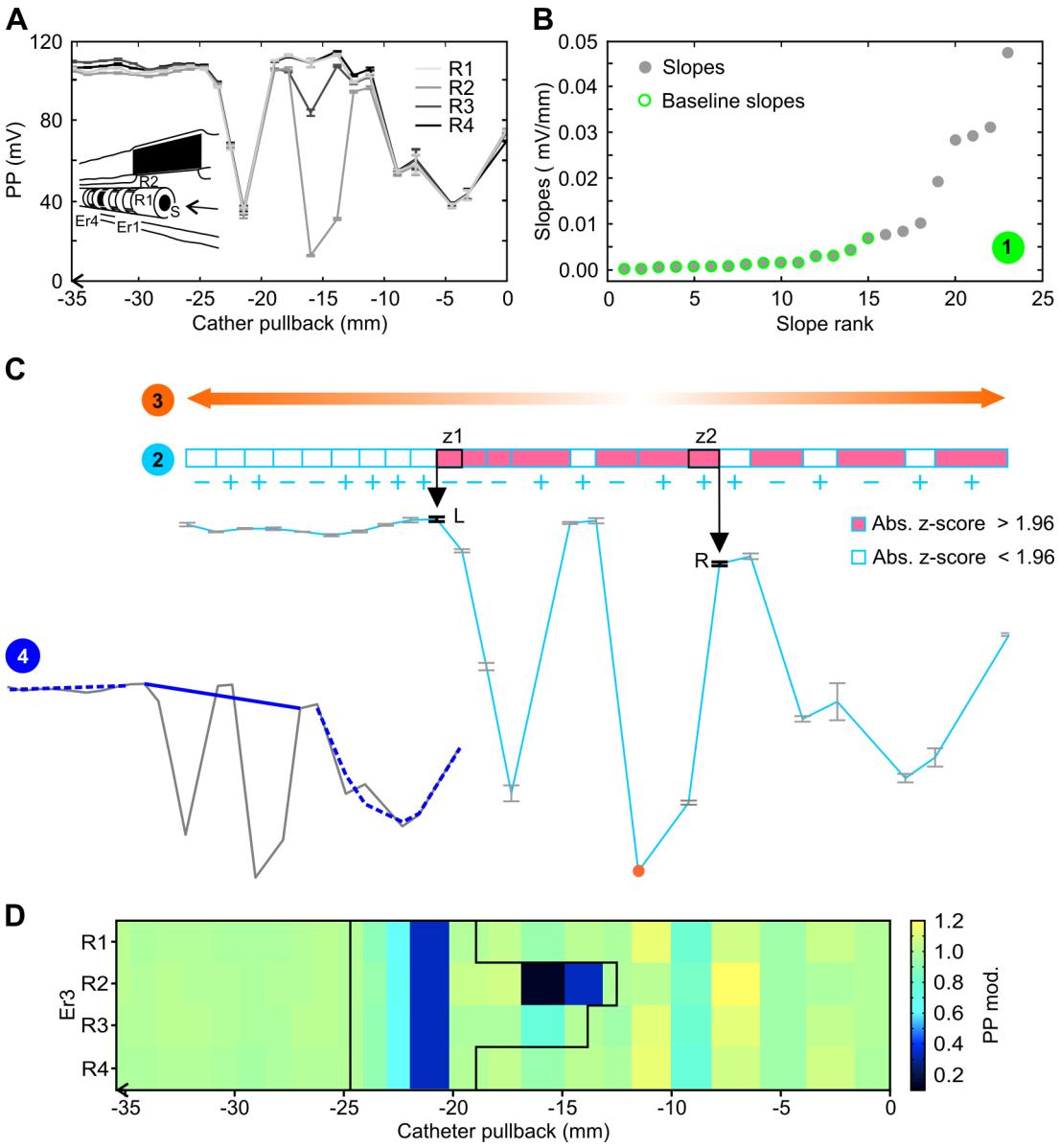
A
PP (mV)
Cather pullback (mm)
R1
R2
R3
R4
Er4
Er1
B
Slopes (mV/mm)
Slope rank
Slopes
Baseline slopes
C
z1
z2
L
R
Abs. z-score > 1.96
Abs. z-score < 1.96
D
Er3
Catheter pullback (mm)
PP mod.

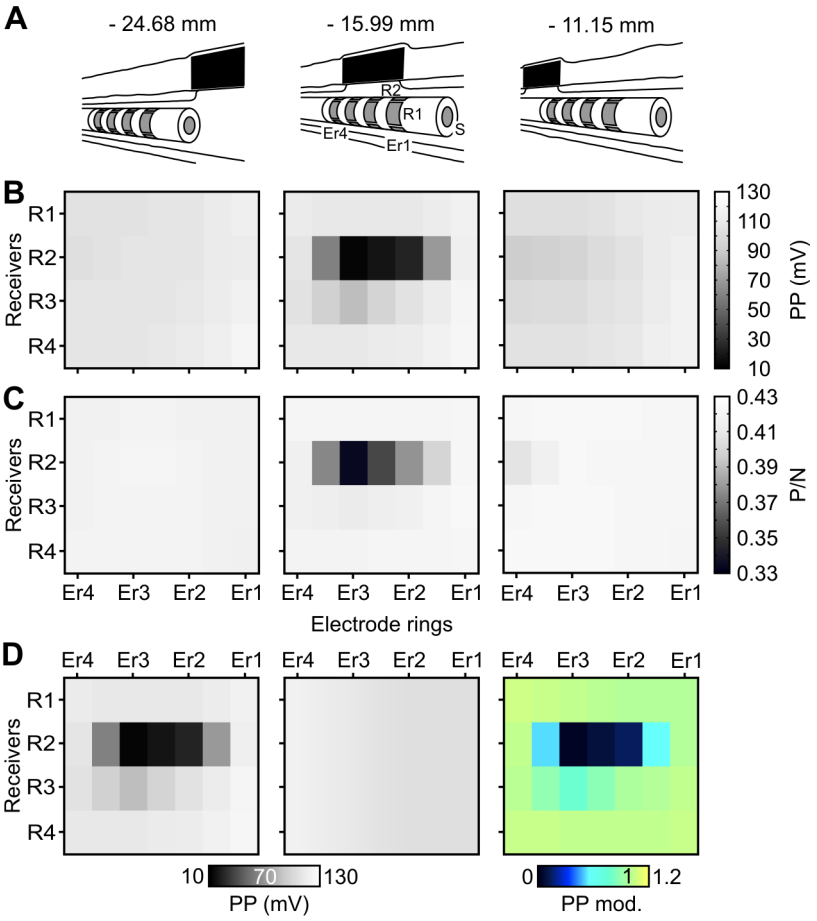

Figure A.2.3: Routine to compute a plaque-evoked, 2-D, static amplitude and waveform image.

(A) Schematic drawings depicting the multi-electrode electrolocation catheter at different pullback positions (labeled above) within the (pig) coronary artery (white), i.e., in front of (leftmost sketch), under (mid. sketch) or (rightmost sketch) behind the synthetic plaque (white/black). The catheter electrodes, i.e., the sender (S) and the electrode rings' receivers (R1-4 of Er1-4) are partly labeled in the middle sketch and are highlighted in gray in all illustrations. **(B)** 2-D, grey-scale amplitude profiles, acquired by all catheter receivers (i.e., R1-4 of Er1-4) at the pullback positions indicated in (A). Each pixel of an amplitude profile depicts the mean of n ≥ 71 PP amplitude values. **(C)** 2-D waveform profiles shown in the same manner as in (A). Each pixel of a waveform profile is a mean of n ≥ 71 P/N values. **(D)** Procedure (custom Matlab routine) for computing the synthetic plaque's 2-D, static electric images. The routine is explicated with the amplitude profiles as input. While not depicted in this figure, the routine works in the same way to process the waveform profiles. The routine requires two profiles, i.e., the one that was acquired with the catheter placed under the plaque (leftmost) and an amplitude profile (middle), which combines those acquired with the catheter in front of and behind the plaque (peripheral profile). The peripheral profile is computed by pooling the PP pixels from the same columns of its two templates, then averaging them and by using these 7 means to form the 7 columns of the peripheral profile. Eventually, the plaque-evoked PP profile is divided by the peripheral PP profile providing the amplitude modulations sculpting the plaque's color-coded amplitude image (rightmost).

A.3 Supplemental information (related to chapter 10)

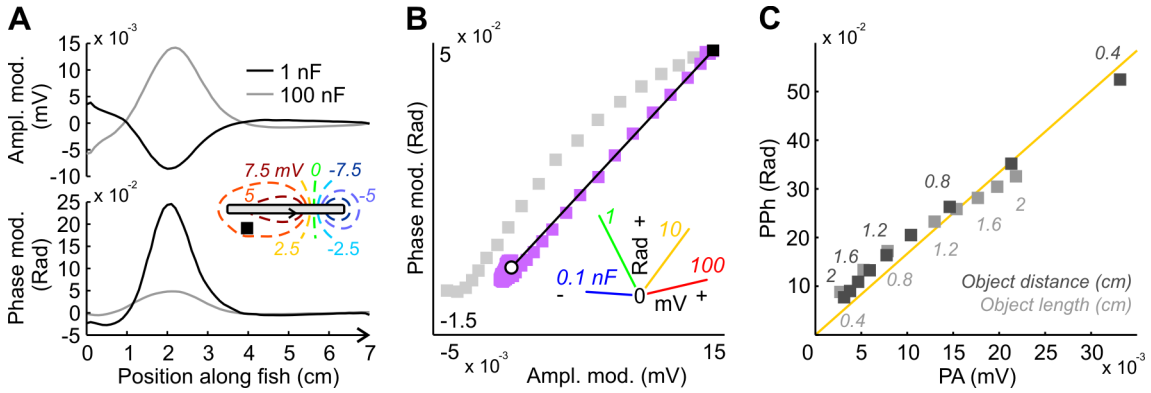

Figure A.3.1: Electric-color cues in weakly electric fish *Eigenmannia*.

(A) Electric amplitude (top) and phase images (bottom) evoked by a 1 or 100 nF target (black square, see inset) close to the side of a simplified *Eigenmannia* model (gray rectangle). Isopotential lines of the electric field that surrounds the fish due to its (continuous) electric emissions are shown color-coded with respect to their local voltages (mV). Electric images were obtained along the electroreceptive fish skin (indicated by the black arrow at the side of the fish). They result from the object-induced modulations of the electric emission's locally received amplitudes and phases. The images' modulations get stronger the more they deviate from 0. Their central peak modulation, i.e., peak amplitude or 'PA' (in the amplitude image) and peak phase or 'PPh' (in the phase image), has the largest deviation from 0. Figure A.3.1A was redrawn after (Fujita and Kashimori, 2010) and modified. Electric-color analyses depicted in figures A.3.1B and C were peformed with the electric image data published in (Fujita and Kashimori, 2010). **(B)** Electric color of the 100 nF object was evaluated by plotting the modulations of its amplitude and phase image against one another, in a scattergram, as amplitude-phase modulation pairs (gray and purple rectangles). Purple highlighted modulation pairs originate from equally shaped areas of the amplitude and phase image. They were determined with the same algorithm that was previously used to explore electric-color estimations in *G. petersii* (chapter 5). Briefly stated, it computes the images' normalized profiles, subtracts them and defines image sections with modulation differences within a certain range (here: ± 0.05) as equally shaped (for more details refer to chapter 5). The linear pathway towards the scattergram's origin (open circle), formed by the purple modulation pairs, indicates a proportional relationship of amplitude and phase modulations, which represents the target's electric color. It can further be estimated by the images' peak modulation pair (black rectangle), which connects to the scattergram's origin via a pathway-congruent 'electric-color line' (black). This way, individual electric-color lines of several capacitive objects (see inset) could accurately be acquired. Encoded by the lines' slopes, electric colors are simply computed as the ratio of both peak modulations, i.e., a mechanism that is proposedly used by *G. petersii* for electric-color extraction (see chapter 5) and, as shown here, is principally also available to *Eigenmannia* species **(C)** Peak modulation (PA-PPh) pairs obtained for a 10 nF target with either varying sizes (light gray rectangles) or proximities to the fish (dark gray rectangles) provide similar PPh-to-PA ratios (electric colors) and fit a single color line (yellow). *Eigenmannia* could thus use electric colors as distinctive identifiers of capacitive targets.

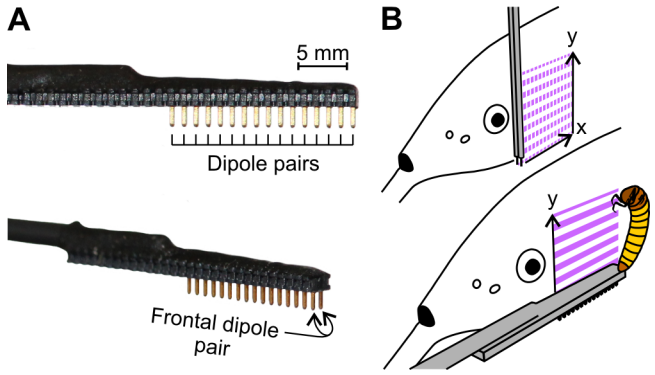

Figure A.3.2: Multipole electrode for electric image acquisitions.

(A) Sideview of a new multipole electrode (designed by M. Gottwald; manufactured by Micromotive GmbH, Mainz, Rhineland-Palatinate, Germany) for recordings of 2-D electric images. It features 16 dipole pairs, the first one of which is shown in detail below. The electrode will be used in combination with a custom-build amplifier (P. Blasczyk, Mechatroniklabor IZMB, Bonn University), providing a differential recording channel for each dipole pair, and two 8-channel oscilloscopes (NI PXI 5051, National Instruments, Austin, Texas, USA). Electric image aqcquisitions with the devices will be monitored via a custom-written LabVIEW program (National Instruments). **(B)** To record electric images, the multipole electrode (dark gray, bottommost) is placed close to the head of a (discharging and anaesthetized) weakly electric fish such as *G. petersii* (white). It is then moved to 9 (dorso-ventral, y) positions in 2 mm steps (purple traces mark positions 3-9, the others are covered by the electrode). Electrode positioning is achieved with a computer-guided motor system as used in previous experiments (chapters 5 and 6). At each position the fish's local electric organ discharges (lEODs) are sampled simultaneously along the electrode's dipole pairs, in the presence and absence of an electrolocation target, e.g., a caddis worm (yellow). The LabVIEW program then calculates the lEOD's peak-to-peak amplitudes (PP) and (for a pulse-type fish like *G. petersii*) lEOD waveform estimators (P/N ratios). Their target-evoked modulations are determined by dividing the PP or P/N values obtained with the caddis worm by those gained without it and by subtracting 1 from these ratios. The caddis worm's amplitude and waveform image (15 mm × 16 mm) is eventually depicted, in full resolution, via linear interpolation of the recorded 16 × 9 (144) to 16 × 17 (272) modulations. Advantagously, electric image acquisitions, as described above, would be conducted whithin a few minutes. Conversely, conventional recordings with a dipole electrode (dark gray, uppermost), which would have to be moved in 1 mm (rostro-caudal, x) and 2 mm (dorso-ventral, y) steps to 144 individual recording positions (purple squares, uppermost), would take ~1.8 hours. In future experiments, the fast image recordings with the multipole electrode could enable extensive investigations of electric image cues that might be commonly perceived among several species of weakly electric fish. Examples of such critical cues may be electric colors as suggested in chapter 10, section 10.1.

Danksagung

An erster Stelle danke ich Herrn Prof. Dr. Gerhard von der Emde für die Möglichkeit diese Dissertation in seiner Arbeitsgruppe anzufertigen und die freundliche, unterstützende Betreuung während der Entstehung dieser Arbeit sowie bereits zuvor. Bei Priv.-Doz. Dr. Helmut Schmitz möchte ich mich für die Übernahme des Korreferats bedanken. Desweitern danke ich Prof. Dr. Lukas Schreiber und Prof. Dr. Stefanie Kürten für ihre Bereitschaft als Gutachter in meiner Promotionskommission zu fungieren.

Ganz herzlich möchte ich mich auch bei Raya Bott, André Haubrich, Anna Matuschek, Sophia Regett und Neha Singh bedanken, die ihre Bachelor/Masterarbeiten im Rahmen meiner Forschungsprojekte angefertigt haben; ohne euer besonderes Engagement wären diese aufwendigen Mess/Verhaltensversuche nicht möglich gewesen.

Mein Dank gilt weiterhin den universitären Werkstätten (Feinmechanik-Werkstatt des IZ und HISKP) welche diverse Messobjekte, als auch Proben-/Katheter-/Elektrische-Kamera- und Fisch-Halterungen für die Versuchsaufbauten hergestellt haben. Dem Mechatroniklabor des IZMB danke ich für die Konstruktion eines Mehrkanal-Messverstärkers der zusammen mit einer neuen Messelektrode künftige Aufnahmen elektrischer Bilder bei schwach elektrischen Fischen erleichtern sollte. Der Firma Micromotive GmbH danke ich für die Fertigung oben genannter Elektrode sowie der Prototypen von Elektroortungskathetern und elektrischer Kamera.

Dr. Hendrik Herzog möchte ich für die Entwicklung der Elektronik der elektrischen Kamera danken und die gute Zusammenarbeit während des Projektes. Bei Sven Rau bedanke ich mich ganz besonders für die Unterstützung bei der Erstellung diverser Messprogramme die in den einzelnen Forschungsvorhaben zum Einsatz kamen.

Der Deutschen Forschungsgemeinschaft (DFG) möchte ich für mein Doktoranden-stipendium im Rahmen des ehemaligen DFG Graduiertenkollegs Bionik (GRK 1572) und den damit verbundenen Fördermitteln danken. Bei den Organisatoren des GRK Bionik bedanke ich mich für die vielen hilfreichen Veranstaltungen/Fortbildungen an denen ich teilnehmen konnte.

Bedanken möchte ich mich auch bei der gesamten Arbeitsgruppe Neuroethologie/Sensorische Ökologie für die gute Arbeitsatmosphäre und insbesondere bei den beiden Technischen Assistentinnen Bärbel Bauch und Ute Grundtner für ihre Hilfe bei der Pflege/Haltung der Versuchstiere und organisatorischen Angelegenheiten. Meinen

beiden ehemaligen Mitdoktoranden Dr. Sarah Schumacher und Dr. Martin Worm gilt ebenfalls ein besonderer Dank für die vielen unterhaltsamen Feierabendgespräche (damals und heute).

Zu guter Letzt ein großes Dankeschön an meine Familie und Freunde für eure Unterstützung während der Zeit meiner Doktorarbeit und ihrer Herausforderungen. Vielen Dank!

Publikationen

Paper

Gottwald, M., Herzog, H. and von der Emde, G. (2019). A bio-inspired electric camera for short-range object inspection in murky waters. *Bioinspir. & Biomim.* **14**, 035002–1–10.

Gottwald, M., Singh, N., Haubrich, A. N., Regett, S. and von der Emde, G. (2018). Electric-Color Sensing in Weakly Electric Fish Suggests Color Perception as a Sensory Concept beyond Vision. *Curr. Biol.* **28**, 3648–3658.

Gottwald, M., Bott, R. A. and von der Emde, G. (2017). Estimation of distance and electric impedance of capacitive objects in the weakly electric fish *Gnathonemus petersii*. *J. Exp. Biol.* **220**, 3142–3153.

Gottwald, M., Matuschek, A. and von der Emde, G. (2017). An active electrolocation catheter system for imaging and analysis of coronary plaques. *Bioinspir. & Biomim.* **12**, 015002–1–17.

Gottwald, M. and von der Emde, G. (2013). Bio-Inspired Active Electrolocation Sensors for Inspection of Tube Systems. *Adv. Sci. Technol.* **84**, 45–50.

Mayekar, K., Damalla, D., **Gottwald, M.,** Bousack, H. and von der Emde, G. (2012). A multi-electrode biomimetic electrolocation sensor. *Proc. SPIE, Bioinspiration, Biomimetics, and Bioreplication* **8339**, 83390A–1–11.

Metzen, M., Biswas, S., Bousack, H., **Gottwald, M.,** Mayekar, K. and von der Emde, G. (2012). A biomimetic active electrolocation sensor for detection of atherosclerotic lesions in blood vessels. *IEEE Sensors J.* **12**, 325–331.

Mayekar, K., Damalla, D., **Gottwald, M.,** Bousack, H. and von der Emde, G. (2011). Characterization of a Bionic Electrolocation Sensor using Finite Element Modeling. *IEEE Sensors 2011 Conf. (Limerick, Ireland)* pp. 978–981.

Gottwald, M., Mayekar, K., Reiswich, V., Bousack, H., Damalla, D., Biswas, S., Metzen, M. G. and von der Emde, G. (2011). Inspection and analysis of the walls of fluid filled tubes by active electrolocation: a biomimetic approach. *Proc. SPIE, Bioinspiration, Biomimetics, and Bioreplication* **7975**, 797510–1–15.

Abstracts

Knechtges, L., **Gottwald, M.,** von der Emde, G. Shape discrimination in weakly electric fish *Gnathonemus petersii*: local or global cues? *111. Jahrestagung der Deutschen Zoologischen Gesellschaft*, Greifswald, Germany, 10–15.09.2018.

Wolf, P., **Gottwald, M.,** von der Emde, G. and Herzog, H. Weakly electric fish as models for electric imaging of objects under water. *111. Jahrestagung der Deutschen Zoologischen Gesellschaft*, Greifswald, Germany, 10–15.09.2018.

Gottwald, M., Rau, S., and von der Emde, G. Biomimetic Catheter Systems for Analysis of Arterial Diseases. *Jahrestagung des Bonner Forum Biomedizin (BFB),* Hennef, Germany, 06–07.02.2014.

Gottwald, M., Hamann, L., Bott, R., Rau, S. and von der Emde, G. Electric images of resistive and capacitive objects at the head of the weakly electric fish *G. petersii*. *106. Jahrestagung der Deutschen Zoologischen Gesellschaft*, München, Germany, 13–16.09.2013.

Gottwald, M. and von der Emde, G. Biomimetic Active Electrolocation Sensors for Inspection of Tube Walls, *International Workshop on Robotic Electrosense*. Maryland, USA 03.08.2012.

Gottwald, M., Mayekar, K. and von der Emde, G. Diagnosis of coronary plaques by active electrolocation – a bionic approach, *BMT Conference*, Freiburg, Germany 27–30.09.2011.